# AN ABSTRACT OF THE DISSERTATION OF

Paul D. Keir for the degree of Doctor of Philosophy in

Electrical & Computer Engineering presented on August 2, 1999. Title:

Fabrication and Characterization of ACTFEL Devices

Redacted for Privacy

Abstract approved: _____

John F. Wager

The goal of this thesis is the identification and synthesis of high-luminance, primary color alternating-current thin-film electroluminescent (ACTFEL) devices. Special attention is paid to the synthesis of primary color green ACTFEL devices because of the lack of an adequate primary green ACTFEL phosphor and the dominance of green wavelengths in the response of the human eye. The sulfide materials family is the focus of this investigation of ACTFEL phosphor hosts due to its importance in the field of electroluminescence, although oxide and selenide phosphor hosts are also considered. Particular attention is paid to the coactivation of the SrS:Cu ACTFEL phosphor because of the ability to control the emission spectrum with coactivators. Green ACTFEL devices exhibiting a high-luminance, high-efficiency, saturated green color are demonstrated via the coactivation of SrS:Cu with alkali metals. In addition, $Zn_2GeO_4$:Mn is demonstrated as a potentially bright and stable ACTFEL phosphor. Finally, the "phosphor sandwich" technique of ACTFEL fabrication is presented as a means of depositing highly-stable, high-luminance ACTFEL phosphors.

The fabrication techniques presented in this thesis are subsequently employed to deposit custom ACTFEL devices for characterization studies aimed at determining fundamental physical properties of ACTFEL phosphors. A method for establishing the relative hot electron distributions inside operating ACTFEL phosphor hosts is presented. In addition, the fabrication of SrS:Cu ACTFEL devices for characteriza-

tion has allowed new insight into the density and physical basis of phosphor space charge. This insight is gained by monitoring the electrical and optical characteristics of SrS:Cu ACTFEL devices coactivated with various non-isovalent impurities to assess the influence of native defects and extrinsic impurities on space charge related behavior. It is found that native sulfur vacancies are not the physical basis for dynamic space charge in SrS:Cu ACTFEL devices.

Fabrication and Characterization of ACTFEL Devices

by

Paul D. Keir

A DISSERTATION

submitted to

Oregon State University

in partial fulfillment of
the requirements for the
degree of

Doctor of Philosophy

Completed August 2, 1999
Commencement June 2000

Doctor of Philosophy dissertation of <u>Paul D. Keir</u> presented on <u>August 2, 1999</u>

APPROVED:

# Redacted for Privacy

Major Professor, representing Electrical & Computer Engineering

## Redacted for Privacy

Chair of the Department of Electrical & Computer Engineering

## Redacted for Privacy

Dean of the Graduate School

I understand that my dissertation will become part of the permanent collection of Oregon State University libraries. My signature below authorizes release of my dissertation to any reader upon request.

## Redacted for Privacy

Paul D. Keir, Author

# ACKNOWLEDGMENT

# TABLE OF CONTENTS

# TABLE OF CONTENTS (Continued)

# LIST OF FIGURES

# LIST OF TABLES

# FABRICATION AND CHARACTERIZATION OF ACTFEL DEVICES

## 1. INTRODUCTION

For many years, the cathode-ray tube (CRT) has dominated the information display marketplace. The reason for this dominance is that the CRT is a relatively mature technology compared to other display technologies. The advantages that CRT displays offer are excellent chromaticity, contrast, and resolution at an affordable price. The main drawbacks of CRT displays are their fragile nature, large size, and high power consumption. These drawbacks have little relevance when a display is intended for use as a home television set or a home computer monitor. However, during the past decade, there has been an intense drive towards portability for many display-utilizing products, necessitating displays that are physically smaller, more rugged and less power-hungry than the venerable CRT.

The drive for portability has fueled a large amount of research into alternative display technologies during the past fifteen to twenty years. Most of the research involving non-CRT display technologies is focused upon developing a thin display, known as a flat-panel display (FPD), that has the quality of a CRT display, but is rugged and much less power hungry than a CRT display of comparable viewing area. The clear front-runner in this effort is the liquid-crystal display (LCD) which is found in virtually every laptop computer manufactured today. [1] Other less well-known display technologies showing promise are the plasma display panel (PDP), the field-emission display (FED), and the thin-film electroluminescent (TFEL) display. All of the flat-panel display technologies require significant amounts of research and development to match the quality and affordability of the CRT, but LCDs are years, if not decades ahead of competing FPD technologies in terms of technological maturity.

It is naive to think that the LCD could be rivaled by any other FPD technology in the very near future; however, the plasma display, the FED, and the TFEL display are all currently commercially produced and are competitive in certain niche markets. The PDP seems ideally suited for use as a large area display (>20" diagonal), a display size far too large to be rivaled by LCDs with the current state of LCD technology. The FED is the least mature of all of the technologies mentioned, but is presently attracting great interest due to the potential for very high brightness FPDs. [2] The TFEL display seems well suited for production of small displays (<4" diagonal) and displays requiring operation in harsh environments. If all of the FPD technologies continue the maturation process, the day may arrive when each display technology owns a portion of the display market in which it excels.

The subject of this thesis is alternating-current TFEL (ACTFEL) displays, and specifically the materials that comprise the ACTFEL display. Since the dominant flat-panel display technology is the LCD, an alternative flat-panel display technology must gauge itself in terms of the LCD. The advantages of ACTFEL displays in comparison with LCDs are the ability to pattern much smaller pixels, performance over a wider temperature range, full-viewing angle, and readability with much greater intensity background light. The disadvantages of ACTFEL displays in comparison with LCDs are larger power consumption, lack of adequate chromaticity of the three primary colors, and much larger driving voltages. Of the three main disadvantages of ACTFEL displays in comparison with LCDs, the most serious and most researched has been the lack of adequate chromaticity. Historically, the main roadblock in the path to manufacturing an adequate full-color ACTFEL display has been the lack of a sufficiently bright blue phosphor. However, recent blue phosphor developments should lead to much improved full-color ACTFEL displays in the very near future. Although strides have been made in improving the blue component of an ACTFEL display, there is still room for improvement in all three of the primary colors of ACT-FEL displays in terms of both brightness and efficiency. Therefore, the goal of this

thesis is to deposit and test materials suitable for ACTFEL displays in an effort to improve the overall performance of the primary phosphor colors in terms of brightness, efficiency, and stability. Especially important in the near future is the development of a green phosphor with enough brightness to maintain the correct ratio of brightness between the red, green and blue phosphors. For this reason, the development of green ACTFEL phosphors is the main emphasis of this thesis, although phosphors of other colors have not been entirely ignored.

The structure of this thesis is as follows. Chapter two provides a review of currently available literature and experimental techniques relevant to this thesis. Chapter three investigates ACTFEL materials and the techniques and processes employed for their deposition. Chapter four presents the results obtained from fabrication of ACTFEL devices of various phosphor hosts. Chapter five investigates the characterization of ACTFEL devices fabricated in-house in an effort to gain insight into the operation of these devices. Finally, Chapter 6 presents conclusions and recommendations for future work.

## 2. LITERATURE REVIEW

This chapter presents a review of currently available literature pertaining to ACTFEL materials, devices, and testing. The chapter begins by examining the structure and operational physics of an ACTFEL device. Then, materials and materials issues in ACTFEL fabrication are considered. Finally, characterization and testing of ACTFEL materials and devices is examined.

### 2.1  ACTFEL Device Structures

An ACTFEL device consists of several constituent thin-film layers that are all important in terms of device operation. All ACTFEL devices consist of a phosphor layer, at least one insulating layer, an opaque conductor, a transparent conductor, and a substrate. However, there are three different general structures comprising the aforementioned layers commonly employed when fabricating ACTFEL devices for testing purposes.

The first structure, the "standard" structure, consists of a phosphor layer encapsulated by two insulating layers, with contact to the top insulator made by an opaque conductor and to the bottom insulator by a transparent conductor. The standard structure for ACTFEL device fabrication is deposited onto a transparent substrate and light reaches the viewer through the substrate, as shown in Fig. 2.1 (a). The second structure, the "inverted" structure, also consists of a phosphor layer encapsulated by two insulating layers, but contact is made to the top insulator by a transparent electrode and to the bottom insulator by an opaque electrode. The inverted structure for ACTFEL device fabrication can be deposited onto either a transparent substrate or an opaque substrate, because the light reaches the viewer through the transparent top electrode, as shown in Fig. 2.1 (b).

The standard and inverted ACTFEL device structures are both used in commercial processes, and the choice of which structure to use is often dictated by pro-
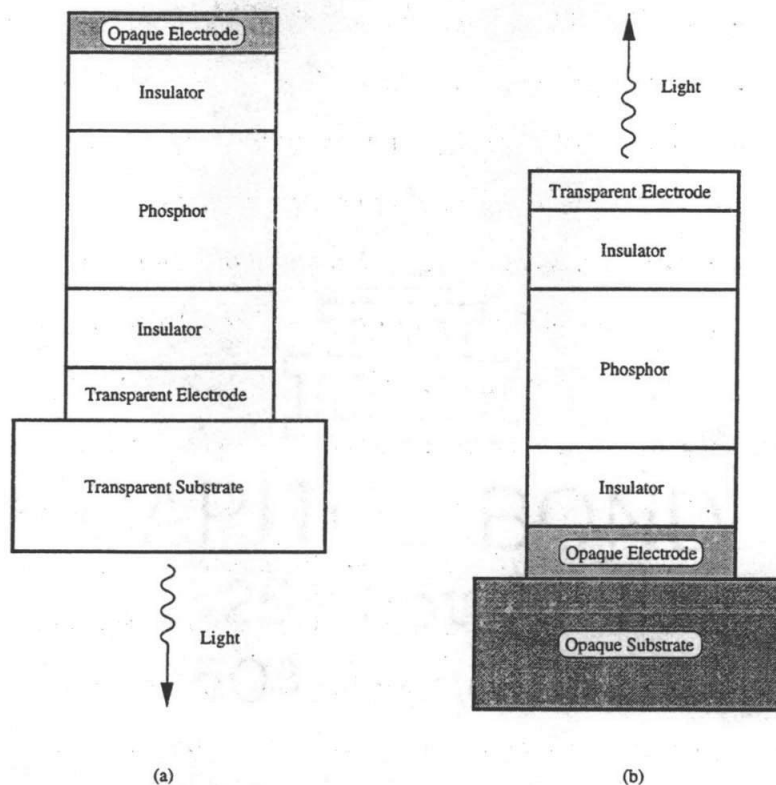
Figure 2.1: (a) The standard ACTFEL device structure. (b) The inverted ACTFEL device structure.

cess requirements, process limitations or intended device applications. The standard structure is the preferred structure for test devices and monochrome passive-matrix displays because it requires a less complex process than the inverted structure. The most important advantage of the standard structure is that it exhibits so-called self-healing breakdown when a suitable top electrode is deposited. [3] The self-healing breakdown property prevents small pinholes and defects from causing catastrophic device failure by effectively open-circuiting microscopic defective areas of the ACTFEL device. Another advantage of the standard structure is inherent durability because the active device layers are shielded from the viewer by the glass substrate. However, the inverted structure possesses several distinct advantages over the standard structure, and is therefore preferred for certain applications. When high temperature process steps are necessary, the standard structure is unusable because the glass sub-

strates necessary for this structure begin melting around 600°C. Unlike the standard structure, there is the option of depositing on opaque substrates when the inverted structure is employed, allowing the use of high-temperature tolerant ceramic or silicon substrates. Another case where the inverted structure is preferred over the standard structure is when color filtering is required. When adding filter layers to a device it is advantageous to deposit these layers on top of a finished device because simple organic color filters that are sensitive to further process steps can be used. [4] However, when the standard structure is employed, it is necessary to deposit the color filter layers first because light is viewed through the substrate. The main disadvantage of the inverted structure is that self-healing breakdown characteristics are not achievable with transparent top-electrodes. This necessitates extremely low defect density ACTFEL devices for stable and reliable inverted structure ACTFEL device operation. This requirement greatly increases the processing complexity, and hence cost, because special processing techniques are required.

The third ACTFEL device structure that is sometimes used for testing purposes is the "one-insulator" structure. The one-insulator structure is essentially either the standard structure or the inverted structure minus either of the insulator layers. This structure is used in ACTFEL testing because the elimination of an insulator deposition process step allows devices to reach the testing phase more rapidly. For certain applications, a one-insulator structure is used with the phosphor layer deposited directly on a thick insulating ceramic sheet that serves the dual purpose of the substrate and an insulator layer. [5] A cross-section of a device of this type is shown in Fig. 2.2. [6] Although the one-insulator structure has advantages in terms of ease of device fabrication, it is not used in commercial products because it exhibits lower luminance, affords less protection for the phosphor layer, and is not compatible with long-term device reliability.

Light Emission
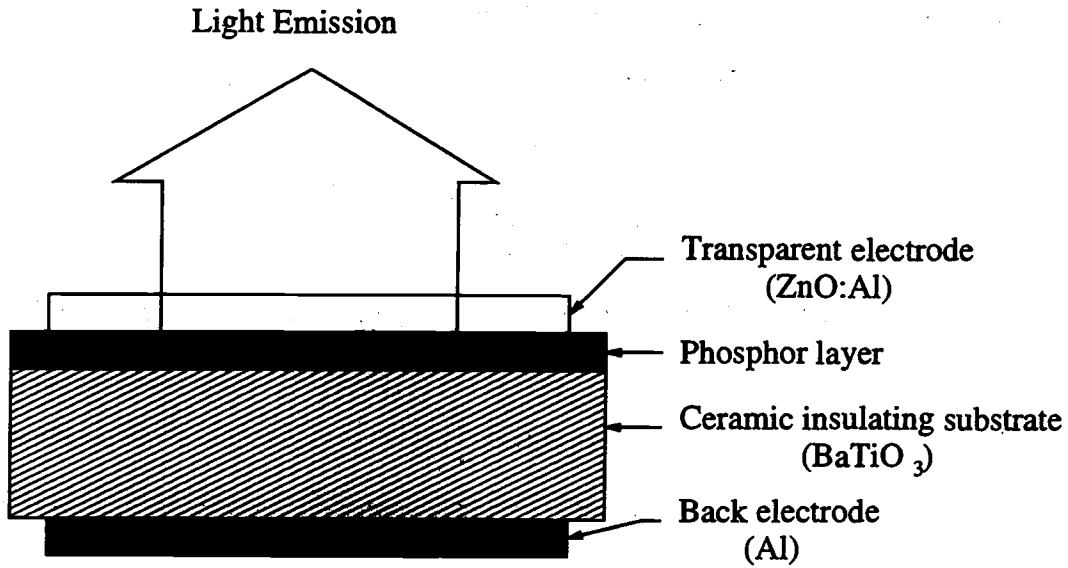


Figure 2.2: Cross-sectional structure of an ACTFEL device deposited on an insulating BaTiO₃ sheet.

## 2.2  ACTFEL operation

Since the advent of ACTFEL devices in the mid-1970's [7], researchers have spent a considerable amount of time trying to fully understand their operation. As a result of this research, most of the basic operation of ACTFEL devices is believed to be understood. However, in the modeling of any electronic device, there are several higher-order effects that may be very important in certain situations, and relatively unimportant in others. This section examines the basic or zero-order operation of a two-insulator ACTFEL device and then introduces some of the higher-order complications to this zero-order model.

When an ACTFEL device is driven at AC voltages with amplitude below the threshold voltage of the device, the electrical characteristics are akin to a simple capacitor. The insulating layers and the wide-bandgap semiconductor phosphor layer all have equivalent capacitances computed from the formula for the capacitance of parallel plates,

$$C_{layer} = \frac{\epsilon_r \epsilon_0}{t_{layer}}. \tag{2.1}$$

Since an ACTFEL device consists of simple layers deposited one atop another, the device looks like a capacitor with a capacitance equal to the capacitances of the individual insulator and phosphor layers in series,

$$C_t = \frac{C_p C_{i,top} C_{i,bottom}}{C_p C_{i,top} + C_p C_{i,bottom} + C_{i,top} C_{i,bottom}}. \tag{2.2}$$

Generally, the insulator layers are lumped together and treated as a single capacitance where

$$C_i = \frac{C_{i,top} C_{i,bottom}}{C_{i,top} + C_{i,bottom}}, \tag{2.3}$$

which leads to the total capacitance being expressed as

$$C_t = \frac{C_i C_p}{C_i + C_p}. \tag{2.4}$$

An important parameter in the operation of an ACTFEL device is the field in the phosphor layer. When a device is driven below the threshold voltage, the phosphor field is given by

$$f_p = \frac{C_i}{C_i + C_p} \frac{V_{applied}}{t_p}, \tag{2.5}$$

where $t_p$ is the thickness of the phosphor layer. Then, when the amplitude of the AC driving voltage reaches the threshold voltage of the ACTFEL device, charge begins to flow through the phosphor, and this purely capacitive behavior is no longer witnessed.

Assuming that an ACTFEL device is being driven by an AC voltage with amplitude greater than its threshold voltage, the zero-order model of device operation proceeds in the following manner. [8, 9, 10] When the magnitude of the applied voltage is below the turn-on voltage of the ACTFEL device, it behaves as a simple capacitor, as described above. Then, when the magnitude of the applied voltage waveform reaches the turn-on voltage of the ACTFEL device, electrons are tunnel emitted from the phosphor-insulator interface on the cathodic side of the device, labeled as process 1 in the energy-band diagram representation shown in Fig. 2.3. [11] The high electric field present in the phosphor layer of the ACTFEL device causes the emitted electrons to drift across the phosphor layer (process 2 in Fig. 2.3). On their
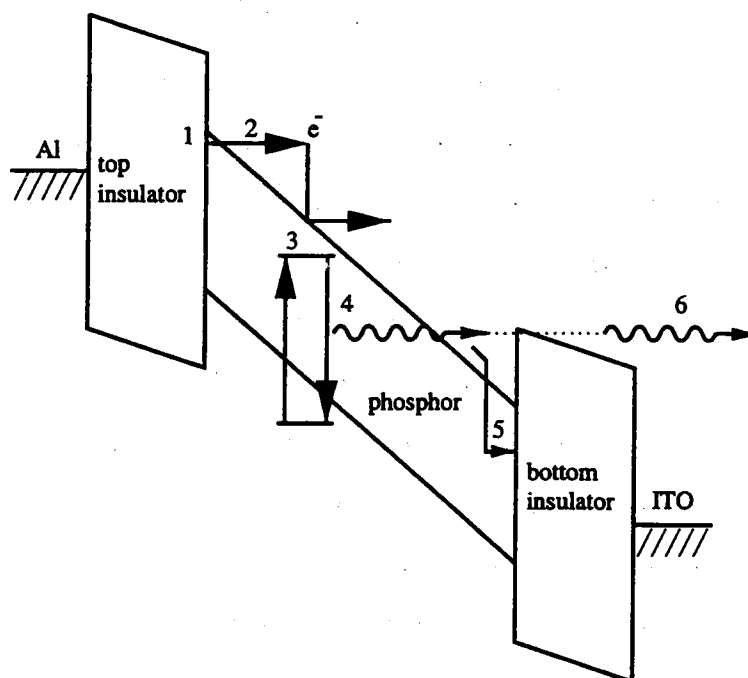
Figure 2.3: Zero-order model of ACTFEL operation.

way across the phosphor layer, electrons may collide with luminescent impurities that absorb some of the energy of impact and are subsequently promoted to an excited state (process 3 in Fig. 2.3). When the luminescent impurities relax to their ground states they may release the additional energy either through the emission of a photon of wavelength particular to the nature of the luminescent impurity (process 4 in Fig. 2.3), or via phonon emission. Obviously, for the sake of optical device efficiency, a large percentage of excited state to ground state transitions that release photons is preferred. The electrons that have slowed from the kinetic energy loss due to the collision quickly gain kinetic energy from the field and may excite additional luminescent impurities as they continue to traverse the remainder of the phosphor layer. Then, as the electrons reach the opposite, or anodic, phosphor-insulator interface, they are captured by one of the many electron traps present due to the disorder of the phosphor-insulator heterojunction (process 5 in Fig. 2.3). Finally, some of the photons released by the luminescent impurities outcouple from the device to reach

the viewer (process 6 in Fig. 2.3). Next, when the AC waveform changes sign, this process repeats in the opposite direction. However, much of the charge that has accumulated at the phosphor-insulator interface persists through interpulse intervals of low duty-cycle waveforms, thereby altering the turn-on voltage of the following pulse of opposite polarity. This is the reason it is necessary to differentiate between the threshold and turn-on voltage of an ACTFEL device.

This simple model of ACTFEL device operation serves to aid in understanding many of the basics of device operation. However, there are several complications to this simple model that occur in real devices which often complicate ACTFEL device analysis. Probably the most important and well-researched deviation from the zero-order ACTFEL device model is phosphor space charge. An operating ACTFEL phosphor is an environment especially prone to the creation of bulk space charge because of the high fields involved in device operation and the large number of defects present. [12, 13, 14] Phosphor space charge has been attributed to three main causes in the literature: field emission from bulk traps [13, 15, 16], impact ionization of deep-level traps [16, 17, 18, 19, 20], and band-to-band impact ionization with subsequent hole trapping. [15, 21, 22, 23, 24, 25] Phosphor space charge has generally been assumed to be positive because all of the II-VI wide bandgap semiconductors that are generally used as ACTFEL phosphors are intrinsically n-type materials. [13] Additionally, most of the luminescent impurities that are added are donor impurities. However, there has always been speculation that negative space charge may arise in certain circumstances [26], although no one has presented conclusive evidence to this end. The presence of space charge in the phosphor layer leads to a non-constant phosphor field profile, as shown in the energy-band diagram of Fig. 2.4. The major complication of this non-constant field profile is that it accentuates the field in certain regions of the phosphor while suppressing it in others. This in turn leads to a non-uniform distribution of space charge throughout the phosphor layer. Furthermore,

since interface emission depends on the phosphor field at the emitting interface [27], phosphor space charge can have a profound effect on current due to interface emission.
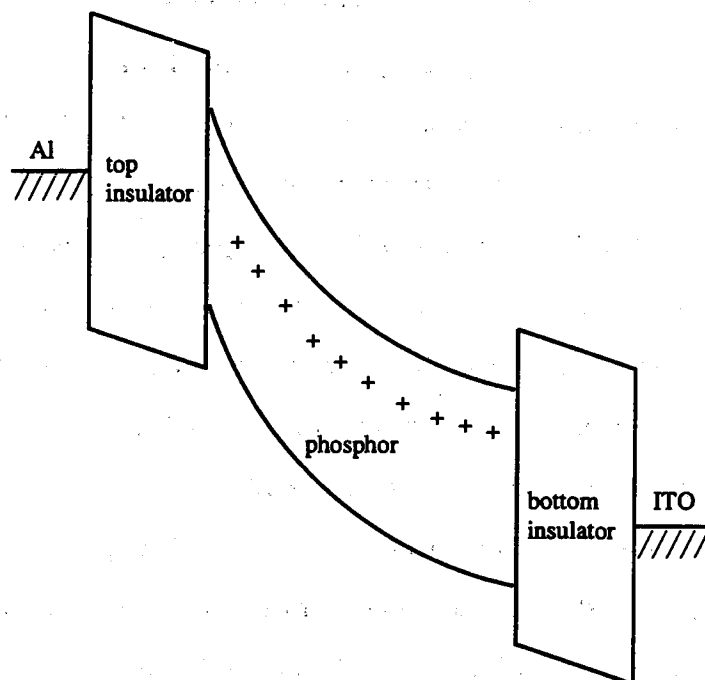


Figure 2.4: Energy-band diagram of an ACTFEL device with positive space charge.

Research has shown that space charge exists in almost all ACTFEL devices. However, quantifying the amount and location of the space charge has proven more difficult. Several papers have been published that give estimates of the average amount of space charge across the phosphor layer for both ZnS:Mn and SrS:Ce phosphors [28, 29], but measurement of the space charge distribution across a phosphor layer has not been reported. However, simulations of ZnS:Mn devices have been performed that yield a space charge distribution across the phosphor. [21] Furthermore, certain phosphor materials have a much greater predisposition to exhibiting space charge related effects, which leads to the belief that certain phosphor layers have much greater levels of space charge than others. However, these effects may have

more to do with the amount of interaction between the conduction charge and the space charge than the physical amount of space charge in the phosphor.

Another area that is not well understood which may affect device performance is the role of holes in the operation of an ACTFEL device. Several authors have reported evidence for the existence of holes during the operation of ZnS based ACTFEL devices. [14, 30, 31, 32, 33, 34] However, it is not known how much of the measured conduction charge is contributed by holes, whether they excite luminescent centers, and how efficiently they can be trapped in the phosphor layer. The II-VI wide-bandgap semiconductors normally employed as ACTFEL phosphors are materials that are known to trap holes because of the high density of native deep-donors [13], so this may contribute to space charge effects considerably. However, the trapping efficiency for carriers in $SiO_2$ is known to decrease exponentially with increasing field [35], implying that the trapping efficiency of the wide-bandgap sulfide phosphors could also be very low at the high fields seen in an operating ACTFEL device. Therefore, it is still debatable what the role of holes might be in ACTFEL operation.

The third great mystery in ACTFEL device operation is the interface state density. Several authors have tried, rather unconvincingly, to measure the interface state density of an ACTFEL device. [27, 36, 37, 38] This has generally led to the conclusion that a high density of interface states exists at energies deeper than about 0.9 eV below the conduction band in ZnS:Mn. However, a field profile change due to the presence of space charge in the phosphor layer invalidates most of these measurements. Also, when band-to-band impact ionization occurs in the phosphor layer, it may appear that much more charge is being sourced from the emitting interface than is actually monitored in an external measuring circuit. Therefore, these difficulties combine to leave little knowledge of the actual interface distribution in ACTFEL devices; although recent insights into the quantity of phosphor space charge present in

an operating ACTFEL device suggest that the peak of the interface state distribution is much deeper than originally thought. [39, 40]

## 2.3 ACTFEL materials

Electroluminescence researchers have constructed ACTFEL devices from a fairly broad range of materials. This section introduces the current commercially viable ACTFEL phosphors along with the phosphors that show potential to become the commercial ACTFEL phosphors of the future. Also examined are the materials commonly used for insulating layers, contacts, and substrates.

### 2.3.1 The phosphor layer

The most important layer of an ACTFEL device in terms of determining its optical characteristics is certainly the phosphor layer because it is the phosphor layer that converts electrical energy into light energy. In addition, the electrical characteristics of an ACTFEL device are strongly dependent upon the nature of the phosphor layer. The phosphor layer of an ACTFEL device is composed of a phosphor host doped with substitutional luminescent impurities at a level on the order of 0.1 molar percent.

The phosphor host material is a material which provides a host lattice for substitutional luminescent impurities. Many different materials and families of materials have been investigated as phosphor host materials. However, the specific demands on ACTFEL phosphors relative to phosphors for other applications renders many phosphor hosts unusable in an ACTFEL device. Due to these strict requirements, only several commercially viable ACTFEL phosphor hosts are known at the present time. Furthermore, these commercially viable ACTFEL phosphor hosts are without exception sulfides, presumably because of superior charge injection properties.

The substitutional luminescent impurities, or activators, that are doped into the phosphor host are the ions from which the light that is visible to the viewer is

emitted. The color spectrum of the light emitted from a phosphor is determined to a large extent by the nature of the luminescent impurity. In addition, the host lattice influences the color spectrum emitted by a luminescent impurity because different phosphor hosts present different local crystal fields in terms of both field strength and field symmetry. However, depending upon the nature of the luminescent transition, the crystal field may be very important or merely a perturbation in determining the color spectrum of the phosphor. For example, the 4f→4f luminescent transitions characteristic of many of the rare-earth ions are relatively insensitive to the crystal field of the host lattice because the 4f orbitals are not the chemically interacting orbitals. Such luminescent transitions are known as "shielded" transitions. On the other hand, the $Mn^{2+}$ luminescent impurity is very sensitive to the crystal field presented by the host lattice because the luminescent transition originates from the outermost electronic shell. This type of luminescent transition is strongly dependent on the host lattice, allowing the possibility to alter the color spectrum by adjusting the crystal field. The crystal field is adjusted in practice by adding additional dopants which affect the lattice constant of a phosphor, thereby influencing its luminescent properties. Additional atoms that are added to a phosphor that influence its luminescent properties, whether they alter the color spectrum or simply affect the luminance, are termed coactivators. As a result, almost all of the naturally occurring atoms in the periodic table have been employed as either luminescent impurities or coactivators in various phosphor hosts.

There are several common deposition techniques for growing phosphor films; rf sputtering, thermal evaporation, electron-beam (e-beam) evaporation, and atomic layer epitaxy (ALE). Each of these deposition techniques has distinct advantages and disadvantages for ACTFEL phosphor deposition. In addition, a deposition technique that is optimal for a specific phosphor material may produce substandard quality thin-films for a different phosphor system. Even when a commercial quality ACTFEL phosphors can be deposited by all of the techniques mentioned above, there are

often noticeable differences in phosphor characteristics depending on the method of preparation. Therefore, it is important to have the capability to deposit an ACTFEL phosphor by a variety of techniques to fully gauge its viability. For example, Tb-activated ZnS is a much brighter and more efficient ACTFEL phosphor when sputtered than when evaporated or deposited by ALE. [4]

The performance of an ACTFEL phosphor is typically gauged by several important output parameters; luminance (brightness), efficiency, and color coordinates. The luminance, or brightness, of an ACTFEL device is a measure of the amount of visible light emitted in a direction normal to its surface. The luminance of an ACTFEL device is typically reported in either the English unit foot-Lamberts (fL or ft-L), or the SI unit candelas per square meter ($cd/m^2$). In addition, the luminances reported for ACTFEL devices are generally photopically corrected to take into account the human eye's sensitivity to the wavelength of light. The efficiency of an ACTFEL device is a measure of light output per unit electrical power input. The efficiency of an ACTFEL device is generally reported in lumens per Watt (lm/W), where a lumen is a measure of the light emitted in all possible emission directions from the surface of the ACTFEL device. Finally, the Commission Internationale de l'Eclairage (CIE) color coordinates are the x and y coordinates on a two-dimensional surface that represents the entire gamut of visible colors. Therefore, CIE coordinates are a method for quantifying the color of an ACTFEL device. It should be noted that while the luminance, efficiency, and CIE coordinates of an ACTFEL device are typically attributed to the phosphor layer, these values are influenced to some degree by the nature and quality of the other layers of the ACTFEL device.

Currently, Mn-activated ZnS and Ce-activated SrS are the only two ACTFEL phosphors with the luminance, efficiency, and stability to be the basis of a commercial product. The most common and well-researched ACTFEL phosphor is ZnS activated with $Mn^{2+}$, or ZnS:Mn. This phosphor material emits amber colored light and is the basis for most of the current commercially available ACTFEL-based products.

The second most common ACTFEL phosphor is SrS:Ce, which has been the subject of considerable research throughout the past 15 years. This phosphor material emits blue to green light depending on the codopants and processing conditions. The SrS:Ce phosphor is most often used commercially in conjunction with ZnS:Mn and color filters to produce multicolor ACTFEL displays. The characteristics of the best reported ZnS:Mn and SrS:Ce ACTFEL devices in terms of the performance criteria discussed above are shown in Table 2.1. [4] It should be noted that $L_{40}$ and $\eta_{40}$ correspond, respectively, to the luminance and efficiency with a driving voltage amplitude 40 volts above the threshold voltage.

Table 2.1: Performance characteristics (60 Hz) of the best reported ZnS:Mn and SrS:Ce phosphors.

| phosphor | $L_{40}$ (cd/m$^2$) | $\eta_{40}$ (lm/W) | CIE x | CIE y |
|----------|---------|---------|-------|-------|
| ZnS:Mn | 310 | 2.0-3.0 | 0.50 | 0.50 |
| SrS:Ce (greenish) | 180 | 1.0 | 0.28 | 0.50 |
| SrS:Ce (blueish) | 155 | 1.0 | 0.20 | 0.38 |

There are two approaches to producing a full-color ACTFEL display, the color-by-white approach and the patterned phosphor approach. The color-by-white approach involves filtering a white ACTFEL phosphor to produce the three primary colors; red, green, and blue. The patterned phosphor approach to full color is based on the idea of patterning pixels of different phosphors that emit the three primary colors. Unfortunately, neither ZnS:Mn nor SrS:Ce is of a color that is similar to white or any of the saturated primary colors. Therefore, these phosphors must either be used for monochrome displays or as components of multi-phosphor ACTFEL devices that try to achieve a white color by mixing two or three phosphor layers in the same device. Due to this lack of adequate chromaticity, there is ongoing research to pro-

duce phosphors of the three primary colors. Table 2.2 presents a list of the target luminancees, efficiencies, and CIE coordinates for the three primary colors.

Table 2.2: Target luminance, efficiency, and CIE coordinates (60 Hz) for a high-luminance full-color ACTFEL display.

| Color | $L_{40}$ (cd/m$^2$) | $\eta_{40}$ (lm/W) | CIE x | CIE y |
|-------|---------------------|--------------------|-------|-------|
| Green | 310 | 2.0-3.0 | 0.30 | 0.60 |
| Red | 155 | 1.0-1.5 | 0.65 | 0.35 |
| Blue | 52 | 0.3-0.5 | 0.15 | 0.10 |

The ambitious goals for the three primary color phosphors shown in Table 2.2 are perhaps not realistic for the short-term future, although significant progress has been made on both the red and blue phosphors recently. A current list of the best primary color phosphors is presented in Table 2.3. The introduction of blue-emitting SrS:Cu and SrS:Cu,Ag phosphors has sparked renewed optimism that competitive full-color ACTFEL displays may soon become a reality. [41, 42] This optimism is fueled by the fact that the best blue phosphors prior to the introduction of SrS:Cu and SrS:Cu,Ag were the Ce-activated alkaline earth thiogallates, $(Sr,Ca)Ga_2S_4$:Ce, which had excellent chromaticity but insufficient luminance and efficiency. The high luminance of blue SrS:Cu and SrS:Cu,Ag phosphors means that corresponding strides in the luminance of the green- and red-emitting phosphors needs to be made. Fortunately, it was discovered that the SrS:Cu phosphor co-doped with Eu results in impressive red ACTFEL devices. Therefore, of particular importance is the green phosphor because the best green phosphors known to date are insufficient for utilization in a practical display. The brightest known green-emitting phosphor, filtered ZnS:Mn, exhibits chromaticity that is significantly different than saturated green, and hence, inadequate for full-color display applications. The only bright, saturated green

ACTFEL phosphor known to date, ZnS:Tb, has poor stability, and is hence unlikely to lead to a robust product. Furthermore, the eye is approximately 6 times more sensitive to green light than blue light and approximately twice as sensitive to green light than red light, making green perhaps the most important of the three primary color phosphors. Additionally, a bright and stable green phosphor would open up certain markets to ACTFEL-based products, because green is the preferred color for monochrome displays.

Table 2.3: The best reported performance characteristics (60 Hz) of primary color phosphors to date.

| Color | Phosphor | $L_{40}$ (cd/m$^2$) | $\eta_{40}$ (lm/W) | CIE x | CIE y |
|-------|----------|------------|----------------|-------|-------|
| Green | ZnS:Mn/filter | 160 | 1.0 | 0.47 | 0.53 |
|       | ZnS:TbOF | 100 | 1.0 | 0.30 | 0.60 |
|       | ZnS:Tb | 90 | 0.6 | 0.30 | 0.60 |
| Red | ZnS:Mn/filter | 70 | 0.8 | 0.65 | 0.35 |
|     | SrS:Eu,Cu | 91 | 0.5 | 0.60 | 0.39 |
|     | SrS:Eu | 31 | 0.18 | 0.60 | 0.39 |
|     | CaSSe:Eu | 25 | 0.25 | 0.66 | 0.33 |
|     | ZnS:Sm,Cl | 12 | 0.08 | 0.64 | 0.31 |
| Blue | SrS:Cu,Ag | 20 | 0.15 | 0.15 | 0.13 |
|      | SrS:Cu,Ag | 35 | 0.23 | 0.15 | 0.21 |
|      | SrS:Cu | 52 | 0.13 | 0.16 | 0.28 |
|      | SrS:Ce/filter | 26 | 0.15 | 0.13 | 0.18 |
|      | $(Sr,Ca)Ga_2S_4$:Ce | 7 | 0.02 | 0.15 | 0.15 |

### 2.3.2 Insulators for ACTFEL applications

In traditional ACTFEL devices, the insulating layers sandwiching the phosphor layer have been quite important for proper device operation. The most important role of the insulator layers is to protect the phosphor layer from large currents that flow when the phosphor is driven to electrical breakdown. In addition, the insulating layers have some influence on the important phosphor-insulator interfaces that supply the electronic current leading to light generation in the phosphor. Furthermore, they must withstand annealing temperatures of up to 800°C for the "standard" structure, and over 1000°C for the inverted structure without significant crystallization or defect formation. Finally, they should prevent ionic diffusion of foreign species into the phosphor layer. The generally accepted requirements of insulators for ACTFEL applications are as follows: [4]

1. sufficient relative dielectric constant, $\epsilon_r$

2. sufficient dielectric breakdown electric field, $F_{BD}$

3. small number of pinholes and defects

4. good adhesion to the electrodes and phosphor layer

5. small loss tangent, $\tan \delta$

As discussed in Section 2.2, the ratio of $C_i$ and $C_p$ is very important in determining how efficiently the applied voltage is dropped across the phosphor layer. Therefore, since the capacitance of the insulator layers depends on the relative dielectric constant, $\epsilon_r$, through Eq. 2.1, $\epsilon_r$ is a crucial parameter in deciding on applicable insulators for a given phosphor. Ideally, $C_i$ should be much greater than $C_p$, which implies that the relative dielectric constant of the insulator layer should be as large as possible, while the insulator thickness should be as small as possible. There are practical limits to both the size of the insulator dielectric constant and the insulator thinness, though. Insulators thinner than about 500 Å tend to show signs of charge

leakage that degrades device performance. [43] Also, if the phosphor layer becomes a virtual short when the device is turned on, the additional voltage applied above the turn-on voltage is dropped across the insulator layers, meaning that thinner insulators will see higher fields than thicker insulators. Therefore, the insulator layers must possess significant breakdown fields if they are to be useful for ACTFEL applications. The engineering tradeoff that occurs is that high-dielectric constant materials generally have fairly low breakdown fields and vice-versa. In addition, most insulators that possess relative dielectric constants above about 40 tend to break down in a mode termed "propagating breakdown". Propagating breakdown means that if a small portion of the insulator breaks down, a short circuit is formed through the insulator that heats up and grows in size, causing catastrophic device failure. The insulator breakdown mode for most of the lower relative dielectric constant materials is the so-called "self-healing breakdown" mode where microscopic insulator breakdowns become open-circuited, and hence, do not grow in size.

A minimum number of pinholes and defects in an insulator is important because displays with diagonals up to several inches are produced, and pinholes and defects will certainly degrade the overall quality of the display. Furthermore, any pinholes or defects in a propagating breakdown mode insulator can lead to catastrophic failure of the display. This is the reason why propagating breakdown mode insulators are generally sandwiched between self-healing breakdown mode insulators if they are used at all in ACTFEL applications. [4] Also, good insulator adhesiveness is quite obviously necessary if an ACTFEL display is going to withstand the test of time.

The ACTFEL phosphor is a relatively closed environment when sandwiched between two insulators as in the standard and inverted device structures. This implies that charge loss or injection through the insulators can disrupt the delicate balance inherently present in the device. In addition, charge leakage through the insulators can lead to reduced device efficiency because of power loss due to this process. For this reason it is generally believed that charge leakage through the insulators is detrimental

to device performance. As a result, it is thought desirable to keep the loss tangent, tan $\delta$, of the insulator layers as small as possible.

A fairly complete list of insulators that have been successfully employed for ACTFEL applications is shown in Table 2.4. [4]

### 2.3.3 Transparent contacts

The light generated by the phosphor layer of an ACTFEL device must reach the viewer for a useful device. Hence, at least one of the electrical contacts needs to be a transparent conductor that possesses high transmittance of the entire visible spectrum. Also of importance is a low electrical resistance of the transparent conductor to avoid excessive resistive heating, and hence, wasted power in the display. Furthermore, the transparent conductor must be able to withstand anneals of up to 800°C in the standard process.

Several materials have been used for this purpose, but the best and by far the most common is indium-tin oxide (ITO), an alloy of approximately 90 wt% $In_2O_3$ and 10 wt% $SnO_2$. Presently, sheet resistances of 5-10 $\Omega/\square$ are obtainable in high-quality ITO films of the standard thickness of approximately 2000 Å. This material is transparent to visible light because the bandgaps of both $In_2O_3$ and $SnO_2$ are about 3.5 eV. This material conducts due to the high density of donor impurities caused by $Sn^{4+}$ ions sitting on $In^{3+}$ sites and oxygen vacancies. Other materials that have been used for the transparent contact in research devices are ZnO:Al, ZnO:Ga, ZnO:In, CdO, and $CdSnO_3$.

The major problem with transparent contacts is that they are not conducive to self-healing breakdown. Self-healing breakdown is not merely a function of the insulator material, but is also dictated to a large extent by the contacts. This is due to the fact that self-healing ACTFEL device behavior is also dependent on either the evaporation or melting and surface migration of the exposed contact above short circuits caused by microscopic pinholes and defects. [3] Inverted structure ACTFEL

Table 2.4: Insulators commonly used for ACTFEL applications and their characteristics.

| Insulator | $\epsilon_r$ | $F_{BD}$ (MV/cm) | $\epsilon_0\epsilon_r F_{BD}$ ($\mu C/cm^2$) | Breakdown Model |
|---|---|---|---|---|
| $SiO_2$ | 4 | 6 | 2 | SHB |
| $SiO_xN_y$ | 6 | 7 | 4 | SHB |
| $Si_3N_4$ | 8 | 6-8 | 4-6 | SHB |
| $Al_2O_3$ | 8 | 5 | 4 | SHB |
| SiAlON | 8 | 8-9 | 5-6 | SHB |
| $Y_2O_3$ | 12 | 3-5 | 3-5 | SHB |
| $BaTiO_3$ | 14 | 3.3 | 4 | SHB |
| $Sm_2O_3$ | 15 | 2-4 | 3-6 | SHB |
| $HfO_2$ | 16 | 0.17-4 | ? | SHB |
| $BaTa_2O_6$ | 22 | 3.5 | 7 | SHB |
| $Ta_2O_5$ | 23-25 | 1.5-3 | 4-6 | SHB |
| $PbNb_2O_6$ | 41 | 1.5 | 6 | SHB |
| $TiO_2$ | 60 | 0.2 | 1 | PB |
| $Sr(Zr,Ti)O_3$ | 100 | 3 | 27 | PB |
| $SrTiO_3$ | 140 | 1.5-2 | 19-25 | PB |
| $PbTiO_3$ | 150 | 0.5 | 7 | PB |
| Westaim proprietary | 1700 | ? | ? | ? |

·devices must employ a transparent top electrode for the light to reach the viewer, making it of extreme importance that these devices are free from defects for the sake of device stability.

### 2.3.4 Opaque contacts

Generally, one of the electrical contacts to an ACTFEL device is an opaque conductor. Almost all standard structure ACTFEL devices are contacted on the top by an Al electrode. Aluminum is used because it adheres well to most insulators, does not migrate through the device under high electric fields, and has low resistivity. There are two main disadvantages of Al as the opaque contact to an ACTFEL device. The first is that it reflects around 90% of incident light such that background light is reflected and emerges along with the electroluminescent light. [4] The second is that the melting point of Al is 660°C, meaning that it is not useful for inverted structure applications where high-temperature post-deposition anneals are used. For this application, a suitable refractory metal is used, usually Mo, Ta, or W. [4]

### 2.3.5 Substrates

In the production of standard structure ACTFEL devices, the substrate is typically Corning 7059 phosphosilicate glass, or its equivalent, with a softening temperature about 600°C. As a result, large size display panels will withstand rapid thermal annealing (RTA) at temperatures below 650° without warping. However, smaller sized test samples ($\leq$ 2" square) will withstand RTA temperatures as high as 850°C for several minutes without significant warpage. However, for certain phosphors it has been essential to perform higher temperature anneals with the standard structure, so higher softening temperature glass substrates are used. However, the drawback of these higher temperature glass substrates is that they are many times more expensive than the Corning 7059 glass; too expensive, in fact, to produce an economical product. Furthermore, these higher softening temperature glass substrates only provide

100-200°C of additional annealing temperature range before they too succumb to the high temperature.

For truly high temperature annealing, the inverted structure is necessary. Since the light is viewed through the top of the device in the inverted structure, opaque substrates are an option. With opaque substrates, silicon wafers are a logical choice because they are readily available and melt at 1412°C. Also, alumina ceramic substrates are often used because of their availability, economy, and extremely high melting temperature.

The final substrate type that is sometimes used for research devices with oxide phosphors is the $BaTiO_3$ substrate that doubles as an insulating layer. [5, 6] These substrates are pressed from powder in-house and sintered and ground into a flat ceramic disc. Then, an oxide phosphor layer is deposited directly onto the substrate. Next, the device is annealed at temperatures on the order of 1000°C. Finally, a transparent conductor is deposited onto the phosphor layer and an Al contact is deposited on the backside of the substrate. A cross-section of this configuration is shown in Fig. 2.2. The main advantage of this configuration is that it allows high temperature anneals. However, there are extreme overvoltage requirements when this device structure is employed because the insulator capacitance dictates how efficiently the applied voltage is coupled to the phosphor layer, and the small insulator capacitance resulting from driving the substrate results in very poor coupling. This problem with the overvoltage requirement makes this structure fairly useless from an industrial perspective, at least with currently available drive electronics.

## 2.4  ACTFEL materials processing

This section examines the deposition techniques used for the fabrication of ACTFEL devices. Virtually every deposition technique has been tried for the fabrication of ACTFEL devices. However, the three techniques that are the most useful for ACTFEL materials processing are certainly evaporation, sputtering, and atomic

layer epitaxy (ALE). Therefore, this section will be limited to a discussion of these three techniques, with an emphasis on evaporation and sputtering because these are the techniques investigated in this thesis.

### 2.4.1 Evaporation of ACTFEL materials

One of the fundamental concepts taught in introductory chemistry courses is the idea of vapor pressure of a condensed phase of matter. The vapor pressure is defined as the pressure of a vapor in equilibrium with its condensed phase at a specified temperature. [44] As implied by its definition, the vapor pressure of a condensed phase of matter is a strong function of its temperature. In fact, vapor pressure tends to be exponentially dependent on the temperature of the condensed matter [45]. Furthermore, the rate of mass lost from a condensed matter source per unit volume per unit time is directly proportional to the vapor pressure of the source. [46] At atmospheric pressure, the vaporized atoms or molecules from condensed matter are certain to suffer collisions with molecules in the air after very short distances of travel, inhibiting them from macroscopic transport. However, when this process takes place in a high-vacuum environment, the mean-free path of the vaporized atoms or molecules is on the order of tens of meters, allowing for condensation at points remote from the condensed matter. This is the fundamental idea behind the technique of evaporation.

The main distinguishing factor in comparing different evaporation techniques is the method of heating the source material. The source material must be heated to a temperature such that its vapor pressure is on the order of 10 mtorr or greater. [46] However, the temperature required to achieve this vapor pressure could fall anywhere in a broad range of temperatures depending on the substance to be evaporated. Due to this broad range of evaporation temperatures, two different techniques for heating the source material are commonly used; resistance heating (thermal evaporation), and electron beam heating (e-beam evaporation). Thermal evaporation is the least

complex method of deposition via evaporation and involves the heating of a crucible, or "boat", made from a refractory, low vapor-pressure metal (*e.g.* W, Ta, or Mo) by passing large currents through it. Although this technique is simple, it is not well suited for deposition of refractory metals or ceramics, mainly because of the enormous currents required to reach the extremely high evaporation temperatures of these materials and the ensuing problems with cross-contamination by the boat at these elevated temperatures. One solution to the problems associated with thermal evaporation is the heating of the source material via an e-beam. Electron beam evaporation involves heating a source material by focusing a stream of high kinetic energy (5-30 keV) electrons onto it. An e-beam can evaporate any material that it can supply enough energy to to counteract the rate of heat loss. This fact makes e-beam evaporators especially useful for evaporating ceramics because they are poor conductors of heat, and not well suited for evaporation of materials that are good conductors of heat. Due to the individual strengths of these two techniques of evaporation, evaporation is a useful technique for deposition of a wide variety of materials in thin-film form.

Evaporation is a simple and widely used technique for deposition of many types of materials. The deposition of ACTFEL materials is certainly no exception as many of the different layers necessary in the fabrication of an ACTFEL device are commonly deposited by evaporation. For example, the Al contacts that are so often used for "standard" structure devices are generally deposited by evaporation, as are most of the commonly used ACTFEL phosphors. The advantages of evaporation for ACTFEL applications are many and include high deposition rates, high-vacuum processing conditions, and process simplicity. The high deposition rates attainable at high-vacuum in evaporation processes lead to low residual gas incorporation into the growing thin-film, which is desirable for ACTFEL phosphor deposition. There are also several drawbacks to the deposition of ACTFEL films via evaporation; namely, poor stoichiometry of alloy and compound thin-films, the possibility of contamination

from the evaporation crucible at the high temperatures required, and the possibility of x-ray damage of the film from electron beams. Of these issues, the inherent problems associated with the evaporation of alloys and compounds is the biggest challenge in the deposition of ACTFEL phosphors and insulators because all of these materials are compounds and many are alloys of compounds.

The major problem with the evaporation of compounds, alloys, and mixtures is that the constituent pieces of these types of materials generally have quite different vapor pressures. [45] As a result, the composition of the thin-film evaporated from a source material is often not the same as that of the source material itself. Many of the materials that are useful for ACTFEL applications tend to dissociate during the transition to the vapor phase, and hence, form thin films that are deficient in one of the constituent species. These films are generally deficient in the anionic species, resulting in vacancy point defects in the resultant thin-films. These vacancy point defects have been identified as a potential source for space charge in ACTFEL phosphor layers, and could also lead to trapped charge in insulating layers. To counteract these difficulties, researchers have used several techniques for increasing the content of the deficient species in the evaporated thin-film. One technique often seen in the production of evaporated sulfide ACTFEL phosphors is multi-source evaporation where a sulphur source is evaporated concomitant with the sulfide source to counteract the sulphur deficiency in the thin-film. [47, 48, 49] Also, excess sulphur is sometimes added to the evaporation source material by annealing the source material in $CS_2$ or $H_2S$ for several hours at elevated temperatures. [50] Furthermore, for oxides and nitrides, reactive evaporation is sometimes used, where small amounts of oxygen or nitrogen gas is introduced to the vacuum chamber during the evaporation. [45, 51]

## 2.4.2 Sputter deposition

Sputtering is a process initiated when a particle strikes a surface with sufficient kinetic energy to subsequently dislodge one or more surface atoms. The particle

in question could be any number of different entities, but inert gas ions are most commonly used for sputtering. The process of sputtering is depicted in Fig. 2.5. If these inert gas ions are in the correct range of energy, they tend to elastically collide with the surface that they are bombarding, rather than implant themselves into the bulk of the material being bombarded. Sputtering of a surface is often characterized by a parameter called sputter yield, which is defined as the ratio of the number of sputter emitted atoms to the number of incident particles, [52] or

$$Y = \frac{\text{sputter emitted atoms}}{\text{incident particles}}. \tag{2.6}$$

Sputter yield depends on many factors, including surface conditioning, chamber geometry, operating pressure, crystallinity of the material being sputtered, and the nature of the material being sputtered [46].
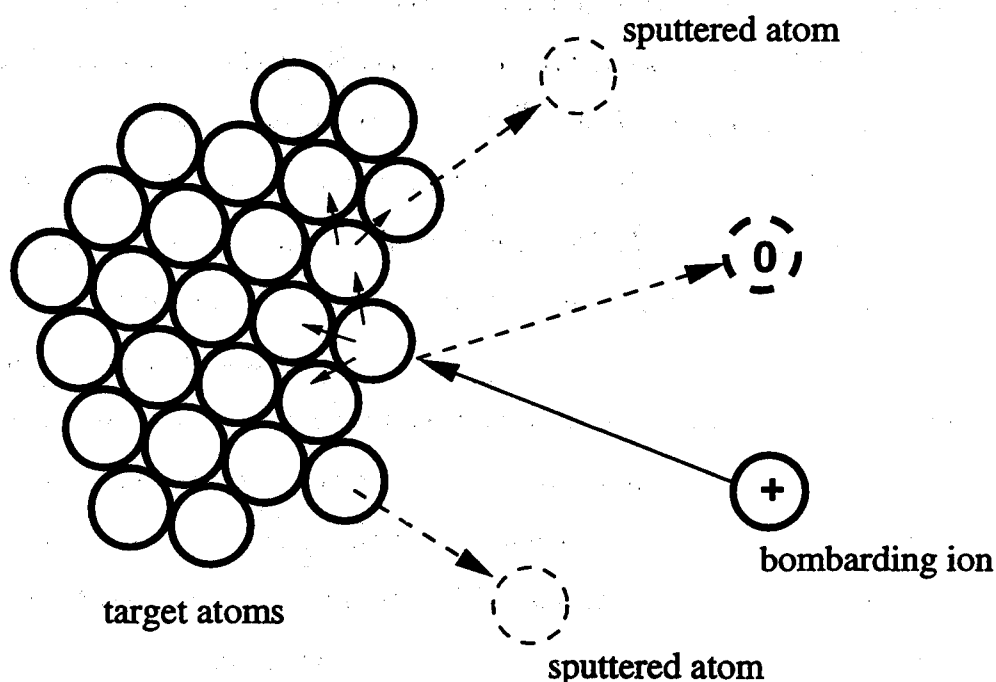


Figure 2.5: The process of sputtering.

Sputter deposition is the process of sputtering a surface where the sputtered atoms subsequently arrive at a substrate remote from the source material and form a thin-film. Sputter deposition as it is used for fabrication of thin-films for ACTFEL applications always involves a glow discharge. Glow discharges can be sustained by both DC voltages and AC waveforms, but the most useful driving technique for sputter deposition of ACTFEL materials is a radio-frequency (RF) AC waveform. Sputter deposition with a DC glow discharge requires the target material to be conducting so as to supply enough electrons to sustain the glow discharge, which rules out most ACTFEL materials. However, a related technique that is sometimes used for ACTFEL materials is where a DC glow discharge is sustained in a contained environment and inert gas ions bombarding one side of the container are extracted and accelerated at a target remote to the glow discharge to induce sputtering. This technique is referred to as secondary-ion beam sputtering, and it could conceivably be used for deposition of any of the layers of an ACTFEL device, although it is most commonly used for deposition of metals. Because DC sputter deposition is rather limited in the scope of materials that are available to be deposited, RF sputter deposition was developed to allow the sputtering of almost any material that can be formed into a suitable source, or "sputter target". Since all ACTFEL phosphors and insulators are non-conducting materials, RF sputtering is the most important sputter deposition technique for such materials.

The process of RF sputter deposition is made possible due to the large difference in mass, and hence mobility, of electrons and inert gas ions. Because electrons are many times less massive than ions, electrons attain much greater velocities and travel much further than ions during each cycle of the applied RF voltage waveform. Since electrons travel much further, they eventually accumulate on the target, substrate, and chamber walls such that the plasma is the most positive potential in the system. These induced negative voltages, or "sheath voltages", cause acceleration of positive ions toward the negatively charged surfaces, which subsequently leads to sputtering

events. The volume adjacent to a surface tends to be relatively free of electrons because of the negatively charged surface. This leads to a "dark-space" because electrons are not available to excite gas atoms. [52]
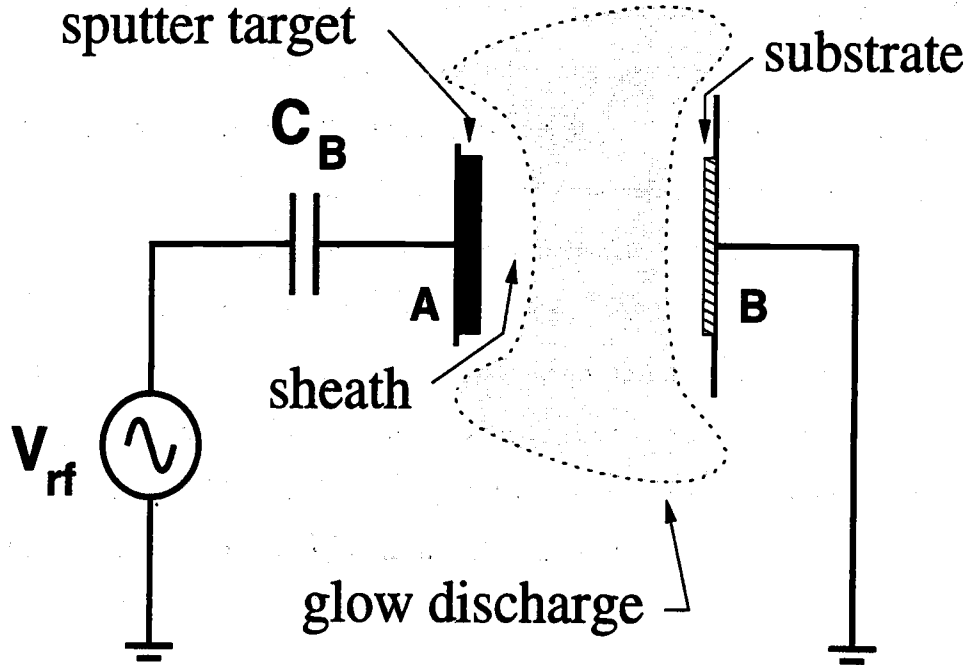


Figure 2.6: A schematic view of an RF sputtering process.

An RF sputter deposition process is schematically shown in Fig 2.6. The target is selectively sputtered by controlling the relative surface areas of the target and the substrate holder. If space-charge limited current is assumed, the ion current flux, J, can be estimated by the Child-Langmuir equation,

$$J = \frac{KV^{3/2}}{\sqrt{m_{ion}}D^2},$$
(2.7)

where $D$ is the dark-space thickness, $V$ is the sheath voltage, $m_{ion}$ is the ionic mass, and K is a proportionality constant. Since the positive ion current must be equal at

both electrodes,

$$A_A \frac{V_A^{3/2}}{D_A^2} = A_B \frac{V_B^{3/2}}{D_B^2}, \tag{2.8}$$

where $A_A$ and $A_B$ are the surface areas of electrodes A and B, respectively. It should be noted that this step differs from that presented in several texts treating the subject of glow discharges which assume that the positive ion current *densities* must be equal. [46, 52] However, if the positive ion current densities were equal, there would be a much greater positive ion current flowing during one half-cycle of the applied voltage waveform than the other due to the much greater area of the grounded substrate electrode. Therefore, because this system is assumed to be in steady-state, the total positive ion *current* per half-cycle should be the relevant quantity.

The glow discharge itself is a region where large quantities of positive and negative charge exist and can be modeled as a wire. Since most of the voltage in the glow discharge is dropped across the dark spaces, and they have small conductivities, they can be modeled as capacitors, such that the capacitances,

$$C \propto \frac{A}{D}. \tag{2.9}$$

Furthermore, an AC voltage will divide across two series capacitors such that

$$\frac{V_A}{V_B} = \frac{C_B}{C_A}. \tag{2.10}$$

Combining Eqs. 2.9 and 2.10, it results that

$$\frac{V_A}{V_B} = \frac{A_B}{D_B} \frac{D_A}{A_A}. \tag{2.11}$$

Substitution of the above equation into Eq. 2.8 yields the result that

$$\frac{V_A}{V_B} = \left( \frac{A_B}{A_A} \right)^2. \tag{2.12}$$

This result tells that the smaller area will see the larger sheath voltage, whereas the larger area will see a smaller sheath voltage by a power of 2. [46] However, the exponent in Eq. 2.12 is generally less than 2 because of idealizations inherent in

the model. The usefulness of this result, though, is that $A_B \gg A_A$ must hold to selectively sputter the target. This is done in practice by grounding the substrate holder to the entire chamber, resulting in a very large $A_B$. For this reason, it is extremely important that the substrate holder and the system are well-grounded to ensure that resputtering of the growing film does not occur.

Several common variations of the RF sputtering process described above are often used in practice, namely, magnetron sputtering, and reactive sputtering. Magnetron sputtering involves the use of permanent magnets placed behind the target that cause electrons to spiral around through the plasma in a path that closes in upon itself, termed "the racetrack". This has the effect of increasing an electron's effective path length and causing more efficient ionization of neutral gas atoms. [53] Magnetron sputtering leads to high discharge currents at significantly lower voltage than would be necessary in the absence of the magnetron. Reactive sputtering is the addition of a reactive gas species to the background gas which reacts with sputtered atoms to form compound thin-films. An example of this is the sputtering of a metallic Ta target with a certain percentage of $O_2$ or $N_2O$ added to the process gas to form a $Ta_2O_5$ thin-film.

### 2.4.3 Atomic layer epitaxy

The third commonly used deposition technique for ACTFEL related thin-films is atomic layer epitaxy (ALE). This technique has proven extremely useful in deposition of high-quality films for ACTFEL applications. One of the reasons this technique is excellent for ACTFEL applications is that ALE films tend to have very few pinhole defects and excellent step coverage, as required for production of displays of all but the very smallest size. [54] The drawbacks of ALE are large initial startup costs for an ALE system and large lead times to determine the proper chemistry of a thin-film process.

The technique of ALE operates by introducing a gaseous source containing the cationic species or precursor of the desired thin-film compound into a vacuum chamber such that several monolayers of this gas are adsorbed on the surface of the heated substrate. Then, a short burst of an inert gas is introduced in the chamber to remove all but the first adsorbed monolayer from the substrate. Next, the anionic precursor is introduced into the chamber such that several monolayers are adsorbed onto the first monolayer of gas molecules containing the cationic species. The close proximity of the cationic and anionic species leads to a reaction and formation of a monolayer of the desired compound, with the remaining atoms left over from the precursors evolving from the growing film as vapor. Finally, a second short burst of inert gas is added to the chamber to hasten the removal of all but the first adsorbed monolayer of the anionic precursor and any vapors emitted from the chemical reaction. The process explained above is depicted in Fig. 2.7. Then, this process is repeated again and again until the desired film thickness is achieved.

## 2.5  Optical characterization of ACTFEL devices

From an industrial standpoint, the only interesting features of an ACTFEL device are the light output, the power required to generate that light, and the color of the light. Hence, the most commonly used techniques to compare and contrast ACTFEL devices worldwide are measurements that explore the luminance (or brightness), the efficiency, and the color spectrum of an ACTFEL device. These three measurements are examined in closer detail in the remainder of this section.

### 2.5.1  Luminance-voltage characterization

The universal measurement performed on ACTFEL devices in ACTFEL characterization laboratories worldwide is the luminance-voltage (L-V) measurement (sometimes referred to as a brightness-voltage, or B-V, measurement). The basic idea of the L-V measurement is to apply waveforms of steadily increasing amplitude to an

For ZnS: $ZnCl_2 + H_2S \longrightarrow 2HCl + ZnS$



ZnCl$_2$ In

Purge Excess
ZnCl$_2$

H$_2$S In

ZnS

Purge Excess

HCl and H$_2$S
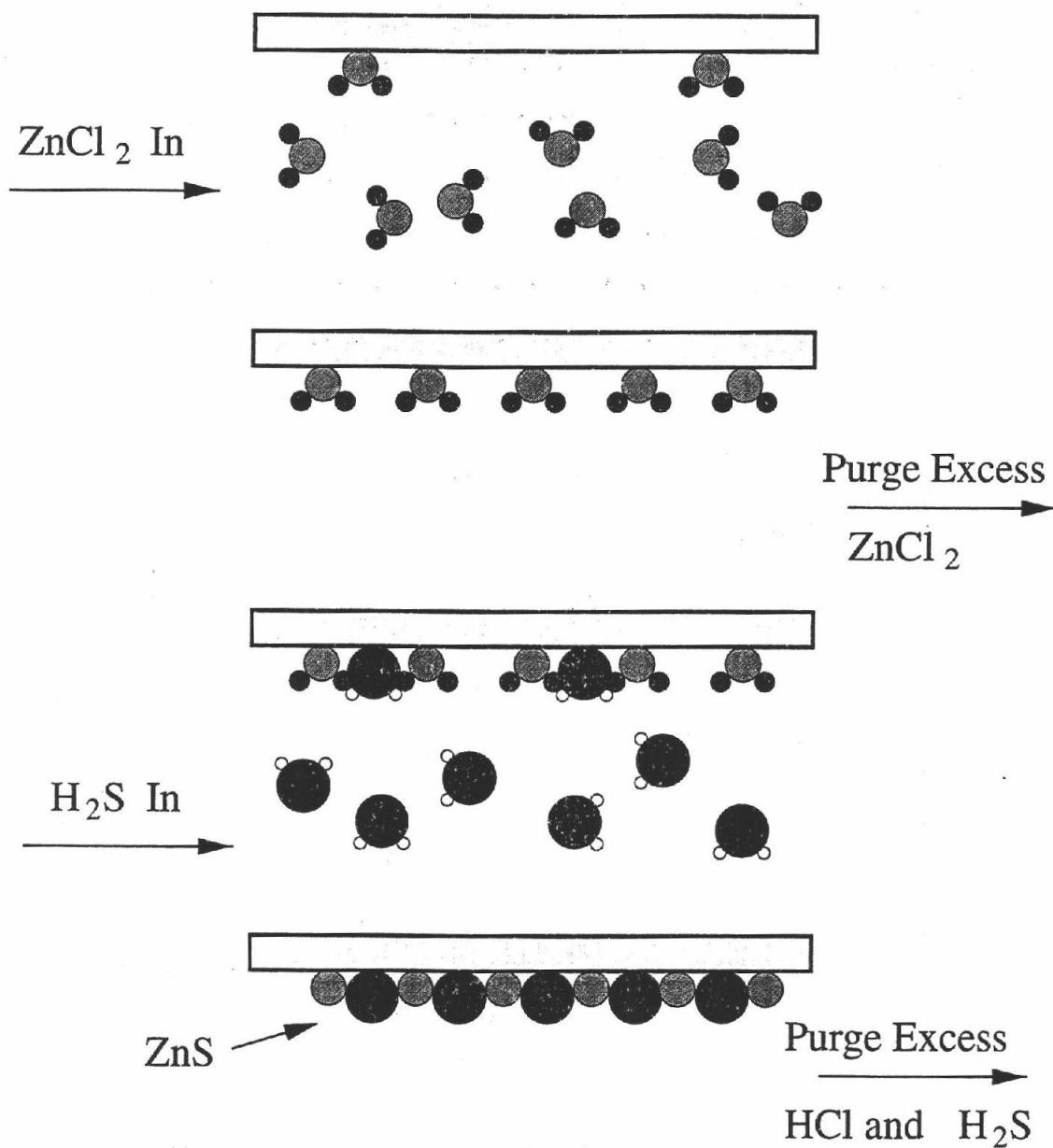
Figure 2.7: The deposition of one monolayer of ZnS by ALE.

ACTFEL device and measure the luminance at each successive amplitude. The L-V measurement proceeds by first applying a voltage waveform with amplitude below the threshold voltage of the device and allowing the device to reach steady-state (usually the time required to apply several hundred pulses). Then, after the device has reached steady-state, the luminance is measured with a photometer, photomultiplier tube, or photodiode. This luminance measurement reports the luminous intensity output in a direction normal to the emitting surface, and is generally reported in either foot-Lamberts or candelas per square meter. This process is then repeated at successively higher voltage amplitudes until a predetermined stopping voltage. Once the data is collected, the L-V curve is plotted by plotting the voltages on the x-axis and the corresponding luminances on the y-axis, as shown in Fig. 2.8.
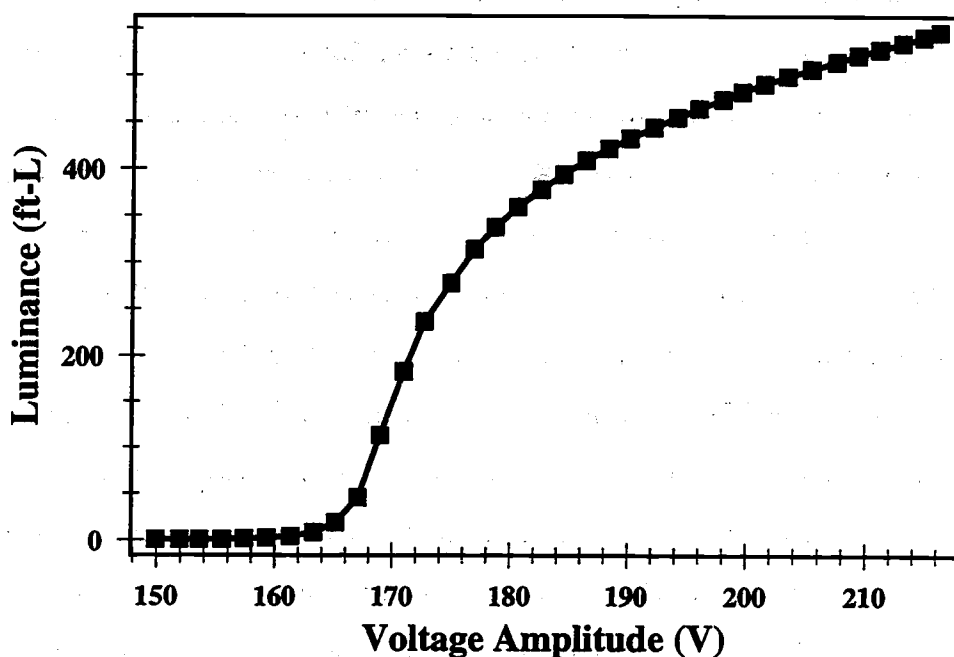
Figure 2.8: A L-V curve from an evaporated ZnS:Mn ACTFEL device driven by a 1 kHz bipolar trapezoidal waveform.

The L-V measurement is very sensitive to the driving waveform, so additional information about the parameters describing the driving waveform should be included. First, the measured luminance depends on the type of waveform used to drive the ACTFEL device. The various laboratories that test ACTFEL devices worldwide often use different types of driving waveforms. The most popular waveforms for performing L-V measurements are sine waves and bipolar trapezoidal waveforms, although some researchers prefer triangle waves. Next, the measured luminance depends to some degree on the rise time, fall time, and pulse width when bipolar trapezoidal waveforms are used to generate L-V data. Finally, the most important driving waveform parameter in terms of the output luminance is the frequency of the driving waveform. The measured luminance at a fixed voltage increases quite noticeably with increasing frequency. This increase is easily reconciled by the fact that at higher frequencies, more pulses are applied to the ACTFEL device per unit time, hence, the luminescent impurities are excited more often. Unfortunately, there is a point of diminishing returns with increasing frequency where the luminance either saturates or decreases at a certain frequency. This effect has to do with both device heating and the de-excitation time of the luminescent impurities. When the device heats up, the probability of de-excitation via non-radiative recombination (phonons) is significantly increased, leading to reduced light output. Additionally, luminescent impurities do not decay instantaneously from their excited state to their ground state; they have some characteristic time associated with this process. When the period of the driving waveform is of the same order as the characteristic decay time of the luminescent impurity, there may be little or no increase in luminance with increasing frequency because many luminescent impurities may already be excited when the following pulse arrives. Essentially, the fraction of time per second that the driving waveform spends above the turn-on voltage determines the relative luminance of the device.

Many materials parameters other than the chemical composition of the phosphor layer contribute to the L-V characteristics of an ACTFEL device. The thickness

of the phosphor layer is one parameter that affects the observed luminance of the ACTFEL device. As the phosphor layer of an ACTFEL device becomes thicker (given a fixed doping concentration), a greater number of luminescent impurities are incorporated into the phosphor layer, and a transiting electron has a greater probability of impact excitation. Therefore, with all else being equal, ACTFEL devices with thicker phosphor layers will exhibit greater luminance than thinner devices. Additionally, a greater phosphor thickness leads to a smaller phosphor capacitance, resulting in a greater percentage of the applied voltage being dropped across the phosphor layer. The main drawback to increased phosphor thickness is that a greater applied voltage is required to achieve the threshold electric field in the phosphor. In fact, extremely thick devices may have threshold voltages too large to be turned on with conventional measurement setups. This in turn affects device reliability, because there is a much greater chance of arcing and device burnout when driven at very high voltages. The insulators affect the luminance characteristics of an ACTFEL device mainly through their effect on the voltage distribution through the device. An increase of the insulator capacitance with respect to a fixed phosphor capacitance results in a greater percentage of the applied voltage being dropped across the phosphor layer, which leads to a lower threshold voltage. The two methods of increasing the insulator capacitance are to either decrease the thickness of the insulator layers or use an insulating material with larger dielectric constant. This is sometimes practical, but the limitation is that essentially all of the applied voltage above the turn-on voltage of an ACTFEL device is dropped across the insulators, requiring high dielectric strength insulators. This is complicated by the fact that high dielectric constant insulating materials tend to have relatively low dielectric strength.

Another materials parameter that is critical in determining the L-V characteristics of an ACTFEL device is the doping level of the luminescent impurity into the phosphor layer. At low dopant concentrations ($\leq 1\%$ for most phosphor materials), the observed luminance increases monotonically with increasing luminescent impurity

concentration. Then, an optimum luminance is achieved, and the luminance declines with increasing luminescent impurity concentration above this doping level. This decline is due to the disruption of phosphor crystallinity and the increased number of non-radiative transition paths that result from high luminescent impurity doping levels [4]. Furthermore, at higher luminescent impurity doping levels, hysteresis in the L-V characteristics is sometimes observed. Generally, this hysteresis is such that the light emission from the ACTFEL device is extinguished at a much lower voltage than the threshold voltage. Throughout the literature, this effect has been linked to the phenomenon of positive space charge build-up in the phosphor bulk [21]. This effect presents practical problems in terms of product operation because of contrast reduction when there is difficulty turning display pixels off. However, it has been postulated in the literature that this effect could be useful for some sort of dynamic memory function. [55]

### 2.5.2 Efficiency-voltage characterization

The second important ACTFEL characterization measurement from an industrial point of view is the efficiency-voltage ($\eta$-V) measurement. When considering an ACTFEL process for production, an important consideration is power consumption because flat-panel displays are often intended to run from batteries. Therefore, product engineers are interested in the amount of light that can be produced per unit of power input, or luminous efficiency, $\eta$. The luminous efficiency of an ACTFEL device is usually reported in lumens per Watt, and is computed from

$$\eta = \pi \frac{L}{P},\qquad(2.13)$$

where $L$ is the measured luminance in cd/m$^2$ and P is the applied power density in W/m$^2$ [4]. The factor of $\pi$ in Eq. 2.13 accounts for the assumption of a perfectly diffuse emission surface of the ACTFEL device under test. This assumption is necessary because the luminance measured from a L-V measurement represents only the light emitted normal to the surface of the ACTFEL device, whereas the desired quantity

is the luminous intensity integrated over all viewable angles. The $\eta$-V measurement is usually performed concomitant with the L-V measurement because the only additional variable that must be measured is the input power density which is computed from

$$P = \frac{1}{A\tau} \int_t^{t+\tau} v(t')i(t')dt', \qquad (2.14)$$

where $A$ is the device area, $\tau$ is the period of the driving waveform, and $v(t)$ and $i(t)$ are the applied voltage and current waveforms, respectively. An $\eta$-V curve for an evaporated ZnS:Mn device is shown in Fig. 2.9. The shape of the curve shown in Fig. 2.9 is typical of most ACTFEL devices.
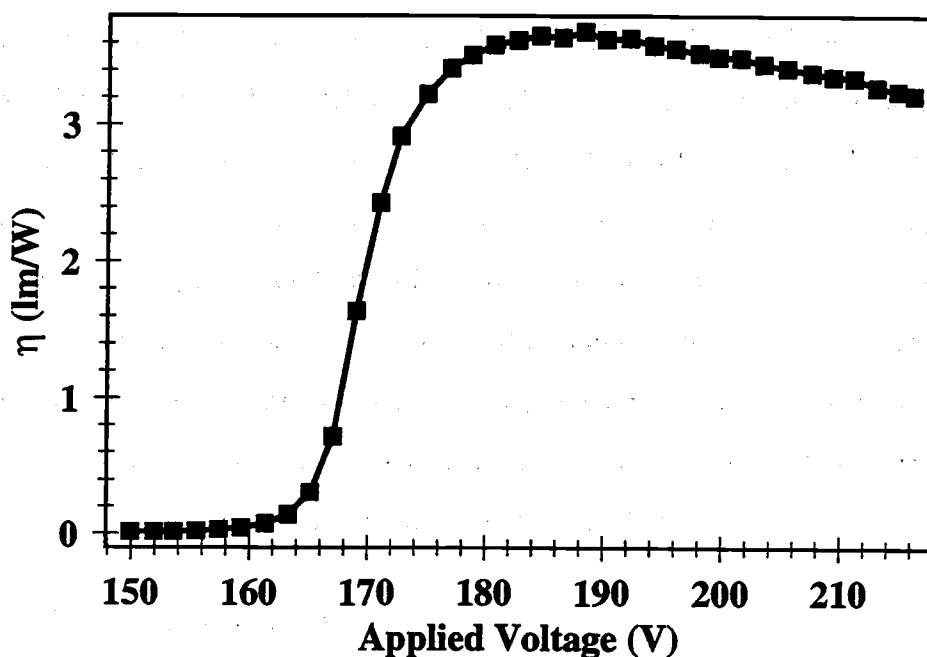


Figure 2.9: An $\eta$-V curve of an evaporated ZnS:Mn ACTFEL device driven by a 1 kHz bipolar trapezoidal waveform.

The $\eta$-V measurement depends on many of the same factors as the L-V measurement because $\eta$ is computed using the luminance data from the L-V curve as

one of the input variables. However, because the power requirements for different driving waveforms may change in a different manner than the luminance, $\eta$-V curves show some very different trends than L-V curves. One of these different trends is that the $\eta$-V curve generally drops with increasing frequency, even for quite moderate frequencies because power density requirements increase more rapidly than the luminance output. The efficiency of an ACTFEL device also depends on the nature of the driving waveform. An ACTFEL device is most efficient during the rising edge portion of the applied waveform, and least efficient when the voltage is held constant above the threshold voltage. This leads to the conclusion that a triangle wave is the most efficient waveform, whereas a square wave is the least efficient. Another factor that affects ACTFEL device efficiency is space charge. The presence of positive space charge leads to regions of the phosphor layer with very high fields, and regions of the phosphor with very low fields. This seems to affect efficiency in an adverse way because only the high-field portion of the phosphor efficiently emits light. [56] Finally, $\eta$ depends on the phosphor thickness, because both device luminance and power consumption depend to a large degree on the phosphor thickness. Thin phosphor layers consume the least power, but also produce the least luminance, whereas thick phosphors produce the most luminance, but consume large amounts of power. Therefore, there is an optimum phosphor thickness for maximum efficiency that generally lies between 0.5 and 1 $\mu$m for most of the common phosphor materials.

### 2.5.3   CIE color coordinates

In 1931, the Commission Internationale de l'Eclairage established an international standard for quantifying all visible colors, known as CIE color coordinates. The CIE coordinates are obtained by first computing the three CIE tristimulus values, X, Y, and Z, and subsequently computing the CIE coordinates, x and y, from these values. The CIE tristimulus values are obtained by integrating the product of the spectrum of the light source in question, $P(\lambda)$, and CIE color matching functions,

$x_\lambda(\lambda)$, $y_\lambda(\lambda)$, and $z_\lambda(\lambda)$, shown in Fig. 2.10 over the visible range of wavelengths. [57] However, in practice, spectra are measured as a discrete set of points, so the
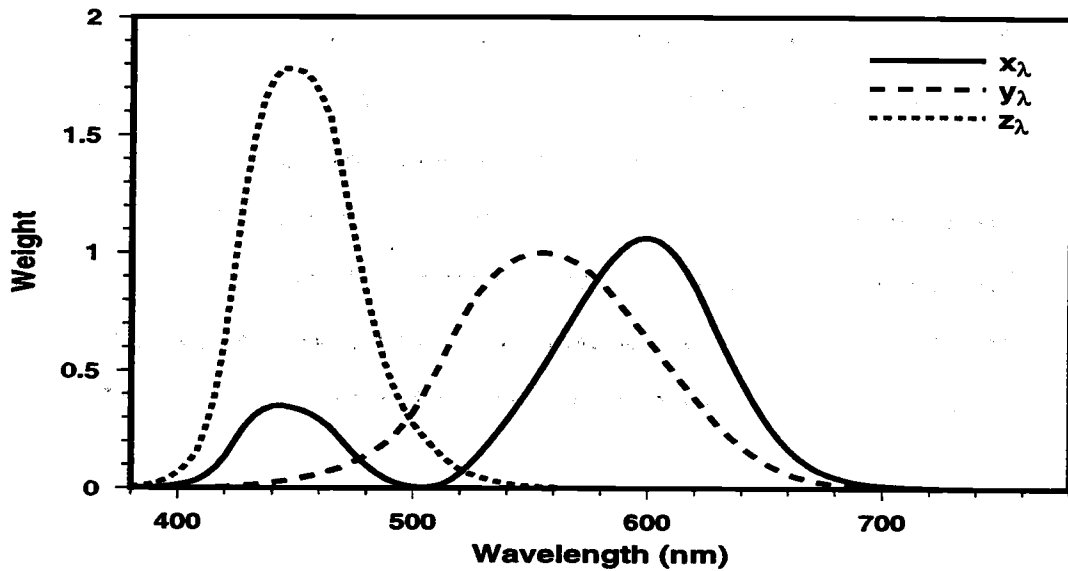


Figure 2.10: The CIE color matching functions.

integrations are replaced by the sums,

$$X \;=\; \Delta\lambda \sum_{\lambda=\lambda_{violet}}^{\lambda_{red}} x_\lambda(\lambda)P(\lambda) \qquad (2.15)$$

$$Y \;=\; \Delta\lambda \sum_{\lambda=\lambda_{violet}}^{\lambda_{red}} y_\lambda(\lambda)P(\lambda) \qquad (2.16)$$

$$Z \;=\; \Delta\lambda \sum_{\lambda=\lambda_{violet}}^{\lambda_{red}} z_\lambda(\lambda)P(\lambda), \qquad (2.17)$$

where $\Delta\lambda$ is the interval between points. Then, once X, Y, and Z are obtained, the CIE color coordinates, x, y, and z are calculated from

$$x \;=\; \frac{X}{X+Y+Z} \qquad (2.18)$$

$$y \;=\; \frac{Y}{X+Y+Z} \qquad (2.19)$$

$$z = \frac{Z}{X + Y + Z}. \tag{2.20}$$

However, because

$$x + y + z = \frac{X + Y + Z}{X + Y + Z} = 1, \tag{2.21}$$

only two of the three CIE color coordinates are independent. Therefore, the CIE color coordinates are completely specified from knowledge of the x and y values, and hence, only the x and y CIE color coordinates are typically reported.

Plotting of the CIE y color coordinate versus the CIE x color coordinate over the visual range of light leads to a horseshoe shaped diagram known as the CIE chromaticity diagram. A black and white representation of this diagram is shown in Fig. 2.11. The large dot in the center of the CIE chromaticity diagram shown in
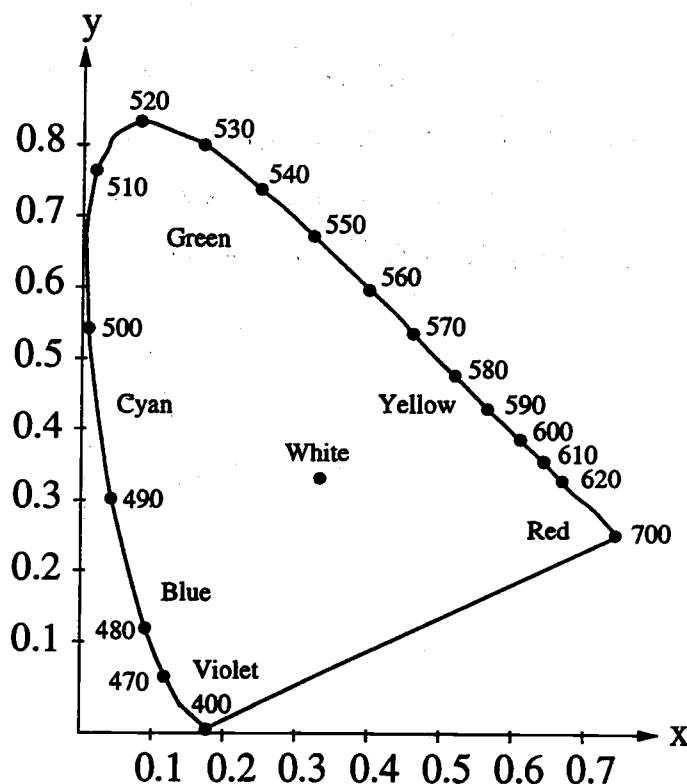


Figure 2.11: The CIE chromaticity diagram.

Fig 2.11 represents white light, and is located at the CIE color coordinate x = 0.333, y = 0.333. Then, when the CIE coordinates of a color are specified, the dominant wavelength of the color is the intersection of the line connecting these CIE coordinates and those of white light with the upper arc of the diagram. [58] This process is depicted in Fig. 2.12 for a hypothetical color, $C_1$, with dominant wavelength $C_2$. Also, the color purity of color $C_1$ is obtained by taking the ratio of the lengths of the line segments $\overline{CC_1}$ and $\overline{CC_2}$. [58] Furthermore, when the light emission from phosphors of two colors are mixed, the range of colors that it is possible to produce by mixing of these two colors is given by the line that ties the CIE coordinates of these two colors together. [58] For example, the range of colors available by mixing phosphors with CIE color coordinates given by C and $C_1$ in Fig. 2.12 is given by the line segment $\overline{CC_1}$. This range of colors is referred to as the color gamut of $C_1$ and $C_2$.

The CIE color coordinates are most useful for the optical characterization of ACTFEL devices as guidelines to gauge the quality of the chromaticity available from a full-color display utilizing the ACTFEL device in question. The color gamut spanned by phosphors of three different colors is obtained by plotting the CIE coor-
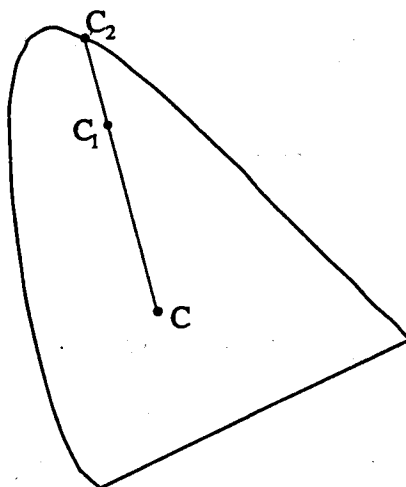
Figure 2.12: Finding the dominant wavelength and color purity from CIE coordinates.
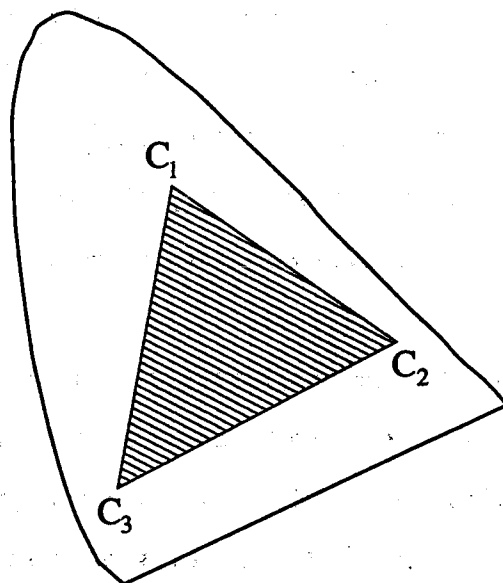
Figure 2.13: The color gamut spanned by the colors $C_1$, $C_2$, and $C_3$.

dinates of these three colors, and the colors falling within the area of this triangle are included in the color gamut. [59] This is illustrated in Fig. 2.13 for three hypothetical phosphors of colors $C_1$, $C_2$, and $C_3$.

The CIE coordinates are an extremely powerful concept because it allows the representation of an entire luminescent spectrum by two numbers. Furthermore, the simplicity of the visual method for obtaining the color gamut of a set of phosphors is quite attractive. The main drawback to the CIE coordinate system is the complexity involved in their calculation. Fortunately, the CIE coordinates are automatically calculated by most modern spectrophotometers, and in the worst case can be calculated by a computer program.

## 2.6  Electrical Characterization of ACTFEL Devices

When testing devices, it is often useful to have a variety of measurements to elicit information about the physics of device operation. In the case of ACTFEL devices, the optical characterization measurements discussed in the previous section

are useful in determining the potential of an ACTFEL process for production. However, these measurements yield little information concerning the physical operation of the device under test. To more closely examine the physics of ACTFEL operation, various electrical characterization techniques are often used. This section describes several of the most common electrical characterization techniques used for ACTFEL devices at Oregon State University.

The electrical characterization measurements described below all have several common characteristics such as the measurement circuit and the driving waveform. The measurement circuit for electrical characterization of ACTFEL devices is shown in Fig. 2.14. The arbitrary waveform generator (AWG) is usually a Wavetek model
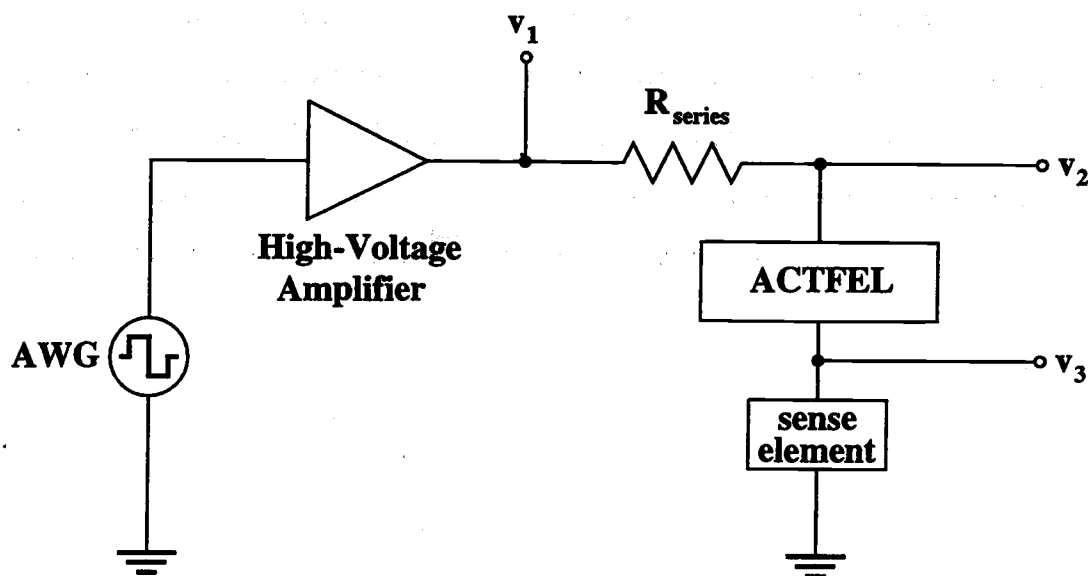


Figure 2.14: The electrical characterization circuit.

395, and is used to produce the voltage waveform that is subsequently amplified by the high voltage amplifier. The output of the high-voltage amplifier then drives the characterization circuit which consists of a resistor and a sense element in series with an ACTFEL device. The function of the resistor, $R_{series}$ is to limit the current to the

ACTFEL device in the event of catastrophic failure. The sense element is generally a capacitor or resistor that is used to reflect information about the ACTFEL device via the voltage across its terminals. A capacitor is the preferred sense element in most of the electrical characterization measurements because its integrating nature makes data acquisition for most measurements more straightforward. The voltages $v_2$ and $v_3$ in Fig. 2.14 are monitored by a Tektronix model 420 digitizing oscilloscope.

The waveform commonly used for electrical characterization of ACTFEL devices at Oregon State University is the bipolar trapezoidal waveform, shown in Fig. 2.15. The "standard" waveform used for most of the electrical characterization techniques is a 1 kHz sequence of bipolar trapezoidal pulses with rise and fall times of 5 $\mu$s and a pulse width of 30 $\mu$s. Note from Fig. 2.15 that an A-J labeling scheme is used to designate certain important points in time on the waveform. The points B and G represent the points in the waveform where the device begins conducting charge, or the turn-on voltage. The other eight points are obvious and require no further explanation. This labeling scheme is used for many of the parametric measurements to match points on a data plot with points of the driving waveform.
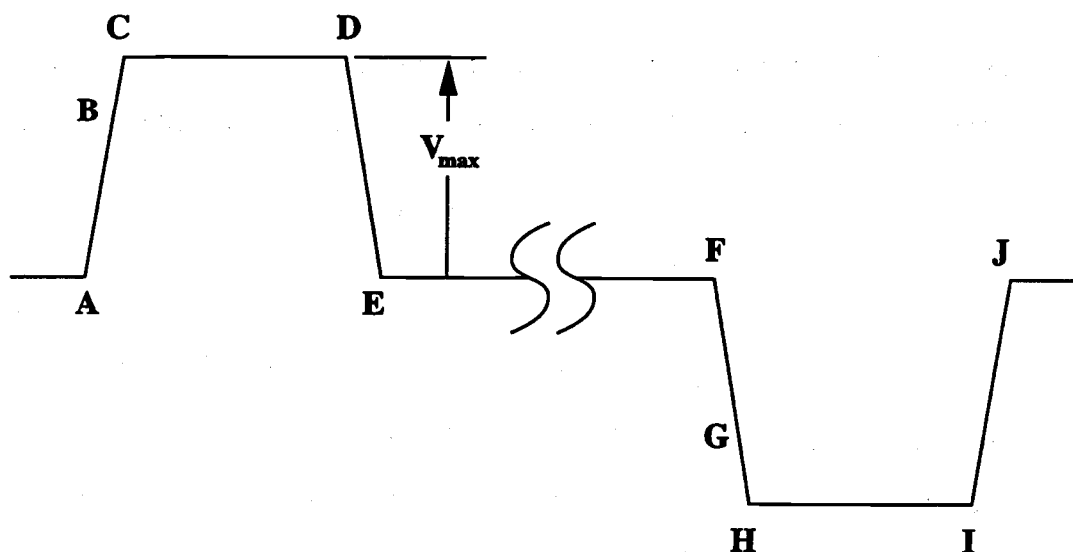


Figure 2.15: The bipolar trapezoidal waveform.

The electrical characterization techniques described in the following sections are based on monitoring the voltage across the sense capacitor. The voltage across the capacitor terminals, $v_3(t)$, is related to the amount of charge stored in the capacitor through the fundamental capacitor equation

$$q_{ext}(t) = C_{sense}v_3(t). \tag{2.22}$$

The charge computed from the above equation, $q_{ext}(t)$, is termed the external charge because it is equal to the charge stored on the external terminals of the capacitive ACTFEL device in series with the sense capacitor. Since it is an insulator that is directly in series with the sense capacitor, the external charge is also given by

$$q_{ext}(t) = C_i V_i, \tag{2.23}$$

where $V_i$ is the voltage dropped across the insulators. External charge is a measure of the charge stored on an ACTFEL device whether it is due to capacitive displacement charge ($q_{disp}$) or actual conduction of charge in the phosphor layer ($q_{int}$), hence, external charge is a measure of the sum

$$q_{ext}(t) = q_{int}(t) + q_{disp}(t). \tag{2.24}$$

If it is recognized that the displacement charge in the above equation is given by the product of phosphor capacitance and the voltage dropped across the phosphor layer,

$$q_{disp}(t) = C_p V_p, \tag{2.25}$$

the expression

$$q_{int}(t) = \frac{C_i + C_p}{C_i} q_{ext}(t) - C_p \left[ v_2(t) - v_3(t) \right] \tag{2.26}$$

is obtained by plugging Eqs. 2.23 and 2.25 into Eq. 2.24, recognizing that the sum of $V_i$ and $V_p$ is the voltage applied to the ACTFEL device, and performing some elementary algebra. This equation is the basis for several of the electrical characterization techniques presented below.

### 2.6.1 Charge-voltage characterization

The most fundamental technique for electrical characterization of ACTFEL devices is the charge-voltage (Q-V) measurement. The Q-V measurement is simply a parametric plot of $q_{ext}(t)$ from Eq. 2.22 versus the voltage across the terminals of the ACTFEL device, $v_2(t) - v_3(t)$. A Q-V plot is always hysteretic when dissipative charge conduction in an ACTFEL device is occurring; hence, it is a straight line with slope equal to $C_t$ when an ACTFEL device is driven below threshold. Therefore, the threshold voltage of an ACTFEL device is the voltage at which the Q-V curve initially becomes hysteretic.
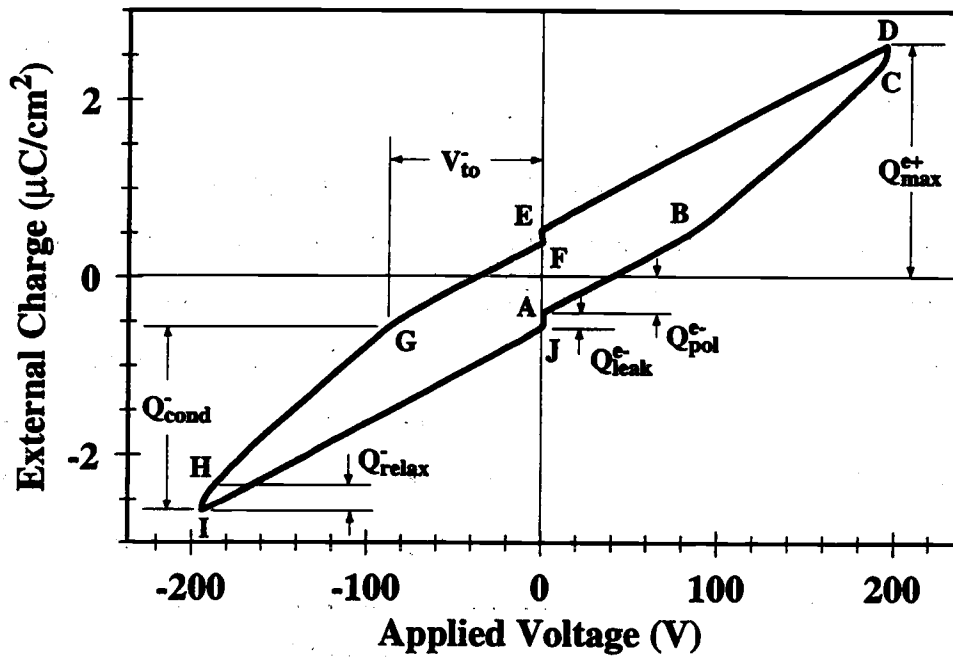
Figure 2.16: A Q-V curve of an evaporated ZnS:Mn ACTFEL device.

A Q-V plot of an evaporated ZnS:Mn device is shown in Fig. 2.16 to illustrate some of the information that is available from a Q-V plot. The voltage labeled $V_{to}^-$ in Fig. 2.16 is termed the negative turn-on voltage; whereas the analogous voltage

during the positive portion of the waveform is known as the positive turn-on voltage, $V_{to}^+$. A distinction is made between these two voltages because they are not in general of equal magnitude, although they are normally very close to the same magnitude. The turn-on voltage differs from the threshold voltage due to the polarization charge, $Q_{pol}^{e-}$ in Fig. 2.16. Polarization charge is a measure of the charge imbalance across the phosphor layer of an ACTFEL device following the conclusion of an applied voltage pulse. The "e-" superscript indicates that polarization charge as measured in a Q-V plot is a purely external quantity that must be transformed by Eq. 2.26 to give a measure of the internal phosphor polarization. The polarization charge existing after the conclusion of a pulse always aids the following pulse of opposite polarity because both result in electric fields of the same polarity. In fact, the threshold voltage, $V_{th}$, may be defined as

$$V_{th} = \lim_{Q_{pol} \to 0} V_{to}(Q_{pol}). \qquad (2.27)$$

One of the factors that can significantly reduce polarization charge is the amount of leakage charge, denoted $Q_{leak}^{e-}$ in Fig. 2.16. The leakage charge is a measure of the amount of charge movement that takes place due to polarization fields during the interpulse intervals (segments EF and JA in Fig. 2.15). The leakage charge as measured by a Q-V is also a purely external quantity, as denoted by the "e-" superscript, and must also be transformed via Eq. 2.26 to get a measure of actual charge movement through the phosphor layer.

The remaining charge terms in Fig. 2.16 are the charge terms that relate to the on time of the ACTFEL device. First, the conduction charge, labeled $Q_{cond}^-$ in Fig. 2.16, is the amount of charge conducted through the phosphor layer of the device from device turn-on until the falling edge of the pulse (segments BD and GI in Fig. 2.15). The conduction charge as measured by the Q-V directly corresponds to the internal phosphor conduction charge, so no "e-" superscript is necessary. Next, the term $Q_{relax}^-$ is termed the relaxation charge, and this is a measure of the charge that flows during the portion of the waveform where the applied voltage is constant at its maximum

value (segments CD and HI in Fig. 2.15). [36] This charge is termed relaxation charge because the flow of this charge gives rise to a field opposite to the applied phosphor field, and since the applied voltage is no longer slewing, the magnitude of the phosphor field tends to decrease, or relax, during this portion of the waveform. Finally, the charge labeled $Q_{max}^{e+}$ in Fig. 2.16 is termed the maximum charge and corresponds to the maximum voltage measured across the sense capacitor for a given applied voltage. Note that $Q_{max}$ is taken with respect to a charge zero reference point, the external charge axis. Thus, $Q_{max}$ differs from all of the other Q-V charges since all of the other charges represent differences in the voltage across the sense capacitor at two distinct points of the applied voltage waveform. As seen in a later section, $Q_{max}$ is a useful quantity for performing transferred charge measurements. It should also be noted that each of the charges discussed above are labeled for only one polarity of the driving waveform in Fig. 2.16, but they exist for both polarities, hence the "+" and "-" superscripts.

The Q-V curve is used to assess several important physical parameters about ACTFEL devices. First, below the turn-on voltage of the ACTFEL device, it behaves as a simple capacitor with the capacitance given by the series combination of the insulator and phosphor capacitances. Since the slope of a Q-V plot is a capacitance, the Q-V slope yields the total device capacitance, $C_t$ in the below turn-on region (segments AB and FG in Fig. 2.16). Next, if the phosphor layer is assumed to be shorted during the post turn-on portion of the driving waveform (segments BC and GH in Fig. 2.16), the slope of the Q-V curve in this region corresponds to the insulator capacitance of the ACTFEL device, $C_i$. This should be approached with some caution, however, because if there is space charge generation during this time, the slope of the Q-V can become much greater than the physical insulator capacitance [8]. On the other hand, sometimes the phosphor layer may be incompletely shunted, and the slope of the Q-V may be much less than the physical insulator capacitance.

Finally, the area enclosed within a Q-V curve is equal to the input electrical power density delivered to the ACTFEL device per pulse. [60]

### 2.6.2 Capacitance-voltage characterization

Capacitance-voltage (C-V) curves are generated by plotting the dynamic capacitance of an ACTFEL device as a function of the voltage across its terminals during the rising edge of the applied voltage waveform. [61] Capacitance-voltage characterization is an extension of Q-V characterization where the slope of the Q-V curve is directly plotted for the rising edge of both the positive and negative portions of the applied voltage waveform (segments AC and FH in Fig. 2.15). The dynamic capacitance is calculated from

$$C = \frac{i(t)}{\frac{d[v_2(t) - v_3(t)]}{dt}},$$ (2.28)

where

$$i(t) = \frac{dq_{ext}}{dt}.$$ (2.29)

A C-V curve of an evaporated ZnS:Mn ACTFEL device is shown in Fig. 2.17 for the standard $V_{th}$ plus 20 V, 40 V, and 60 V amplitudes. Each C-V curve has three turn-on voltages that are labeled $V_{to1}$, $V_{to2}$, and $V_{to3}$ in Fig. 2.17. The voltage $V_{to1}$ corresponds to the onset of carrier conduction through the phosphor layer. The voltage $V_{to3}$ corresponds to the applied voltage at which the phosphor layer is conducting at its full capacity. Finally, $V_{to2}$ corresponds to an average turn-on voltage and is closely related to the turn-on voltage as assessed from a Q-V curve. The measured capacitance below turn-on is $C_{tot}$ and generally closely agrees with the physical capacitance from film thickness measurements, $C_t^{phys}$ as seen in Fig. 2.17. In an ideal ACTFEL device, the above turn-on capacitance is equal to the insulator capacitance, $C_i$, because the phosphor layer is shorted and the ACTFEL device now responds like the series combination of two capacitors. In practice, however, there are very few devices that exhibit this ideal behavior where the on capacitance as assessed from

the C-V, $C_i^{cv}$, is equal to the physical insulator capacitance, $C_i^{phys}$ assessed from film thickness measurements.
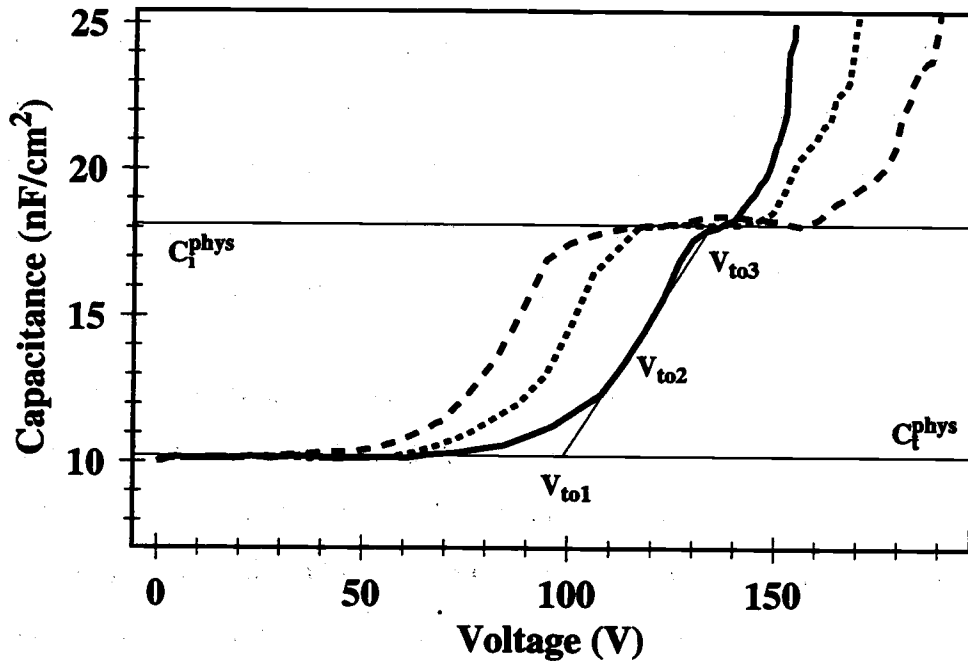


Figure 2.17: A family of C-V curves of an evaporated ZnS:Mn ACTFEL device taken at 20, 40, and 60 V above threshold.

There are two deviations from the ideal situation, $C_i^{cv} < C_i^{phys}$, and $C_i^{cv} > C_i^{phys}$. When $C_i^{cv} < C_i^{phys}$, the amount of conduction current during the rising edge of the applied voltage waveform is insufficient to completely short the phosphor layer. This behavior has been attributed to two different mechanisms; an inadequate interface distribution, or carrier trapping in the bulk during the rising edge of the applied voltage waveform. [62] An inadequate interface distribution implies that there are either too few interface states or that the distribution lies too deep in energy for a sufficient number of carriers to be tunnel-emitted. The trapping of carriers during the rising edge of the applied voltage pulse implies that enough space charge is present

in the phosphor layer to significantly lower the phosphor field in a portion of the phosphor layer to allow for efficient carrier trapping. This is necessary because high-field trapping is not a very likely event; in fact, the capture cross-section for carrier trapping decreases exponentially with field. [35] The second situation, $C_i^{cv} > C_i^{phys}$, is much more common than the $C_i^{cv} < C_i^{phys}$ case. This situation arises when an incremental increase of the applied voltage leads to an incremental decrease of the phosphor field, or the incremental phosphor capacitance is negative. This effect arises when positive space charge is created in the phosphor layer which serves to decrease the average phosphor field as the applied voltage slews to greater values.

### 2.6.3   Internal charge-phosphor field characterization

The internal charge-phosphor field $Q$-$F_p$ characterization technique was developed to provide device physics information that is difficult to determine from a $Q$-$V$. [63] The problem with a $Q$-$V$ plot is that the capacitive displacement charge is lumped together with the physically transported charge in the measurement results. Furthermore, the applied voltage on the x-axis of the $Q$-$V$ measures the voltage across the entire device, while it is more interesting from a device operation point of view to know the voltage, or more exactly, the field across the phosphor layer only. The $Q$-$F_p$ characterization technique solves these problems by displaying the charge that has been transported in the phosphor layer versus the phosphor field.

A $Q$-$F_p$ curve is generated by driving an ACTFEL device in the circuit shown in Fig. 2.14 with a bipolar trapezoidal waveform and parametrically plotting the internal charge as given by Eq. 2.26 versus the phosphor field, $f_p(t)$, as obtained from

$$f_p(t) = \frac{1}{d_p} \left\{ \frac{q_{ext}(t)}{C_i} - [v_2(t) - v_3(t)] \right\}. \tag{2.30}$$

These equations essentially transform the raw data from the $Q$-$V$ measurement to remove the capacitive displacement charge and to compute the phosphor field from the available data. These equations arise from electrostatic equations developed to describe an ACTFEL device with a phosphor layer free of space charge. [9] However,

in the more general case when space charge is present, the measured phosphor field represents the average phosphor field across the phosphor layer, and the measured internal charge is the dipole moment of the charge distribution in the phosphor layer [13],

$$q_{int}(t) = \frac{1}{d_p} \int_0^{d_p} x\rho(x,t)dx, \qquad (2.31)$$

where $\rho(x,t)$ is the charge density at a distance $x$ from the phosphor/insulator interface designated as the zero point of the x-axis.

A Q-$F_p$ curve of an evaporated ZnS:Mn ACTFEL device is shown in Fig. 2.18. In contrast to a Q-V curve, a Q-$F_p$ loop proceeds in a clockwise direction due to the sign convention used to develop Eqs. 2.26 and 2.30. A Q-$F_p$ plot shows the same types of charges that are seen in a Q-V plot ($Q_{cond}$, $Q_{pol}$, $Q_{leak}$, $Q_{relax}$, and $Q_{max}$), however, because of the transformation with Eq. 2.26, these charges are all internal quantities and are directly comparable. The other device parameters that are directly available from a Q-$F_p$ plot are the steady-state fields, $F_{ss}^+$ and $F_{ss}^-$. By plotting Q-$F_p$ curves for different voltages above the threshold voltage, the degree of field-clamping of the device under test is assessed by comparing the steady-state fields at the different voltages. If the steady-state fields are quite similar, the ACTFEL device is said to exhibit strong field-clamping. These fields are sometimes nearly constant fields, but for certain devices that exhibit dynamic space charge effects, there may be overshoot in the field. This overshoot generally occurs around points B and/or G in the Q-$F_p$ plot. Furthermore, for certain devices with severe space charge effects, the field may never reach a steady-state value [64, 65]. Finally, the fields at points A and F in the Q-$F_p$ plot shown in Fig. 2.18 are referred to as the positive and negative polarization fields. These fields correspond to the average field in the phosphor layer just before the arrival of a pulse of opposite polarity to the pulse that set up the polarization field.

The major weakness of Q-$F_p$ characterization of ACTFEL devices is that the plot depends directly on the phosphor and insulator capacitances, as seen in the
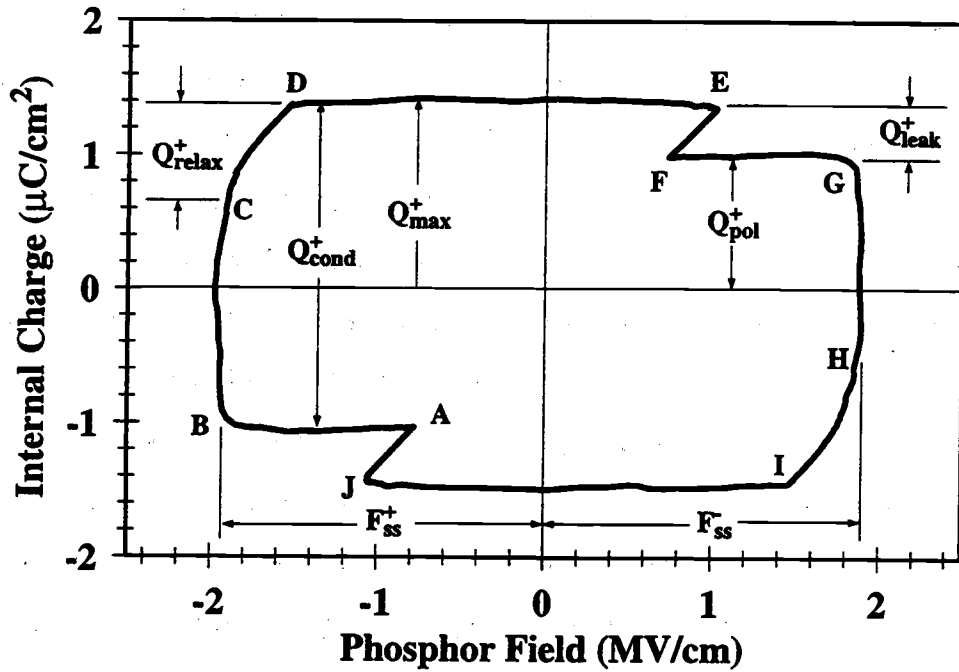
Figure 2.18: A Q-F$_p$ curve of an evaporated ZnS:Mn ACTFEL device.

equations used to create the plot, Eqs. 2.26 and 2.30. An uncertainty in the phosphor thickness directly translates into an uncertainty in the phosphor field and, hence, an uncertainty in the scaling of the phosphor field axis of the Q-F$_p$ curve. Furthermore, uncertainties in the measurements or estimates of $C_i$ and $C_p$ lead to distortions in the shape of the Q-F$_p$ curve. [66] However, the shape of the Q-F$_p$ plot can be used as a guide to how accurately $C_i$ and $C_p$ have been measured. The final difficulty in Q-F$_p$ characterization arises when dynamic space charge is present in the device under test. The difficulty in this case is that the phosphor field may be constantly changing through the rising edge of the applied voltage waveform, resulting in non-physical capacitances which lead to the most "normal" shaped Q-F$_p$ plot. [64]

### 2.6.4 Maximum charge - maximum voltage analysis ($Q_{max}$-$V_{max}$)

The final standard electrical characterization technique often employed for the testing of ACTFEL devices is maximum charge - maximum voltage ($Q_{max}$-$V_{max}$)

analysis. [31, 67] In this measurement, the maximum charge represents the maximum charge stored on the sense capacitor during one cycle of the voltage waveform, and the maximum voltage is the amplitude of the applied voltage pulse leading to the corresponding maximum charge. There are two types of maximum charge that are typically monitored, the internal charge and the external charge. The internal charge values of the $Q_{max}$-$V_{max}$ are analogous to the points of maximum charge from Q-$F_p$ plots (points D and I on the Q-$F_p$). In contrast, the external charge values of the $Q^e_{max}$-$V_{max}$ measurement (also known as the $\Delta$Q-V measurement) [60] are analogous to the points of maximum charge from Q-V plots. Furthermore, the maximum charge magnitude from both the positive and negative half-cycle of the applied voltage waveform are often plotted together to verify the symmetry of charge transfer in the device. Finally, transferred charge analysis such as described above is a classic technique for characterizing ACTFEL devices, however, there are many variations on this technique in the literature which all yield similar results. [9, 25, 28, 23, 56]

$Q_{max}$-$V_{max}$ and $Q^e_{max}$-$V_{max}$ are meaningful measurements for ACTFEL devices, but can be misleading if care is not exercised in the interpretation of the data. The main issue with the $Q_{max}$-$V_{max}$ measurement is that it is unreliable in terms of the magnitudes of the $Q_{max}$ values when the phosphor and insulator capacitances are unknown and unreliable to measure (such as when serious dynamic space charge effects are occurring). However, the $Q_{max}$-$V_{max}$ measurement is important because the amount of internal charge movement versus maximum voltage has roughly the same shape as a L-V curve and gives an idea of how much charge movement internal to the device is required to achieve a level of luminance in a specific ACTFEL device. The derivative of this curve, $\frac{\partial Q_{max}}{\partial V_{max}}$-$V_{max}$, is sometimes examined to obtain the above threshold slope of the $Q_{max}$-$V_{max}$ [39], but this plot is meaningless if the device capacitances are not accurately known. In contrast, the external charge measurement monitors the magnitude of the charge at either point D or I in the Q-V curve, and is referred to as the $Q^e_{max}$-$V_{max}$ technique. A $Q^e_{max}$-$V_{max}$ curve of an evaporated

ZnS:Mn ACTFEL device is shown in Fig. 2.19. The $Q^e_{max}$-$V_{max}$ measurement yields more reliable data than the $Q_{max}$-$V_{max}$ measurement because $Q^e_{max}$ is a directly measured quantity. However, the importance of the $Q^e_{max}$-$V_{max}$ measurement is mainly as a vehicle to obtain its derivatives, the $\frac{\partial Q^e_{max}}{\partial V_{max}}$-$V_{max}$ curve, which is analogous to the dynamic C-V measurement. This derivative curve generally provides more device physics insight into the operation of the ACTFEL device than the parent $Q^e_{max}$-$V_{max}$ curve does because the derivative of a charge with respect voltage is a capacitance. [68] Furthermore, the insulator capacitance as measured from a $\frac{\partial Q^e_{max}}{\partial V_{max}}$-$V_{max}$ plot often correlates with the insulator capacitance of the ACTFEL device better than what is measured from a C-V curve. A $\frac{\partial Q^e_{max}}{\partial V_{max}}$-$V_{max}$ is shown in Fig. 2.20.
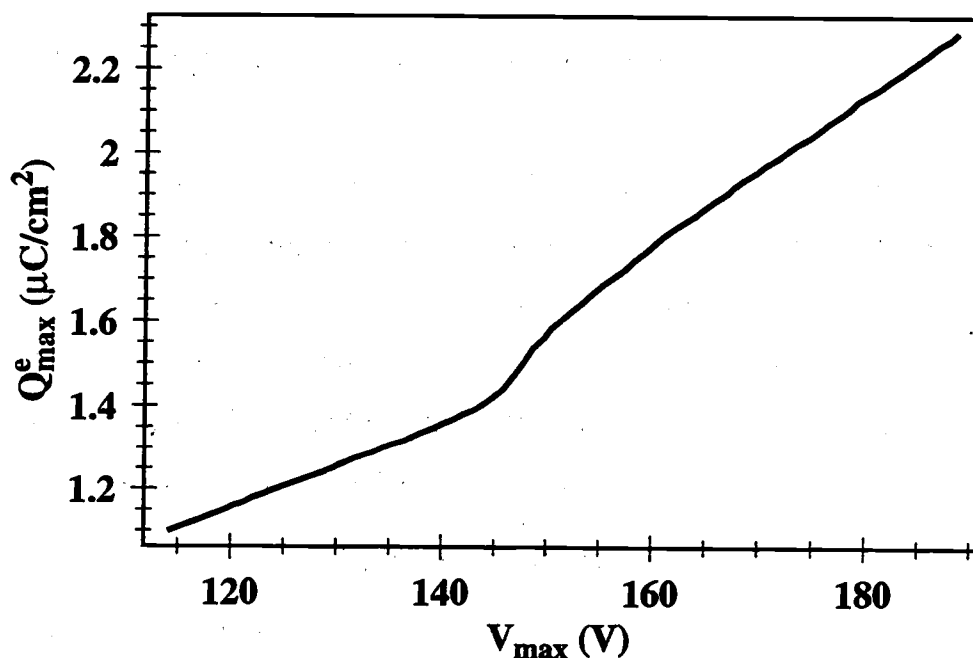


Figure 2.19: A $Q_{max}$-$V_{max}$ curve of an evaporated ZnS:Mn ACTFEL device.

To analyze a $Q_{max}$-$V_{max}$ or $Q^e_{max}$-$V_{max}$ plot and its corresponding derivative curve, it is helpful to determine the components that combine to form the $Q_{max}$ and
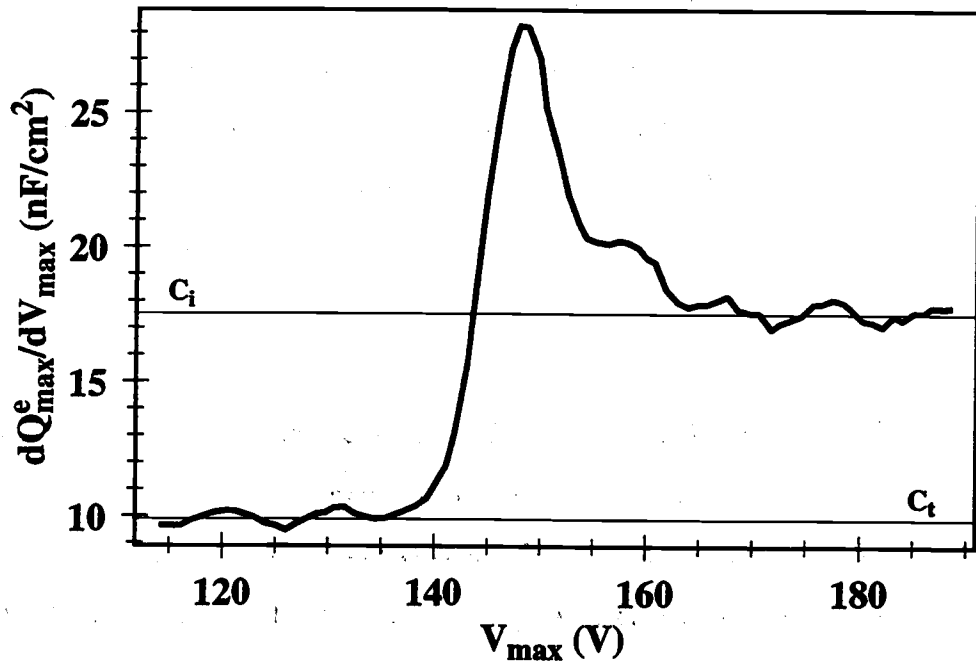
Figure 2.20: A $\frac{\partial Q^e_{max}}{\partial V_{max}}$-$V_{max}$ curve of an evaporated ZnS:Mn ACTFEL device.

$Q^e_{max}$ data. In this case, the components of a $Q^e_{max}$-$V_{max}$ plot are examined, but the analysis proceeds identically for a $Q_{max}$-$V_{max}$ except that all values are internal quantities in that case. When a $Q^e_{max}$-$V_{max}$ curve is examined, it should be kept in mind that the $Q^e_{max}$ data comes from either point D or point I of the Q-V curve. If the $Q^e_{max}$-$V_{max}$ is plotted from point D of the Q-V curve, its components are available by examining a Q-V curve and summing the charges to yield $Q^e_{max}$,

$$Q^{e+}_{max} = Q^{e-}_{pol} + C_t V^+_{to} + C_{on} \left[ V_{max} - V^+_{to} \right] + Q^+_{relax}. \qquad (2.32)$$

It should be noted that the $Q_{max}$-$V_{max}$ measurement can be broken down in a similar fashion by examining the charge components of $Q_{max}$ in a Q-$F_p$ curve. Then, when the derivative of Eq. 2.32 is taken with respect to $V_{max}$, the components of the derivative curve are known, lending more insight into the meaning of the plot. When this derivative is performed,

$$\frac{\partial Q^{e+}_{max}}{\partial V_{max}} = \frac{\partial Q^{e-}_{pol}}{\partial V_{max}} + C_t \frac{\partial V^+_{to}}{\partial V_{max}} + C_{on} \left( 1 - \frac{\partial V^+_{to}}{\partial V_{max}} \right) + \frac{\partial Q^+_{relax}}{\partial V_{max}}, \qquad (2.33)$$

results. Then, certain terms of Eq. 2.33 can be eliminated by driving the ACTFEL device with a modified waveform and comparing them to the results from the bipolar trapezoidal waveform. For example, a modified bipolar trapezoidal waveform with the CD and HI portions removed could be used to eliminate the $\frac{\partial Q^+_{relax}}{\partial V_{max}}$ term in Eq. 2.33.

## 2.7 <u>Conclusion</u>

This chapter is intended as a prelude to the experimental design and results sections in order to provide background information that the reader may find useful for a deeper understanding of subsequent sections. Certainly there is not the space to review all of the topics presented in this chapter in great detail, so an effort was made to present pertinent and practical matters in a clear and concise manner. Additional information regarding many of these topics is available in the cited references.

# 3. ACTFEL PHOSPHOR DEVELOPMENT

This chapter examines the development of phosphor materials in various stages, from the theoretical phase to the practical phase. The chapter begins with a discussion of phosphor host materials with an emphasis on materials parameters that are important in determining the viability of a compound as a phosphor host. Next, issues pertaining to luminescent activators and coactivators are discussed. Following this, a discussion of the advantages and disadvantages of various families of materials for the application of ACTFEL phosphor hosts is undertaken. Then, synthesis and fabrication techniques for the source material from which ACTFEL thin-films are produced are discussed. Finally, the deposition of ACTFEL phosphors is covered, including process details concerning rf sputtering and evaporation.

## 3.1  Important properties of potential ACTFEL phosphor hosts

The identification of new compounds for application as ACTFEL phosphor hosts is a complex and poorly understood area of phosphor science at this point in time. This is mainly due to the fact that only two materials, ZnS and SrS, have been thoroughly investigated as ACTFEL phosphor hosts. However, there are certainly insights to be gained regarding potential phosphor host materials by examining relevant materials properties. Therefore, this section concerns itself with discussion of various materials properties of potential phosphor host materials that impact the characteristics of an operating ACTFEL device.

### 3.1.1  Band structure

A wealth of knowledge concerning the physics of a material is contained in the band structure. As a result, it is quite informative for the device physicist to have knowledge of the band structure of an ACTFEL phosphor host material to aid in unraveling the physics of device operation. However, the band structure of only the

most common ACTFEL phosphor hosts is known with some degree of certainty, and may be completely unknown for many prospective ACTFEL phosphors. Fortunately, only one relatively easily obtained parameter from the band structure is absolutely essential for ACTFEL phosphor development; namely, the forbidden energy gap, or bandgap of the material. It is also helpful, but not absolutely essential, to know the transition type of the bandgap and the effective masses of the principal conduction bands.

The bandgap of a phosphor host material intended for ACTFEL applications is extremely critical to device performance because it is closely intertwined with carrier injection from the interfaces. A material with a bandgap that is too small often has relatively shallow interface states that emit at a field too low to result in a hot enough electron distribution to efficiently impact excite the activator ions. On the other hand, a material with a bandgap that is too large often has relatively deep interface states that do not emit an appreciable number of carriers at realizable driving voltages (<300 V). Also, if the bandgap of the phosphor material is too small, optical absorption of emitted photons may occur in the phosphor layer, and therefore the emitted light will never reach the viewer. In this framework, the absolute minimum and maximum for phosphor bandgap are 3.0 and 5.5 eV, respectively. However, the practical minimum and maximum for the bandgap of commercially relevant phosphor materials is probably closer to 3.5 and 4.5 eV, respectively. With these limits in mind, it should be noted that bandgap values for many materials are either unknown, difficult to locate, or unreliable. Furthermore, although bandgap values for many binary compounds are available and known with some degree of confidence, bandgap values of ternary compounds are often quite difficult, if not impossible, to locate.

The transition type of the bandgap and the effective masses are interrelated materials parameters that allow significant insight into the potential of a material for ACTFEL phosphor applications. The transition type of the bandgap is either direct or indirect depending on whether the conduction band minima and valence band maxima

occur at the same wavevector in the first Brillouin zone. The bandgap transition type is extremely important in determining the performance of many optoelectronic devices because it strongly affects the likelihood of certain optical transitions. However, the importance of the bandgap transition type of an ACTFEL phosphor lies mainly in its influence on carrier injection from the interfaces. Direct bandgap materials typically possess small values of electron effective mass because the curvature of the $\Gamma$ minimum in the conduction band is usually quite sharp. On the other hand, indirect bandgap materials generally possess larger values of electron effective mass because the curvature of conduction bands with minima not coinciding with the zone center is usually small. Effective mass impacts electronic injection because the emission rate due to pure tunneling from a coulombic interfacial trap is governed by [69]

$$e_n^{PT}(f_p) = \frac{q f_p}{4(2m^* E_{it})^{1/2}} exp\left[\left(-\frac{4}{3}\frac{(2m^*)^{1/2} E_{it}^{3/2}}{q\hbar f_p}\right)\left(1 - \left(\frac{\Delta E_{it}}{E_{it}}\right)^{5/3}\right)\right], \quad (3.1)$$

which is exponentially dependent on the square root of the effective mass of the lowest lying conduction band. Furthermore, the band structure of the higher-lying conduction bands plays a large role in determining the high-field electronic transport characteristics of a phosphor material.

### 3.1.2   Dielectric permittivity

For efficient ACTFEL device operation, the goal is to generate a high field in the phosphor layer to initiate charge conduction, and hence, electroluminescence. When an external voltage, $V_{applied}$, is applied to an ACTFEL device, only a fraction appears across the phosphor and the remainder drops across the insulators. The phosphor field generated due to an applied voltage below the threshold voltage of the device is given in Eq. 2.5. This equation shows that the relative capacitances of the phosphor and insulator layers are very important in determining how efficiently the applied voltage is coupled to the phosphor field. Examination of Eq. 2.5 shows that the ideal situation for an ACTFEL device is to have $C_p << C_i$. This means that the relative dielectric constant of the phosphor layer should be low enough such that

phosphor fields of a magnitude that initiate charge conduction in standard thickness ACTFEL phosphors (2000 Å $\leq$ $t_{phosphor}$ $\leq$ 2.0 $\mu$m) can be achieved well within the limits of the available power supplies. With the current insulators used for ACTFEL applications, the practical maximum for phosphor relative dielectric constant is about 15. However, positive space charge in the phosphor layer that is generated prior to the threshold voltage may relax this limit for phosphors prone to this behavior.

### 3.1.3 Melting temperature

The successful fabrication of an ACTFEL device critically relies on the rearrangement and ordering of the atoms composing the phosphor thin-film during some stage in the processing. Numerous studies have shown that ACTFEL luminance and efficiency are closely coupled to the polycrystalline grain size of the phosphor film. [70, 71, 72, 73, 74] The degree of crystallinity of a phosphor material is critically important in determining the luminance and efficiency of an ACTFEL phosphor because it determines the potential for delocalized carrier transport through the phosphor. [49] Delocalized transport is critical because it allows the carrier distribution to become much hotter than if conduction occurs via hopping, such as what occurs in amorphous materials. A hotter carrier distribution results in better impact excitation efficiency, and hence brighter and more efficient light output. In addition, a broadening of the color spectrum in an amorphous phosphor host may occur for some luminescent activators whose emission transitions are strongly affected by the crystal field. [75]

To obtain the phosphor host crystallinity necessary to generate bright and efficient ACTFEL phosphors of a repeatable color spectrum, thermal post-deposition heat treatments are typically performed. The thermal post-deposition heat treatment typically applied to ACTFEL phosphor thin-films is the rapid thermal anneal (RTA). This is an advantageous technique because the substrate temperature can be ramped up and cooled very rapidly, allowing temperatures well in excess of the

substrate melting temperature to be obtained for short periods of time. Due to the exponential dependence of the atomic diffusivity with temperature, this technique holds inherent advantages over furnace sintering from the standpoint of providing greater recrystallization at a higher throughput.

Unfortunately, prediction of the annealing temperature and time required to achieve polycrystalline grain growth for a hypothetical phosphor host often proves difficult. To determine an annealing cycle for a hypothetical phosphor *a priori*, knowledge of the activation energy for atomic motion is necessary. However, this value is not a well-known quantity for most materials because it is typically very dependent upon preparation conditions and impurity levels. [76] It is suggested in the literature that polycrystalline grain growth typically begins at temperatures approximately one-half of the absolute melting temperature. [77] Therefore, the melting temperature of a material is probably the best insight available into the annealing cycle required to reach the onset of polycrystalline grain growth.

This simple rule-of-thumb regarding the onset of sintering implies that potential phosphor hosts with melting temperatures above roughly 1300°C are too refractory to lead to bright and efficient ACTFEL devices on substrates that cannot withstand anneals in excess of 650°C. It is for this reason that the temperature of grain growth is perhaps the most important constraint on ACTFEL phosphors because many well-known phosphors require ~1000°C post-deposition anneals for bright and efficient operation. This situation can be alleviated by the deposition of ACTFEL devices onto ceramic or silicon substrates in an inverted structure, allowing for very high temperature annealing cycles (≤1200°C). However, the inverted structure is prone to unstable ACTFEL devices unless deposited essentially pinhole and defect free, as discussed in Section 2.3.3. As a result, other means are often necessary to circumvent this strict restriction on the annealing temperature. The means typically employed to achieve a reduction of the temperature required to achieve polycrystalline grain growth is the addition of so-called "flux agents." Flux agents are coactivators which

are added to a phosphor host material in small quantities ($\leq$ 5 wt%) that encourage grain growth at a much lower temperature than possible with the pure phosphor host material. The important topic of flux agents for ACTFEL phosphors will be examined in further detail in the Section 3.2.5.

### 3.1.4 Ionicity

The important electronic properties of most semiconducting and insulating materials are governed to a large extent by defects, whether intentionally added or not. For example, in the well-known silicon system, control is exercised over the properties of the silicon through the addition of minute amounts of impurities to the lattice. This type of impurity is known as an extrinsic impurity. However, stoichiometric defects, or intrinsic impurities, may be important in certain materials. The principal element in determining the concentration of stoichiometric defects in a material is the degree of ionic bonding of a compound. Ionic materials typically have large concentrations of stoichiometric defects, especially Schottky defects, or vacant lattice sites, whereas covalently bonded materials tend to have very few imperfections of this sort. [78]

Since the currently known ACTFEL phosphor hosts have an appreciable ionic bonding character and rely quite heavily on defects and impurities for effective operation, the ionicity of a potential phosphor host is an important parameter. It has long been theorized that stoichiometric defects are responsible for the space charge in ACTFEL phosphors that is so intertwined with their operation. [79] The greater tendency for the more ionic SrS phosphor host to exhibit space charge related phenomena than ZnS lends credence to the theory that stoichiometric defects are the underlying cause of space charge in ACTFEL phosphors. [80] Furthermore, the addition of luminescent activators and coactivators of different valence than the phosphor host constituents is known to lead to an effect called "self-compensation" in which it is energetically favorable to create additional stoichiometric defects than to further shift the Fermi level toward the band edge. [81] However, the self-compensation mech-

anism typically acts preferentially towards creating either anion or cation vacancies depending on the energetics of formation of the given defect. Therefore, the degree of ionicity of a phosphor host gives an indication of the degree to which it should be extrinsically compensated to avoid potentially deleterious effects of self-compensation, as noted by Lehmann in his study of alkaline earth sulfide phosphors. [82]

It is also likely that the important interface behavior of an ACTFEL device is impacted to a certain degree by the ionicity of the phosphor host. It has long been known that the Schottky barrier height of covalent semiconductors such as Si and Ge is largely unaffected by the work function of the metal layer because the Fermi level is "pinned" by an abundance of interface states. [83] On the other hand, it is also known that the Schottky barrier height of the more ionic semiconductors such as ZnSe, ZnS, and CdS is primarily dependent upon the work function of the metal because of a much lower density of interface states. [84] Furthermore, it has been experimentally confirmed that significant surface reconstruction occurs with the purely covalent elemental semiconductors and the primarily covalent compound semiconductors. [85] However, surfaces of highly ionic compounds such as alkali halides show almost abrupt termination of the lattice, with very little surface reconstruction. [86] Presumably, because of the very different surface behavior in terms of surface reconstruction and Schottky barrier interface states between ionic and covalent compounds, the ionicity of a compound should somewhat determine its ability to form the interface states that source the electronic charge in an ACTFEL device. This leads to the conclusion that the degree of ionicity roughly corresponds to the degree to which a prospective phosphor departs from the interfacial model of ACTFEL operation. In fact, the best known ACTFEL material in terms of interface injection is ZnS, which is much less ionic than the other well-known ACTFEL phosphor hosts.

In addition to its role as a predictor of the defect chemistry of materials, the ionicity of a compound is also related to both the bandgap and cohesive bonding energy of a compound. As compounds become more ionic in character, their crystals

exhibit larger bandgaps because highly electronegative anions more tightly bind valence electrons. [81, 86] This, in turn, may also be related back to interface states, for larger bandgap materials typically possess deeper interface states. The ionicity of a compound has also been correlated with the cohesive energy per bond or bonding energy. [86] In fact, the bonding energy for isoelectronic compounds decreases almost linearly with increasing ionic bonding contribution. [86]

### 3.1.5 Thermodynamic stability

Thermodynamic stability of the constituent materials is an absolute necessity for the production of long-lived, stable electronic devices of any type. Certainly, the harsh environment seen by an ACTFEL phosphor host in terms of high fields and temperatures implies that thermodynamic stability is an absolute must. Furthermore, materials that are near the edge of stability should be avoided for ACTFEL applications because high operating temperatures may drive such materials to spontaneously dissociate. Therefore, the Gibbs free energies of formation for many binary compounds are tabulated in later sections of this thesis. These values are given in units of kcal/gm atom to provide a rough estimate of the relative stability of compounds of differing molecular complexity. It should be noted that thermodynamic quantities in kcal/gm atom are computed by dividing the standardly available values in kcal/mol by the number of atoms in one molecule of the compound.

### 3.1.6 Moisture sensitivity

A classic problem with many otherwise excellent phosphor host materials is their instability in the presence of moisture. Materials that are unstable in the presence of moisture are classified as either hygroscopic or moisture sensitive, or sometimes both, depending on the mechanism that leads to their moisture-related instability. Hygroscopic compounds are compounds that electrostatically bind polar water molecules, thereby becoming hydrated molecules. [87] Since hygroscopic

behavior is an electrostatic interaction, the odds of a material being hygroscopic increase with increasing molecular polarity. Therefore, compounds with a high degree of ionic bonding character are much more likely to exhibit hygroscopic behavior. In addition, the high density of atomic vacancies typically present in ionic compounds allow water molecules to diffuse easily into the bulk of the material. [88] On the other hand, compounds that are deemed "moisture sensitive" are typically compounds that are easily hydrolyzed. Unfortunately, some of the best phosphor host materials for ACTFEL devices exhibit hygroscopic behavior and moisture sensitivity, leading to increased processing cost and complication.

A major problem with determining suitable new ACTFEL phosphor hosts is the unreliable and unquantified information regarding moisture related instability. Sources in the literature are often contradictory in their analysis of the behavior of compounds in the presence of moisture. Fortunately, a thermodynamic analysis of the reaction of a compound with moisture to form the hydroxide reveals whether a reaction with water is energetically favorable or not. In addition, the amount by which the products or reactants are favored in this reaction gives a crude estimate of the relative moisture sensitivity of a compound. The role of steric effects, protective oxide layers, and uncertainties in standard Gibbs free energies certainly limits the absolute reliability of this type of estimate, but it is a straightforward technique for determining moisture sensitivity from standardly available chemical data. Furthermore, the results of such thermodynamic analyses correspond quite well to moisture sensitivity behavior witnessed in the laboratory. Therefore, this data has been compiled for several compounds of interest in later sections.

### 3.1.7 Transport

The velocity versus electric field characteristics of materials typically show two regimes of operation; a constant slope, low-field regime, and a velocity saturated, high-field regime. Depending upon which regime a material is to be operating in,

transport analyses are conducted either by assuming low-field behavior described by a carrier mobility, or by assuming high-field behavior where carriers travel at a constant, saturated velocity. As a result, transport analyses are initiated by recognition of which regime the material in question is operating in. Since it is well known that ACTFEL phosphors operate at extremely high electric fields compared to other semiconductor devices, the relevant transport in ACTFEL phosphors must be of the high-field variety. When carrier transport occurs in this high-field regime, carrier velocity is $\simeq 10^5$ m/s, almost independent of temperature or the nature of the host lattice. [4]

The ultimate goal of a transport analysis of an ACTFEL phosphor material is to obtain an electron energy distribution for phosphor fields of interest. With an electron energy distribution, it can be determined what percentage of electrons transiting the phosphor possess sufficient energy to impact excite luminescent impurities. Furthermore, the electron energy distribution can be convolved with the impact excitation cross-section to yield an internal excitation efficiency. The electron energy distribution, n(E,F), is a product of the distribution function and the conduction band density of states,

$$n(E, F) = f(E, F)N_c(E), \qquad (3.2)$$

where E is electron energy and F is electric field. As a result, the determination of the electron energy distribution is dependent upon the ability to properly determine both the distribution function, $f(E,F)$, and the conduction band density of states, $N_c(E)$.

The distribution function, $f(E,F)$, for a material subjected to high electric fields is determined largely by the scattering processes that siphon energy from the electron distribution. The scattering mechanisms that are dominant at high electric fields are those that are able to absorb large amounts of energy from the distribution. This is because the electron distribution very rapidly gains energy from these high electric fields and this energy must be efficiently dissipated to result in a stable electron

distribution. The scattering mechanisms that are able to absorb enough energy to stabilize hot electron distributions are electron-lattice interactions. Depending upon the applied electric field and the ACTFEL phosphor material, any of these scattering mechanisms may be important: deformation potential scattering, polar optical phonon scattering, intervalley transfer, and band-to-band impact ionization. The relative importance of the two optical phonon scattering mechanisms is determined largely by the ionicity of the phosphor material in question. The general rule is that the larger the ionicity of the compound, the larger the role that polar optical phonon scattering plays. [4] The importance of intervalley scattering should be quite materials dependent, and is closely related to the band structure through the relative effective masses and energy separation of the valleys in question. Finally, band-to-band impact ionization must be initiated by electrons with energy greater than the bandgap of the material. As a result, this scattering mechanism applies to only the high-energy tail of the electron energy distribution in materials of sufficient bandgap for ACTFEL phosphor applications.

The conduction band density of states, $N_c(E)$, is the other critical parameter in determining the electron energy distribution. The conduction band density of states is given by

$$N_c(E) = \frac{2V}{(2\pi)^3} \int_S \frac{dS}{|\nabla_k E|}, \tag{3.3}$$

where V is the volume of the crystal, S is a constant energy surface, and $\nabla_k E$ is the gradient of the energy with respect to k at the differential surface element of S in question. [78] This equation can often be simplified for examination of low-field transport, but for high electric fields, little simplification is possible because electrons reside in much higher energy parts of the conduction bands. Consequently, the evaluation of the conduction band density of states can be a major stumbling block because it requires a rather intimate knowledge of the band structure, which is often not well-known for less-common materials.

### 3.1.8   Conclusions

The identification of suitable phosphor hosts for ACTFEL applications is often a difficult task because for all but the most well studied of materials there exists considerable uncertainty in many of the parameters discussed in this section. As a result, it is often necessary to make educated guesses for these parameters by using chemical trends. Most of these parameters are completely unknown for ternary and higher order compounds, often necessitating bounding or averaging of parameters through knowledge of the parameters for the associated binary compounds. For example, the bandgap of $ZnGa_2O_4$ is approximated as 3.9 eV, halfway between 3.2 eV, the bandgap of ZnO, and 4.6 eV, the bandgap of $Ga_2O_3$. Although this provides a reasonable estimate of parameters, in many situations there may be significant deviations from linearity that allow only for bounding of the parameters.

## 3.2   Activators and coactivators

This section examines issues pertinent to ACTFEL phosphor activators and coactivators and their incorporation into the host lattice. The section begins with discussions of two of the classic criteria for selecting ACTFEL phosphor luminescent impurities; activator ionic radius and valence. Following this, a discussion of two phosphor host dependent effects that influence the luminescent transitions of certain activators is presented. Finally, the section concludes with an examination of coactivators and killer centers.

### 3.2.1   Ionic radius

Several bright and efficient ACTFEL phosphors are known where ionic radii of the activator and the atom it replaces in the lattice, typically the cation, are not closely matched. However, the matching of the activator and cation ionic radii may be advantageous for several reasons. First, gross discrepancies between the ionic radii of the activator and cation lead to lattice strain induced defects, poor crystallinity, and

device stability problems. The defects so produced can provide non-radiative paths to the ground state for excited activator ions, and hence reduce ACTFEL device luminance and efficiency. Activators much larger than the atom that they replace in the lattice may inhibit polycrystalline grain growth because their large size may prevent ionic diffusion during annealing. [4] In addition, these large activators may be difficult to incorporate into the lattice because they may have difficulty diffusing into proper sites in the lattice during annealing. Activators that are much smaller than the cation which they replace are potential interstitial impurities that can lead to device stability problems. In addition, a small activator ion replacing a large cation may be induced to move in the lattice as a result of high temperature operation or the high fields typical of an ACTFEL phosphor. With this having been said, ZnS:Tb and SrS:Cu are still the brightest known ACTFEL phosphors for their respective colors, although both show instabilities that may be linked to ionic radii mismatches.

### 3.2.2   Valence

The valence of the activator of an ACTFEL phosphor has important impli-cations in terms of material defect chemistry. As a result of the charge neutrality condition and the ionicity of most ACTFEL phosphor host materials, it is often en-ergetically favorable to self-compensate impurities that are not isovalent with the atoms of the host lattice. Self-compensation in most materials with an appreciable ionic character occurs via the creation of Schottky defects, also known as vacancies. [81] Therefore, if widespread formation of Schottky defects is not desired, the valence of the activator and the cation should match. Alternatively, a non-matching acti-vator and cation valence can be extrinsically compensated through the addition of additional dopants, termed coactivators in phosphor terminology. Although valence matching is one of the classic criteria for determining a suitable phosphor host for a given activator, many of the brightest known ACTFEL phosphors violate this rule.

### 3.2.3 Stokes shift

One of the main effects associated with host lattice-activator interaction is Stokes shift. Stokes shift is a measure of the shift of the emission spectrum relative to the excitation spectrum of a phosphor material. [75] Since ACTFEL phosphors are excited by a hot electron distribution that is typically only qualitatively known, Stokes shift is thus identified only by changes in the emission spectrum with changes in the host lattice for this type of phosphor. The presence of Stokes shift is largely determined by the phosphor activator, whereas the magnitude of the Stokes shift is determined by the interaction between the activator and phosphor host.

The physical mechanism leading to Stokes shift is most easily explained with the aid of a configurational coordinate diagram. A configurational coordinate diagram is a plot of the electron energy versus the interatomic distance for an activator in the lattice. Superimposed upon this plot are parabolas representing the harmonic oscillator force constants of the excited and ground states of the activator. Furthermore, the lowest energy states of these harmonic oscillators are typically shown explicitly on a configurational coordinate diagram, as seen in Fig. 3.1. The most important property of the various harmonic oscillator states in terms of the configurational coordinate diagram is the peak of the probability distribution, or the most probable R value. The most probable R value of the harmonic oscillator vibrational states is near the turning points (the parabola), except for the lowest energy state whose distribution peak is at the center of the parabola, $R_0$ and $R_0'$ in Fig. 3.1.

With the aid of the configurational coordinate diagram, the Stokes shift phenomenon can be explained in a simple and straightforward manner. When an activator absorbs energy, it is promoted from the ground state to the excited state, as shown in Fig. 3.1. This transition is represented by an arrow pointing straight up from the center of the lowest vibrational state to the point on the excited state parabola directly above it. This arrow points straight up because the transition is an electronic transition, which occurs on a much smaller timescale than an atomic
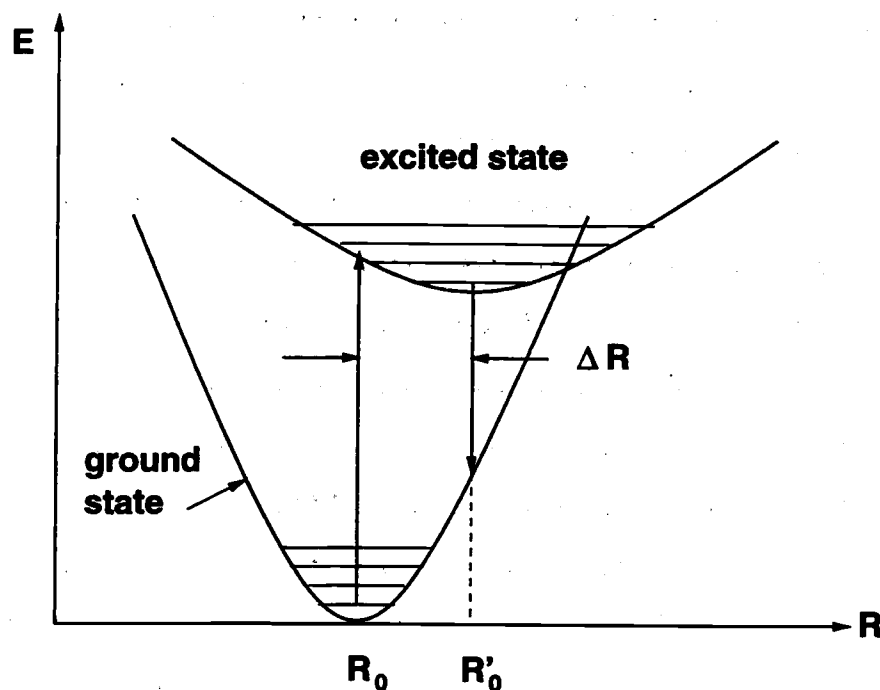
Figure 3.1: A configurational coordinate diagram of an activator with absorption and emission transitions leading to Stokes shift.

transition due to the mass difference between electrons and atoms. The arrow begins at the center of the lowest vibrational state, $R_0$, because it is most likely that the activator is in the lowest vibrational state and the most probable interatomic distance for this vibrational state is $R_0$. The transition probability is proportional to the convolution of the probability distribution of the emitting vibrational state with the vibrational state that is emitted into. Therefore, the arrow ends at the point on the excited state parabola with an interatomic distance value $R_0$ because the most probable interatomic distance at upper vibrational levels is near the parabola. Then, when the activator is in upper vibrational levels of its excited state, it typically relaxes to the lowest vibrational level of the excited state before returning to its ground state, as shown in Fig. 3.1. As a result, the emission wavelength and the absorption wavelength differ by the amount of energy lost to vibrational relaxation. This non-radiative energy loss to vibrational relaxation is termed Stokes shift. In addition to

a change in the emission wavelength, Stokes shift also leads to a broadening of the absorption and emission spectra because different vibrational levels may be involved depending on what interatomic distance the absorption and emission occur at.

Stokes shift is a very activator-dependent phenomenon both in terms of its magnitude and its presence. Many of the rare earth activators luminesce via an f→f intrashell transition, where there is little or no offset in interatomic distance between the ground and excited states. Therefore, for these activators, Stokes shift is nearly imperceptible and the emission spectrum is only weakly dependent on the host lattice. In addition, because there is little Stokes shift, and hence spectral broadening, for these activators, the emission transitions appear as lines in the emission spectrum. All of the rare earth activators except $Eu^{2+}$, $Sm^{2+}$, $Yb^{2+}$, $Ce^{3+}$, $Pr^{3+}$, and $Nd^{3+}$ luminesce via f→f intrashell transitions, and therefore are line emitters. [75] All activators other than the rare earth activators discussed above exhibit Stokes shift because the levels involved in the emission transitions are affected by the crystal field. These activators are affected by the crystal field because the luminescent transitions involve the outermost electronic shell. Activators of this type include the transition metal activators (d intrashell transition), and the sp→$s^2$ and 5d→4f activators. Activators exhibiting Stokes shift have been the most important type of activator for ACTFEL devices to date, although someday the rare earth line-emitters may become more important, as they have for fluorescent lighting.

Stokes shift has many implications in terms of ACTFEL devices because of the potential for chromaticity control via lattice size modifications. Obviously, there is little opportunity for control of the emission spectra of the line emitting rare-earth activators. However, since the brightest and most efficient known ACTFEL phosphors are activated by ions that exhibit Stokes shift, there is the opportunity to alter the phosphor host lattice of some of these phosphors to achieve appropriate chromaticity values. This can be accomplished in practice by increasing or decreasing the lattice constants of the phosphor hosts through alloying or the addition of additional impu-

rities. In addition, the presence of defects in the immediate vicinity of the activator can have profound effects on the spectral distribution of an activator known to exhibit Stokes shift. [89]

### 3.2.4 The nephelauxetic effect

Another effect that can strongly influence the emission characteristics of non-line emitting activators is the nephelauxetic effect. The nephelauxetic effect is the terminology used to describe the effect of electron cloud expansion on the luminescent transitions of activators. [90] Electron cloud size is a phenomenon that is related the covalency of a compound because as the degree of electron sharing increases, the electrons spread out over wider orbitals. [91] As the electron cloud expands, electron-electron repulsion is reduced and charge-transfer transitions shift to lower energies. [75] This leads to an increase in the emission wavelength with an increase in phosphor host covalency. Similar to Stokes shift, the nephelauxetic effect is principally observed in non-line emitting activators because their luminescent transitions generally lie on or near the surface of the ion.

The nephelauxetic effect has important ramifications in terms of ACTFEL phosphors because it implies the possibility of engineering the emission wavelength of a phosphor by altering the local surroundings of the activator. Certainly, the choice of phosphor host will have an effect on the emission wavelength through the nephelauxetic effect, among other things. However, since the nephelauxetic effect is concerned mainly with the covalency in the *local* environment of the luminescent activator, the choice of activator source may have a profound effect upon the emission spectra of the phosphor if the activator is involved in complexing with defects or coactivators. The nephelauxetic effect has been postulated as the physical mechanism behind the spectral shift of SrS:Ce ACTFEL phosphor emission with Ce source. The peak emission wavelength of SrS:Ce,X ACTFEL devices lies in the blue or the green depending on whether X is F or Cl, respectively. This was interpreted as a result of Ce complexing

with the halogen ions from the halide activator source, which determine the spectral characteristics due to their electronegativity and the nephelauxetic effect. [92]

### 3.2.5  Coactivators

A phosphor coactivator is an atomic species in addition to the phosphor host and activator that induces a beneficial or potentially useful modification of the luminescent properties of the phosphor. The field of phosphor coactivation is especially important for ACTFEL phosphor development. In fact, many of the recent developments in ACTFEL phosphor technology can be directly attributed to improved phosphor coactivation. Coactivators are quite varied in nature and are employed for several different tasks in the improvement of ACTFEL phosphors. Generally, ACTFEL phosphor coactivators fall into three different classes according to the function that they perform; flux agents, compensators, and luminescent coactivators. Furthermore, one coactivator can perform two or more of the functions mentioned above in certain situations.

The most important class of ACTFEL phosphor coactivators in a broad sense are flux agents. The purpose of a flux agent in a phosphor material is to improve the crystallinity of the phosphor host lattice by assisting atomic diffusion during high temperature processing. Flux agents are extremely important for ACTFEL phosphors because they provide a means of achieving crystallinity at the low processing temperatures necessary for deposition onto glass substrates. Flux agents are typically non-isovalent with the constituent elements of the phosphor host and either readily diffuse into or react with the phosphor host. The most effective flux agents are non-isovalent with the constituent atoms of the phosphor host because their operation relies upon their ability to generate vacancies to compensate for their presence. It is these vacancies that lead to enhanced atomic motion through the phosphor, enhancing the formation of a crystalline lattice. The most effective flux agents are also either reactive of diffusive because these types of atoms are most easily incorporated

into a phosphor host. With this in mind, the most effective flux agents for ACTFEL phosphors are typically Li, Na, K, Cu, Ga, F, and Cl. [71, 93, 92, 94].

The activators of many of the most important ACTFEL phosphors known today are non-isovalent with the atom that they replace in the host lattice, motivating the use of compensating coactivators. When a phosphor activator is non-isovalent with the atom that it replaces in the host lattice, charge compensation is accomplished via the formation of vacancies (Schottky defects) in compounds with appreciable ionic character. The electrical and optical characteristics of ACTFEL devices based on such phosphor materials suggest that these defects heavily influence device operation. As a result, performance gains may be realized by controlling the defect chemistry through the addition of compensating coactivators. [95, 96] In addition, the emission spectrum of an ACTFEL phosphor may also be modified through the addition of compensating coactivators because all activators that are not line emitters are sensitive to their immediate surroundings, as discussed in the previous subsections. As a result, when these activators complex with a defect, rather dramatic color shifts are sometimes observed.

Another class of ACTFEL phosphor coactivators that sometimes offer performance benefits are luminescent coactivators. Luminescent coactivators are ions that emit radiation of a wavelength that is strongly absorbed by the activator, and hence, enhances its light output. The red $Eu^{2+}$ activator is often coactivated in this manner because it strongly absorbs blue light. [97] Therefore, blue-emitting $Ce^{3+}$ and $Cu^{1+}$ are efficient luminescent coactivators of $Eu^{2+}$. Since many luminescent impurities absorb strongly in the ultraviolet (UV) region of the spectrum, a UV emitter is a good luminescent coactivator candidate for a highly PL active phosphor.

### 3.2.6 Killer centers

The presence of certain atoms in a phosphor can severely degrade or even eliminate its luminescent properties. These atoms, the so-called "killer centers", degrade

overall phosphor performance even when present in minute quantities. Some killer centers operate by strongly absorbing visible wavelength photons from the phosphor and subsequently relaxing by emitting non-visible infrared (IR) photons. [98] Other killer centers extinguish a phosphor's luminescent properties by existing as a deep-level that provides a non-radiative path to the ground state for the excited activator ions. The most well-known killer centers in ZnS phosphors are the iron-group elements, $Fe^{2+}$, $Ni^{2+}$, and $Co^{2+}$, which strongly absorb visible light. The presence of these atoms is also likely to cause degradation of overall phosphor performance for other phosphor materials and contact with these atoms should be avoided. The killer center effect often presents processing problems because many standard pieces of deposition equipment are fabricated from stainless steel, which is rich in these iron group elements. In addition, heating elements are often constructed from nichrome wire that can emit Ni at elevated temperatures. Therefore, many processing systems need to be custom-tailored to meet the specific needs for phosphor deposition due to killer centers.

### 3.2.7 Conclusions

This section is intended as an introduction to some of the issues concerning the activators and coactivators of ACTFEL phosphors. The activation and coactivation of general phosphor materials for fluorescent lighting, cathode-ray tubes, and X-ray phosphors are well-researched topics that are covered in significant detail in references [75] and [99]. Although many useful insights are gained from researching phosphors for other applications, this section has attempted to bring to light issues particular to ACTFEL phosphors.

## 3.3 Materials families for ACTFEL phosphor applications

Although ACTFEL phosphors are predominantly sulfides, there may be advantages to examining other materials families for this application. Only limited

investigations have been undertaken to determine the viability of non-sulfide materials families for ACTFEL applications. This section aims to examine the various families of materials with an emphasis placed on the issues discussed in the prior two sections.

### 3.3.1 Nitrides

Several researchers have investigated nitride materials for ACTFEL applications with varying degrees of success. Nitride materials have recently received a great deal of attention for light-emitting diode (LED) applications because they allow the fabrication of bright and efficient blue and green LEDs. The III-V nitride materials system (AlN, GaN, and InN) was identified as a prospect for the production of bright and efficient blue and green LEDs long ago, but materials fabrication techniques were not advanced enough to fabricate high-quality material necessary for this application. In the last decade, however, materials processing has become advanced enough to grow III-V nitride films with very low defect densities that are suitable for LED applications. These III-V nitride films are mostly grown via molecular beam epitaxy (MBE) [100] and metal-organic chemical vapor deposition (MOCVD). [101] However, high-quality sputtered films have also been reported. [102] The ability to reliably grow high-quality III-V nitride thin-films has certainly revolutionized LED technology, and it may do the same for ACTFEL technology someday.

The main inhibitor to the development of III-V nitride materials for LEDs was the extreme difficulty involved with growth of nitride thin-films. Nitride thin-films are very difficult to grow because the formation of oxides of all elements are heavily favored over the formation of nitrides in terms of thermodynamic considerations. In fact, the nitrides of many elements either do not exist or exist only in thermodynamically metastable states, as shown in Fig. 3.2, and are therefore unusable for high-quality phosphor applications. [103, 104, 105, 106, 107, 108, 109, 110, 111, 112] Therefore, oxygen-containing gases in the background during a nitride deposition pro-

**Figure 3.2:** Standard Gibbs free energies of formation, $\Delta_f G^\circ$, of binary nitrides in $\frac{kcal}{gm\ atom}$.

| | Ia | IIa | IIIb | IVb | Vb | VIb | VIIb | VIII | | | Ib | IIb | IIIa | IVa | Va | VIa |
|---|---|---|---|---|---|---|---|---|---|---|---|---|---|---|---|---|
| 2 | Li$_3$N -7.7 ■ | Be$_3$N$_2$ -25.5 □ | | | | | | | | | | | BN -27.3 O | C$_3$N$_4$ ? O | N$_2$ 0 | NO$_2$ +3.9 |
| 3 | Na$_3$N ? ■ | Mg$_3$N$_2$ -19.2 ■ | | | | | | | | | | | AlN -34.1 □ | Si$_3$N$_4$ -23.1 O | P$_3$N$_5$ -5.2 □ | S$_4$N$_2$ ? O |
| 4 | K$_3$N ? ■ | Ca$_3$N$_2$ -17.6 ■ | ScN -33.9 □ | TiN -37.0 O | VN -22.8 O | CrN -11.1 O | Mn$_5$N$_2$ -5.3 ? | Fe$_4$N +0.2 O | Co$_3$N +2.1 | Ni$_3$N ? ? | Cu$_3$N ? □ | Zn$_3$N$_2$ +1.9 □ | GaN -9.6 O | Ge$_3$N$_4$ -1.3 O | As | Se$_4$N$_4$ ? ◆ |
| 5 | Rb$_3$N ? ■ | Sr$_3$N$_2$ -15.7 ■ | YN -32.1 ◪ | ZrN -40.2 O | NbN -24.6 O | Mo$_2$N -4.4 ? | Tc | Ru | Rh | Pd | Ag$_3$N ? ? | Cd$_3$N$_2$ ? ? | InN -11.1 ? | Sn$_3$N$_4$ ? O | SbN ? ■ | Te$_4$N$_4$ ? ◆ |
| 6 | Cs$_3$N ? ■ | Ba$_3$N$_2$ -14.1 ■ | LaN -32.4 ◪ | HfN -41.4 O | TaN -26.7 O | WN$_2$ ? ◪ | Re | Os | Ir | Pt | Au | Hg$_3$N$_2$ ? ■ | Tl$_3$N ? ■ | Pb | BiN ? ■ | Po |

| | | | | | | | | | | | | | | |
|---|---|---|---|---|---|---|---|---|---|---|---|---|---|---|
| 6 | CeN -34.6 ◪ | PrN ? ◪ | NdN ? ◪ | Pm | SmN -35.2 ◪ | EuN ? ◪ | GdN ? ◪ | TbN ? ◪ | DyN ? ◪ | HoN -37.0 ◪ | ErN -39.5 ◪ | TmN ? ◪ | YbN -40.3 ◪ | LuN ? ◪ |
| 7 | ThN -46.8 ? | Pa | UN -34.8 O | | | | | | | | | | | |

Legend: O = Moisture Insensitive     ■ = Extremely Moisture Sensitive
□ = Mildly Moisture Sensitive     ◆ = Hygroscopic
◪ = Moderately Moisture Sensitive     ? = Unknown

81

cess lead to the formation of an oxide or oxynitride rather than the desired nitride. Unfortunately, even very small concentrations of oxygen-containing gases ($>0.001\%$ $O_2 + H_2O + CO_2$) leads to an appreciable oxygen content in the depositing film because of the extreme thermodynamic predisposition of oxide formation. As a result, nitride growth is very well suited to ultra-high vacuum (UHV) deposition techniques, such as MBE. However, certain processing techniques can be employed to aid in the deposition of nitride materials by more mainstream processing techniques such as sputtering, evaporation, and chemical vapor deposition (CVD).

There are two main prerequisites for success in the growth of nitride thin-films by sputtering, evaporation, and CVD; drastic reduction of oxygen-containing background gases, and chemically activated nitrogen in the deposition chamber. Of the oxygen-containing background gases that present problems for the growth of nitride thin-films, water vapor is the biggest problem because it tends to adhere to surfaces inside the vacuum chamber, and hence, is not efficiently pumped. Two simple techniques to selectively pump water vapor in a vacuum system are chamber baking and the use of cold-traps. Chamber baking imparts energy to adsorbed water molecules inside the vacuum system which decreases their sticking coefficient and thereby increases the probability of capture by the pumping system. Cold traps are generally liquid nitrogen ($LN_2$) cooled, high surface area protrusions into the vacuum system that selectively pump water vapor because the sticking coefficient of water vapor at $LN_2$ temperature (77 K) is very high, resulting in water vapor being effectively "trapped" at these cooled surfaces.[113] Cold traps are also effective, but to a lesser degree, in the capture of $CO_2$ and $O_2$ molecules. Reduction of residual $O_2$ concentration in a vacuum chamber is often accomplished via gettering. [114] Gettering generally involves coating some or all of the vacuum chamber with a material that reacts with background $O_2$ to form a non-volatile oxide. Ti is often used for this purpose because it is easily evaporated and relatively inexpensive; however, Ta is the most effective oxygen-gettering element, but its refractory nature makes it much

more difficult to evaporate. [115] Chemical activation of nitrogen always involves plasma-processing for the deposition of nitride thin-films. The presence of nitrogen in a plasma environment leads to a non-negligible quantity of N radicals that are many times more chemically active than $N_2$ or $NH_3$. Furthermore, $N_2$ or $NH_3$ process gas may be chemically activated by a microwave resonant cavity that generates N radicals prior to admission into the process chamber. [116] Finally, it is important to use the highest-purity process gas available when attempting to deposit nitride materials because of the aforementioned predisposition of elements to form oxides over nitrides. Gas purifiers may help further purify very high-purity process gases for deposition of nitride thin-films.

Assuming that high-quality nitride thin-films can be deposited, they possess some potential advantages over competing materials systems. Unfortunately, due to the difficulty inherent in the synthesis of nitride compounds, little is known about many of the nitride compounds. However, there is a relative abundance of literature available concerning BN, AlN, GaN, InN, and $Si_3N_4$ due to their significance in LEDs and semiconductor devices. It is known that the group IIIa nitrides, AlN, GaN, and InN are all direct-bandgap materials typically of the sphalerite or wurtzite crystal structure, [117] leading to small effective masses for electrons, and hence, excellent carrier injection and transport characteristics as discussed in Section 3.1. Similarly, there is data available on some of the transition metal nitrides, in particular, TiN, ZrN, CrN, $Mo_2N$, NbN, and TaN because of their importance as coatings for high speed tools. The transition metal nitrides have found applications as wear and corrosion inhibitors for high-performance tools, low-friction, and non-stick coatings, optical coatings, and diffusion barriers. However, the transition metal nitrides mentioned above are all extremely refractory materials, hence, their applications are primarily as protective materials for demanding environments.

In addition to the difficulties in the deposition of nitride thin-films discussed above, nitride materials are mostly very expensive to purchase and difficult to work

into suitable forms for processing. Generally, the synthesis of nitride materials is very difficult because the oxides are always thermodynamically preferred over the competing nitride. This requires formation of nitride source materials in an atmosphere devoid of oxygen-containing gases. Furthermore, many nitrides are sensitive to oxygen and moisture at room temperature and will convert to an oxide or hydroxide if left idle in the atmosphere. Therefore, nitride materials should be stored and handled in an inert atmosphere to ensure against chemical composition changes due to contact with the atmosphere. However, some of the nitrides that are sensitive to moisture form protective oxide layers that prevent further oxidation. [118] It is this type of nitride that results in an efficient barrier to moisture when deposited as a high-quality thin film. [119] Finally, many of the binary nitrides are highly refractory, as shown in Fig. 3.3, necessitating extremely high-temperature sintering of sputter and evaporation sources, ideally in an $NH_3$ atmosphere. In addition, the refractory nature of nitride materials implies that it is difficult to achieve polycrystalline grain-growth at standard ACTFEL structure processing temperatures. However, the use of a suitable flux agent may help in this regard, but flux agents have been identified for very few nitrides because most nitrides are uncommon and difficult to work with.

The final difficulty with nitride materials for ACTFEL applications is that very few of the binary nitrides possess sufficiently large bandgaps to prevent absorption of visible light. Of the nitride materials that are thermodynamically stable at room temperature, only BN, AlN, $Si_3N_4$, $P_3N_5$, $Ge_3N_4$, TiN, and GaN are known to possess bandgaps greater than the 3 eV absolute minimum requirement, as shown in Fig. 3.4. [120, 121, 122, 123, 124, 125, 126, 127] However, bandgap values for many of the binary nitrides are not currently available in the literature. The bandgaps of $Be_3N_2$, VN, and CrN are potentially larger than 3 eV, but these values have not yet been reported in the literature. Of the materials known to possess a sufficiently large bandgap for ACTFEL applications, only $Ge_3N_4$ falls in the range of bandgaps for potential commercial utilization. However, Ge is a +4 valence cation, which limits its

| | Ia | IIa | IIIb | IVb | Vb | VIb | VIIb | VIII | | | Ib | IIb | IIIa | IVa | Va | VIa |
|---|---|---|---|---|---|---|---|---|---|---|---|---|---|---|---|---|
| 2 | $Li_3N$ 813 M N | $Be_3N_2$ 2200 M | | | | | | | | | | | BN 2325 D | $C_3N_4$ ? ? | $N_2$ -210 M | $NO_2$ -11.2 M |
| 3 | $Na_3N$ 300 D | $Mg_3N_2$ 800 D | | | | | | | | | | | AlN 2517 D | $Si_3N_4$ 1878 D | $P_3N_5$ ? ? | $S_4N_2$ 23 M |
| 4 | $K_3N$ ? D | $Ca_3N_2$ 1195 M | ScN 2650 M | TiN 2930 M | VN 2320 M | CrN 1700 D | $Mn_5N_2$ ? ? | $Fe_4N$ ? ? | $Co_3N$ ? ? | $Ni_3N$ ? ? | $Cu_3N$ 300 D | $Zn_3N_2$ 246 D | GaN 800 S | $Ge_3N_4$ 1000 D | As | $Se_4N_4$ 160 E |
| 5 | $Rb_3N$ ? ? | $Sr_3N_2$ 1030 M | YN ? ? | ZrN 2980 M | NbN 2573 M | $Mo_2N$ ? ? | Tc | Ru | Rh | Pd | $Ag_3N$ ? ? | $Cd_3N_2$ ? ? | InN ? ? | $Sn_3N_4$ ? ? | SbN 550 D | $Te_4N_4$ ? ? |
| 6 | $Cs_3N$ ? ? | $Ba_3N_2$ 1000 M | LaN ? ? | HfN 3305 M | TaN 3360 M | $WN_2$ >400 M V | Re | Os | Ir | Pt | Au | $Hg_3N_2$ ? E | $Tl_3N$ ? ? | Pb | BiN ? ? | Po |

| | | | | | | | | | | | | | |
|---|---|---|---|---|---|---|---|---|---|---|---|---|---|
| 6 | CeN ? ? | PrN ? ? | NdN ? ? | Pm | SmN ? ? | EuN ? ? | GdN 2330 M | TbN ? ? | DyN ? ? | HoN ? ? | ErN ? ? | TmN ? ? | YbN ? ? | LuN ? ? |
| 7 | ThN ? ? | Pa | UN 2630 M | | | | | | | | | | | |

Legend:  
D = Decomposes  
E = Explodes  
M = Melts  
N = in Nitrogen  
P = under Pressure  
S = Sublimes  
V = in Vacuum  
? = Unknown

Figure 3.3: Transition temperatures of binary nitrides in °C.

Figure 3.4: Room temperature bandgaps of binary nitrides in eV.

| | Ia | IIa | IIIb | IVb | Vb | VIb | VIIb | VIII | | | Ib | IIb | IIIa | IVa | Va | VIa |
|---|---|---|---|---|---|---|---|---|---|---|---|---|---|---|---|---|
| 2 | $Li_3N$ 2.00 ? | $Be_3N_2$ ? ? | | | | | | | | | | | BN 7.2 I | $C_3N_4$ 6.4 I | $N_2$ N/A | $NO_2$ N/A |
| 3 | $Na_3N$ ? ? | $Mg_3N_2$ 2.9 ? | | | | | | | | | | | AlN 6.2 D | $Si_3N_4$ 5.1 ? | $P_3N_5$ 5.2 ? | $S_4N_2$ ? ? |
| 4 | $K_3N$ ? ? | $Ca_3N_2$ ? ? | ScN 2.6 ? | TiN 3.4 ? | VN ? ? | CrN ? ? | $Mn_5N_2$ ? ? | $Fe_4N$ ? ? | $Co_3N$ ? ? | $Ni_3N$ ? ? | $Cu_3N$ 0.5 I | $Zn_3N_2$ 3.2 I | GaN 3.39 D | $Ge_3N_4$ 4.2 D | As | $Se_4N_4$ ? ? |
| 5 | $Rb_3N$ ? ? | $Sr_3N_2$ ? ? | YN 1.9 ? | ZrN ? ? | NbN ? ? | $Mo_2N$ ? ? | Tc | Ru | Rh | Pd | $Ag_3N$ ? ? | $Cd_3N_2$ ? ? | InN 1.8 D | $Sn_3N_4$ ? ? | SbN ? ? | $Te_4N_4$ ? ? |
| 6 | $Cs_3N$ ? ? | $Ba_3N_2$ ? ? | LaN 1.1 ? | HfN ? ? | TaN 2.3 ? | $WN_2$ ? ? | Re | Os | Ir | Pt | Au | $Hg_3N_2$ ? ? | $Tl_3N$ ? ? | Pb | BiN ? ? | Po |

| | | | | | | | | | | | | | | |
|---|---|---|---|---|---|---|---|---|---|---|---|---|---|---|
| 6 | CeN 0.7 ? | PrN 1.03 ? | NdN 0.8 ? | Pm | SmN 0.7 ? | EuN 0.76 ? | GdN 0.98 ? | TbN 0.8 ? | DyN 0.91 ? | HoN 1.05 ? | ErN 1.2 ? | TmN 1.1 ? | YbN 1.03 ? | LuN 1.55 ? |
| 7 | ThN ? ? | Pa | UN ? ? | | | | | | | | | | | |

Legend: D = Direct Bandgap  N/A = Not Applicable
I = Indirect Bandgap  ? = Unknown

compatibility with luminescent impurities because most of the important luminescent impurities are +2 or +3 valence. Of the remaining nitride compounds, only GaN and TiN, fall near the range of bandgaps of potential commercial utility. Actually, of these three compounds with bandgap in the correct range for consideration as ACTFEL phosphors, GaN is the most attractive choice because it is one of the most well-studied of the nitrides, it is stable in the presence of moisture, it is thermodynamically stable, and it is not tremendously refractory. This is a large part of the reason why GaN has been a major component of the most successful nitride phosphor ACTFEL devices witnessed to date. [128]

With the limited choice of binary nitride compounds meeting the criteria as potentially useful ACTFEL phosphors, there is motivation to examine ternary and quaternary alloys and compounds. Since information on the properties of ternary and quaternary nitride is quite scarce, educated guesses must be made to obtain a rough estimate of their materials properties. This generally involves interpolation between the associated binary compounds constituting the higher-order compound. However, there is limited literature available for certain higher-order nitride compounds. From the combination of the available literature and educated guesses concerning the materials properties, the materials properties of higher-order nitride compounds with the most potential for ACTFEL phosphor applications can be roughly determined.

An examination of the group I nitrides leads to definite conclusions about the feasibility of synthesizing higher-order nitride compounds containing group I elements. The only group I nitride that is known to be thermodynamically stable is $Li_3N$, making Li the first choice for use in any group I containing ternary or quaternary nitride compounds for ACTFEL applications. [129] However, $Li_3N$ is highly moisture sensitive and ignites spontaneously in moist air and should be avoided unless it can be handled in a moisture-free environment. [130] In addition, all of the remaining group I nitrides are quite moisture sensitive. Therefore, a group I element should combine with an element that forms a highly stable, large bandgap, moisture-insensitive nitride

to have any hope of achieving a robust material. These criteria leave only B, Si, and possibly Al as elements that could potentially combine with a group I element for a robust material. In fact, the existence of $Li_2SiN_2$ and $Li_3AlN_2$ have recently been reported, but no mention is made of their moisture sensitivity other than they are not explosive. [130] Considering these facts, the risks far outweigh the benefits of synthesizing group I containing nitrides for ACTFEL applications.

Ternary and quaternary nitride compounds containing group II elements are certainly more promising than those containing group I elements for ACTFEL phosphor applications, but very serious problems also arise in the realization of these compounds. As far as thermodynamic stability is concerned, all group IIa nitrides are thermodynamically stable, whereas all group IIb nitrides are thermodynamically unstable. The most severe problem with the group II nitrides, however, is their extreme moisture sensitivity. In fact, it has been reported that $Mg_3N_2$, $Ca_3N_2$, $Sr_3N_2$, and $Ba_3N_2$ powders all rapidly react to form the corresponding hydroxides almost immediately upon exposure to the atmosphere. [112] This type of water vapor sensitivity leads to severe contamination problems during the preparation of source material because it is nearly impossible to avoid incidental contact with the atmosphere for short periods of time when transferring specimens to and from furnaces, weighing stations, etc. These materials are certainly most moisture sensitive while in powder form because the high surface area to volume ratio of a powder provides a much greater amount of area for condensation of water than a thin-film or a ceramic block of material. Therefore, the source material for nitride compounds containing group IIa elements must be prepared in a closed environment that is virtually free of water vapor, necessitating costly equipment and extreme care. Furthermore, it is unclear whether group IIa nitrides have the potential to produce compounds that lead to high-quality thin-films, owing to their extreme moisture sensitivity. The reason for the moisture sensitivity of group II nitrides is that they readily react with water to

Table 3.1: Standard reaction Gibbs free energies for the reaction of group II nitrides with water vapor ($II_3N_2 + 6H_2O \longrightarrow 3II(OH)_2 + 2NH_3$).

| Group II Nitride | $\Delta_r G°$ ($\frac{kcal}{mol}$) |
|---|---|
| $Be_3N_2$ | -138.9 |
| $Mg_3N_2$ | -182.4 |
| $Ca_3N_2$ | -236.4 |
| $Sr_3N_2$ | -234.4 |
| $Ba_3N_2$ | -225.8 |
| $Zn_3N_2$ | -20.5 |

form hydroxides and ammonia, as in

$$X_3N_2 + 6H_2O \longrightarrow 3X(OH)_2 + 2NH_3, \tag{3.4}$$
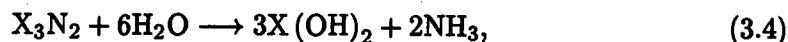
where X is Be, Mg, Ca, Sr, Ba, or Zn. An examination of the standard reaction Gibbs free energies for the reactions between the group II nitrides and water gives a relative measure of the stability of these compounds in the presence of humidity, as discussed in Section 3.1. The standard reaction Gibbs free energies of the group II nitrides are tabulated in Table 3.1. From this data, certainly the most attractive group II nitride to work with are $Be_3N_2$ and $Zn_3N_2$. However, $Be_3N_2$ can be excluded from any potential group II nitride compound because the highly toxic nature of Be compounds makes their large-scale use a health and environmental hazard. Furthermore, $Zn_3N_2$ is thermodynamically unstable, as discussed above. Judging by the thermodynamic and moisture stability problems with group II nitrides, any ternary or quaternary compound containing a group II cation must also contain an element that forms a highly stable, large bandgap, moisture-insensitive nitride for the possibility of forming a compound fitting the specifications for an ACTFEL phosphor. This implies that Si, B, Ge, or possibly Al must be included in the compound. There have been reports of

synthesis of $ZnSiN_2$, $ZnGeN_2$, $MgSiN_2$, $CaSiN_2$, and $XCN_2$, where $X = Mg$, $Ca$, $Sr$, or $Ba$. [131, 132, 133, 134] However, no reports of the moisture sensitivity of these compounds are available.

The nitride compounds containing group III elements are certainly the most promising of the nitride materials for ACTFEL applications. This class of nitrides consists of alloys of III-V nitrides, which are currently commercially produced for LED applications, and III-IV-V compounds. Alloys of AlN and GaN are the nitride phosphors that have demonstrated the brightest and most efficient nitride ACTFEL devices to date, as shown in Table 3.2 [128], and certainly deserve mention when examining the potential of nitride materials as ACTFEL phosphors. In addition, alloys

Table 3.2: Luminance and color of III-V nitride ACTFEL devices (all devices driven with a 500 Hz, 120 VRMS sine wave).

| phosphor | color | L (cd/m$^2$) |
|---|---|---|
| $Al_{0.35}Ga_{0.65}N$:Sm | Red | 83 |
| $Al_{0.35}Ga_{0.65}N$:Eu | Red | 57 |
| GaN:Sm | Orange | 43 |
| AlN:Sm | Orange | 1 |
| $Al_{0.35}Ga_{0.65}N$:Tb,Zn | Green | 130 |
| $Al_{0.4}Ga_{0.6}N$:Tb | Green | 97 |
| GaN:Tb | Green | 54 |
| AlN:Tb | Green | 3 |
| $Al_{0.35}Ga_{0.65}N$:Ce | Blue-Green | 25 |
| $Al_{0.35}Ga_{0.65}N$:Tm | Blue | 3 |
| GaN:Tm | Blue | 2 |
| AlN:Tm | Blue | 0.5 |

of AlN and InN have been investigated as ACTFEL phosphors, but oxygen incorporation during thin-film deposition has precluded a definitive conclusion regarding their potential as ACTFEL phosphors. [135, 136] Furthermore, it may be possible to alloy either AlN or BN with group IIIb, transition metal, or lanthanide nitrides to achieve a proper bandgap. Once again, however, there are moisture sensitivity issues with many of the group III nitrides which lead to difficulties in the synthesis of source material for thin-film deposition. The standard reaction Gibbs free energies for the reaction of the group III nitrides are shown in Table 3.3. For comparison purposes, BN and GaN are both considered to be stable in the presence of water vapor, whereas AlN is considered to be mildly sensitive to the presence of water vapor. It should be noted that the mild moisture sensitivity of AlN is similar in nature to the mild moisture sensitivity of pure Al and Si, which both form a thin native oxide layer that protect the underlying material from further contamination. [118] According to the data in Table 3.3, the group IIIb nitrides have a much greater potential for moisture sensitivity, and should be avoided in favor of the group IIIa nitrides unless the necessary equipment is available to prepare these materials in a moisture-free environment.

Table 3.3: Standard reaction Gibbs free energies for the reaction of group II nitrides with water vapor ($IIIN + 3H_2O \longrightarrow III(OH)_3 + NH_3$).

| Group III Nitride | $\Delta_r G^\circ$ ($\frac{kcal}{mol}$) |
|---|---|
| BN | -17.0 |
| AlN | -45.1 |
| GaN | -19.5 |
| InN | +10.0 |
| ScN | -67.0 |
| YN | -82.9 |
| LaN | ? |

The data on the bandgaps of binary nitrides shown in Fig. 3.4 coupled with the moisture sensitivity data presented in Table 3.3 yields several alloys of group IIIa nitride materials which deserve investigation as ACTFEL phosphors. The extremely small ionic radius of B limits its utility as a phosphor cation due to the fact that most of the +3 valence luminescent impurities are relatively large. However, the remaining group IIIa nitrides, AlN, GaN, and InN are worthy choices for the synthesis of III-V nitride alloys because they provide for the correct range of bandgap energy, they are relatively stable in the presence of moisture compared to many other nitrides, and there is sufficient literature available concerning their synthesis. Additionally, alloys of AlN and InN for optimum bandgap should be doped with the standard lanthanide luminescent impurities to investigate whether the three primary colors can be achieved with this type of phosphor. The major stumbling block impeding realization of this goal is the extreme expense of GaN and InN source material. Therefore, this material should be fabricated in-house for economic reasons. A review of the literature concerning the synthesis of binary nitrides that are potential components of ACTFEL phosphor hosts is presented in Appendix A.

The choice of group IV nitrides for ternary and quaternary compounds and alloys is limited because only $Si_3N_4$ and $Ge_3N_4$ are known to exist as stable compounds. However, there has been ongoing research in an effort to synthesize $C_3N_4$ because it has been theorized that it should possess some unique materials properties. Unfortunately, $C_3N_4$ is a compound that cannot be synthesized by traditional high-temperature solid-state reactions, making source material synthesis an imposing proposition. [124] As for Sn and Pb nitrides, there is evidence that $Sn_3N_4$ is thermodynamically metastable and slowly breaks down into Sn and $N_2$, whereas Pb is not known to form a nitride. [112] Therefore, any alloy of group IV nitrides should be composed exclusively of $Si_3N_4$ and $Ge_3N_4$ for stability reasons. Unfortunately, very few luminescent impurities of the correct valence and size match with Si or Ge are known, leaving to chance the possibility for efficient luminescence from these com-

pounds. It is also feasible to synthesize phosphor compounds containing group IV elements, but the most stable and robust should be of the IIIa-IV-V variety. However, a IIIa-IV-V compound nitride phosphor is probably not worth the effort to synthesize because the added complexity of producing a ternary compound is not adequately compensated by an increase in flexibility of the choice of luminescent impurities or of bandgap control from alloys of group IIIa nitrides. Therefore, although several group IV nitrides are known to be stable, robust materials, their potential as components of ACTFEL phosphors is considerably less than the attractive group IIIa nitrides.

The final classes of nitrides to be considered for ACTFEL applications are the transition metal nitrides and the nitrides of the lanthanide series of elements. The nitrides of the transition metals of groups IVb, Vb, and VIb are all thermodynamically stable compounds that are quite rugged. In fact, these compounds main applications are as coatings to increase the working life of bits for cutting tools. These nitrides are quite effective in this area because they generally have low coefficient of friction against steel, carbides, and ceramics. In addition, these compounds are all quite refractory, adhere well to substrates, and are inert to attack from acidic and basic solvents. These are all positive qualities for coatings to protect tool bits, but for phosphor applications, highly refractory materials are undesirable because most are amorphous, not polycrystalline, at temperatures that are compatible with glass substrates. Furthermore, the stoichiometry of these compounds is such that they are naturally nitrogen deficient, resulting in moderate to high conductivity, which is highly undesirable for an ACTFEL phosphor. [137] However, nitrogen-rich dielectric thin-films of some of these materials have been demonstrated. [138]

The nitrides of the elements of the lanthanide series are all quite similar in their physical and thermodynamic properties, as shown in Figs. 3.2 - 3.4. The bandgap of all of these nitrides is on the order of 1 eV, as shown in Fig. 3.4, meaning that for these materials to be a component of a phosphor host, they must be part of an alloy or compound. The lanthanide series elements are interesting to consider as

possible constituents of a phosphor host because their similar ionic radii and chemical properties lead to the conclusion that any one of them should easily substitute into a lattice with another as a cation. However, there are three problems with these materials: moisture sensitivity, refractory nature, and high cost. Although little is known about the moisture sensitivity of the nitrides of the lanthanide series elements, chemical intuition dictates that their moisture sensitivity should be on the order of that of LaN, which is moderately moisture sensitive. The moisture sensitivity issue always presents problems in handling of source materials, and probably leads to decreased thin-film stability. The refractory nature of the nitrides of the lanthanide elements is seen in the high melting points of all of these materials shown in Fig. 3.3. Furthermore, these materials, when available, are prohibitively expensive, which when coupled with their finite shelf-life owing to moisture sensitivity, makes them difficult and costly to experiment with. Therefore, the use of lanthanide series nitrides should probably be limited to dopant source applications.

The preceding statements concerning nitride materials for ACTFEL phosphor applications leads to the conclusion that there are only a small number of nitride materials that show potential as ACTFEL phosphor hosts, namely GaN or alloys of AlN, GaN, and InN. All other nitrides have inherent problems that are not likely to be worth the expenditure of time and resources to overcome. The increasingly large amount of literature available concerning AlN, GaN, and InN for LED applications should be used as a guide to try to grow phosphor-quality thin-films of alloys of these materials. Unfortunately, the deposition equipment currently available at Oregon State University is probably not well-suited for a meaningful examination of nitride compounds for phosphor applications. In addition, the difficult chemistry associated with the synthesis of nitride compounds should not be taken lightly; competent chemists should be sought out to aid in the synthesis of any source material to be used for the deposition of nitride thin-films.

### 3.3.2 Phosphides, arsenides, and antimonides

Phosphides, arsenides, and antimonides are families of materials that have shown promise for specific applications as semiconductors. However, none of the binary compounds from any these families of materials has a sufficiently large bandgap to warrant consideration as an ACTFEL phosphor for full-color applications. In addition, since no binary compound from any of these three families of materials exhibits a sufficient bandgap, it is expected that no ternary or quaternary compound from these materials families should exhibit a sufficient bandgap for ACTFEL applications. Therefore, these three families of materials should not be considered as potential full-color ACTFEL phosphor hosts. Although the bandgaps of all of these materials are too small for full-color, certain members of these families possess sufficient bandgap to transmit red light as was demonstrated by an ACTFEL device with a GaP:Pr phosphor layer which output 13 cd/m$^2$ of red light with a 120 Vrms sinusoidal drive. [128]

### 3.3.3 Oxides

Of the known luminescent materials, oxygen-containing materials are by far the most numerous. Of these materials, many are pure oxides, while others are combinations of oxides with other families of materials, such as the oxyhalides. However, this subsection focuses strictly on oxide phosphors. Early research on phosphors mostly focused on oxide phosphors because almost every element combines with oxygen to form a thermodynamically stable oxide, as shown in Fig. 3.5. Furthermore, many oxide phosphors were first discovered as naturally occurring minerals that exhibited luminescent properties. [139] As a result, many of the technologically important phosphors for mature applications such as fluorescent lamps and CRTs are oxides or contain oxygen. Therefore, there is a more significant amount of knowledge available concerning oxide phosphors than exists for most other families of phosphor materials. In addition, the main reactive components of the atmosphere are $O_2$ and $H_2O$, which

Figure 3.5: Gibbs free energies of formation, $\Delta_f G°$, of binary oxides in $\frac{kcal}{gmatom}$.

| | Ia | IIa | IIIb | IVb | Vb | VIb | VIIb | VIII | | | Ib | IIb | IIIa | IVa | Va | VIa |
|---|---|---|---|---|---|---|---|---|---|---|---|---|---|---|---|---|
| 2 | $Li_2O$ -44.7 ■ | BeO -69.3 ○ | | | | | | | | | | | $B_2O_3$ -57.1 ◆ | $CO_2$ -31.4 | $NO_2$ +3.9 | $O_2$ 0 |
| 3 | $Na_2O$ -30.1 ■ | MgO -68.0 ○ | | | | | | | | | | | $Al_2O_3$ -75.6 ○ | $SiO_2$ -68.2 ○ | $P_2O_3$ -49.8 ■ | $SO_2$ -27.1 |
| 4 | $K_2O$ -24.0 ■ | CaO -72.1 ◆ | $Sc_2O_3$ -87.0 ○ | $TiO_2$ -70.8 ○ | $V_2O_3$ -54.9 ○ | $Cr_2O_3$ -50.6 ○ | MnO -43.4 ○ | $Fe_2O_3$ -35.5 ○ | $Co_3O_4$ -27.4 ○ | NiO -25.3 ○ | CuO -15.3 ○ | ZnO -38.3 ○ | $Ga_2O_3$ -47.7 ○ | $GeO_2$ -41.5 ○ | $As_2O_3$ -27.5 ○ | $SeO_2$ -17.3 ○ |
| 5 | $Rb_2O$ -23.9 ■ | SrO -67.0 ◨ | $Y_2O_3$ -86.8 ○ | $ZrO_2$ -83.1 ○ | $Nb_2O_5$ -60.3 ○ | $MoO_2$ -42.5 ○ | $TcO_2$ -30.1 ? | $RuO_2$ -20.1 ◆ | $Rh_2O_3$ -13.2 ◆ | PdO -10.2 ◆ | $Ag_2O$ -0.9 ○ | CdO -27.3 ○ | $In_2O_3$ -39.7 ○ | $SnO_2$ -41.4 ○ | $Sb_2O_4$ -31.7 ○ | $TeO_2$ -26.0 ○ |
| 6 | $CsO_2$ -24.6 ■ | BaO -62.1 ◨ | $La_2O_3$ -81.5 ○ | $HfO_2$ -84.5 ○ | $Ta_2O_5$ -65.3 ○ | $WO_3$ -45.7 ○ | $ReO_2$ -31.2 ○ | $OsO_2$ -19.1 ○ | $IrO_2$ -15.0 ○ | $Pt_3O_4$ -5.6 ○ | $Au_2O_3$ +3.7 ○ | HgO -7.0 ○ | $Tl_2O_3$ -14.9 ○ | PbO -22.6 ○ | $Bi_2O_3$ -23.6 ○ | $PoO_2$ ? ? |

| | | | | | | | | | | | | | | |
|---|---|---|---|---|---|---|---|---|---|---|---|---|---|---|
| 6 | $CeO_2$ -81.6 ○ | $Pr_2O_3$ -82.2 ○ | $Nd_2O_3$ -82.3 ○ | $Pm_2O_3$ ? ? | $Sm_2O_3$ -83.0 ○ | $Eu_2O_3$ -74.9 ○ | $Gd_2O_3$ -83.2 ○ | $Tb_2O_3$ -84.9 ○ | $Dy_2O_3$ -84.7 ○ | $Ho_2O_3$ -85.6 ○ | $Er_2O_3$ -86.5 ○ | $Tm_2O_3$ -85.8 ○ | $Yb_2O_3$ -82.5 ○ | $Lu_2O_3$ -85.5 ○ |
| 7 | $ThO_2$ -97.7 ○ | $PaO_2$ ? ? | $UO_2$ -86.4 ○ | | | | | | | | | | | |

Legend:
○ = Moisture Insensitive
□ = Mildly Moisture Sensitive
◨ = Moderately Moisture Sensitive
■ = Extremely Moisture Sensitive
◆ = Hygroscopic
? = Unknown

results in most oxide materials being insensitive to storage and handling in air. This is in stark contrast to other families of materials which have many members that decompose when stored and handled in the presence of the slightest trace of moisture. Finally, the synthesis of oxide materials is generally easier and safer than any of the other families of materials because the reactive gases that other families of materials require for synthesis, sintering, and annealing are invariably dangerous and toxic.

Although oxide phosphors possess many advantages as candidates for ACT-FEL phosphors in terms of stability, ease and safety of handling, and technological knowledge, there are several factors that have prevented oxides from becoming the dominant class of ACTFEL phosphor. Most importantly, oxide materials are generally quite refractory and possess bandgaps too large for the fabrication of bright and efficient ACTFEL devices, as shown in Figs. 3.6 and 3.7. The brightest and most efficient ACTFEL devices based on oxide phosphors fabricated to date have required annealing temperatures in excess of 1000°C to achieve a high enough degree of polycrystallinity. These temperatures are beyond what is feasible for deposition of phosphors onto glass substrates, and require the use of the inverted structure with a high-temperature tolerant substrate with refractory insulator and bottom electrode. However, proper selection of the constituents of oxide phosphors has yielded oxide phosphor materials that exhibit polycrystallinity in the temperature range of conventional sulfide phosphors. [140] Unfortunately, the materials that tend to crystallize at lower temperatures may not always provide the luminance and efficiency attainable by the phosphor materials that require extremely high-temperature annealing. The other major problem with oxide phosphors is that the threshold of oxide ACTFEL devices is typically quite gradual compared to the abrupt threshold of the sulfide ACTFEL phosphors. This is presumably because the large bandgaps and effective masses typically seen in oxide materials lead to inefficient carrier injection, hence large driving voltages and non-abrupt device thresholds, as discussed in Section 3.1. An examination of Fig. 3.7 reveals that some of the binary oxides possess energy gaps

| | Ia | IIa | IIIb | IVb | Vb | VIb | VIIb | VIII | | | Ib | IIb | IIIa | IVa | Va | VIa |
|---|---|---|---|---|---|---|---|---|---|---|---|---|---|---|---|---|
| 2 | $Li_2O$ 1570 M | BeO 2530 M | | | | | | | | | | | | $B_2O_3$ 450 M | $CO_2$ -56.5 P | $NO_2$ -11.2 M | $O_2$ -218 M |
| 3 | $Na_2O$ 1275 S | MgO 2852 M | | | | | | | | | | | | $Al_2O_3$ 2072 M | $SiO_2$ 1723 M | $P_2O_5$ 580 M | $SO_2$ 16.83 M |
| 4 | $K_2O$ 350 D | CaO 2614 M | $Sc_2O_3$ 2450 M | $TiO_2$ 1825 M | $V_2O_5$ 1970 M | $Cr_2O_3$ 2266 M | MnO 1650 M | $Fe_2O_3$ 1565 M | CoO 1795 M | NiO 1984 M | CuO 1326 M | ZnO 1975 M | $Ga_2O_3$ 1795 M | $GeO_2$ 1115 M | $As_2O_3$ 312.3 M | $SeO_2$ 340 S |
| 5 | $Rb_2O$ 400 D | SrO 2430 M | $Y_2O_3$ 2410 M | $ZrO_2$ 2700 M | $Nb_2O_5$ 1520 M | $MoO_3$ 801 M | $TcO_2$ 1100 S | $RuO_2$ ? D | $Rh_2O_3$ 1100 D | PdO 870 M | $Ag_2O$ 230 D | CdO 1540 M | $In_2O_3$ 1565 M | $SnO_2$ 1630 M | $Sb_2O_3$ 656 M | $TeO_2$ 733 M |
| 6 | $CsO_2$ 272 D | BaO 1918 M | $La_2O_3$ 2307 M | $HfO_2$ 2758 M | $Ta_2O_5$ 1872 M | $WO_3$ 1473 M | $ReO_3$ 1000 D | $OsO_4$ 40.6 M | $IrO_2$ 1100 D | $Pt_3O_4$ 550 D | $Au_2O_3$ 150 D | HgO 500 D | $Tl_2O_3$ 717 M | PbO 886 M | $Bi_2O_3$ 825 M | Po 550 D |

| 6 | $CeO_2$ 2600 M | $Pr_2O_3$ 2125 D | $Nd_2O_3$ 2272 M | Pm 2320 ? | $Sm_2O_3$ 2350 M | $Eu_2O_3$ 2050 M | $Gd_2O_3$ 2330 M | $Tb_2O_3$ 2387 M | $Dy_2O_3$ 2340 M | $Ho_2O_3$ 2370 M | $Er_2O_3$ 2400 M | $Tm_2O_3$ 2425 M | $Yb_2O_3$ 2346 M | $Lu_2O_3$ 2489 M |
|---|---|---|---|---|---|---|---|---|---|---|---|---|---|---|

| 7 | $ThO_2$ 3050 M | $PaO_2$ ? ? | $UO_2$ 2865 M |
|---|---|---|---|

Legend:  D = Decomposes        N = in Nitrogen        V = in Vacuum

E = Explodes        P = under Pressure        ? = Unknown

M = Melts        S = Sublimes

Figure 3.6: Melting points of binary oxides in °C.

Figure 3.7: Bandgaps of binary oxides in eV.

| | Ia | IIa | IIIb | IVb | Vb | VIb | VIIb | VIII | | | Ib | IIb | IIIa | IVa | Va | VIa |
|---|---|---|---|---|---|---|---|---|---|---|---|---|---|---|---|---|
| 2 | $Li_2O$<br>?<br>? | BeO<br>10.5<br>D | | | | | | | | | | | | $B_2O_3$<br>7.0<br>? | $CO_2$<br>N/A | $NO_2$<br>N/A | $O_2$<br>N/A |
| 3 | $Na_2O$<br>?<br>? | MgO<br>7.8<br>D | | | | | | | | | | | | $Al_2O_3$<br>9.7<br>? | $SiO_2$<br>11.0<br>I | $P_2O_5$<br>?<br>? | $SO_2$<br>N/A |
| 4 | $K_2O$<br>?<br>? | CaO<br>7.7<br>I | $Sc_2O_3$<br>6.0<br>? | $TiO_2$<br>3.2<br>? | $V_2O_5$<br>2.3<br>D | $Cr_2O_3$<br>3.3<br>? | MnO<br>3.6<br>? | $Fe_2O_3$<br>1.9<br>? | CoO<br>2.6<br>? | NiO<br>3.8<br>? | CuO<br>1.4<br>? | ZnO<br>3.2<br>D | $Ga_2O_3$<br>4.5<br>D | $GeO_2$<br>5.6<br>? | $As_2O_3$<br>4.0<br>? | $SeO_2$<br>?<br>? |
| 5 | $Rb_2O$<br>?<br>? | SrO<br>5.7<br>I | $Y_2O_3$<br>5.6<br>? | $ZrO_2$<br>5.0<br>? | $Nb_2O_5$<br>3.5<br>I | $MoO_3$<br>2.9<br>? | $TcO_2$<br>?<br>? | $RuO_2$<br>?<br>? | $Rh_2O_3$<br>?<br>? | PdO<br>1.5<br>? | $Ag_2O$<br>1.2<br>? | CdO<br>1.8<br>? | $In_2O_3$<br>3.2<br>? | $SnO_2$<br>3.5<br>? | $Sb_2O_3$<br>3.3<br>? | $TeO_2$<br>3.0<br>? |
| 6 | $Cs_2O$<br>?<br>? | BaO<br>5.1<br>I | $La_2O_3$<br>4.<br>? | $HfO_2$<br>5.6<br>? | $Ta_2O_5$<br>4.6<br>? | $WO_3$<br>2.8<br>? | $ReO_3$<br>2.3<br>? | $OsO_4$<br>?<br>? | $IrO_2$<br>?<br>? | $Pt_3O_4$<br>?<br>? | $Au_2O_3$<br>?<br>? | HgO<br>2.5<br>? | $Tl_2O_3$<br>1.8<br>? | PbO<br>2.8<br>? | $Bi_2O_3$<br>2.8<br>? | $PoO_2$<br>?<br>? |

| | | | | | | | | | | | | | | |
|---|---|---|---|---|---|---|---|---|---|---|---|---|---|---|
| 6 | $CeO_2$<br>5.5<br>? | $Pr_2O_3$<br>?<br>? | $Nd_2O_3$<br>?<br>? | $Pm_2O_3$<br>?<br>? | $Sm_2O_3$<br>?<br>? | $Eu_2O_3$<br>?<br>? | $Gd_2O_3$<br>5.3<br>? | $Tb_2O_3$<br>?<br>? | $Dy_2O_3$<br>?<br>? | $Ho_2O_3$<br>?<br>? | $Er_2O_3$<br>?<br>? | $Tm_2O_3$<br>?<br>? | $Yb_2O_3$<br>?<br>? | $Lu_2O_3$<br>?<br>? |
| 7 | $ThO_2$<br>4.7<br>? | $PaO_2$<br>?<br>? | $UO_2$<br>2.18<br>? | | | | | | | | | | | |

Legend: D = Direct Bandgap    N/A = Not Applicable

I = Indirect Bandgap    ? = Unknown

that are in the appropriate range for ACTFEL applications, and some of these oxides have small enough bandgaps that they could help to counteract the large bandgap oxides if a suitable ternary compound or alloy exists.

The sheer number of potential oxide phosphor materials systems makes a thorough examination of all of these systems impossible. Therefore, the discussion of potential oxide materials systems for ACTFEL phosphor applications focuses specifically on the binary and ternary oxide materials systems that have shown luminescent properties. However, other oxide materials other than those considered in the subsequent discussion may exhibit desirable properties for ACTFEL applications. Although a vast number of oxides have been shown to exhibit phosphor qualities, only a very small percentage of these materials have been investigated as ACTFEL phosphors. In addition, none of the oxide materials that have been investigated for ACTFEL applications have been studied nearly as thoroughly as their sulfide cousins. A listing of the oxides that have been investigated as ACTFEL phosphors and their relevant characteristics is shown in Table 3.4. [141] It should be noted that the data presented in Table 3.4 is somewhat misleading because the researchers working on oxide ACTFEL phosphors typically report peak luminance and efficiency instead of the 40 V above threshold values typically reported for sulfide phosphors. This discrepancy tends to significantly overstate the luminance of these devices, but Table 3.4 can be used for a comparison of the relative luminances of these phosphors.

The examination of oxide phosphor materials systems most logically begins with consideration of binary oxides and their luminescent qualities. Since almost every element forms a stable compound with oxygen, there is an abundant choice of potential binary oxide phosphors. Indeed, many binary oxides have been used successfully as phosphors in applications such as fluorescent lighting and CRTs. However, the differing requirements of ACTFEL phosphors certainly leaves some doubt as to the utility of many of these materials for this application. As discussed previously, the main problems are the refractory nature and large bandgaps of most of the binary oxides.

Table 3.4: Oxide phosphors for ACTFEL applications and their characteristics (all devices driven with a 1 kHz sine wave) .

| color | phosphor | $V_{th}$ (V) | $L_{max}$ (cd/m$^2$) | $\eta_{max}$ (lm/W) | CIE x | y |
|---|---|---|---|---|---|---|
| Red | $Ga_2O_3$:Cr | 175 | 375 | 0.04 | 0.654 | 0.293 |
| | $CaGa_2O_4$:Eu | 225 | 215 | 0.026 | 0.687 | 0.331 |
| | $ZnGa_2O_4$:Cr | 250 | 196 | 0.02 | 0.584 | 0.398 |
| | $Ga_2O_3$:Eu | 210 | 152 | 0.02 | 0.587 | 0.385 |
| | $Y_2O_3$:Eu | 130 | 144 | 0.14 | 0.573 | 0.393 |
| | $ZnGa_2O_4$:Eu | 175 | 62 | 0.009 | 0.584 | 0.398 |
| | CaO:Mn | 390 | 55 | 0.016 | 0.603 | 0.391 |
| | $GeO_2$:Mn | 180 | 7 | 0.018 | 0.521 | 0.413 |
| | $Gd_2O_3$:Eu | 235 | 4.9 | 0.002 | 0.524 | 0.352 |
| Yellow | $CaGa_2O_4$:Mn | 150 | 2790 | 0.25 | 0.479 | 0.518 |
| | $CaGa_2O_4$:Dy | 215 | 30 | 0.02 | 0.479 | 0.518 |
| Green | $Zn_2Si_{0.75}Ge_{0.25}O_4$:Mn | 170 | 4220 | 0.75 | 0.272 | 0.662 |
| | $Zn_2SiO_4$:Mn | 160 | 3020 | 0.78 | 0.251 | 0.697 |
| | $Zn_2Si_{0.7}Ge_{0.3}O_4$:Mn | 110 | 1751 | 2.53 | 0.271 | 0.671 |
| | $Ga_2O_3$:Mn | 110 | 1018 | 1.7 | 0.116 | 0.676 |
| | $ZnGa_2O_4$:Mn | 135 | 758 | 1.2 | 0.082 | 0.676 |
| | $Zn_2GeO_4$:Mn | 55 | 341 | 0.08 | 0.331 | 0.645 |
| | $ZnAl_2O_4$:Mn | 130 | 21 | 0.006 | 0.150 | 0.708 |
| White | $SrP_2O_7$:Eu | 145 | 5.6 | 0.005 | 0.334 | 0.270 |
| Blue | $Zn_2SiO_4$:Ti | 280 | 15.8 | 0.017 | 0.142 | 0.115 |
| | $Y_2SiO_5$:Ce | 235 | 13.2 | 0.054 | 0.176 | 0.138 |
| | CaO:Pb | 470 | 5.5 | 0.001 | 0.166 | 0.113 |

Taking into account the special requirements for ACTFEL phosphors, only a few binary oxides seem attractive as ACTFEL phosphor candidates. An examination of the data presented in Figs. 3.6 and 3.7 reveals that only the following binary oxides are acceptable based on the criteria presented is Section 3.1: $MnO$, $NiO$, $SnO_2$, $Nb_2O_5$, $Ga_2O_3$ and $As_2O_3$. Of these materials, only $Ga_2O_3$, and $SnO_2$ have been shown to possess luminescent properties. [141, 142] This does not, however, mean that $MnO$, $NiO$, $Nb_2O_5$, and $As_2O_3$ have no potential as ACTFEL phosphor materials, but it is certainly more sensible to begin an exploration of oxide phosphors with known luminescent materials.

Although several binary oxides can be considered to be ACTFEL phosphor candidates, the best-known and brightest oxide phosphors are ternary compounds or their alloys, resulting in their examination as the next logical step in the assessment of the oxide family of phosphors for ACTFEL applications. Ternary oxides comprise a vast number of compounds, so it is sensible to focus on the materials classes that are known phosphors. Many classes of ternary oxides have seen use in phosphor applications, including the borates, phosphates, vanadates, tungstates, molybdates, aluminates, silicates, sulfates, germanates, niobates, titanates, gallates, and tantalates. Thus far, the most studied groups of ternary oxide phosphors for ACTFEL applications are the silicates and gallates. In addition, oxide phosphor groups such as the phosphates and the germanates have also shown some promise as potential ACTFEL phosphors. [141] The initial results from oxide ACTFEL phosphors have been encouraging, but have not been promising enough for serious consideration as commercial ACTFEL phosphors. However, with continued research, commercial oxide ACTFEL phosphors may become a reality in the not so distant future.

The silicate family of materials have long been known as efficient fluorescent lamp phosphors, primarily because the green phosphor of the earliest models of these lamps was the synthetic version of the mineral willemite, $Zn_2SiO_4$:$Mn^{2+}$. Later versions of the fluorescent lamp also employed the broadband, single-component phos-

phor, $(Zn,Be)_2SiO_4:Mn^{2+}$. Further research into silicate phosphors found $CaSiO_3:Pb$, Mn to be another bright and efficient phosphor of the silicate family. In light of the history of this family of phosphors, it should come as no surprise that these were some of the first oxide phosphors to lead to working ACTFEL devices. Despite interest in a broad range of the silicate family of phosphors for fluorescent lamp applications, $Zn_2SiO_4$ and $Y_2SiO_5$ seem to be the only silicate phosphor hosts investigated for ACT-FEL applications thus far. The results obtained from Mn doped $Zn_2SiO_4$ annealed at very high temperatures ($>1000°C$) have been encouraging for oxide ACTFEL phosphors in general because they compare very well with the best sulfide phosphors. Furthermore, the green emission of $Zn_2SiO_4:Mn^{2+}$ with CIE coordinates x=0.25, y=0.70 is respectably close to the target green color for green ACTFEL phosphors of x=0.30, y=0.60. In addition, $Zn_2SiO_4:Ti^{4+}$ and $Y_2SiO_5:Ce^{3+}$ have also exhibited marginal blue electroluminescence as ACTFEL phosphors. However, the requirement for high-temperature annealing and the large bandgaps of $Zn_2SiO_4$ (5.4 eV) and $Y_2SiO_5$ ($>5.6$ eV) result in materials that are far from optimal in terms of ACT-FEL device processing and operation. From the perspective of designing ACTFEL phosphors according to the criteria presented earlier, $Cd_2SiO_4$ is probably the most interesting phosphor host of the silicate family, primarily because of bandgap and melting point concerns. Unfortunately, one of the precursors of $Cd_2SiO_4$, CdO, is a known human carcinogen that affects the lungs, and extreme care should be exercised when processing this material in powdered form. [143] However, proper disposal of Cd compounds involves conversion to the silicate, so $Cd_2SiO_4$ is perhaps one of the most tolerable of the Cd compounds. [144]

The gallate family of phosphor materials is the other family of ternary oxide phosphor materials that has provided encouraging results as ACTFEL phosphors. The gallate phosphor hosts that have been studied for ACTFEL applications are $ZnGa_2O_4$ and $CaGa_2O_4$. The brightest and most efficient gallate ACTFEL phosphors yet reported are yellow $CaGa_2O_4:Mn^{2+}$ and green $ZnGa_2O_4:Mn^{2+}$ as shown in Table

3.4. However, these results may be a bit misleading in terms of standard ACTFEL phosphors because they are from devices deposited on $BaTiO_3$ sheets, annealed at temperatures in excess of 1000°C, and driven several hundred volts above threshold. Still, these phosphors may have some utility in a more conventional ACTFEL device, but literature pertaining to this is scarce. Of the phosphors of the gallate family, $ZnGa_2O_4:Mn^{2+}$ is the most promising as a primary color phosphor, but its CIE color coordinates of x=0.08, y=0.68 are significantly different than the target green color of x=0.30, y=0.60.

The ternary germanate oxide phosphor $Zn_2GeO_4:Mn^{2+}$ has been investigated as an ACTFEL phosphor by deposition on $BaTiO_3$ sheets and subsequent high-temperature annealing, with respectable luminance and efficiency results. However, this phosphor material shows signs of polycrystallinity at temperatures as low as 600°C, and generally has a very low threshold field compared to other oxide phosphors. In fact, it was reported that this phosphor had a threshold voltage as low as 55 V when deposited on a $BaTiO_3$ ceramic sheet. In addition, the bandgap of this phosphor should be between the practical limits of 3.5 and 4.5 eV for high-quality ACTFEL phosphors if it is assumed that the bandgap lies somewhere between that of ZnO (3.2eV) and $GeO_2$ (5.6 eV). Furthermore, the CIE color coordinates of $Zn_2GeO_4:Mn^{2+}$ are x=0.33, y=0.65, which are very close to the target green color for ACTFEL applications. Therefore, this phosphor is investigated as a potential primary color phosphor in this thesis.

The final oxide materials systems that have been successfully deposited as ACTFEL phosphors are the phosphates and the aluminates. However, neither of these materials systems have shown enough promise to prompt researchers to pursue significant follow-up work with these families of materials. The pyrophosphate of Sr activated with Eu, $Sr_2P_2O_7:Eu$, has been investigated, resulting in relatively dim and inefficient phosphors ($L_{max} = 5.6$ cd/m$^2$, $\eta_{max} = 0.005$ lm/W at 1 kHz). The alkaline earth phosphates are probably not the best choice of materials for ACTFEL applica-

tions because both the binary alkaline earth oxides and $P_2O_5$ are moisture-sensitive materials, leading to the conclusion that any of their compounds will probably be similarly moisture sensitive. The phosphates are excellent fluorescent lamp and CRT phosphors because they exist in an evacuated space for these applications. However, the chance of exposure to moisture is much greater for ACTFEL phosphors because one of the major advantages of the technology is its ruggedness, and hence, they need to withstand hostile environments to retain this as a selling point. Therefore, phosphates are probably not worthwhile for consideration as ACTFEL phosphors. The aluminates have yielded similarly marginal results, but for quite different reasons. The aluminate of Zn, $ZnAl_2O_4$:Mn, has been deposited as an ACTFEL phosphor, and even after extremely high temperature annealing yields devices with maximum luminance of 21 cd/m$^2$ and maximum efficiency of 0.006 lm/W driven by a 1 kHz sine wave. [141] Zinc aluminate is probably the only aluminate investigated for ACTFEL applications, but other aluminates should produce similar results unless the melting point and bandgap can be significantly reduced from those of $Al_2O_3$. As a result, research resources are probably best focused on other phosphor families.

At this point in time, oxide ACTFEL devices can only be considered a research novelty because they have not demonstrated the type of performance necessary for consideration as products. The potential advantages of oxide ACTFEL phosphors are too great to overlook, however, so continued research on their feasibility is necessary. The fundamental problems with most oxide phosphors for ACTFEL applications are their large bandgaps and refractory nature. The bandgap issue can be circumvented by selecting only compounds that exhibit bandgaps within the range set forth for ACTFEL phosphors in Section 3.1. In addition, the crystallinity issue with refractory oxide phosphors may be alleviated through the addition of grain growth promoting flux agents. The identification of these flux agents is often difficult, but the ceramics literature often has hints on suitable grain growth fluxes for many oxides.

### 3.3.4 Sulfides

No discussion of ACTFEL phosphors can even scratch the surface of the subject without some discussion of sulfide phosphors. The entire ACTFEL technology is built around sulfide phosphors, almost exclusively because of the success of ZnS:Mn, the prototypical ACTFEL phosphor. In addition, recent advances with SrS:Ce and SrS:Cu phosphors have determined that they are extremely important phosphors for the realization of full-color ACTFEL displays. These sulfide phosphors possess two properties that thus far seem to be unique to these phosphors; excellent charge injection and polycrystallinity at low processing temperatures. The charge injection characteristics of these phosphors seem to be due to the fortuitous combination of a high density of interface states at the proper energy for tunnel emission at readily attainable driving voltages. The polycrystallinity attainable in these sulfide phosphors at temperatures under 800°C is good enough to lead to bright and efficient devices, thereby leading to the conclusion that transport is delocalized and not amorphous-style hopping conduction. This is remarkable considering that the melting points of ZnS and SrS are 1700°C and >2000°C, respectively. In fact, this gives hope that other refractory compounds may also become polycrystalline at processing temperatures commensurate with glass substrates. Finally, the deposition of sulfides is less complicated than that of oxides and nitrides because sulphur is significantly more condensable than oxygen or nitrogen. This allows the simple evaporation of sulfides, without the addition of a gaseous species to provide lost anionic atoms.

Although ZnS and SrS phosphors have several properties that help to create bright and efficient ACTFEL devices, the sulfide family as a whole tends towards mediocrity in terms of physical and thermodynamic properties. The bulk of the binary sulfide materials are thermodynamically stable; however, their thermodynamic formation energies are for the most part less than those of the corresponding oxides, as seen by comparison of Figs. 3.5 and 3.8. In addition, there are many more sulfides that exhibit moisture sensitivity than oxides, leading to stability problems with several

| | Ia | IIa | IIIb | IVb | Vb | VIb | VIIb | VIII | | | Ib | IIb | IIIa | IVa | Va | VIa |
|---|---|---|---|---|---|---|---|---|---|---|---|---|---|---|---|---|
| 2 | $Li_2S$ -35.0 ◆ | BeS -27.3 ◪ | | | | | | | | | | | $B_2S_3$ -11.8 ? | $CS_2$ +5.4 | $S_4N_2$ ? O | $SO_2$ -27.1 |
| 3 | $Na_2S$ -28.3 ◆ | MgS -40.8 ◪ | | | | | | | | | | | $Al_2S_3$ -30.6 ■ | $SiS_2$ -16.9 ■ | $P_2S_5$ -4.8 ? | $S_8$ ? O |
| 4 | $K_2S$ -28.9 ◆ | CaS -55.9 ◪ | $Sc_2S_3$ ? O | TiS -33.1 ■ | $V_2S_3$ -24.6 O | CrS -16.5 O | MnS -26.2 O | $FeS_2$ -13.3 O | $Co_3S_4$ -16.6 O | NiS -10.7 O | $Cu_2S$ -6.5 O | ZnS -28.6 O | $Ga_2S_3$ -24.2 ◪ | $GeS_2$ -12.3 ■ | $As_2S_3$ -7.9 O | $SeS_2$ ? ? |
| 5 | $Rb_2S$ -29.7 ◆ | SrS -55.4 ◆ | $Y_2S_3$ ? O | $ZrS_2$ -45.1 O | $NbS_{1.8}$ ? O | $MoS_2$ -21.3 O | Tc | $RuS_2$ -15.0 O | RhS ? O | PdS -8.0 O | $Ag_2S$ -3.1 O | CdS -17.4 O | $In_2S_3$ -16.7 O | SnS -12.8 O | $Sb_2S_3$ -6.7 O | Te |
| 6 | $Cs_2S$ -29.8 ◆ | BaS -54.8 ◪ | $La_2S_3$ -57.7 O | $HfS_2$ -46.1 ? | $TaS_2$ -27.5 O | $WS_2$ -18.5 O | $ReS_2$ -13.3 O | $OsS_2$ -10.8 O | $IrS_2$ -9.9 O | PtS -9.3 O | $Au_2S$ ? O | HgS -6.1 O | $Tl_2S$ -7.4 O | PbS -11.6 O | $Bi_2S_3$ -6.7 O | PoS +26 ? |

| | | | | | | | | | | | | | | |
|---|---|---|---|---|---|---|---|---|---|---|---|---|---|---|
| 6 | $Ce_2S_3$ -56.0 O | $Pr_2S_3$ ? O | $Nd_2S_3$ -53.0 ? | Pm | $Sm_2S_3$ ? ? | EuS -52.5 O | $Gd_2S_3$ ? ? | $Tb_2S_3$ ? O | $Dy_2S_3$ -57.7 O | $Ho_2S_3$ ? O | $Er_2S_3$ ? ? | $Tm_2S_3$ ? ? | $Yb_2S_3$ -55.1 O | $Lu_2S_3$ ? ? |
| 7 | $ThS_2$ -49.5 O | Pa | $US_2$ -41.4 □ | | | | | | | | | | | |

Legend:  O = Moisture Insensitive   ■ = Extremely Moisture Sensitive

□ = Mildly Moisture Sensitive   ◆ = Hygroscopic

◪ = Moderately Moisture Sensitive   ? = Unknown

potentially important sulfides. The melting points of binary sulfides tend to be several hundred degrees centigrade lower than the corresponding oxide, on average, as shown in Fig. 3.9. This leads to a much greater chance that sulfide compounds will exhibit polycrystallinity at standard ACTFEL processing temperatures than corresponding oxide and nitride compounds. The other problem that severely limits the number of potential sulfide phosphors is that only a few of the binary sulfides possess bandgap energies that are sufficient for ACTFEL applications, as shown in Fig. 3.10.

The limited number of sulfide materials of sufficient bandgap results in only several sulfide compounds that are applicable to ACTFEL fabrication. In addition, extreme moisture sensitivity of several sulfide compounds ($SiS_2$, $Al_2S_3$, and $GeS_2$) renders them and their derivatives useless as ACTFEL phosphor hosts from a stability standpoint. [145] Of the compounds of the sulfide family, only CaS, SrS, BaS, ZnS, and $Ga_2S_3$ or the resulting ternary thiogallates exhibit properties consistent with ACTFEL applications. The main limiting factors in terms of ACTFEL application for sulfides are insufficient bandgap and moisture sensitivity. Although the number of sulfide phosphor hosts is quite limited, the sulfide phosphor hosts, CaS, SrS, and ZnS are known to be versatile phosphor hosts in terms of the number of potential activators. In fact, Lehmann's pioneering work on CaS phosphors identified no less than 31 luminescent activators in CaS. [82] In addition, both ZnS and SrS activated with many different ions are known luminescent materials. The same could be expected for BaS, although significantly less work has been conducted with BaS phosphor hosts.

The aforementioned issues regarding sulfide phosphors allows an examination to be made concerning the potential for new phosphors to be discovered amongst the sulfide family. With the sulfides, the limited number of potential phosphor hosts results in the conclusion that no new sulfide phosphor hosts will be discovered. However, because of the versatility of the known sulfide phosphor hosts, there remains significant research work to be done in terms of determining proper activators, and

| | Ia | IIa | IIIb | IVb | Vb | VIb | VIIb | VIII | | | Ib | IIb | IIIa | IVa | Va | VIa |
|---|---|---|---|---|---|---|---|---|---|---|---|---|---|---|---|---|
| 2 | $Li_2S$ 900 M | BeS ? ? | | | | | | | | | | | $B_2S_3$ 310 ? | $CS_2$ -110.8 M | $S_4N_2$ ? ? | $SO_2$ 16.83 M |
| 3 | $Na_2S$ 950 M | MgS >2000 D | | | | | | | | | | | $Al_2S_3$ 1100 M | $SiS_2$ 1100 S | $P_2S_5$ 288 ? | $S_8$ 112.8 M |
| 4 | $K_2S$ 840 M | CaS ? D | $Sc_2S_3$ ? ? | TiS ? ? | $V_2S_3$ >600 D | CrS 1550 M | MnS 1610 D | $FeS_2$ 1171 M | CoS >1116 M | NiS 797 M | $Cu_2S$ 1100 M | ZnS 1700 M | $Ga_2S_3$ 965 M | $GeS_2$ 800 M | $As_2S_3$ 300 M | $SeS_2$ <100 M |
| 5 | $Rb_2S$ 530 D V | SrS >2000 M | $Y_2S_3$ ? ? | $ZrS_2$ 1550 M | $NbS_{1.8}$ ? ? | $MoS_2$ 1185 M | Tc | $RuS_2$ 1100 D | RhS ? ? | PdS 950 D | $Ag_2S$ 825 M | CdS 1477 M | $In_2S_3$ 1050 M | SnS 882 M | $Sb_2S_3$ 550 M | Te |
| 6 | $Cs_2S$ ? ? | BaS 1200 M | $La_2S_3$ 2125 V | $HfS_2$ ? ? | $TaS_2$ >1300 M | $WS_2$ 1250 D | $ReS_2$ ? D | $OsS_2$ ? D | $Ir_2S_3$ 300 D | PtS ? D | $Au_2S_3$ 197 D | HgS 583.5 S | $Tl_2S$ 448.5 M | PbS 1114 M | $Bi_2S_3$ 685 D | PoS 275 D |

| | | | | | | | | | | | | | | |
|---|---|---|---|---|---|---|---|---|---|---|---|---|---|---|
| 6 | $Ce_2S_3$ 2060 D V | $Pr_2S_3$ 1795 D | $Nd_2S_3$ 2010 D | Pm | $Sm_2S_3$ 1780 ? | EuS 1667 ? | $Gd_2S_3$ 1885 ? | $Tb_2S_3$ ? ? | $Dy_2S_3$ 1490 ? | $Ho_2S_3$ ? ? | $Er_2S_3$ 1730 ? | $Tm_2S_3$ ? ? | $Yb_2S_3$ ? ? | $Lu_2S_3$ ? ? |
| 7 | $ThS_2$ 1925 V | Pa | $US_2$ >1100 ? | | | | | | | | | | | |

Legend: D = Decomposes  N = in Nitrogen  V = in Vacuum
E = Explodes  P = Under Pressure  ? = Unknown
M = Melts  S = Sublimes

Figure 3.9: Melting points of binary sulfides in °C.

| | Ia | IIa | IIIb | IVb | Vb | VIb | VIIb | VIII | | | Ib | IIb | IIIa | IVa | Va | VIa |
|---|---|---|---|---|---|---|---|---|---|---|---|---|---|---|---|---|
| 2 | $Li_2S$ ? ? | BeS 4.2 I | | | | | | | | | | | | $B_2S_3$ ? ? | $CS_2$ N/A | $S_4N_2$ ? ? | $SO_2$ N/A |
| 3 | $Na_2S$ 2.4 ? | MgS 5.4 ? | | | | | | | | | | | | $Al_2S_3$ 4.1 ? | $SiS_2$ ? ? | $P_2S_5$ ? ? | $S_8$ 3.82 D |
| 4 | $K_2S$ ? ? | CaS 4.8 I | $Sc_2S_3$ 2.78 ? | TiS ? ? | $V_2S_3$ ? ? | CrS ? ? | MnS 6.2 ? | $FeS_2$ 1.2 ? | CoS ? ? | NiS 0.1 ? | $Cu_2S$ 1.2 I | ZnS 3.87 D | $Ga_2S_3$ 3.59 ? | $GeS_2$ 3.5 ? | $As_2S_3$ 2.43 I | $SeS_2$ 1.9 ? |
| 5 | $Rb_2S$ ? ? | SrS 4.4 I | $Y_2S_3$ 2.9 ? | $ZrS_2$ 2.21 I | $Nb_2S_3$ 0.12 ? | $MoS_2$ ? ? | Tc | $RuS_2$ 1.8 ? | RhS ? ? | PdS 0.5 ? | $Ag_2S$ 0.87 D | CdS 2.41 D | $In_2S_3$ 2.03 D | SnS 1.08 ? | $Sb_2S_3$ 1.7 ? | Te |
| 6 | $Cs_2S$ ? ? | BaS 3.8 I | $La_2S_3$ 2.94 I | $HfS_2$ 1.96 I | $TaS_2$ 0.1 ? | $WS_2$ 1.1 ? | $ReS_2$ 1.1 ? | $OsS_2$ 2. ? | $Ir_2S_3$ ? ? | PtS 0.8 ? | $Au_2S_3$ ? ? | HgS 1.998 I | $Tl_2S$ 0.19 ? | PbS 0.41 D | $Bi_2S_3$ 1.2 ? | PoS ? ? |

| | | | | | | | | | | | | | | |
|---|---|---|---|---|---|---|---|---|---|---|---|---|---|---|
| 6 | $Ce_2S_3$ 2.24 I | $Pr_2S_3$ 2.60 I | $Nd_2S_3$ 2.66 I | Pm | $Sm_2S_3$ 2.00 I | EuS 1.65 I | $Gd_2S_3$ 2.55 I | $Tb_2S_3$ 1.83 I | $Dy_2S_3$ 2.91 I | $Ho_2S_3$ 2.7 I | $Er_2S_3$ 2.8 I | $Tm_2S_3$ 2.68 I | $Yb_2S_3$ 2.51 I | $Lu_2S_3$ ? ? |
| 7 | $ThS_2$ ? ? | Pa | $US_2$ ? ? | | | | | | | | | | | |

Legend: D = Direct Bandgap    N/A = Not Applicable
I = Indirect Bandgap    ? = Unknown

Figure 3.10: Bandgaps of binary sulfides in eV.

especially, coactivators for these sulfide phosphors. As a result, much of this thesis is devoted to determining suitable activators and coactivators for sulfide phosphors.

### 3.3.5 Selenides

A chronic problem for compounds with anions from the fourth row or lower of the periodic table in terms of potential as ACTFEL phosphors is that it is difficult to achieve a sufficiently large bandgap. The situation is no different for the selenide family of materials, which has only a few members with sufficiently large bandgaps for ACTFEL applications. The most notable group of selenides with sufficient bandgap are the alkaline earth selenides which exhibit bandgap energies between 3.6 eV and 5.6 eV, as shown in Fig. 3.11. This leaves only a limited choice of potential selenide phosphors, but the selenide phosphor hosts that fit the bill of specifications for ACTFEL phosphors may indeed prove valuable.

Certain members of the selenide family of materials, notably ZnSe and CdSe, have been known to be luminescent materials for quite some time. [146] Part of the reason that ZnSe and CdSe find use in luminescence applications is that these are direct bandgap materials that allow free selection of bandgap between 1.5 eV and 3.8 eV by alloying with CdTe, ZnTe, CdS, and ZnS. For similar reasons, the AlN, GaN, and InN family of compounds has become a groundbreaking group of compounds in the field of luminescent materials. Although early ACTFEL devices were based on the ZnSe phosphor host despite its 2.7 eV bandgap, the bandgap range that is available to be explored by this group of compounds does not fit with the range necessary for the production of a full-color display. [147, 148] Therefore, perhaps the alkaline earth selenides, MgSe, CaSe, SrSe, and BaSe are a better choice for a family of selenide phosphor hosts to be investigated.

The alkaline earth selenides certainly have potential as ACTFEL phosphors, largely because extrapolation of their properties from the trends of the periodic table suggest that they may be valuable phosphor hosts. The general trend of the periodic

| | Ia | IIa | IIIb | IVb | Vb | VIb | VIIb | VIII | | | Ib | IIb | IIIa | IVa | Va | VIa |
|---|---|---|---|---|---|---|---|---|---|---|---|---|---|---|---|---|
| **2** | Li$_2$Se ? ? | BeSe 3.61 ? | | | | | | | | | | | B$_2$Se$_3$ ? ? | CSe$_2$ ? ? | Se$_4$N$_4$ ? ? | SeO$_2$ ? ? |
| **3** | Na$_2$Se ? ? | MgSe 5.6 ? | | | | | | | | | | | Al$_2$Se$_3$ 3.1 ? | SiSe$_2$ 1.72 ? | P$_2$Se$_5$ ? ? | SeS$_2$ ? ? |
| **4** | K$_2$Se 1.8 ? | CaSe 3.87 I | Sc$_2$Se$_3$ 2.31 ? | TiSe$_2$ 0.69 ? | V | Cr$_2$Se$_3$ 0.025 ? | MnSe 1.8 ? | FeSe$_2$ 0.6 ? | CoSe ? ? | NiSe$_2$ ? ? | Cu$_2$Se 1.23 ? | ZnSe 2.72 D | Ga$_2$Se$_3$ 2.05 ? | GeSe$_2$ 2.38 ? | As$_2$Se$_3$ 1.77 ? | Se 1.71 ? |
| **5** | Rb$_2$Se ? ? | SrSe 3.73 I | Y$_2$Se$_3$ 2.00 ? | ZrSe$_2$ 2. ? | NbSe$_2$ 1.4 ? | MoSe$_2$ ? ? | Tc | RuSe$_2$ 1. ? | RhSe$_2$ 0.6 ? | PdSe$_2$ 0.4 ? | Ag$_2$Se 0.13 ? | CdSe 1.74 D | In$_2$Se$_3$ 1.2 ? | SnSe$_2$ 1.03 ? | Sb$_2$Se$_3$ 1.03 ? | Te |
| **6** | Cs | BaSe 3.2 I | La$_2$Se$_3$ 1.65 ? | HfSe$_2$ 2.2 ? | Ta | WSe$_2$ 1.35 ? | ReSe$_2$ 0.99 ? | Os | IrSe$_2$ 1. ? | PtSe$_2$ 0.1 ? | Au | HgSe 0.24 ? | TlSe 0.73 ? | PbSe$_2$ 0.27 ? | Bi$_2$Se$_3$ 0.21 ? | Po |

| | | | | | | | | | | | | | | |
|---|---|---|---|---|---|---|---|---|---|---|---|---|---|---|
| **6** | Ce$_2$Se$_3$ 1.714 ? | Pr$_2$Se$_3$ 1.9 ? | Nd$_2$Se$_3$ 1.75 ? | Pm | Sm$_2$Se$_3$ 2.3 ? | EuSe 1.78 ? | Gd$_2$Se$_3$ 2.23 ? | Tb$_2$Se$_3$ ? ? | Dy$_2$Se$_3$ 2.11 ? | Ho$_2$Se$_3$ 2.35 ? | Er$_2$Se$_3$ 2.43 ? | Tm$_2$Se$_3$ 2.63 ? | Yb$_2$Se$_3$ 1.45 ? | Lu$_2$Se$_3$ 2.47 ? |
| **7** | Th | Pa | U | | | | | | | | | | | |

Legend: D = Direct Bandgap    N/A = Not Applicable
I = Indirect Bandgap    ? = Unknown

Figure 3.11: Room temperature bandgaps of binary selenides in eV.

table is that bandgap and melting temperature decrease with downward progression through a given column of the periodic table. This implies several things about the alkaline earth selenides; they will possess smaller bandgap and lower melting temperature than the corresponding sulfides. One of the primary factors inhibiting SrS:Cu from impacting the display market is that the post-deposition annealing temperature of ~810°C required to achieve the optimum blue color is too high to be directly considered for production. Assuming that the behavior of luminescent impurities in SrS such as $Cu^{1+}$ behave similarly in CaSe or SrSe, SrSe may be a better phosphor host for $Cu^{1+}$ than SrS because the lower melting temperature of SrSe could lead to adequate crystallinity at lower temperatures. In addition, the dielectric constant of selenides is correspondingly lower than the analogous sulfides because the dielectric constant trend is such that dielectric constant is lower with increasing anionic row number.

The selenide family of materials, and in particular the alkaline earth selenides, are not without drawbacks, however. First, the alkaline earth selenides are similar to the alkaline earth sulfides in that they have problems with moisture sensitivity. Actually, this is the case for most binary alkaline earth compounds, due to the relatively large thermodynamic stability of the alkaline earth hydroxides and carbonates. Hopefully, these moisture sensitivity issues are no more severe than those of the alkaline earth sulfides which have proven to be excellent ACTFEL phosphor hosts. As discussed previously, the number of potential Se compounds that have potential as ACTFEL phosphor hosts is limited because relatively few possess sufficient bandgap for ACTFEL applications. In light of the success of the sulfide phosphors, and the similarly limited choice of ACTFEL phosphors, two or three different phosphor hosts may be all that is necessary for success in the ACTFEL field. Finally, a serious issue with the synthesis of Se compounds is the toxicity of this element and its compounds. Synthesis of many Se compounds requires a flow of a Se providing vapor at elevated temperature to drive the selenization of source materials. This generally means that

either the synthesis is performed by either flowing elemental Se vapor over the reacting sample with an inert carrier gas or flowing $H_2Se$ gas over the cation-providing reactant at elevated temperatures. Unfortunately, $H_2Se$ is one of the most toxic and flammable gases known, resulting in extremely expensive equipment outlays for safe handling of this gas. The Se vapor approach is certainly more attractive from a safety and economic standpoint, and may be a more attractive option than direct purchase of selenides from a vendor, because they tend to be costly and not of phosphor quality.

There are also several ternary selenides that deserve mention as potential ACTFEL phosphor hosts. The selenide analogs of the alkaline earth thiogallates that have been shown to produce deep blue electroluminescence may be useful phosphor hosts. The reduced melting temperature and bandgap of Se compounds may provide the increased carrier injection so desperately needed by the terribly inefficient $Ce^{3+}$ doped alkaline earth thiogallates, $CaGa_2S_4$:Ce and $SrGa_2S_4$:Ce. Finally, perhaps alloys of the alkaline earth selenides may provide some flexibility in the production of bright and efficient selenide phosphors.

### 3.3.6    Tellurides

The telluride family of compounds suffers the same malady as the sulfide and selenide families; only a handful of compounds possessing sufficient bandgap for serious consideration as ACTFEL phosphor hosts. However, for the tellurides, the problems are even more severe than for the selenides. The alkaline earth tellurides are the only Te compounds with even close to a sufficient ACTFEL phosphor host bandgap, so the discussion of Te compounds as phosphor hosts is limited to the tellurides of Mg, Ca, Sr, and Ba. Of the tellurides, only CaTe and SrTe have bandgaps that fall within the range of commercially useful ACTFEL phosphors, as shown in Table 3.5, and as a result, any investigation of tellurides as ACTFEL phosphors should begin with these compounds.

Table 3.5: Room temperature bandgaps of group II tellurides (eV).

| Group II Telluride | $E_g$ (eV) |
|---|---|
| BeTe | 2.89 |
| MgTe | 4.7 |
| CaTe | 4.07 |
| SrTe | 3.73 |
| BaTe | 3.4 |
| ZnTe | 2.25 |
| CdTe | 1.517 |

All that was asserted concerning Se compounds in the previous section also applies to Te compounds, except that the bandgap and melting temperatures should be further reduced from the sulfide values, whereas the dielectric constant should further increase. However, ternary tellurides of sufficient bandgap for ACTFEL applications are not feasible, so only group II tellurides or alloys thereof should be considered for this application. Similar to the selenides, telluride compounds are also a general health hazard. The alkaline earth tellurides are prohibitively expensive to purchase from a vendor, necessitating their synthesis to obtain phosphor quality source material. Synthesis of tellurides generally proceeds by flowing Te vapor over a sample containing the cationic species by flowing an inert gas over a heated sample of pure Te. This is necessary since the gas $H_2Te$ is thermodynamically unstable, and hence, unavailable.

### 3.3.7 Halides

Electroluminescence has been demonstrated from lanthanide and Mn-doped halide phosphors. [149, 150, 151] As is the case with most of the non-sulfide families

of materials, the threshold voltage is not as abrupt in these films as it is in sulfide phosphors. Halides are attractive for ACTFEL applications because they crystallize at very low temperatures and they have low dielectric constants due to their highly ionic character. However, the drawbacks of halide compounds include extremely large bandgaps, relatively weak chemical bonding, and severe moisture sensitivity problems. The weak chemical bonds formed in the microstructure of halides directly affect the thin-film density because weakly bound compounds tend to nucleate poorly. [88] Low density films are by their very nature susceptible to moisture penetration, and the moisture that penetrates low-density halide films remains because water molecules help to satisfy dangling bonds in a vacancy-rich low-density film. Since the major market advantage of ACTFEL displays is their durability in the face of harsh operating conditions, halide phosphor efforts are not likely to progress any further than the research phase.

### 3.3.8 Materials family combinations

Several important phosphor hosts for fluorescent lighting, cathode-ray tube, and X-ray phosphor applications are combinations of two of the materials families discussed above. The most notable of these phosphor hosts are the oxyhalides and oxysulfides for these applications. In fact, some success has been achieved with the use of oxysulfide phosphors for ACTFEL applications. [150, 152] In addition, alkaline earth sulfoselenide phosphors have been demonstrated that improve upon the properties of the corresponding sulfide phosphors. [153] However, oxyhalides are probably best left to the domain of fluorescent lighting because the weak chemical bonds of the halide are not likely to lead to long-lived ACTFEL devices, as discussed above. Therefore, combinations of certain materials families are an option to consider when looking at techniques for improvement of ACTFEL phosphors.

### 3.4   Laboratory facilities

To implement a plan to synthesize phosphor materials and subsequently fabricate ACTFEL devices, the coordination of numerous pieces of equipment is necessary. The purpose of this section is to describe the equipment available to this project at Oregon State University (OSU).

#### 3.4.1   Synthesis furnaces

There are currently two synthesis furnaces dedicated to the synthesis of ACTFEL phosphor materials at OSU. The first is a 1500°C programmable alumina tube furnace located in the Chemistry department. This furnace is located in a fume hood and is equipped for $H_2S$ and inert gas atmospheres, and hence, is used exclusively for sulfide synthesis and sintering. The second is a 1200°C alumina tube furnace located in the Electrical & Computer Engineering (ECE) department. This furnace is equipped for compound synthesis under an $NH_3$ atmosphere, and hence is primarily used for synthesis of nitride materials.

#### 3.4.2   Electron-beam evaporator

The main technique used for ACTFEL phosphor deposition for this project is electron-beam evaporation (EBE). The EBE system used for this project is a 6" diffusion pumped system backed by a hydrocarbon oil lubricated rotary vane pump. In addition, there is a $LN_2$ cooled cold trap around the inlet of the diffusion pump to selectively pump condensable vapors during deposition. The electron gun is a three pocket gun powered by a 4 kW power supply. In addition to the electron gun, this system has two additional thermal evaporation sources. The substrate is heated by a pyrolytic boron nitride coated graphite trace heater. The substrate temperature is regulated by an on/off temperature controller, and comprises the entire range of useful temperatures for deposition on glass substrates. The film thickness and deposition rate of EBE deposited films are monitored *in situ* by a quartz crystal

thickness monitor. There is one metering valve controlled process gas input to this system for the ability to perform reactive evaporation. The EBE is located in the ECE department solid-state processing laboratory.

### 3.4.3   RF sputtering system

The other technique used for phosphor deposition for this project is radio-frequency (RF) sputtering. The system that is used for RF sputtering is a significantly modified system acquired from a Hewlett-Packard donation. The system is a 6" diffusion-pumped main chamber with a load-lock and a $LN_2$ cooled moisture trap. The roughing/backing and load lock mechanical pumps are both rotary vane pumps lubricated with hydrocarbon vacuum pump oil. Process gases are fed into the chamber through 3 mass flow controller (MFC) regulated gas input lines. RF sputtering is accomplished with 2-2" water-cooled, magnetron sputtering guns powered by a 500 W RF power supply. The substrate holder is a Ti sheet attached to an aluminum/brass base that is driven by a stepper motor and heated by 2 500 W tungsten halogen lamps. The background gas in the chamber is monitored by a residual gas analyzer (RGA) to determine the concentration of oxygen-containing gases for sulfide and nitride depositions. Resistive sheet heating elements are used to bake the chamber walls to reduce $H_2O$ levels when necessary. This system is located in the ECE department solid-state processing laboratory.

### 3.4.4   Rapid thermal annealing

The annealing of ACTFEL devices is accomplished via the rapid thermal annealing (RTA) system located in the ECE solid-state processing laboratory. The RTA system is a commercial system manufactured by Advanced Energy, Inc. This system is capable of annealing at temperatures up to 1200°C, with fully programmable annealing cycles. In addition, there is one MFC-controlled process gas input for annealing in custom atmospheres.

### 3.4.5 Plasma-enhanced chemical vapor deposition

The ACTFEL insulator layer for this project is most often deposited via plasma-enhanced chemical vapor deposition (PECVD). The PECVD system is a commercial model that is pumped by a Fomblin™ lubricated mechanical pump/roots booster pump stack. In addition, there is a cryopump for capturing moisture prior to critical depositions. The PECVD system has four MFC regulated process gas inputs, that are controlled by a microprocessor controller. The substrate is heated with a resistive element-style heater that is capable of attaining temperatures up to 350°C. This system is located in the ECE department solid-state processing lab and is currently configured for $SiO_2$, $SiO_xN_y$, and $Si_3N_4$ deposition.

### 3.4.6 Thermal evaporators

The Al top electrodes of the ACTFEL devices fabricated for this project are deposited by thermal evaporation. There are currently two systems for performing this function. The first is a desktop model pumped by a 2" diffusion pump that is capable of rapid cycling because of the small chamber size. The ultimate pressure in this system is approximately $10^{-5}$ Torr, so this system is not used for critical depositions. The second system is a full-size thermal evaporation system pumped by a 6" diffusion pump with a $LN_2$ cooled cold trap. This system is capable of achieving vacuum well into the $10^{-7}$ Torr range, and is used for higher-quality depositions. The film thickness is monitored in both system via quartz crystal monitors. Both of these thermal evaporators are located in the ECE solid-state processing lab.

### 3.4.7 Film thickness measurement

It is important to have knowledge of the film thicknesses for the constituent layers of the ACTFEL devices fabricated for this project. Film thickness measurement for this project is accomplished mainly by a mechanical thickness profiling system. This system operates by sliding a stylus across a step that transitions from the sub-

strate to the top of the film. Then, a control unit reads the vertical position of the stylus that is translated into a thickness. This system is accurate to within roughly 500 Å, and it is difficult to obtain repeatable film thicknesses for films that are under 2000 Å thick. As a result, it will be necessary for the future of this project to develop a reliable optical film thickness measurement system.

## 3.5 Source material preparation

Upon identification of promising ACTFEL materials, the next logical step towards realization of new ACTFEL phosphors is the preparation of processable pieces of phosphor material. The two steps involved in the progression from raw materials to a form suitable for evaporation or sputtering are the synthesis of the phosphor material and the forming of the phosphor material into a suitable form for processing. The following subsections analyze these steps in some detail.

### 3.5.1 Phosphor materials synthesis

Deposition of thin-films always requires source material to supply the reactive species that lead to the formation of a thin-film upon the substrate surface. Many common elements and compounds can be purchased in very pure form for use as source material for thin-film deposition. For example, highly pure ZnS sputtering targets and evaporation cubes are available at reasonable prices from many vendors. However, most phosphor materials of interest are not compounds that are readily available for purchase at affordable prices. In addition, these phosphor materials require doping with luminescent impurities to varying degrees, greatly increasing the complexity and cost of source materials when purchased from a vendor. Furthermore, many vendors of sputtering and evaporation source materials are not aware of the special requirements of materials to be used for phosphor deposition. For these reasons, it is necessary to synthesize most source materials in-house for both cost effectiveness and quality control.

The synthesis of source material is a process that requires knowledge of chemistry, appreciation of the toxic properties of materials, and care to avoid contamination. A background in inorganic chemistry is invaluable in the synthesis of source materials for phosphor deposition because it provides chemical intuition that may only be partially compensated for by significant amounts of trial and error. Appreciation of the toxic properties of materials is important because many of the phosphor compounds and the chemicals required for their processing have undesirable effects on human health. For example, inorganic powders and certain gases should be contained and handled in well-ventilated areas such as fume hoods. Finally, a great deal of care needs to be exercised when synthesizing phosphor materials to avoid contact with materials that contain killer centers, as discussed in Section 3.2.6. It is especially important to avoid contact with steel-based products because these are rich in killer centers. For example, when scooping phosphor powders, it is desirable to use a porcelain, plastic, or teflon spatula instead of the standard stainless steel variety.

The synthesis of source materials generally involves the high-temperature formation of phosphor compounds. For the most part, the high-temperature synthesis of these phosphor compounds requires several high-temperature cycles in an atmosphere that provides the anionic species of the compound to achieve stoichiometry. For many oxide materials, firing of source materials in air to achieve a solid-state reaction is sufficient. However, certain oxides should be fired in an inert atmosphere to prevent changes in valence states of constituent elements. For sulfides, compound synthesis generally requires high-temperature cycles in a $H_2S$ atmosphere, as discussed in Appendix B. Similarly, the synthesis of nitride compounds is usually performed in an $NH_3$ atmosphere, as discussed in Appendix A. Finally, selenides and tellurides should be synthesized by a vapor-transport reaction because it is difficult to work with the extremely toxic and flammable $H_2Se$ and $H_2Te$.

From the standpoint of university research, oxide phosphors are by far the most attractive because they are easier, safer, and less expensive to synthesize than any

other family of materials. The synthesis of oxides is easier than other families of materials because many can be synthesized in air, leading to far less complication and expense than the synthesis of other families of materials that require synthesis in alternate atmospheres. Safety is also a primary concern in any research environment. Therefore, oxides are attractive because they almost never require synthesis in atmospheres of toxic gas. Finally, oxides are attractive because oxides of a cationic species are almost always more available and less expensive than compounds of other anions.

### 3.5.2 Formation of sputtering and evaporation sources from powdered source material

The formation of sputtering and evaporation sources from powdered source materials is a step in the process leading to the deposition of phosphor materials that is often either overlooked or taken for granted. The main issues regarding the formation of sputtering and evaporation sources are the final density and purity of the powder compact. Density is a key issue that is often overlooked because it is possible to sputter and evaporate from marginally dense materials. However, the denser the source material for both evaporation and sputtering leads, the greater the deposition rate and the higher the film purity. [154] Finally, the importance of the purity of sputtering and evaporation sources should be self-evident.

The major issue regarding evaporation and sputtering source density is the porosity of the source material, because porosity of source material implies trapped gas inside of the powder compact. This trapped gas definitely poses a threat to the purity of the sample because of the possibility of reaction with this gas. In addition, the volume that a given quantity of gas occupies increases greatly both when they are heated and when they are placed in a vacuum. Since the source material for both evaporation and sputtering is both heated and placed into a vacuum, the gas trapped in pores in the source material may cause intense localized pressure on the walls of these pores that may lead to explosions on a microscopic scale. These small

explosions imply that the source material will subsequently emit macroparticles that are too large and heavy to reach the substrate and become part of the growing film. In addition, if these macroparticles are emitted with enough initial kinetic energy to reach the substrate, they are not consistent with normal film nucleation and lead to film degradation through increased morphology and subsequent defect formation. Finally, since the emission of these macroparticles does not lead to efficient thin-film nucleation, they represent wasted source material, and hence a loss in the thin-film deposition rate. This loss in deposition rate affects the final purity of the thin-film because the longer the deposition time is, the more chance the nucleating film has of reacting with background gases present in the deposition chamber.

The two techniques that are available to increase the density of a powder compact are pressure treatment and sintering. In most cases, a combination of pressure treatment and sintering are used to achieve the highest practical density of source material possible. Generally, sputter target and evaporation source vendors specify source material density at 99+% of the theoretical density. Depending on the nature of the source material to be densified, it may or may not be feasible to achieve this level of densification in-house.

The pressure treatment/sintering process that is used for the preparation of sputtering and evaporation sources at Oregon State University and the David Sarnoff Research Center, the supplier of sputtering targets for Planar America, Inc., is the cold press/sinter technique. This technique operates on the principle that the powdered source material is first pressed into the required form at a large enough pressure to ensure that the powder compact holds together for subsequent handling. Then, the powder compact is sintered at high temperatures to achieve densification. This procedure provides fairly good results for source material purity and requires the least elaborate equipment of the densification techniques. However, because of the vast differences in physical properties of materials, certain materials may be extremely difficult to densify in this way. The other important issue to consider when press-

ing source material into a form is the die material. The most common and easily machined material available in machine shops is carbon steel. However, because all steels contain a significant quantity of Fe, and some contain Co and Ni, a steel target die is a very poor choice for pressing phosphor powders. For most materials families, the best choice for the target die material is graphite. This is particularly true of oxides because the graphite reacts with $O_2$ at temperatures greater than 650°C to form $CO_2$ to effectively remove any residual carbon contamination from the target die.

The other major consideration when the cold press/sinter technique is used for densification of powder compacts is the compressibility of the powdered source material. Some powdered materials compress readily under less than one ton per square inch and hold their compressed form well after removal from pressure. However, some powdered materials do not hold together after removal from pressure unless they are compressed at extremely high pressures. Sulfides in general tend to be readily compressible materials, whereas oxides do not. To combat problems with materials that are not readily compressible, one of two techniques are generally used; pressing with a backing plate or the use of binders. Pressing with a backing plate involves pressing the powdered material along with a non-reactive, rigid ceramic plate to allow transfer of the fragile powder compact to the furnace for sintering. As long as the powder compact is not to be sintered above 1300°C, where the alumina ceramic may begin to diffuse into the powder compact, this is an attractive and simple method for handling troublesome powder compacts. It should be noted that these laser-cut 98% alumina ceramic plates have been purchased from the Coors Ceramic Co.'s electronic substrate division. This method is depicted in Fig. 3.12. The other method for handling difficult to compress powders is to use an appropriate binding material. The binder is usually a powder such as poly-vinyl alcohol (PVA) that is mixed to around 10 wt.% with the powder to be compressed. Then, when the powder compact is sintered, the binder is boiled away by slowly heating the powder compact to the boiling point of

the binder and holding that temperature for several hours to completely volatilize the binder. If the powder compact is heated too rapidly, the binder may quickly volatilize and result in pitting of the surface of the powder compact. For the preparation of targets with PVA binder, a ramp rate of 1°C / min to 500°C, followed by a rest of 4-6 hours at 500°C works well to completely volatilize the PVA without damaging the integrity of the surface of the powdered compact.
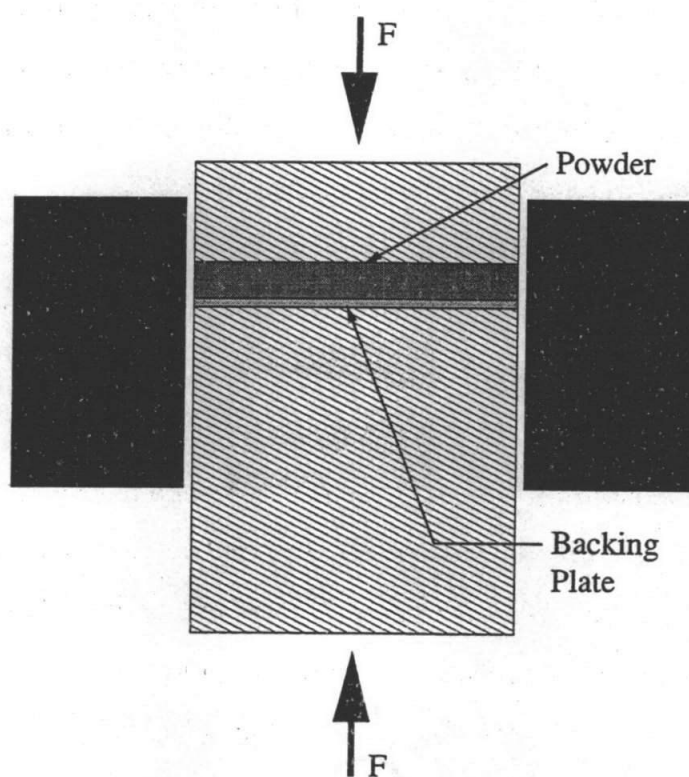
Figure 3.12: Powder compression with a ceramic backing plate.

Another powder compact densification technique is the axial hot-press method, in which the powder compact is heated during the compression cycle. This technique is arguably the least practical method for preparation of high-quality phosphor materials for several reasons. First, the problems with diffusion of atoms from the target

die into the powder compact is greatly increased at elevated temperatures. Furthermore, graphite is the best target die material for the pressing of a wide variety of phosphor materials, but graphite begins to react with $O_2$ to form $CO_2$ at temperatures above 650°C, rendering it useless for most of the fairly refractory phosphor materials unless hot-pressed in an inert atmosphere. Also, most of the common metals are materials that should not be allowed to come into contact with phosphor materials. Therefore, this technique must be performed either with a target die made of exotic material or in an inert atmosphere. Finally, since this is the axial hot-press method, lateral shrinkage of the powder compact would be expected to be enhanced only marginally. As a result, these requirements increase the cost of performing the axial hot-press method considerably over the cold-press/sinter method, without increased performance, rendering it a poor method for phosphor source material densification.

The final method for powder compact densification is the hot isostatic press (HIP) method. The HIP method produces uniform densification because the powder compact is heated under the isostatic pressure of a fluid. The HIP method is generally performed by heating a powder compact under the pressure of an inert gas, usually Ar, to a pressure of several hundred atmospheres. The high isostatic pressure coupled with elevated temperatures produces extremely dense targets at a fraction of the time and temperature necessary for complete densification via other techniques. [77] For this reason, the HIP technique is the method preferred by target vendors to produce the highest density targets. However, the major drawback to this method is the equipment cost necessary to process powder compacts in this manner. As a consequence, HIP produced source material is considerably more expensive to purchase from target vendors than otherwise manufactured material.

The main issue regarding purity of the source material is in regard to how completely the compound of interest is formed from its precursors. The process of sputtering and the process of evaporation both remove material from the source on an atomic level. Therefore, it is possible to create a working sputter target or evaporation

source by pressing stoichiometric mixtures of the constituent powders together and sintering. However, this is not the preferred method for producing source material because the sintering behavior of materials are in general quite different, leading to poor control of the dimensions of the sintered powder compact. In addition, because the constituent powders may partially react at elevated temperatures, there may be expansion of the source material during sintering. Therefore, for the sake of quality control of the source material, it is preferable to prereact the compound of interest prior to the densification cycle.

### 3.5.3   Sputter target bonding

The sputtering of insulating and conducting targets is different, primarily because of the different rates of heat transfer through these types of materials. Metals are usually good conductors of heat, and the heat generated by the bombardment of the cathode is efficiently carried away via the cooling water. However, ceramic insulators are in general poor conductors of heat, and a large temperature gradient may exist between the surface of the sputter target and the base of the target that directly contacts the cooled surface. This increased surface temperature of ceramic insulating targets leads to non-uniform thermal expansion, which causes problems with the integrity of the sputter target when not properly allowed to expand.

Most commercial sputtering cathodes are designed for the sputtering of metallic targets and require some modifications to reliably sputter ceramic insulating targets. Generally, commercial sputtering cathodes directly clamp the target to the cathode, as shown in Fig. 3.13. Direct clamping of the target to the cathode is fine for sputtering metals because they conduct heat away efficiently, and hence do not expand appreciably during sputtering. Furthermore, metals tend to be malleable and thus will not be permanently affected if undue pressure is exerted due to thermal expansion during sputtering. On the other hand, ceramic materials tend to be poor conductors of heat, and thus greater target heating occurs when sputtering insulators. This

enhanced target heating leads to greater thermal expansion of the target, and hence more pressure exerted when clamped to the cathode. In addition, ceramic materials by nature are brittle, and tend to fissure or even crack apart when undue stress is exerted on them. For these reasons, it is often difficult to sputter ceramic targets with enough power to achieve adequate deposition rate without permanently damaging the target.
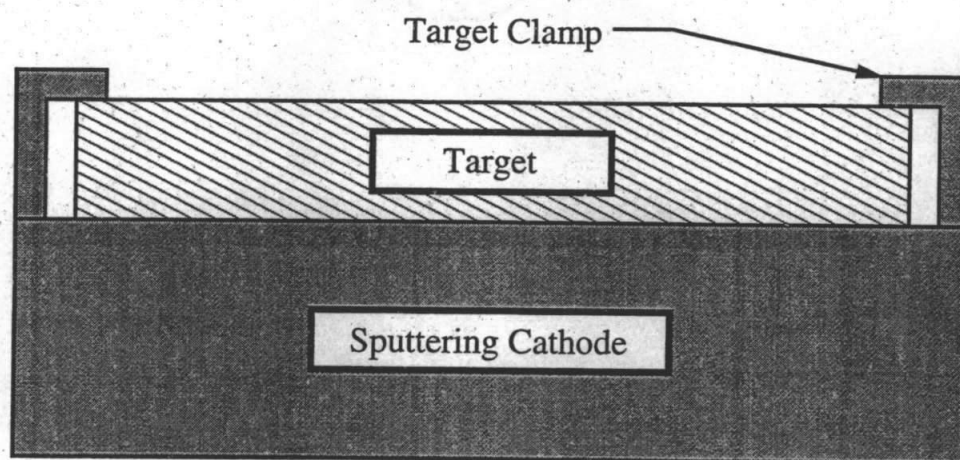


Figure 3.13: Commercial metal sputtering cathode.

The concerns cited above are sufficient to require the modification of sputtering cathodes designed for metals when they are to be used for the sputtering of ceramics. The major concern, as outlined above, is target heating and associated thermal expansion. To allow the target to expand more or less freely, ceramic targets are bonded to a backing plate, which is clamped to the rf cathode instead of the target itself, as shown in Fig. 3.14. This allows the ceramic target to expand relatively freely when it is heated during sputtering, making it possible to sputter at greater power without target damage. This not only reduces the chance for target damage during processing, but is a major step towards improving film quality because greater

power leads to a greater deposition rate, which in turn leads to reduced incorporation of background gases during sputter deposition.

Target Clamp

Target

Sputtering Cathode
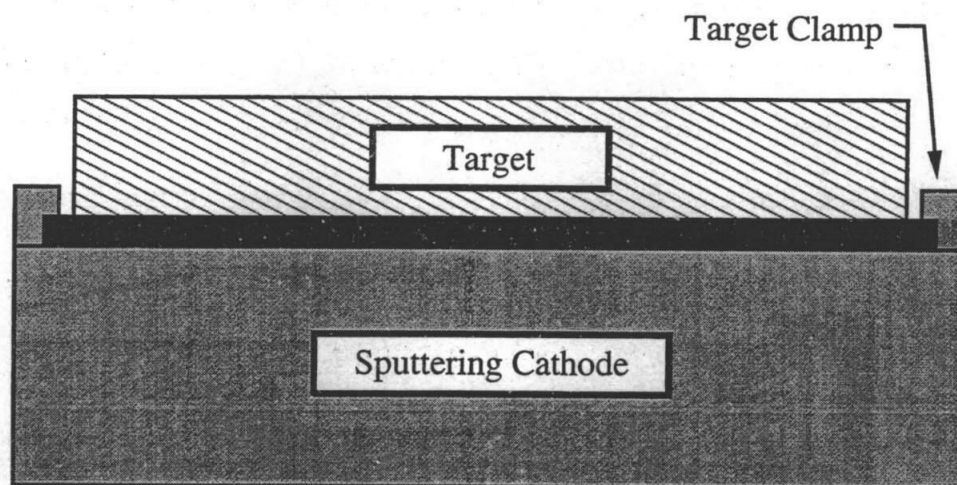
Figure 3.14: A modified sputtering cathode for sputtering ceramics.

To sputter ceramic targets with the modified sputter gun shown in Fig. 3.14, it is first necessary to bond the target to a conducting backing plate. The backing plate should be made from a metal of high electrical and thermal conductivity; Cu is the best choice for this application, but Al also performs adequately. The best bonding material currently available for this application is silver-filled epoxy, available from Cerac, Inc. The major drawbacks of using Cerac's silver-filled epoxy are that it is expensive and difficult to work with. Specifically, the tolerance on the catalyst weight ratio is quite strict. In addition, the bonding instructions supplied by Cerac advocate mixing of approximately twice the amount of silver epoxy than is necessary to satisfactorily bond a target of a given size. The major advantage of this epoxy, though, is that it is conductive, unlike standard epoxies. However, standard epoxies have been used for this application, although targets bonded to backing plates with standard epoxy should be driven gently because of the danger of debonding the target.

## 3.6 ACTFEL device fabrication

Once suitable source material has been synthesized, pressed, and sintered, the next step is the fabrication of ACTFEL devices. This section examines ACTFEL device fabrication with the facilities currently available in the ECE department solid-state processing laboratory at OSU. Currently, this laboratory is configured to deposit only standard structure ACTFEL devices, so this section is devoted exclusively to this type of ACTFEL device.

### 3.6.1 Substrates, transparent conductor, and bottom insulator

The substrates for ACTFEL device deposition are provided by Planar America, Inc., pre-coated with ITO and ATO. The glass substrate is typically either Corning 7059 glass or Nippon electronic grade (NEG) glass. The ITO transparent conductive layer is sputter deposited to a thickness of about 2000 Å. The ATO insulating layer is ALE deposited to a thickness of 2000 Å, with a relative dielectric constant of approximately 11.5. The thin-film deposition equipment in the OSU ECE processing lab is currently set up for deposition onto 1" square substrates. As a result, these substrates must be specially requested from Planar America, Inc. because their sample size is typically 2" square or larger.

### 3.6.2 Thin-film phosphor deposition by EBE

The EBE system is the phosphor deposition system that is most versatile in its ability to deposit ACTFEL phosphor materials. This versatility is due to the relative ease with which EBE pellets can be fabricated, the ability to multi-source evaporate to study dopant concentration, and the ability to rapidly cycle through phosphor hosts and dopants. For these reasons, the multi-source feature of the EBE system is primarily used to rapidly test new ideas regarding phosphor hosts, activators, and coactivators. Unfortunately, the controllability of multi-source EBE ACTFEL phosphor depositions is limited by the accuracy of the quartz crystal thickness monitor,

which is sometimes unreliable when the substrate is heated. However, better control of activator and coactivator concentrations is achieved through the synthesis of pre-doped EBE pellets, although the activator and coactivator concentrations in the pellet and the film are not, in general, equal. Therefore, the EBE system is primarily used for developing new phosphor ideas with multi-source evaporations and bringing promising ideas to fruition with the increased control of pre-doped EBE pellets.

When depositing phosphor films via EBE, polycrystallinity, stoichiometry, and contamination are the important factors in determining overall film quality. Since most of the polycrystallinity is generally achieved during post-deposition annealing cycles, the most important methods for achieving polycrystallinity are discussed in Section 3.6.5. However, a degree of polycrystallinity is achieved during the deposition of the phosphor thin-film by heating the substrate. Heating the substrate is important because the thermal energy imparted to the constituent species of the growing thin-film results in greater atomic migration. Substrate heating is especially important for an evaporation process because the kinetic energy of species arriving at the substrate is very low. The atomic migration resulting from substrate heating results in better crystallinity because more of the constituent atomic species are of sufficient kinetic energy to locate proper lattice sites. In addition, slower deposition rates may aid in film nucleation because species arriving at the substrate have more time to migrate on the surface before being coated. Unfortunately, each material is quite different in its requirements for substrate temperature and deposition rate, so information must be gathered for proper values of these parameters.

The major source of contamination in an evaporation process is the evaporation of contaminants along with the evaporant. Obviously, the material to be evaporated should be as pure as possible to minimize evaporation of contaminants along with the source material. In addition, dust particles and other contaminants from the atmosphere may adsorb or react with the evaporant during handling. For this reason, contact with the atmosphere should be minimized by storing evaporant in clean,

tightly sealed containers. Furthermore, reactive evaporants should be stored in an inert atmosphere to preclude spontaneous decomposition in the air. To purify the evaporant *in situ*, a shuttered evaporation should be performed in which the shutter is kept closed until a suitable evaporation rate is reached. This allows the desorption of low-evaporation temperature organic contaminants and water that may have adsorbed to the evaporant before the phosphor thin-film growth is begun. Finally, thermal evaporation is especially prone to contamination from evaporation boats, because these structures must be heated to extremely high temperatures to evaporate most materials. Although evaporation boats are always fabricated from refractory materials, the evaporant may react with the boat, and small amounts of these refractory materials may also be evaporated. For this reason, electron-beam evaporation is a cleaner evaporation technique because all of the heating of the evaporant is supplied by electrons and the crucible supporting the evaporant is force-cooled.

Stoichiometry is a more nagging issue in evaporation processes than plasma processes because evaporation is by nature a high-vacuum process. Depending on the compound to be evaporated, the evaporant may be emitted as constituent atoms, molecules, or molecular fragments. Unfortunately, most compounds tend to decompose before evaporation, leading to their emission from the evaporant on an atom-by-atom basis. [45] This presents problems when one or more of the components of a compound are volatile or difficult to condense. When plasma processes are used, loss of volatile species can usually be counteracted by adding a gas containing the troublesome species to the process gas. However, evaporation is ideally performed in a high-vacuum environment to maximize the mean-free path of evaporant atoms and molecules. Therefore, only small amounts of process gas can typically be introduced during an evaporation because of mean-free path issues. Furthermore, the process gas that is introduced is less reactive than in a plasma process because the gas exists almost solely in its stable molecular form, without the reactive radicals that are generated by a plasma. As far as families of potential ACTFEL phosphor materials

go, the stoichiometry issues with sulfides, selenides, and tellurides are typically minor compared to those of oxides and nitrides. This has lead to the development of microwave cavities that "crack" process gases into radicals to increase their reactivity, and activated reactive evaporators (ARE) where evaporants are emitted through a low-pressure plasma. [116] When deposition of stoichiometric oxides and nitrides via standard thermal or electron-beam evaporation is difficult, it may be necessary to employ these techniques to boost the incorporation of oxygen or nitrogen into the growing film.

### 3.6.3 Thin-film phosphor deposition by RF sputtering

The general topic of sputtering is covered in Section 2.4.2, whereas this section analyzes sputtering issues of particular relevance to the deposition of phosphor thin-films with the equipment currently available in the OSU ECE solid-state processing lab. The RF sputtering system is used primarily in this project as a tool for the deposition of oxide materials. This is due to the necessity of performing reactive evaporation in flowing $O_2$ to deposit stoichiometric oxide thin-films. Due to the fact that the EBE system is not configured for precise controls of $O_2$ flow, it is not a particularly useful tool for oxide evaporation. Furthermore, better oxygen incorporation is achieved with plasma processing because of the ultra-reactive oxygen radicals that are formed in a glow discharge. In combination with the MFC process gas inputs of the RF sputtering system, precise control of oxygen incorporation can be achieved with this system. Unfortunately, some of the versatility of the EBE system is lost due to the necessity of fabricating a new sputter target each time a new activator or coactivator concentration is desired.

The three basic goals in the deposition of a phosphor thin-film are to achieve films with adequate crystallinity for electronic transport via delocalized band states, and to achieve a stoichiometric, contamination-free film. The theoretical issues regarding the importance of these three issues are discussed in Section 3.1. This section

focuses on the practical aspects of achieving a polycrystalline, stoichiometric, and contamination-free phosphor film.

Similar to evaporated phosphor films, most of the polycrystallinity of RF sputter deposited ACTFEL phosphors is typically obtained during a post-deposition annealing cycle. In addition, substrate heating plays a role in determining final crystallinity of RF sputter deposited ACTFEL phosphors. However, the importance of substrate heating during RF sputter deposition is somewhat diminished from evaporation because the constituent species of the phosphor thin-film arrive at the substrate with a much greater kinetic energy. As a result, the optimum substrate temperature for RF sputter deposition of a given material is often significantly lower than that for evaporation.

The importance of minimization of film contamination is self-evident; however, the steps that are taken to minimize contamination are often quite elaborate. Of primary importance for the deposition of phosphor thin-films is the minimization of contact with killer centers. The problem is that vacuum system apparatus is quite often constructed from steel or stainless steel, both of which are to a large extent Fe, and may contain small quantities of Co and Ni. For example, the dark-space shield and target clamping mechanisms for most sputtering cathodes are constructed from stainless steel. Unwanted sputtering of these surfaces during phosphor deposition may cause some contamination of the growing film with killer centers and lead to phosphor films that do not exhibit luminescence, termed "dead films." Furthermore, the substrate holder should be constructed of a conductive material that is free of Fe, Co, and Ni, such as Cu or Al. For minimization of killer center incorporation, it is not advisable to etch the film that builds up over time from these surfaces unless it begins to peel.

The other important source of killer centers in a vacuum system is the heating element. Heating elements are often constructed from a length of nichrome wire in which a large current is passed to obtain a resistive heater. The use this type of

heater in a vacuum system requires preconditioning of the wire by heating it in air to allow nickel and chromium oxides to form at the surface. However, for phosphor deposition, this type of heater should be avoided unless it is completely enclosed due to routine thermal emission of Ni atoms when at high temperature. In addition, if the heating coils are exposed to the plasma, there is potential to sputter Ni from this type of heater. The cleanest heating element available is a halogen lamp because the filament is enclosed in an evacuated glass tube. In addition, high-power halogen lamps are readily available and inexpensive. As a result, tungsten halogen lamps are used for substrate heating in the RF sputtering system used for this project. The only concern with halogen lamp heating is that the substrate holder should be an optically absorbing material. Other more exotic heating elements are also acceptable for phosphor film deposition, such as carbon cloth heaters and pyrolytic boron nitride coated graphite-trace resistive heaters. However, these options are many times more expensive than heating by halogen lamps.

A persistent, but more subtle, problem with contamination is the incorporation of gas-phase contaminants into sputtered films. There is always a certain level of background gas present in a vacuum system that is a ready source of contaminants. These background gases are generally compounds of H, C, N, and O. Although it is unclear the general effect of incorporation of these elements into phosphors in general, their incorporation has the potential to lead to non-stoichiometry and defects in the deposited phosphor. By far the most troublesome compound falling into this class is water vapor, which adsorbs to vacuum surfaces, and hence, is very difficult to efficiently pump. This is the underlying reason why it is beneficial to isolate a vacuum system from the atmosphere as much as possible. The reduction in adsorbed water vapor is one of the primary advantages of the load lock feature of the RF sputtering system used for this project. Other techniques for reducing the level of water vapor in a vacuum system are discussed in Section 3.3.1. Another source of gas-phase contaminants into a phosphor sputtering process that is often overlooked is from the

process gas sources. The gas purity specified is typically the purity of the gas from the source tank that a cylinder is filled from, not the cylinder itself, unless very high purity gas analyzed cylinders are specifically requested ($\gtrsim$99.999%). Less stringent control of background gas and process gas impurities is possible when sputtering oxide phosphors because the most aggressive element of the gas phase contaminants is oxygen. However, when sputtering sulfides, and in particular, nitrides, gas-phase impurities pose a serious threat. The background gases are monitored in the RF sputtering system used for this project with a RGA, and chamber baking is initiated when unacceptable levels of water vapor are present.

There are also potential problems with nonstoichiometry of the deposited thin-film when sputtering phosphor materials. The problem with non-stoichiometry typically involves deficiency of the anionic species of the compound, because these atoms tend to be less condensable than the cationic species. This problem is a direct result of the sputtering process removing material from the sputter target on an atom-by-atom basis rather than a molecule-by-molecule basis. Of particular importance in phosphor materials are oxygen and nitrogen deficiencies because these are the least condensable anionic species encountered in ACTFEL phosphor deposition. When sputtering nitrides, the process gas composition should be at least 50% $N_2$ or $NH_3$ to approach stoichiometry in the phosphor film. The reactive nature of oxygen allows growth of near stoichiometric films when $O_2$ comprises 10-20% of the process gas. Care needs to be exercised when sputtering with oxygen, however, because its reactivity can lead to breakdown of hydrocarbon pump oil. When the oxygen content of the process gas exceeds 25-30%, inert pump oil such as Fomblin$^{TM}$ must be used. In addition, cryopumps should not be used for the pumping of oxygen because large volumes of $O_2$ will be released during regeneration, leading to a fire and explosion hazard.

Several additional issues merit attention regarding the sputtering of ceramic targets and phosphor thin-films. First, to avoid target damage, the target must be

slowly ramped up to the intended operating power on its first use. The maximum rate for the break-in of ceramic targets is to ramp the power up to the intended operating power at a rate no greater than 10 $\frac{W}{hr\,in^2}$ of target surface area. [155] Second, the power density at which ceramic targets are driven at should be much less than that of metal targets because ceramic targets are much more easily damaged than metal targets. Metallic targets are often driven with power densities up to 140 $\frac{W}{in^2}$, whereas ceramic targets should not be driven with much more than 10 $\frac{W}{in^2}$. [155] Next, since the power density that ceramic targets are driven with should be kept at reasonably low values, this must be compensated by a decrease in the target-substrate separation to keep the deposition rate high enough to deposit a high-quality phosphor film. Whereas typical target-substrate separations for the sputtering of metallic targets is around 4", the target-substrate separation when sputtering phosphor targets is typically in the range between 1" and 2". This decreased target-substrate separation leads to a greater thickness variation across the substrate than large target-substrate separations, unless a moving substrate is used.

A classic problem when sputtering ceramic materials is known as resputtering. Resputtering occurs when highly electronegative atoms such as O or F bind an electron, become negatively charged, and are accelerated by the sheath potential and strike the substrate after traversing the plasma. The acceleration by the sheath potential imparts negative ions with tremendous kinetic energy because the sheath potential may be as large as kilovolts. This effect is possible while sputtering any type of ceramic target, but is most likely in compounds with a highly electronegative anionic species. Oxides are the ACTFEL phosphor materials family that is the most prone to this effect due to the high electronegativity of oxygen. Traditionally, this effect is dealt with by off-axis sputtering, but this tremendously decreases the overall deposition rate, and hence, leads to much more residual gas incorporation. The best solution for this problem when depositing ACTFEL phosphors is to employ a moving substrate that begins from an off-axis position and slowly moves through

the plasma to the opposite off-axis position. This technique improves the overall film quality because an underdense film is deposited while in the off-axis position that is subsequently densified by the bombardment of the negative ions while in the on-axis position. Finally, the deposition pressure should be throttled in the 20-40 mTorr range to reduce the mean free path of sputtered atoms enough to impede the motion of negative ions emitted from the target surface, but to keep the mean free path large enough to achieve adequate deposition rate.

### 3.6.4  Coactivator incorporation via "fluxing"

A technique for incorporation of coactivators after deposition of the phosphor film, called "fluxing", was recently developed at the University of Florida (UF). [156] The results of the fluxing study at UF lead to the conclusion that fluxing of certain coactivators leads to much improved crystallinity over non-fluxed samples. The fluxing technique begins with the evaporation of a coactivator containing compound, or flux, atop the phosphor thin-film. Following evaporation of the flux onto the phosphor, the structure is then annealed in an RTA to drive the flux into the phosphor bulk. Due to the simplicity and versatility of this technique, it is employed regularly in the ACTFEL devices deposited in this thesis. However, this technique is most useful for diffusive coactivators such as the lighter alkali metals, Cu, Ag, and Ga.

### 3.6.5  Post-deposition annealing

The polycrystallinity of phosphor thin-films is a very important issue, as discussed previously. Thin-film polycrystallinity is typically achieved by post-deposition annealing. Post-deposition annealing is performed either in a traditional furnace, or more commonly, a rapid thermal annealing (RTA) furnace. The RTA furnace is preferred for phosphor annealing cycles because it can be ramped up to temperature in a matter of seconds and subsequently cooled very quickly. This is especially advantageous for thin-film phosphors on glass substrates because temperatures of 200°C above

the softening temperature of glass can be realized for a short time without noticeable warpage of the substrate. The type of gas flowing during the furnace annealing cycle also plays an important role in the final quality of the thin-film phosphor. Although the choices of possible furnace annealing gases are too numerous to list, it is often a good idea to perform the post-deposition anneal in a gas that provides the anionic species of the compound. In addition, $H_2$ is sometimes beneficial in post-deposition annealing cycles.

Post-deposition annealing is generally performed on freshly deposited ACTFEL phosphor layers with the RTA furnace for this project. The small 1" square substrate that are used in this process can be annealed at temperatures up to around 850°C for several minutes without significant warping. When determining the potential of an ACTFEL phosphor material, it is usually annealed in the 800-850°C range because this usually leads to the brightest and most polycrystalline ACTFEL phosphors. However, RTA temperatures above 650°C are not manufacturable, and as the development of a promising phosphor progresses, every effort should be made to reduce the required RTA temperature to within this limit. The atmosphere for annealing sulfide phosphors is usually Ar, and the chamber is purged for 10 minutes before the initiation of the high-temperature cycle. Oxides, however, are usually annealed in $O_2$, $N_2/H_2$, or Ar, depending upon the nature of the oxide film.

### 3.6.6 Top insulator deposition

A high-quality top insulator process is critical for ACTFEL device performance in terms of both phosphor protection and electro-optical characteristics. The top insulator is the layer that shields the phosphor layer from the atmosphere, so it is imperative that it prevents water vapor and other contaminants from reaching the phosphor layer. In addition, the top insulator helps determine many of the electrical characteristics of an ACTFEL device through its affect on the capacitance, as discussed in section 2.2. Finally, the top insulator layer also plays a role in determining

the device charge injection, and hence, luminance by helping determine the extent to which the applied voltage couples to the phosphor field.

Due to the importance of the top insulator to a finished ACTFEL device, several different top insulator deposition processes have been developed for this project to meet different needs. The first is the RF sputter deposition of $Ta_2O_5$. The main advantage of this process is the high relative dielectric constant of $Ta_2O_5$ ($\epsilon_r = 23$-$25$). The disadvantages of this process include slow deposition rate ($\sim 2000$ Å/hr), low dielectric strength ($\sim 1.5$ MV/cm), film non-uniformity due to the small size of the sputtering cathode, and the necessity to occupy a sputter gun normally used for phosphor deposition. The second insulator process is PECVD-deposited $SiO_xN_y$. The advantages of this process include high deposition rate ($\sim 100$ Å/min), high dielectric strength ($\sim 4$ MV/cm), low loss tangent ($< 0.3\%$), good thin-film uniformity, and good repeatability. The main disadvantage of this process is the low relative dielectric constant of $SiO_xN_y$ The final insulator deposition process is reactive e-beam evaporated $Al_2O_3$. The advantages of this process are excellent uniformity, high dielectric strength ($F_{BD} \simeq 4$ MV/cm), very high deposition rate ($\sim 300$ Å/min), and low loss tangent ($< 0.3\%$). The disadvantages of this process are inadequate repeatability due to poor reactive gas flow control, low relative dielectric constant ($\epsilon_r = 8$), and the need to use a phosphor deposition system for insulator deposition. From the analysis of the various options for insulator deposition, PECVD deposited $SiO_xN_y$ is the clear choice in most circumstances. As a result, the e-beam evaporated and rf sputtered insulator processes are used mainly when the PECVD system is non-operational, or a higher relative dielectric constant insulator layer is required.

Due to the importance of the top insulator and the advantages of the PECVD $SiO_xN_y$ process for this application, a design of experiments (DOE) process optimization experiment was performed on this process to achieve high dielectric strength. The unoptimized process for optical $SiO_xN_y$ yielded films that averaged about 2.5 MV/cm dielectric strength and about 0.5-1.0% loss tangent, both of which are worse

than what should be attainable with this process. Therefore, a $2^{5-1}$ DOE process optimization experiment was performed to determine the gradient pointing towards the region of optimal dielectric strength. Following the path of steepest ascent provided by this analysis, the average breakdown field was increased to around 4 MV/cm. In addition, the dependency of dielectric strength on the various processing parameters was determined. The relative importances of each of the process parameters and their interactions in terms of determining the dielectric strength of the resulting $SiO_xN_y$ thin-film are shown in Figs. 3.15. The parameters and interactions that are statistically significant have magnitudes greater than the horizontal line at a standardized effect of 2. It should be noted that the process generated from this analysis is: RF power, 90 W (14.0%), throttle pressure, 700 mTorr, $SiH_4$+He flow rate, 110 SCCM (22.0%), $N_2$ flow rate, 26.5 SCCM (5.3%), $N_2O$ flow rate, 3.7 SCCM (3.7%).
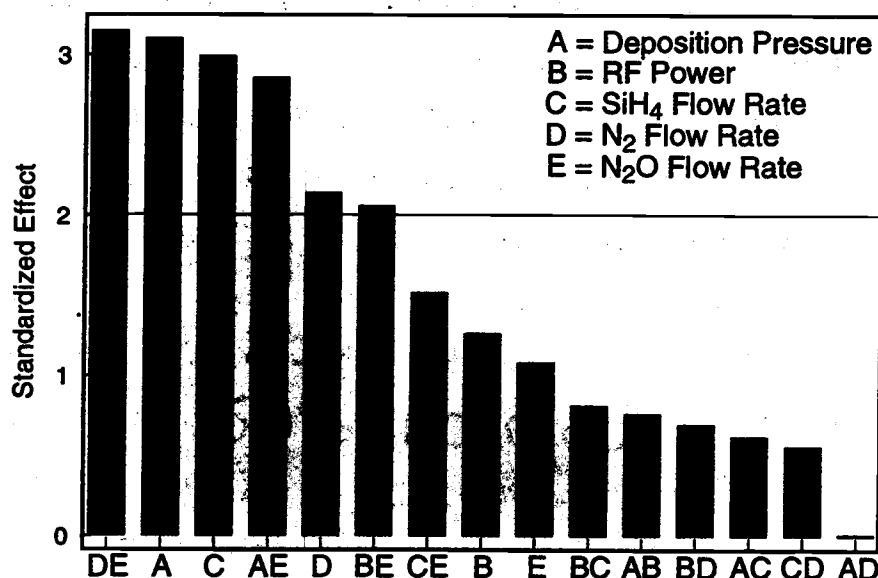


Figure 3.15: Pareto chart showing the relative importance of processing parameters in determination of the dielectric strength of PECVD deposited $SiO_xN_y$ thin-films (statistically significant process variables and interactions have a standard effect greater than 2).

### 3.6.7   Top electrode deposition

The Al top electrode is deposited by thermal evaporation to a thickness between 1000 and 1500 Å. The optimum thickness is between 1000 and 1500 Å because the top electrode should be thick enough to be reflective, yet thin enough such that self-healing behavior is obtained. To perform this evaporation, one 60 mg evaporation clip is sufficient. A good technique for obtaining the proper thickness is to watch the sample, and at the instant when the freshly evaporated Al electrode no longer allows light to be transmitted, the evaporation shutter should be closed.

## 3.7   Characterization of ACTFEL phosphor thin-films

After the deposition of an ACTFEL phosphor, it is necessary to gather information regarding the quality of the thin-film to acquire feedback for improvement of future processes. The first test of the quality of an ACTFEL phosphor is typically the observation of the photoluminescent (PL) response when exposed to short wavelength ultraviolet (UV) light from a Hg discharge. Another more sophisticated technique that is sometimes used is grazing-angle X-ray diffraction (XRD), which provides information concerning the crystallinity of the thin-film, growth orientation, and the presence of anomalous phases within the phosphor host. This technique should be used when examining annealing cycles because of its ability to detect most of the consequences of post-deposition annealing. Scanning electron microscopy (SEM), may also be useful in certain circumstances to view the phosphor on a microscopic scale. When serious contamination or stoichiometry problems are suspected, it may also be necessary to perform Auger electron spectroscopy (AES) or microprobe measurements to determine the composition of the phosphor thin-films. However, the ultimate test of an ACTFEL phosphor is of course its luminance, efficiency, and aging performance, as discussed previously.

## 3.8  Conclusion

This chapter provides a fundamental game plan for deposition of ACTFEL phosphor materials starting from the theoretical and progressing to the practical. The chapter opens with a discussion of phosphor hosts, activators, and relevant materials families from a theoretical standpoint. Then, as the chapter progresses, practical matters regarding the deposition of ACTFEL phosphors are addressed. Special attention is paid to troublesome issues particular to the solid-state processing equipment presently available to the ACTFEL phosphor fabrication project at Oregon State University. Finally, the chapter closes with a brief summary of the characterization techniques presently available for this project.

# 4. ACTFEL FABRICATION

This chapter is concerned with the fabrication of ACTFEL devices of the primary colors, with an emphasis on phosphors that produce green electroluminescence. Various approaches to achieving bright and efficient primary color phosphors are reported, but the emphasis is on sulfide phosphors due to their importance in the field of thin-film electroluminescence. However, both oxide and selenide phosphors are also investigated in this chapter because they possess some interesting properties that may be beneficial for the ACTFEL displays of the future.

## 4.1  SrS:Tb

The $Tb^{3+}$ ion is an interesting activator in the field of electroluminescence because it is well-known to produce a saturated green color (CIE x=0.3, y=0.6) in a ZnS phosphor host. Although the luminance and efficiency of this phosphor are second only to the venerable ZnS:Mn ACTFEL phosphor, its applicability to commercial products is poor because it has never exhibited the long lifetime that is characteristic of other ACTFEL phosphors. This flaw in ZnS:Tb ACTFEL devices is typically attributed to the large difference in ionic radius, valence, and chemical properties between the $Zn^{2+}$ cation and the $Tb^{3+}$ activator that substitutionally replaces it. The SrS phosphor host, however, more readily accomodates rare earth activators than ZnS due to the much greater size of the $Sr^{2+}$ cation. [4] In addition, the bonding in SrS has a much greater ionic character than in ZnS, and as a result, SrS crystallizes in the rocksalt structure whose 6-coordination better accomodates rare earth activators than the 4-coordinated wurtzite crystal structure of ZnS. For these reasons, SrS may be an acceptable phosphor host for the $Tb^{3+}$ activator, even with the valence mismatch between $Sr^{2+}$ and $Tb^{3+}$. Therefore, SrS:Tb is investigated as a potential primary color green-emitting ACTFEL phosphor.

The investigation of SrS:Tb for ACTFEL phosphor applications is carried out via EB/thermal multi-source evaporation. Undoped SrS pellets are electron-beam evaporated at varying rates concomitant with thermal evaporation of $TbF_3$ sintered pieces, yielding SrS:Tb,F phosphor layers. The undoped SrS pellets are provided by Ben Clark of the Oregon State University Chemistry Department, and are synthesized by sulfurization of $SrCO_3$ with $H_2S$, as discussed in Appendix B. The activator source material is 99.9% pure $TbF_3$ sintered pieces purchased from Cerac, Inc., and is evaporated from an alumina crucible heated with a W wire heater. The deposition rate and film thickness are monitored via a quartz crystal oscillator thickness monitor. Following deposition of the phosphor film, an RTA cycle is performed at 650°C for 120 seconds for recrystallization. After post-deposition annealing, approximately 3000 Å of $SiO_xN_y$ is PECVD deposited atop the phosphor layer. Finally, 1000-1500 Å Al top electrodes are deposited through a shadow mask by thermal evaporation.

The initial experiment performed with SrS:Tb,F is a study of the effect of $Tb^{3+}$ concentration on the performance of the ACTFEL device. Five SrS:Tb,F-based ACTFEL devices are fabricated with the $TbF_3$ deposition rate 0.25%, 0.50%, 0.75%, 1.0%, and 1.25% that of the SrS. The deposition rate of SrS is chosen to be the maximum possible without compromising pellet integrity during the deposition. The maximum deposition rate for the undoped SrS pellets used for this study is experimentally determined to be approximately 40 Å/s. It is desirable to deposit as rapidly as possible when performing concentration studies by multi-source evaporation so that dopant levels can be achieved more precisely. The substrate temperature for all depositions in this study is 250°C as measured by the thermocouple attached to the substrate holder. However, the actual temperature may be significantly higher because it is difficult to directly measure the temperature of the surface of the growing film during the deposition. Each of the five devices is deposited to a thickness of 8000 Å as measured by the thickness monitor, although the actual phosphor layer thicknesses vary between 6200 and 8300 Å, presumably due to oscillator crystal aging effects. It

should be noted that the actual concentrations of $Tb^{3+}$ in the films of these five devices is determined to be approximately 0.15 at%, 0.30 at%, 0.45 at%, 0.60 at%, and 0.75 at%, respectively. The actual film concentrations are determined by evaporation of pure $TbF_3$ layers of varying thickness under the SrS:Tb process conditions and subsequently measuring their thickness with a profilometer to determine the correction factor for the comparison of the thickness as measured by the thickness monitor and the actual thickness. As a result, if the evaporation rate is multiplied by the deposition time and the correction factor, a total $TbF_3$ thickness in the film can be obtained, which allows for a crude estimate of the actual $TbF_3$ concentration.

The five SrS:Tb,F devices deposited for this study all exhibit green electroluminescence, characteristic of the $Tb^{3+}$ activator. However, the color coordinates of the devices are all somewhat blue-shifted compared to those obtained from ZnS:Tb ACTFEL devices. In addition, the luminance and efficiency of these devices are significantly less than that reported for sputtered ZnS:Tb ACTFEL devices. The results of this concentration study are presented in Table 4.1.

Table 4.1: SrS:Tb,F ACTFEL device performance under a 60 Hz bipolar trapezoidal drive as a function of $Tb^{3+}$ concentration.

| at% $Tb^{3+}$ | $t_{phosphor}$ (Å) | $V_{th}$ (V) | $L_{40}$ (cd/m$^2$) | $\eta_{40}$ (lm/W) | CIE x | CIE y |
|---|---|---|---|---|---|---|
| 0.15 | 8300 | 176 | 0.826 | 0.008 | 0.305 | 0.511 |
| 0.30 | 8200 | 180 | 1.87 | 0.015 | 0.311 | 0.499 |
| 0.45 | 7800 | 166 | 1.91 | 0.019 | 0.311 | 0.555 |
| 0.60 | 6800 | 132 | 1.21 | 0.049 | 0.304 | 0.567 |
| 0.75 | 6200 | 138 | 1.75 | 0.057 | 0.302 | 0.568 |

The low luminance and efficiency of the ACTFEL devices fabricated for the concentration study suggests the possibility of improved device performance with

different processing conditions. Therefore, the deposition rate and substrate temperature are varied in order to determine the effects of these process variables on device performance. During these depositions, the relative dopant evaporation rate is kept as close to 0.75% that of the SrS as possible, within the limits of the thickness monitor. It is found that variation of either process parameter does not strongly affect the performance of the resultant ACTFEL device. Marginal improvement in the luminance is achieved by depositing the phosphor layer at 30 Å/s, as seen by comparison of Fig. 4.1 and Table 4.1. The additional luminance is obtained at the expense of efficiency and color purity, however.
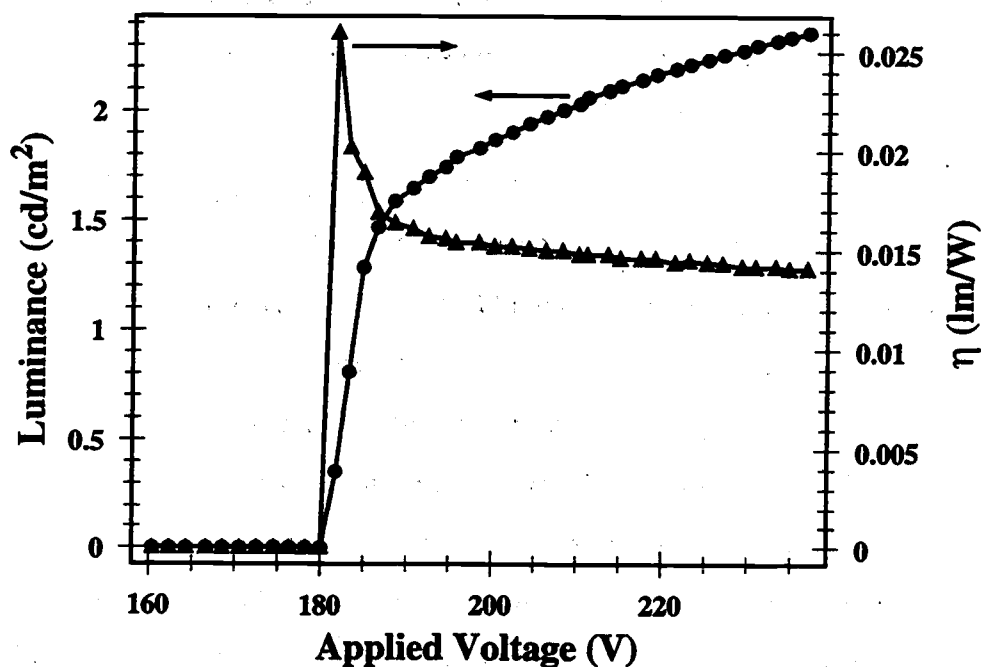


Figure 4.1: A L-V/$\eta$-V plot of a SrS:Tb,F ACTFEL device deposited at 30 Å/s (60 Hz bipolar trapezoidal drive).

The results presented above regarding SrS:Tb,F are poor in terms of the Planar target luminances and efficiencies given in Table 2.2. However, similar to ZnS:Tb,

this phosphor may perform at a much higher level when deposited by RF sputtering, as discussed in Section 2.3.1. The advantage of sputtering rare earth activated phosphor layers is apparently due to the larger kinetic energy imparted to the impinging atoms. This larger kinetic energy allows the relatively massive rare earth atoms to migrate along the surface of the growing film more effectively and find suitable lattice sites. To test this, several ZnS:Tb,F samples are fabricated to compare to sputtered ZnS:TbOF samples provided by Planar America. The sputtered ZnS:TbOF samples from Planar America prove to be approximately 20 times brighter than the brightest EBE-deposited ZnS:Tb,F samples. In fact, the brightest EBE-deposited ZnS:Tb,F samples exhibit a 40 volt above threshold luminance ($L_{40}$) of 2.02 cd/m$^2$ at 60 Hz, less than for the brightest SrS:Tb,F device. Therefore, SrS:Tb is a material that may prove to be an adequate green ACTFEL phosphor when deposited by RF sputtering.

## 4.2 SrS:Cu ACTFEL phosphors

Currently, the SrS:Cu ACTFEL phosphor is generating a great deal of interest due to its ability to generate bright and efficient blue electroluminescence. In addition to the importance of SrS:Cu as a primary color blue ACTFEL phosphor, evidence has been presented that SrS:Cu may also be a bright and efficient green primary color phosphor when doped with suitable coactivators. [89, 97] However, all of the work that demonstrate SrS:Cu as a bright and efficient green primary color phosphor has been carried out only for powder phosphors. Therefore, it is the aim of this section to investigate SrS:Cu as both a blue and a green primary color ACTFEL phosphor.

### 4.2.1 SrS:Cu,F

The investigation of SrS:Cu as an ACTFEL phosphor most naturally begins with $Cu_2S$ as the activator source because it is inexpensive and non-toxic. This is the approach that is taken for this project in an effort to determine the feasibility of fabricating SrS:Cu ACTFEL devices with the present EBE system. However,

the high currents required to thermally evaporate $Cu_2S$ at a sufficient rate for a concentration study and the inconsistent deposition rate due to preferential sulfur evaporation result in difficulties in repeatably fabricating high-luminance ACTFEL phosphors. As a result, other activator source compounds are investigated in order to achieve more consistent phosphor depositions.

The second choice of a Cu activator source is $CuF_2$ because it has previously been demonstrated that the use of $CuF_2$ as the Cu source for sputtered SrS:Cu ACTFEL phosphors results in bright ACTFEL devices of a more saturated blue color than straight SrS:Cu ACTFEL phosphors. [41] For this reason, $CuF_2$ is investigated as the thermally evaporated activator source for EB/thermal multi-source evaporation of SrS:Cu,F ACTFEL phosphors.

The deposition of these phosphor layers is achieved by EB evaporation of un-doped SrS pellets while thermally evaporating $CuF_2$ powder from a quartz crucible heated by a W wire heater. Following phosphor deposition, the samples are rapid thermal annealed at a temperature of 810°C in an Ar atmosphere for 120 seconds. Next, a 3000 Å thick top insulator of $SiO_xN_y$ is deposited via PECVD. Finally, Al electrodes are thermally evaporated to a thickness of 1000-1500 Å.

The goal of the deposition of SrS:Cu,F ACTFEL phosphors is to first perform a concentration study by evaporating the activator at successively greater rates until an optimum is obtained. However, it was quickly discovered that $CuF_2$ readily dissociates into Cu and $F_2$ when heated in vacuum, resulting in poor repeatability. As a result of this dissociation, a stable evaporation rate of $CuF_2$ and excess $F_2$ can be achieved for several minutes, after which time only Cu remains. When only Cu remains, little evaporation of Cu is witnessed because the evaporation temperature of Cu is significantly higher than that of $CuF_2$. Therefore, to deposit good-quality SrS:Cu,F, the undoped SrS pellet must be evaporated rapidly as soon as a stable evaporation rate of $CuF_2$ is obtained. A concentration study could be performed in this manner, except for the fact that larger initial deposition rates may lead to smaller Cu concentrations in

the phosphor film because the $CuF_2$ is converted into Cu more rapidly, and hence, less Cu may incorporate into the phosphor. This property of $CuF_2$ makes a concentration study of EB/thermal multi-source deposited SrS:Cu,F prone to error.

Although a concentration study is not feasible for the EB/thermal multi-source evaporation of SrS:Cu,F, a process is devised that leads to repeatable results. The process in question involves the thermal evaporation of $CuF_2$ powder at 0.4-0.5 Å/s with concomitant EB evaporation of an undoped SrS pellet at 40 Å/s as soon as this rate of $CuF_2$ evaporation is achieved. However, for this process to be repeatable, the quartz crucible that is used to contain the $CuF_2$ powder evaporant must be cleaned of residue following each deposition and subsequently refilled to a predetermined level prior to each deposition. This procedure is complicated by the high toxicity of $CuF_2$, which leads to doubts concerning the long-term implementation of this process. Nevertheless, reasonably bright and efficient SrS:Cu,F ACTFEL phosphors can be fabricated by this method. The typical 60 Hz $L_{40}$ obtained is just under 10 cd/m$^2$ with efficiency on the order of 0.1 lm/W and CIE coordinates of x=0.16, y=0.28. A B-V/$\eta$-V plot and spectrum of a SrS:Cu,F ACTFEL device fabricated by this process are shown in Figs. 4.2 and 4.3, respectively.

### 4.2.2    Alkali metal coactivated SrS:Cu,F

The process employed throughout the investigation of alkali metal coactivated SrS:Cu,F is to first perform an EB/thermal multi-source evaporation of a SrS:Cu,F phosphor layer in the same manner as discussed in Section 4.2.1. Following the deposition of the phosphor layer, a thin layer of an alkali metal fluoride is deposited atop one-half of the sample and diffused into the phosphor by the fluxing process discussed in Section 3.6.4. This technique is depicted in Fig. 4.4 for the purpose of visualization. Then, a 3000 Å thick $SiO_xN_y$ top insulator is PECVD-deposited. Finally, Al top electrodes are thermally evaporated to a thickness between 1000 and 1500 Å.
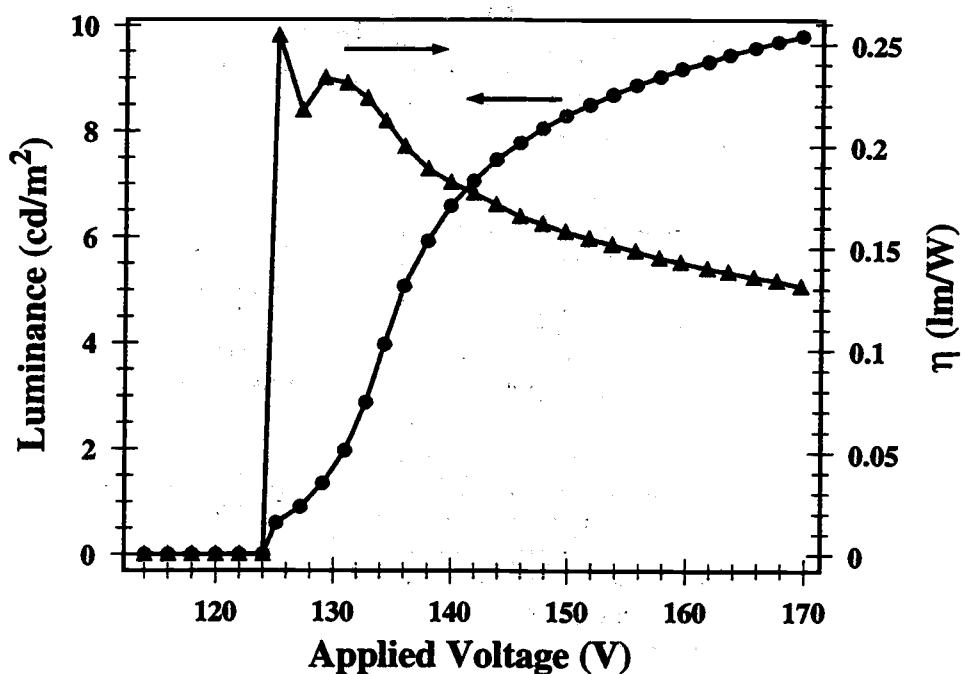
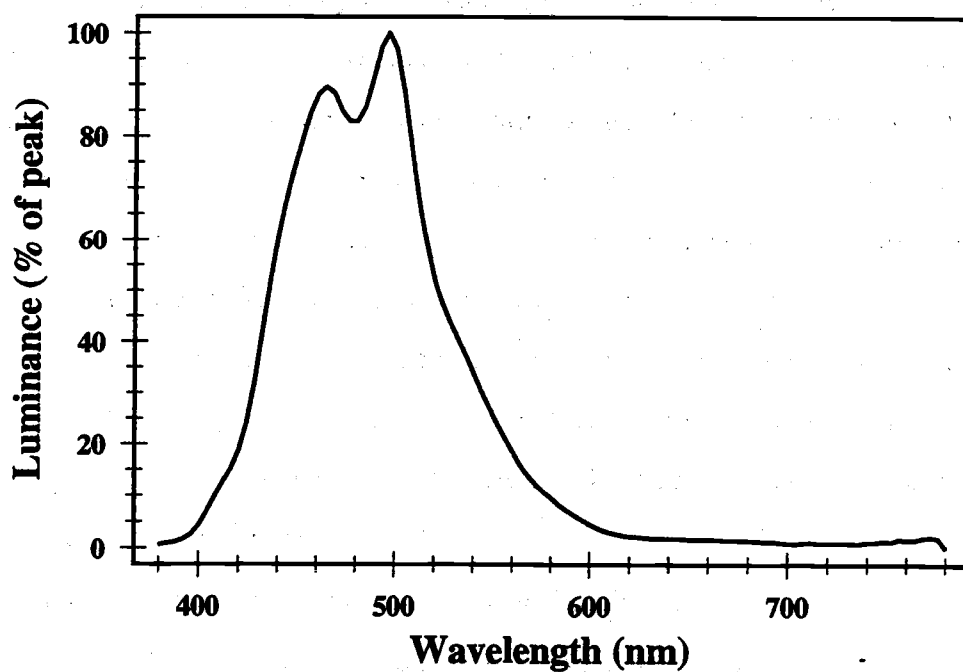Figure 4.2: A B-V/$\eta$-V plot of a SrS:Cu,F ACTFEL device (60 Hz bipolar trapezoidal drive).



Figure 4.3: The electroluminescent spectrum of a SrS:Cu,F ACTFEL device.

Step 1: Deposit the
SrS:Cu,F phosphor
layer by EBE.

| SrS:Cu,F |
| ATO |
| ITO |
| NEG Glass |

Step 2: Deposit a thin
layer of NaF over
1/2 of the sample
by thermal
evaporation.

| | NaF |
| SrS:Cu,F | |
| ATO | |
| ITO | |
| NEG Glass | |

Step 3: RTA sample to
drive NaF into 1/2
of the phosphor.

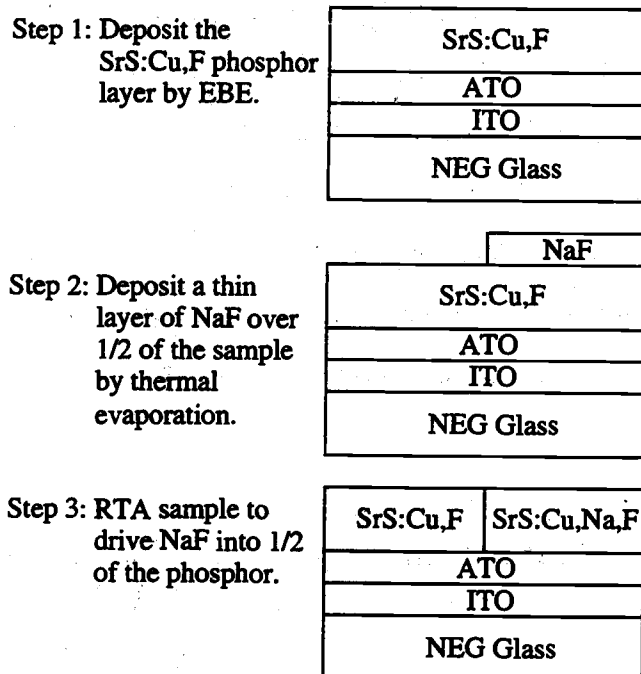| SrS:Cu,F | SrS:Cu,Na,F |
| ATO | |
| ITO | |
| NEG Glass | |

Figure 4.4: The phosphor deposition procedure for fabrication of samples with half of the phosphor area coactivated.

The coactivator used for the powder studies of alkali metal activated SrS:Cu was Na, [89] so the alkali metal coactivation of SrS:Cu,F ACTFEL phosphors is initiated with a study of Na coactivation. Several samples are fabricated with different amounts of NaF deposited atop the phosphor layer to determine the proper Na concentration. It is determined that a concentration of at least 0.5 mol% NaF is necessary to completely green-shift a SrS:Cu,F device fabricated via the process discussed in Section 4.2.1. Furthermore, it is also found that devices fabricated with above 2.5 mol% NaF are extremely prone to burn-out. Therefore, for the the study of alkali metal coactivation, the SrS:Cu,F samples are fluxed with approximately 1.5 mol% alkali metal fluoride for evaluation.

The results of coactivation of SrS:Cu,F with NaF indicate this to be a quite promising green ACTFEL phosphor in terms of chromaticity. A drastic green shift is witnessed with the incorporation of the $Na^+$ ions into the SrS:Cu,F phosphor, as

seen in Fig. 4.5. It should be noted that the spectra presented in Fig. 4.5 are the electroluminescence spectra of two devices on the same substrate, the green device on the half fluxed with NaF, and the blue device on the non-fluxed half. The CIE coordinates shift from x=0.164, y=0.268 for the blue, non-Na coactivated half to x=0.317, y=0.585 for the Na coactivated half. Comparison of the CIE coordinates of the SrS:Cu,Na,F device to the target green phosphor color given in Table 2.2 reveals that the color of SrS:Cu,Na,F is essentially a saturated green.
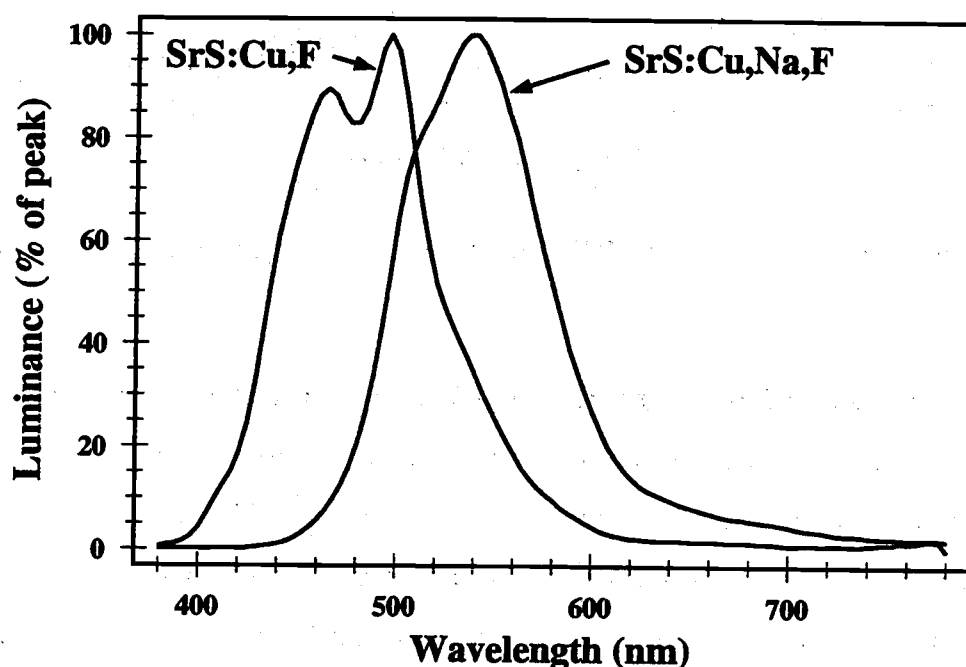


Figure 4.5: The electroluminescence spectral shift resulting from the flux doping of SrS:Cu,F with NaF.

In addition to the drastic color shift observed with Na coactivation of SrS:Cu, there is also considerable impact on other important electro-optical device characteristics. Comparison L-V and $\eta$-V plots of the Na and non-Na coactivated halves of this samples are shown in Figs. 4.6 and 4.7, respectively. As seen in Fig. 4.6, a $L_{40}$ in-
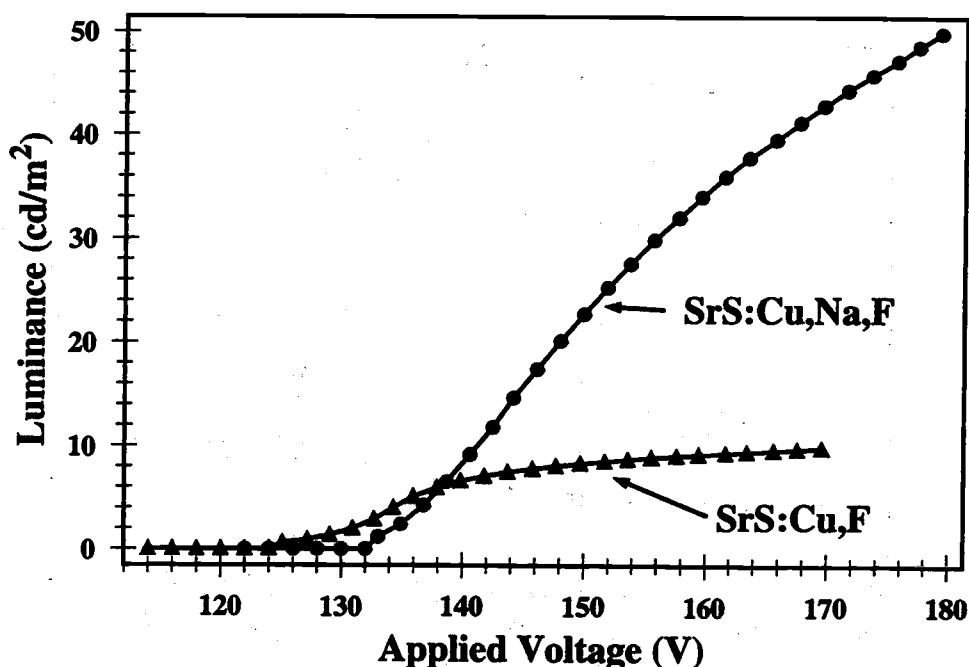
Figure 4.6: A L-V curve comparison of a SrS:Cu,F ACTFEL device with and without NaF fluxing.

crease of almost five times to 45.8 cd/m$^2$ is observed for the Na coactivated half of the ACTFEL device. However, this brightness increase is in large part due to the color shift of the phosphor from blue to green because of the eye's heightened sensitivity to green light. In addition to the brightness increase shown in Fig. 4.6, Fig. 4.7 reveals an increase in $\eta_{40}$ of almost six times. This large increase in efficiency is expected in view of the large increase in brightness, however, the fact that efficiency increases approximately six-fold while brightness increases only five-fold indicates that additional factors are at work in this case.

Since the efficiency of an ACTFEL device is proportional to the ratio of brightness to power density, there must be a reduction of the power requirements of SrS:Cu,Na,F from those of SrS:Cu,F to result in the observed efficiency increase. Therefore, the Q-V plots of both SrS:Cu,F and SrS:Cu,Na,F are compared in Fig. 4.8 to illustrate this power savings. As discussed in Section 2.6.1, the area enclosed
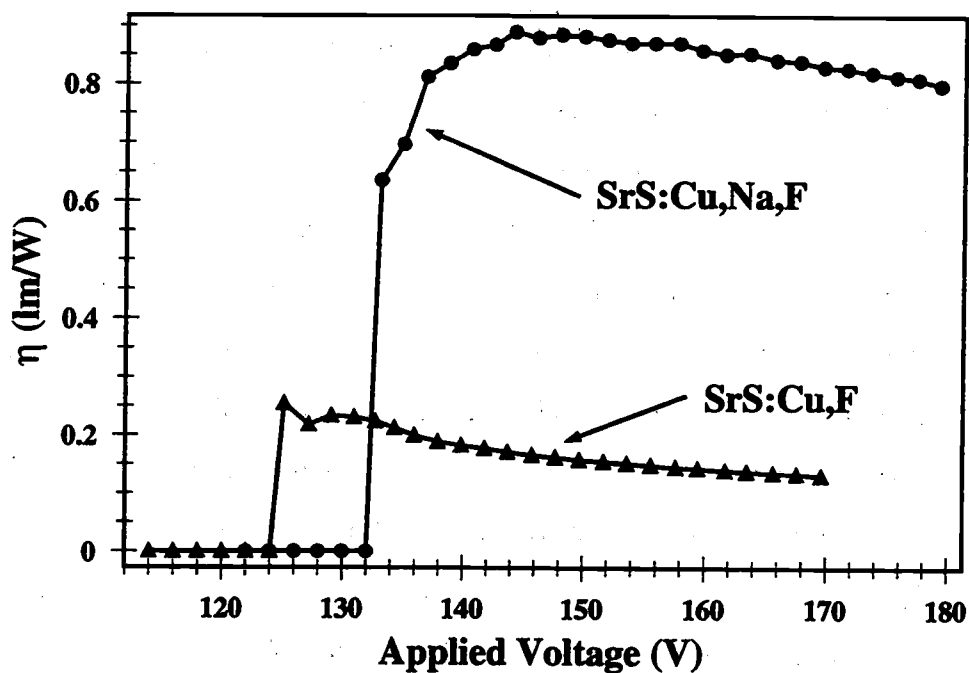
Figure 4.7: An $\eta$-V curve comparison of a SrS:Cu,F ACTFEL device with and without NaF fluxing.
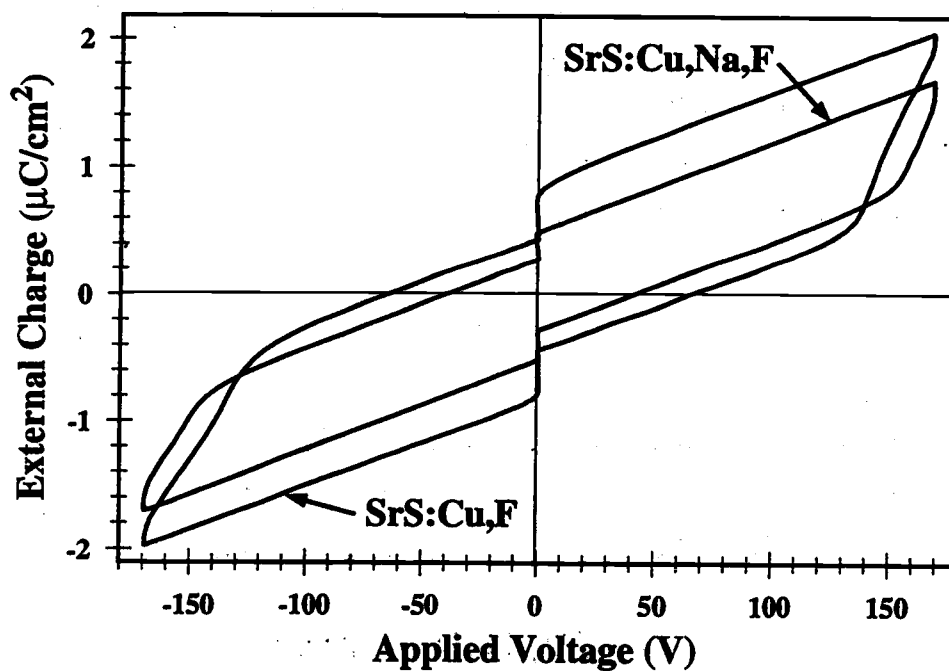


Figure 4.8: A Q-V curve comparison of a SrS:Cu,F ACTFEL device with and without NaF fluxing.

by the Q-V plot is equal to the input power density, and clearly the Q-V plot of the SrS:Cu,F device encloses a much greater area than that of the SrS:Cu,Na,F. In addition, the Q-V plot of the SrS:Cu,F device shows signs of space charge generation, as evidenced by the non-constant slope of the Q-V plot above the turn-on voltage; whereas no such effects are witnessed in the Q-V plot of the SrS:Cu,Na,F device. This is perhaps the reason why the SrS:Cu,Na,F consumes less power, there is no need to drive the space charge generation process and its associated capacitance overshoot.

The insights gained from the comparison of the Q-V plots of a SrS:Cu,F and a SrS:Cu,Na,F device reveal the need for a more in-depth electrical characterization analysis of these devices to obtain a better grasp of the differences in their operation. A primary tool for accomplishing this feat is $Q\text{-}F_p$ characterization; hence, $Q\text{-}F_p$ measurements of both the SrS:Cu,F and SrS:Cu,Na,F devices are measured and shown in Fig. 4.9. A comparison of the $Q\text{-}F_p$ plots of these devices immediately leads to
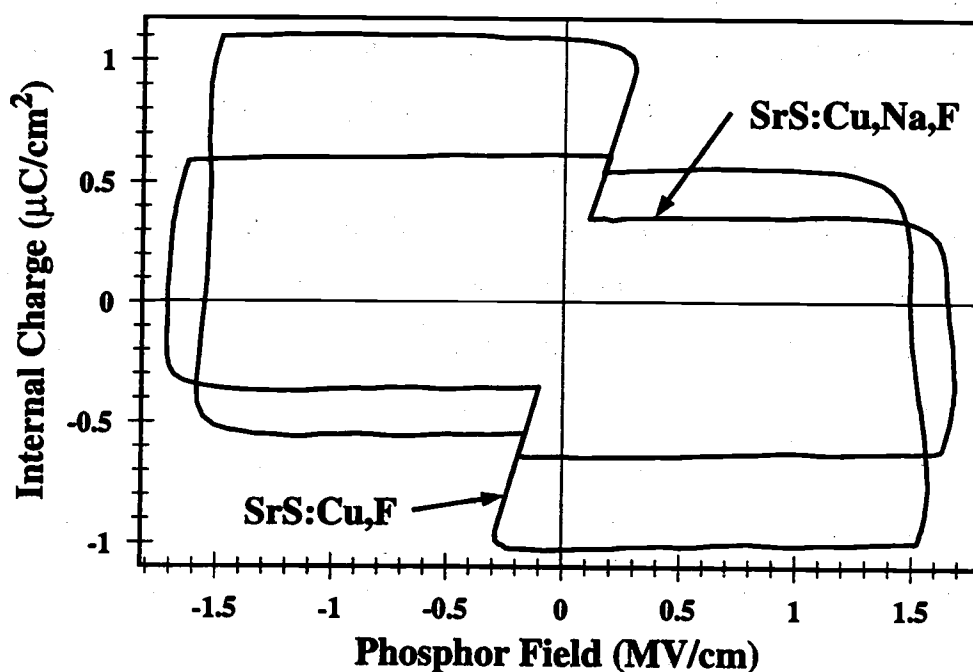


Figure 4.9: A $Q\text{-}F_p$ curve comparison of a SrS:Cu,F ACTFEL device with and without NaF fluxing.

two important observations; namely that the charge transfer in the SrS:Cu,Na,F ACTFEL device is significantly smaller and occurs at a larger average field than in the SrS:Cu,F device. Of primary importance is the fact that a higher average internal field is present in the SrS:Cu,Na,F ACTFEL device because a higher field leads to a hotter electron distribution, and hence, more efficient impact excitation of $Cu^+$. In addition, the $Q$-$F_p$ distortions that are known to be caused by space charge are present in the $Q$-$F_p$ plot of the SrS:Cu,F ACTFEL device, but disappear in the plot of the SrS:Cu,Na,F device, as expected from the $Q$-$V$ results.

The final electrical characterization technique that is employed to compare the SrS:Cu,F ACTFEL devices with and without NaF fluxing is the $Q_{max}^e$-$V_{max}$ technique. The conclusion of the $Q$-$V$ and $Q$-$F_p$ plot comparisons presented above that space charge generation is significantly reduced is also supported by the $Q_{max}^e$-$V_{max}$ comparison shown in Fig. 4.10. The primary manifestation of space charge in terms of the $Q_{max}$-$V_{max}$ transferred charge measurements is the appearance of a high-slope region of the curve just above the threshold voltage which eventually gives way to a lower slope region. As shown in Fig. 4.10, this high-slope region is apparent for the SrS:Cu,F device, but is almost nonexistent for the SrS:Cu,Na,F device. It should be noted that the below threshold $Q_{max}^{e+}$ values for the SrS:Cu,F ACTFEL device of Fig. 4.10 are slightly less than those of the SrS:Cu,Na,F device because the SrS:Cu,F device is especially prone to small burn-out spots that reduce the total device active area. As a result, with the evidence from all of these electrical characterization techniques, it can safely be concluded that the addition of NaF to a SrS:Cu,F ACTFEL device drastically reduces the amount of space charge present in the phosphor layer. In addition, it seems that this reduction in space charge is part of the reason that the SrS:Cu,Na,F ACTFEL device is much more efficient than the SrS:Cu,F device.

The determination that NaF fluxing of SrS:Cu,F leads to bright and efficient saturated green ACTFEL devices implies that other alkali metals may provide similar
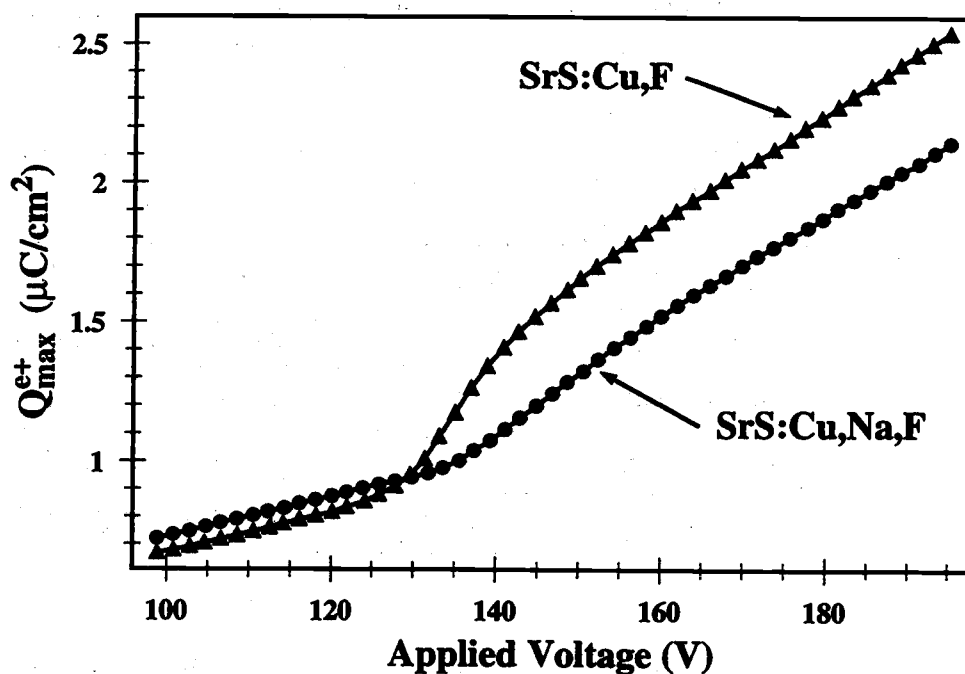
Figure 4.10: A $Q^e_{max}$-$V_{max}$ curve comparison of a SrS:Cu,F ACTFEL device with and without NaF fluxing.

results if the emission color is determined by the Cu coordination number. As a result, the fluxing of SrS:Cu,F with each of the alkali metal fluorides is undertaken to determine if a better green shifting flux than NaF exists. The luminance, efficiency, and chromaticity results from this study are shown in Table 4.2. Table 4.2 shows that chromaticity near saturated green results from fluxing all of the alkali metal fluorides into SrS:Cu,F ACTFEL phosphors, lending credence to the coordination theory of $Cu^+$ emission.

Although the fluxing of all of the alkali metal fluorides into SrS:Cu,F leads to near saturated green EL chromaticity, very different behavior amongst these samples in terms of luminance and efficiency is observed. As shown in Table 4.2, fluxing half of a SrS:Cu,F ACTFEL phosphor with LiF results in a color near saturated green, but the luminance and efficiency of the resultant ACTFEL device are both reduced from that of the blue side of the device. The drop in brightness suggests that LiF

Table 4.2: Luminance, efficiency, and CIE color coordinates of SrS:Cu,F fluxed with alkali metal fluorides (60 Hz bipolar trapezoidal drive).

| phosphor | $L_{40}$ (cd/m$^2$) | $\eta_{40}$ (lm/W) | CIE x | CIE y |
|----------|---------|----------|-------|-------|
| SrS:Cu,F | 9.57 | 0.136 | 0.164 | 0.268 |
| SrS:Cu,Li,F | 4.53 | 0.0537 | 0.293 | 0.561 |
| SrS:Cu,Na,F | 45.8 | 0.819 | 0.317 | 0.585 |
| SrS:Cu,K,F | 52.7 | 0.973 | 0.289 | 0.596 |
| SrS:Cu,Rb,F | 30.6 | 0.193 | 0.285 | 0.577 |
| SrS:Cu,Cs,F | 21.6 | 0.138 | 0.291 | 0.577 |

provides more non-radiative paths for activator relaxation, because the human eye's heightened sensitivity to green should lead to a much larger brightness of the green side of the device compared to the blue side for photopically corrected brightnesses. The spectrum of the SrS:Cu,Li,F sample is shown in Fig. 4.11 to lend insight into the processes leading to the decline in brightness and efficiency resulting from LiF fluxing. The spectrum shown in Fig. 4.11 shows that there are many competing transitions in the case of the SrS:Cu,Li,F ACTFEL phosphor. This indicates that the $Li^+$ ions are incorporating into the SrS:Cu,F phosphor differently than the $Na^+$ ions, perhaps occupying interstitial sites as a result of the small ionic radius of $Li^+$.

In addition to LiF and NaF, the larger alkali metal fluorides are also fluxed into SrS:Cu,F ACTFEL phosphors to assess their coactivation properties. Unfortunately, due to the reduced melting points of KF, RbF, and CsF, it is not possible to fabricate flux-doped half samples from these compounds because they tend to laterally diffuse across the phosphor layer during the RTA drive-in cycle. As seen in Table 4.2, KF provides the best results in terms of luminance and efficiency of any of the alkali metal fluorides. In fact, the efficiency of the KF fluxed SrS:Cu,F device is of world-record quality for a green ACTFEL phosphor. The electroluminescence spectrum of
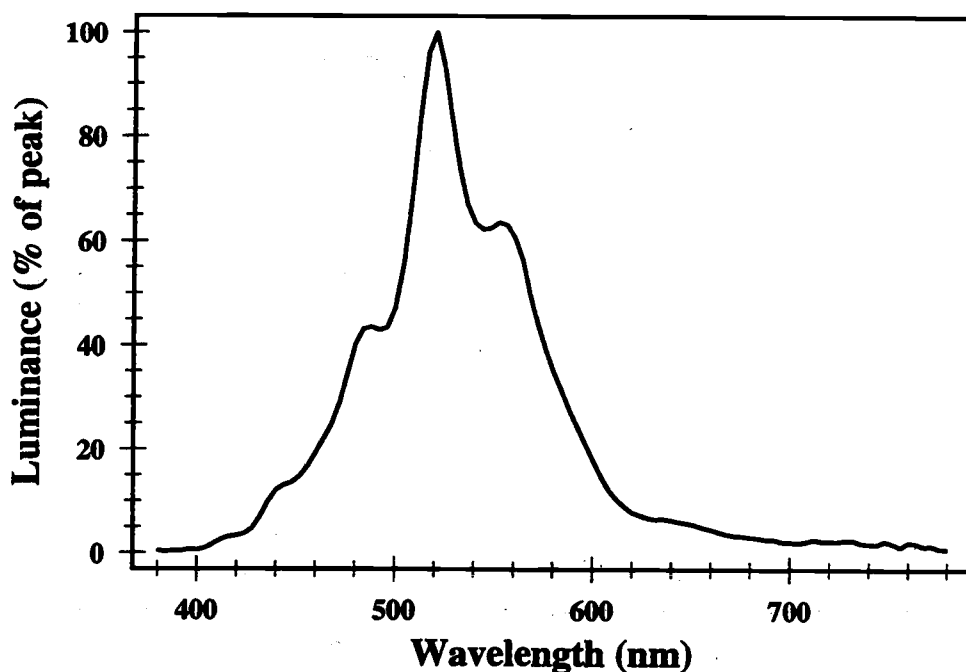
Figure 4.11: The electroluminescent spectrum of a SrS:Cu,Li,F ACTFEL device.

this sample is shown in Fig. 4.12, revealing a complete shift of the spectrum to the green. Fluxing of the alkali metal fluorides RbF and CsF into SrS:Cu,F also leads to saturated green electroluminescence, although the luminance and in particular, efficiency of these devices is reduced from the NaF- and KF-fluxed samples. That these compounds can be fluxed into SrS:Cu,F is a somewhat surprising result in view of the large ionic radii of $Rb^+$ and $Cs^+$. However, the spectra resulting from these samples shown in Figs. 4.13 and 4.14 clearly shows the existence of two competing transitions, leading to the conclusion that the incorporation of $Rb^+$ and $Cs^+$ is not nearly as complete as that of $Na^+$ and $K^+$.

Alkali metal fluoride fluxing of SrS:Cu,F reveals a dramatic green-shift of the electroluminescent spectrum from the blue to saturated green, as evidenced by the data presented above. In addition, NaF fluxing has been shown to almost completely eliminate space charge generation related effects in these devices, improving the power consumption and hence efficiency of these devices. From the spectral data presented
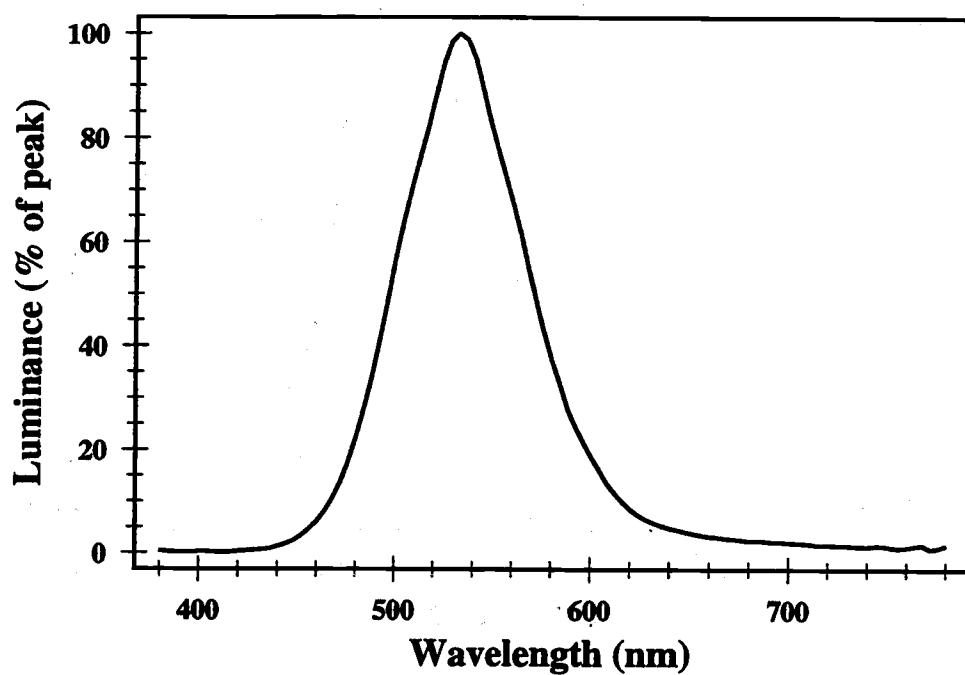
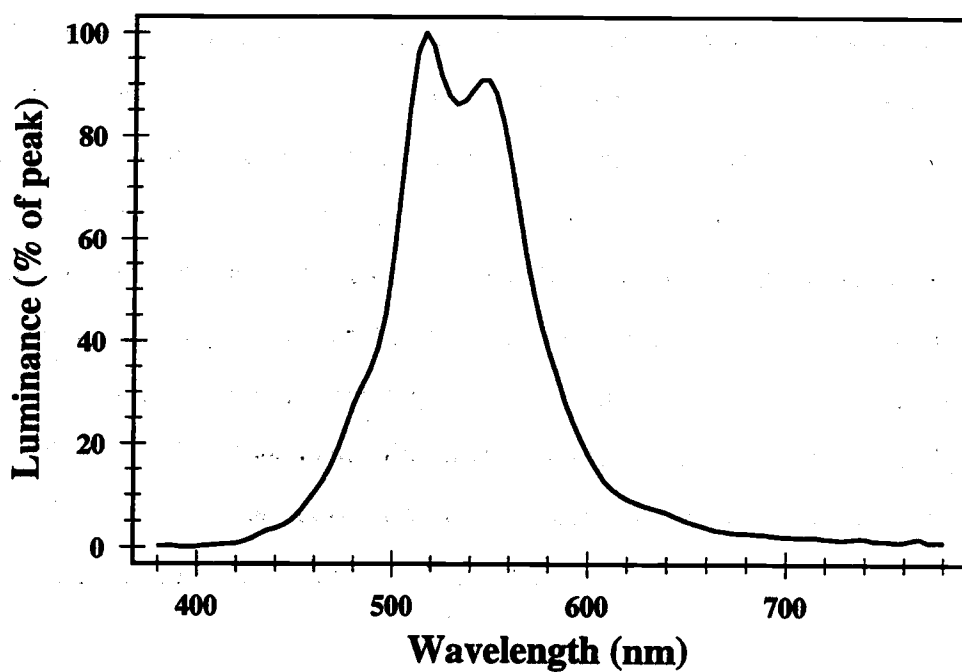Figure 4.12: The electroluminescent spectrum of a SrS:Cu,K,F ACTFEL device.



Figure 4.13: The electroluminescent spectrum of a SrS:Cu,Rb,F ACTFEL device.
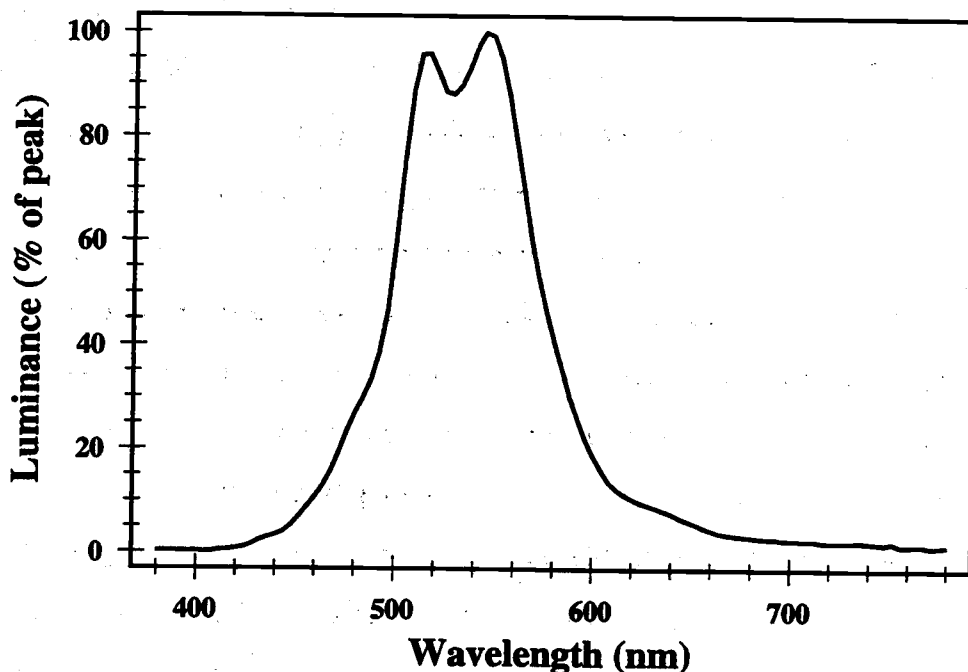
Figure 4.14: The electroluminescent spectrum of a SrS:Cu,Cs,F ACTFEL device.

above, KF appears to be the most effective flux agent for SrS:Cu,F of the alkali metal fluorides due to the essentially complete shift of the electroluminescence spectrum to the green. Unlike the other alkali metal fluoride fluxed samples, the KF fluxed sample reveals only one prominent emission peak, leading to the conclusion that the vast majority of the $Cu^+$ activators are sitting on identically coordinated sites. In addition, the NaF-fluxed SrS:Cu,F sample shows only a very minor "shoulder" to the peak emission wavelength, indicating that most of the $Cu^+$ activators are located in identically coordinated sites, but a non-negligible amount are located in a differently coordinated site. On the other hand, the electroluminescence spectra of the LiF-, RbF-, and CsF-fluxed samples shows two or more prominent peaks, indicating the presence of several differently coordinated $Cu^+$ sites.

### 4.2.3 SrS:Cu,Cl

Due to the difficulties encountered in evaporating $Cu_2S$ and $CuF_2$, $CuCl_2$ is investigated as the Cu activator source in an effort to discover a more desirable process for the multi-source EB/thermal evaporation of SrS:Cu ACTFEL phosphors. Preliminary results from the multi-source deposition of SrS:Cu,Cl suggest that $CuCl_2$ is indeed an activator source that is readily evaporable and does not significantly dissociate when heated in vacuum. These properties of $CuCl_2$ thus allow a fairly thorough investigation of the effects of the Cu concentration in SrS:Cu,Cl via EB/thermal multi-source evaporation. The investigation of SrS:Cu,Cl proceeds with a concentration study by evaporating $CuCl_2$ at increasing rates with respect to that of SrS to determine the optimum relative evaporation rate. For this study, undoped SrS pellets are evaporated at an average rate of about 40 Å/s to provide enough accuracy for the $CuCl_2$ concentration study. The undoped SrS source material is synthesized from $SrCO_3$ by sulfurization with $H_2S$, as discussed in Appendix B, and subsequently cold-pressed and sintered. The $CuCl_2$ is obtained by the kiln-drying of $CuCl_2 \cdot 2H_2O$ (Alfa Aesar, 99+%), and is thermally evaporated from a W wire heated alumina crucible. Following phosphor deposition, samples are subjected to a post-deposition RTA cycle at 810°C for 120 seconds in an Ar atmosphere. After the annealing, a 2000 Å $SiO_xN_y$ top insulator is PECVD-deposited, followed by the thermal evaporation of 1000-1500 Å Al top electrodes.

The concentration study of SrS:Cu,Cl proceeds with the deposition of five samples of varying relative $CuCl_2$ evaporation rates; 0.25%, 0.50%, 0.75%, 1.0%, and 1.25% that of the SrS. The kiln-dried $CuCl_2$ evaporates very uniformly, and does not appear to decompose under evaporation conditions as does the $CuF_2$, so this activator source is excellent for a concentration study via EB/thermal multi-source evaporation. The results of the concentration study presented in Table 4.3 exemplify the need for precise control over the activator concentration in the phosphor host in order to achieve a bright and efficient ACTFEL phosphor. The lowest concentration

Table 4.3: SrS:Cu,Cl ACTFEL device performance as a function of the relative evaporation rate of $CuCl_2$ (60 Hz bipolar trapezoidal drive).

| Relative $CuCl_2$ evaporation rate | $L_{40}$ (cd/m$^2$) | CIE x | CIE y |
|---|---|---|---|
| 0.25% | <0.5 | 0.271 | 0.257 |
| 0.50% | 9.38 | 0.155 | 0.240 |
| 0.75% | 2.91 | 0.169 | 0.202 |
| 1.00% | 2.55 | 0.169 | 0.228 |
| 1.25% | 0.99 | 0.183 | 0.267 |

sample (0.25% SrS rate) emits very little light, while the minimum increment in activator evaporation rate yields very bright, blue ACTFEL devices (0.5% SrS rate). The B-V/$\eta$-V plot and electroluminescence spectrum of this bright SrS:Cu,Cl device are shown in Figs. 4.15 and 4.16, respectively. It should be noted that the EL spectrum of SrS:Cu,Cl is measured at several angles to eliminate the possibility of optical interference causing the presence of the many emission peaks seen in Fig. 4.16. Additional $CuCl_2$ evaporation rates above 0.5% of the SrS rate, however, decrease the device brightness considerably from the optimum brightness at 0.5% of the SrS rate. The fact that should be noticed from Table 4.3 is that the chromaticity values of all of the SrS:Cu,Cl devices are blue-shifted relative to the "standard" chromaticity of SrS:Cu, CIE x=0.16, y=0.28. In fact the SrS:Cu,Cl devices with relative $CuCl_2$ evaporation rates of 0.5%, 0.75%, and 1.0% that of SrS emit a blue color as deep as many SrS:Cu,Ag devices. [157]

The deep-blue emission of these SrS:Cu,Cl ACTFEL devices indicates that Cl is causing a shift in the emission transition of the Cu$^+$ activators. If this shift is interpreted in the context of the coordination theory of Cu$^+$, [89] this implies that Cl$^-$ is incorporated into the lattice as a substitutional donor on sulfur sites within the SrS:Cu lattice. The result of the incorporation of Cl donors is that the SrS:Cu
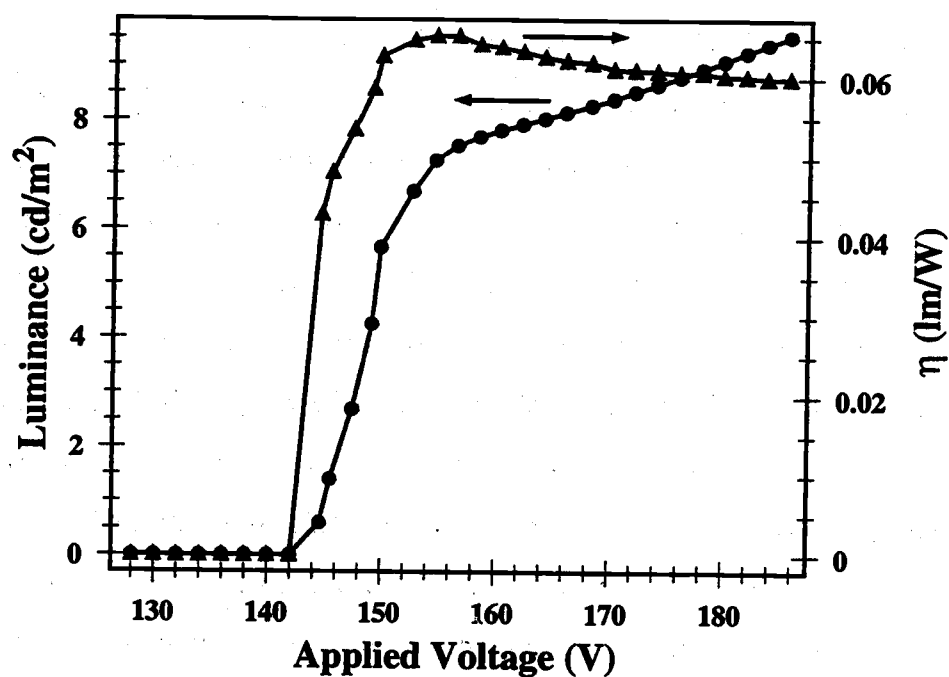
Figure 4.15: The L-V/$\eta$-V plot of a SrS:Cu,Cl ACTFEL device (60 Hz bipolar trape-
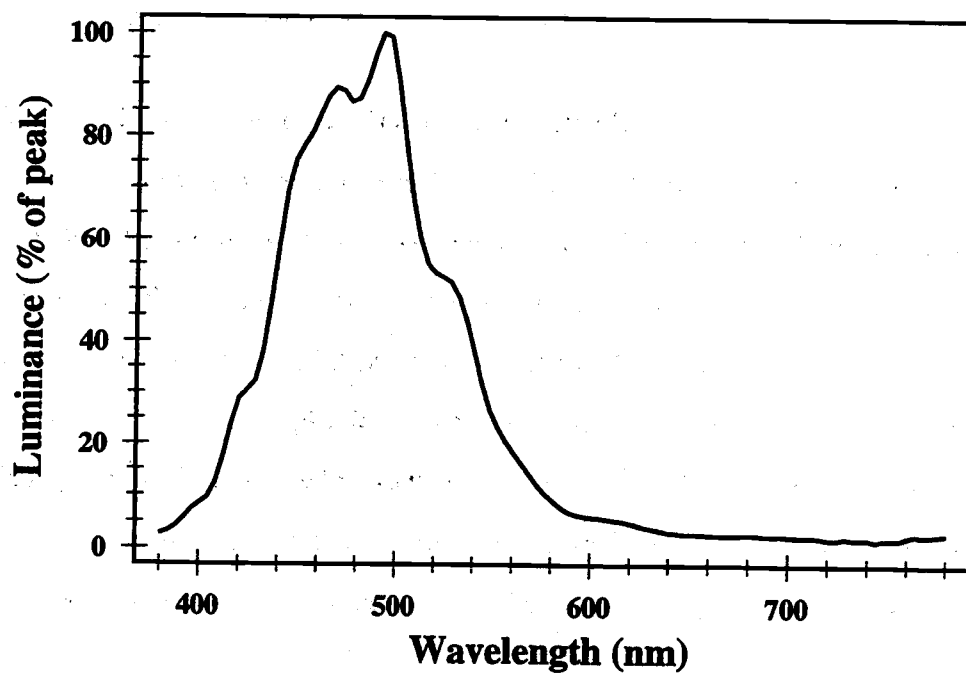zoidal drive).



Figure 4.16: The electroluminescent spectrum of a SrS:Cu,Cl ACTFEL device.

phosphor is extrinsically compensated due to the presence of the Cl donors, eliminating, or at least reducing, the process of self-compensation. The drastic reduction of S vacancies through extrinsic compensation results in the presence of few green-emitting $Cu^+$-$V_S$ complexes, and hence, the majority of the $Cu^+$ centers are either of the blue-emitting, 6-coordinated variety or $Cu^+$-$Cl^-$ complexes. The activation of SrS by $CuCl_2$ probably results in a deeper blue than activation by $CuF_2$, because the more volatile F atoms are less likely to incorporate into the film both because of the decomposition of $CuF_2$ during evaporation and the lower likelihood of a more volatile species "sticking" to a heated substrate. In addition, if F atoms are incorporated into the growing film, the insolubility of $SrF_2$ in SrS is likely to result in a phase separation of $SrF_2$ to the grain boundaries. When $CuCl_2$ is employed as the activator source, Cl is much more likely to be incorporated into the growing phosphor film, because $CuCl_2$ does not seem to readily dissociate upon heating and because $SrCl_2$ is soluble in SrS. Furthermore, the Cl atoms are much less volatile than the F atoms, and hence, are more likely to incorporate into the growing phosphor thin-film because they are certainly more condensable.

### 4.2.4   Alkali metal coactivated SrS:Cu,Cl

Due to the success of fluxing SrS:Cu,F with alkali metal fluorides and the relative stability of the SrS:Cu,Cl process, the fluxing of SrS:Cu,Cl with alkali metal fluorides is investigated. There are no fundamental modifications to the process employed for the investigation of SrS:Cu,Cl in Section 4.2.3 except an alkali metal fluoride is diffused into the samples following phosphor deposition. A relative $CuCl_2$ evaporation rate of 0.5% is selected in view of the results of Section 4.2.3. In addition, LiF and NaF half-fluxed samples are fabricated for the ability to directly compare the difference between fluxed and non-fluxed SrS:Cu,Cl under exactly the same deposition conditions.

The investigation of alkali metal coactivated SrS:Cu,Cl begins with the fabrication of two phosphor layers where one-half of each is fluxed by LiF and NaF, respectively. The LiF-fluxed sample shows only a slight change in emission spectrum under PL excitation from deep blue to blue-green, which directly correlates to the electroluminescent spectrum in this case. The shift in electroluminescent spectrum with LiF fluxing for this sample is shown in Fig. 4.17. From comparison of Figs. 4.11 and 4.17, it is seen that the LiF induces a much smaller spectral shift in the SrS:Cu,Cl phosphor than in the SrS:Cu,F phosphor for comparable concentrations of LiF. This supports the conclusion of Section 4.2.3 that Cl is incorporated as a
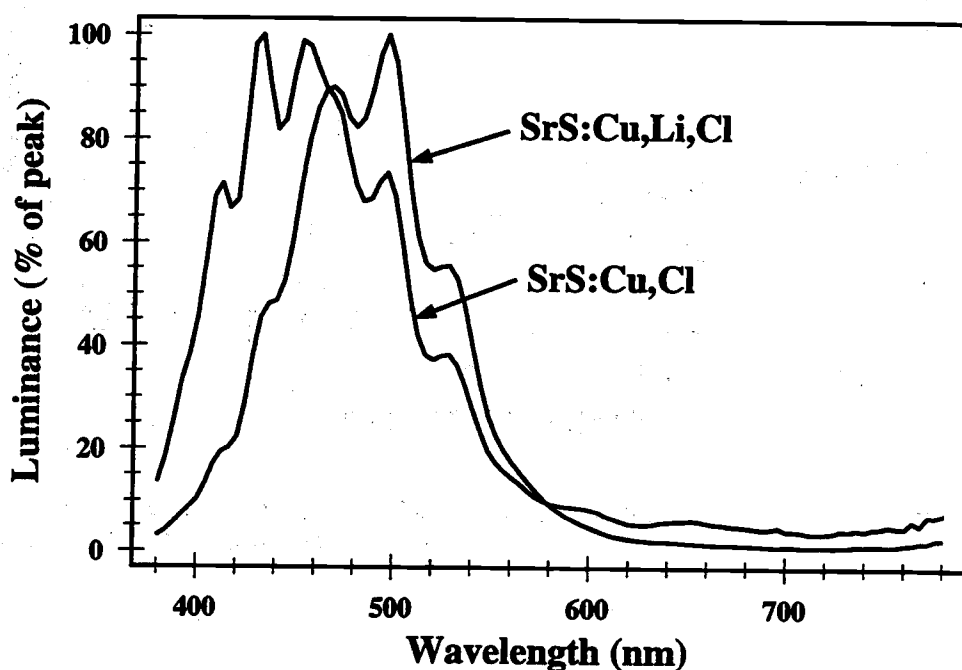


Figure 4.17: The electroluminescent spectra of a SrS:Cu,Li,Cl and a SrS:Cu,Cl ACT-FEL device from the same substrate.

substitutional donor in SrS because Li was shown to have the weakest effect on the color of SrS:Cu,F of the alkali metals, and its incorporation is not expected to result

in a drastic color-shift with donor impurities present. However, the incorporation of LiF into SrS:Cu,Cl results in an increase in luminance over the non-fluxed half of the sample in contrast to LiF incorporation into SrS:Cu,F, as shown in Fig. 4.18. This seems to be largely a result of the red-shift of the emission spectrum from deep blue to blue-green.
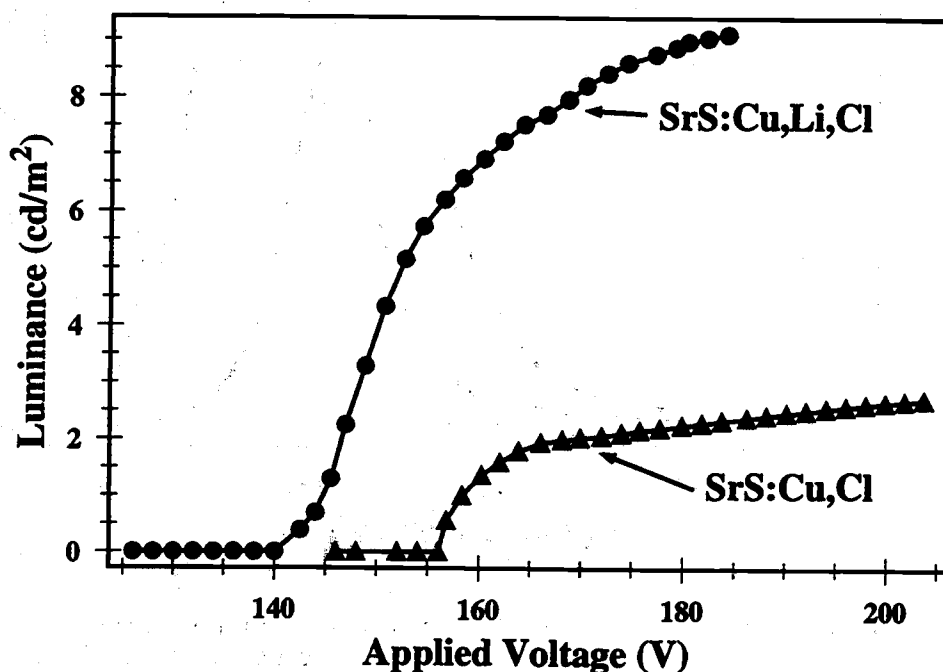


Figure 4.18: The L-V plots of a SrS:Cu,Li,Cl and a SrS:Cu,Cl ACTFEL device from the same substrate (60 Hz bipolar trapezoidal drive).

The coactivation of SrS:Cu,Cl with NaF proves to be a much more effective method of inducing green electroluminescence than LiF coactivation. The thermal evaporation of 1.5 mol% of NaF atop the freshly deposited SrS:Cu,Cl phosphor layer yields bright green PL following annealing. As expected, the NaF coactivated side of the sample that exhibits green PL also exhibits bright green electroluminescence. The EL spectral shift shown in Fig. 4.19 that is induced by the incorporation of NaF leads

to a saturated green color with CIE coordinates x=0.302, y=0.570. This SrS:Cu,Na,Cl ACTFEL device yields a $L_{40}$ and $\eta_{40}$ of 49.9 cd/m$^2$ and 0.680 lm/W, respectively, as shown in Fig. 4.20. The luminance of this SrS:Cu,Na,Cl device is greater than that
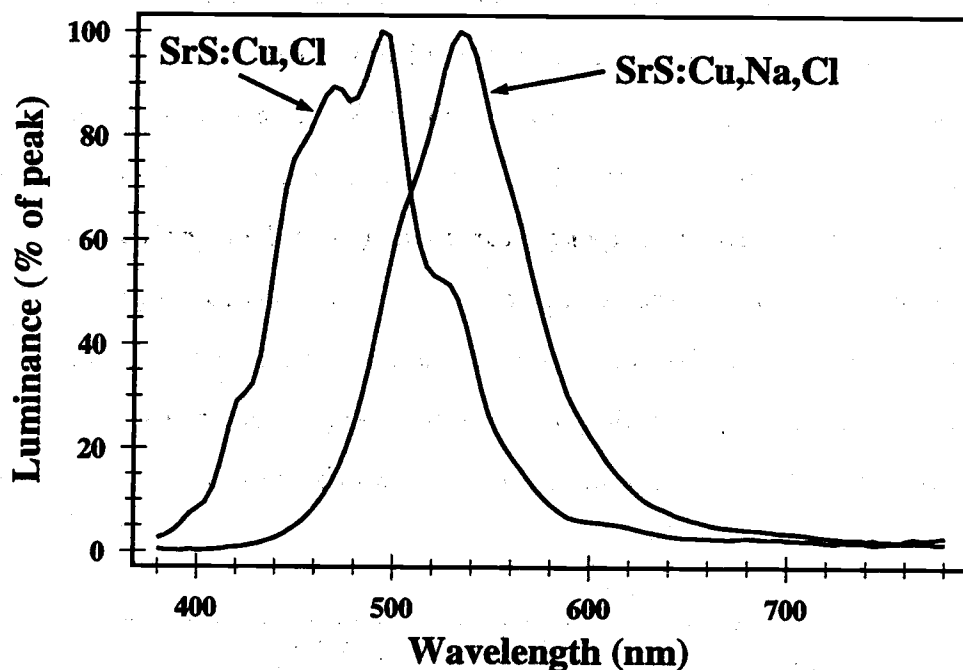


Figure 4.19: The electroluminescent spectra of a SrS:Cu,Na,Cl and a SrS:Cu,Cl ACTFEL device from the same substrate.

witnessed for the SrS:Cu,Na,F device reported in Section 4.2.2, although this device is approximately 20% less efficient. The reasons behind this increase in luminance with a corresponding decrease in efficiency are two-fold; less charge is transferred in the SrS:Cu,Na,F device due to a thicker SiO$_x$N$_y$ top insulator, and the presence of capacitance overshoot in the SrS:Cu,Na,Cl ACTFEL device reduces efficiency. The fact that capacitance overshoot is not completely eliminated for SrS:Cu,Na,Cl, but is effectively eliminated for SrS:Cu,Na,F indicates that Cl is responsible for space

charge related effects when incorporated into SrS:Cu. It is unclear, however, whether the space charge related effects are a result of Cl donors or complexes containing Cl.

The heavier alkali metals, K, Rb, and Cs, are also investigated as green-shifting coactivators for SrS:Cu,Cl by the flux doping of KF, RbF, and CsF. In attempting to fabricate a green SrS:Cu,K,Cl ACTFEL device, it is found that a larger concentration of KF is required to achieve the desired color shift to green. However, once the necessary relative thickness of KF to deposit atop the SrS:Cu,Cl phosphor layer is determined, a significant green color shift of the film PL is witnessed. This larger relative amount of KF required for a green-emitting phosphor is presumably a consequence of Cl entering the SrS:Cu lattice as a donor, as discussed earlier. In addition, EL results indicate a bright, efficient, saturated green ACTFEL device results from this technique, as seen in the L-V/$\eta$-V and spectral plots of Figs. 4.21 and 4.22, respectively. The results from fabrication of SrS:Cu,Rb,Cl and SrS:Cu,Cs,Cl are

Figure 4.20: The L-V/$\eta$-V plot of a SrS:Cu,Na,Cl ACTFEL device (60 Hz bipolar trapezoidal drive).

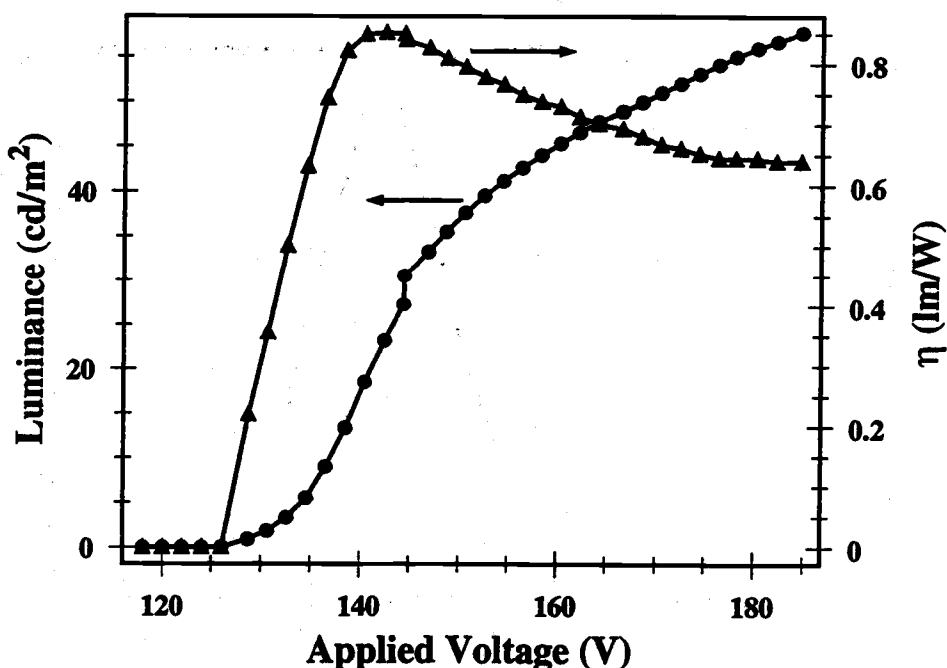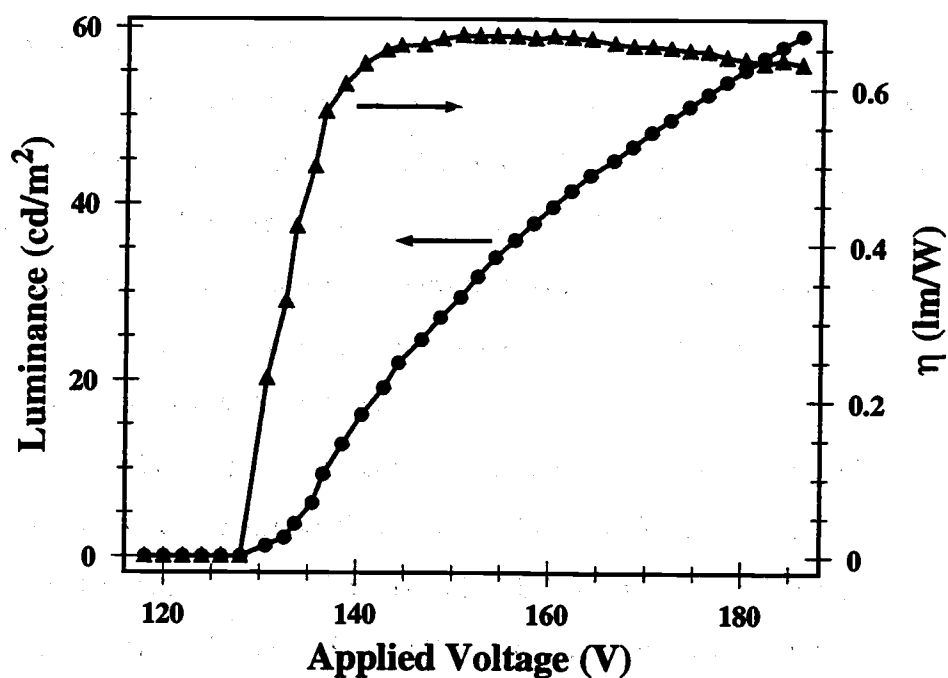Figure 4.21: The L-V/$\eta$-V plot of a SrS:Cu,K,Cl ACTFEL device (60 Hz bipolar trapezoidal drive).
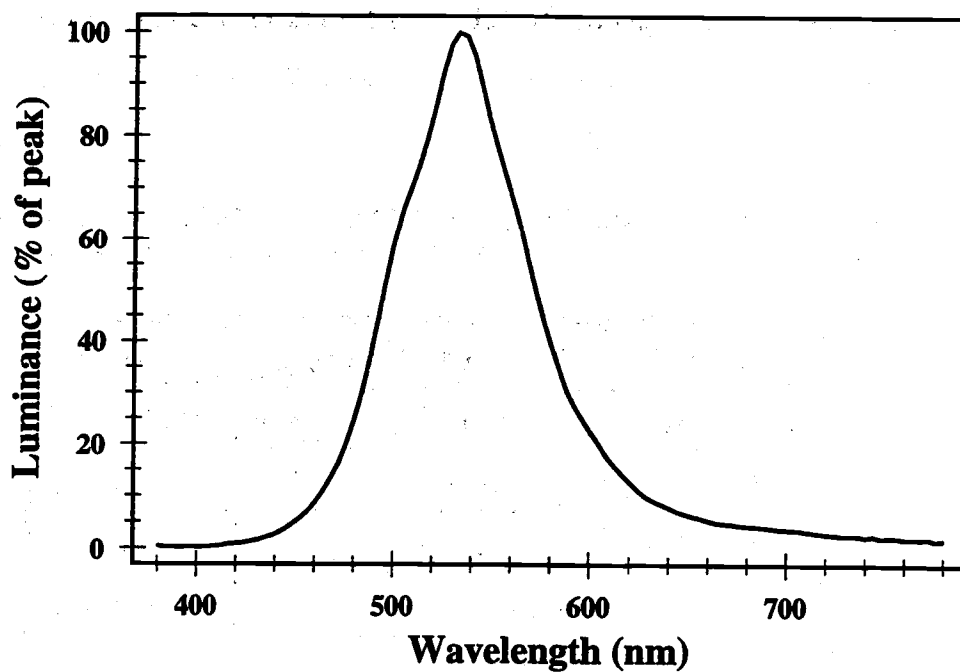


Figure 4.22: The electroluminescent spectra of a SrS:Cu,K,Cl ACTFEL device.

not as encouraging, however. These devices never completely shift to green, and the amount of RbF and CsF required to shift these devices at all leads to severe device instabilities such that these devices typically burn-out at applied voltages less than the threshold voltage. Since the results of Section 4.2.2 suggest that Rb and Cs are incorporating into SrS:Cu,F via flux doping with RbF and CsF, and the results of this section suggest that Rb and Cs are only slightly incorporated into SrS:Cu,Cl, it seems that the concentration of atomic diffusion aiding vacancies present in SrS:Cu,F must be much larger than that of SrS:Cu,Cl.

In terms of producing bright, efficient, saturated green ACTFEL phosphors, the results of this section indicate that coactivation of SrS:Cu,Cl with Na or K is quite effective. However, the fact that the color-shifting of SrS:Cu,Cl is much more difficult than the color-shifting of SrS:Cu,F implies the presence of an appreciable concentration of donor impurities. These donor impurities must be either Cl or Cl-related complexes because the only significant difference between the phosphors for the studies presented in Section 4.2.2 and this section is the replacement of F with Cl. A summary of the results generated for the flux doping of alkali metal fluorides into SrS:Cu,Cl is presented in Table 4.4.

Table 4.4: Luminance, efficiency, and CIE color coordinates of SrS:Cu,Cl fluxed with alkali metal fluorides (60 Hz bipolar trapezoidal drive).

| phosphor | $L_{40}$ (cd/m$^2$) | $\eta_{40}$ (lm/W) | CIE x | CIE y |
|---|---|---|---|---|
| SrS:Cu,Li,Cl | 9.04 | 0.070 | 0.159 | 0.258 |
| SrS:Cu,Na,Cl | 49.9 | 0.680 | 0.302 | 0.570 |
| SrS:Cu,K,Cl | 48.1 | 0.654 | 0.317 | 0.578 |
| SrS:Cu,Rb,Cl | Unstable | | | |
| SrS:Cu,Cs,Cl | Unstable | | | |

### 4.2.5 SrS:Cu

For the preliminary investigation of SrS:Cu, $Cu_2S$ is thermally evaporated concomitant with the EB evaporation of undoped SrS pellets. Again, the SrS starting material is synthesized via the sulfurization of $SrCO_3$, and formed into pellets by the cold-press and sinter technique. The activator source is 99.5% pure $Cu_2S$ powder purchased from Cerac, Inc. that is thermally evaporated from an alumina crucible heated by a W wire heater.

Although the evaporation of $Cu_2S$ as the activator source is at first glance the optimal technique for achieving stoichiometric, contamination-free ACTFEL phosphors, there are two issues that complicate matters somewhat. First, $Cu_2S$ tends to dissociate when heated in vacuum, preferentially releasing S. As a result, the activator evaporant melt is constantly changing in composition, and hence, constantly changing in evaporation temperature, with the limit being the evaporation temperature of pure Cu. This results in difficulties in accurately controlling the evaporation rate of the $Cu_2S$ during the deposition, and hence, accurately controlling the final Cu concentration in the phosphor film. In addition to the problems with control of the evaporation rate of $Cu_2S$ during the evaporation, the high currents required to evaporate $Cu_2S$ lead to problems with the evaporation crucibles. At these high currents, Cu from the $Cu_2S$ melt tends to diffuse through the $Al_2O_3$ crucibles, thereby reducing their structural integrity, and perhaps contaminating the growing film with Al and O.

The inconsistencies with coevaporation of SrS and $Cu_2S$ described above necessitate the implementation of alternate processing techniques for repeatable, high-quality SrS:Cu thin-film phosphors. The first method attempted to overcome these difficulties is the EB evaporation of $Cu_2S$ doped SrS pellets. However, the results of this study suggest that much of the Cu is evaporated from the pellets during the sintering cycle. In fact, there seems to be a maximum $Cu^+$ concentration in the sintered pellets because the ACTFEL device characteristics change very little for pre-sintering

Cu concentrations above 1.7 at%. As a result, doped pellets are probably not useful
as a means for achieving high-quality, repeatable SrS:Cu thin-film phosphors.
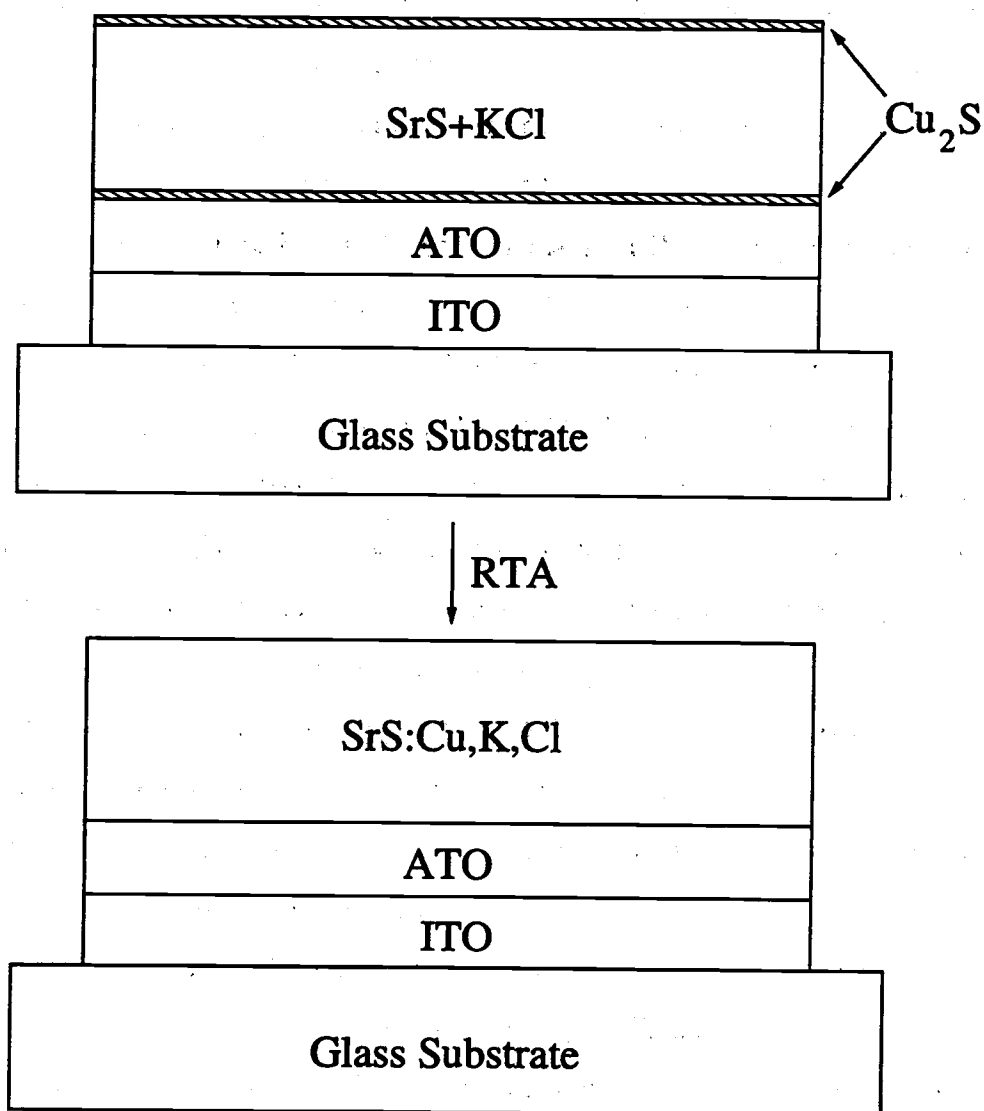


Figure 4.23: Depiction of the "phosphor sandwich" technique for activator incorporation in an ACTFEL phosphor.

The second technique to overcome these difficulties that is investigated is the
"phosphor sandwich" technique in which Cu is thermally diffused into undoped SrS

films, as illustrated in Fig. 4.23. The processing steps for implementation of this technique with $Cu_2S$ begin with the deposition of a thin-film of $Cu_2S$ by thermal evaporation. This layer is typically very thin because the final concentration of $Cu^+$ in the phosphor thin-film is to be on the order of 0.2 at%. Next, an undoped SrS pellet is EB evaporated concomitant with a charge of KCl flux that is thermally coevaporated. The KCl flux is found to greatly enhance the quality of the phosphor thin-film in terms of device stability, and is thus coevaporated with the SrS for all of the SrS:Cu samples deposited by this technique. Then, a cap layer of $Cu_2S$ is deposited atop the KCl fluxed SrS layer to approximately the same thickness as the initial $Cu_2S$ layer to ensure device uniformity. Finally, the $Cu_2S$/SrS:K,Cl/$Cu_2S$ film is removed from the evaporator and rapid thermal annealed at 810°C in an Ar atmosphere to drive the Cu into the SrS. This technique is much more accurate in achieving activator concentration levels than trying to match evaporation rates of the SrS and the $Cu_2S$ because the measure of film thickness is a much more reliable quantity than deposition rate as measured by the quartz crystal monitor due to the inherent noise associated with differentiation. In addition, the $Cu_2S$ can be evaporated at an extremely low rate, preserving the integrity of the alumina evaporation crucible and minimizing Al and O contamination. Therefore, this technique is employed for the deposition of the SrS:Cu thin-films required for this study.

A group of samples with varying relative thicknesses of the constituent SrS and $Cu_2S$ layers are fabricated to determine the viability of diffusing Cu activators into SrS. Six samples are fabricated, with $Cu_2S$ thicknesses 0.06%, 0.13%, 0.25%, 0.50%, 0.75%, and 1.0% that of the SrS layer, as measured by the quartz crystal thickness monitor. The final thickness of all of these phosphor layers was 5000Å±200Å as measured by a mechanical profilometer. All samples exhibit blue PL and EL that green-shifts in accordance with the relative thickness of the $Cu_2S$ films. The EL spectra of the five samples with the lowest relative $Cu_2S$ concentrations are shown in Fig. 4.24 (the spectrum of the 1.0% $Cu_2S$ relative thickness sample is not shown

because the high $Cu^+$ concentration leads to sample instability). It is seen in Fig. 4.24 that the spectrum of the sample with the lowest relative $Cu_2S$ thickness is dominated by short-wavelength light, whereas the addition of increasing relative thicknesses of $Cu_2S$ shifts the spectrum to longer wavelengths. However, once a relative $Cu_2S$ thickness of 0.50% is reached, the spectral shift approximately saturates.
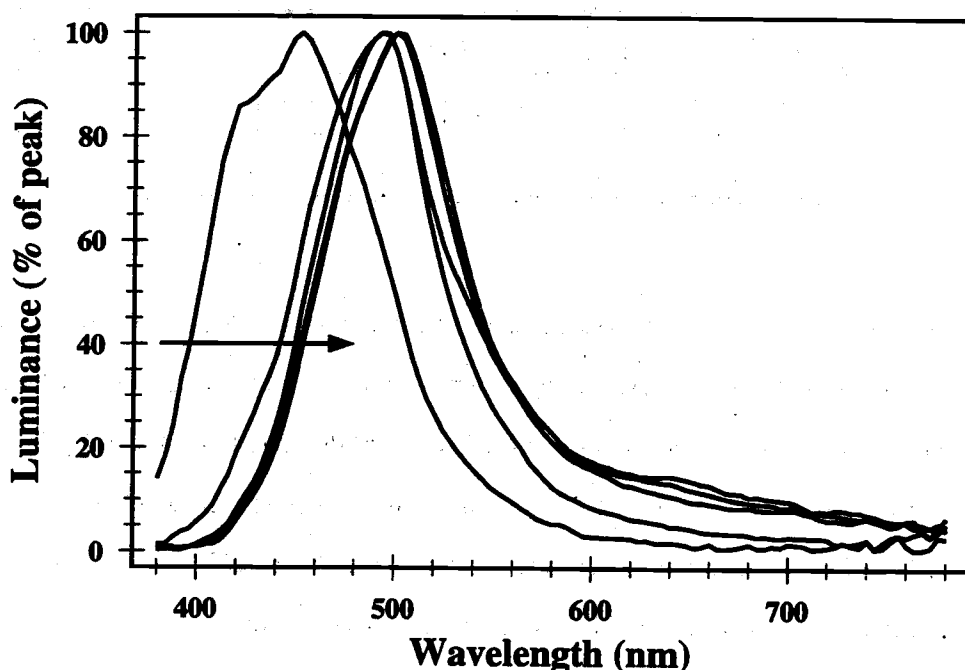


Figure 4.24: Electroluminescence spectra of SrS:Cu,K,Cl ACTFEL devices fabricated with the "phosphor sandwich" technique (arrow indicates increasing $Cu_2S$ relative thickness).

The brightness, efficiency, and CIE coordinates of these devices are shown in Table 4.5 to reveal the effect of $Cu_2S$ concentration on these important device output parameters. A monotonic increase in all of these parameters is witnessed, except for the 0.25% $Cu_2S$ sample which was slightly dimmer than the 0.13% $Cu_2S$ sample, although the small magnitude of this difference suggests experimental error as the cause. Previous research on the SrS:Cu ACTFEL phosphor has identified 0.2-0.3 at%

Table 4.5: SrS:Cu,K,Cl ACTFEL device performance as a function of relative $Cu_2S$ thickness for devices fabricated with the "phosphor sandwich" technique (60 Hz bipolar trapezoidal drive).

| thickness (% $Cu_2S$) | $L_{40}$ (cd/m$^2$) | $\eta_{40}$ (lm/W) | CIE x | CIE y |
|---|---|---|---|---|
| 0.06 | 0.689 | 0.00532 | 0.159 | 0.132 |
| 0.13 | 4.23 | 0.078 | 0.179 | 0.277 |
| 0.25 | 4.16 | 0.087 | 0.213 | 0.332 |
| 0.50 | 7.13 | 0.144 | 0.210 | 0.342 |
| 0.75 | 8.36 | 0.184 | 0.220 | 0.365 |
| 1.0 | Unstable | | | |

as the optimum range of $Cu^+$ concentrations in the phosphor film. The CIE coordinates of ACTFEL phosphors with this optimum Cu concentration are approximately x=0.16, y=0.28, indicating that a relative $Cu_2S$ thickness of about 0.13% is near the optimum range for ACTFEL phosphors fabricated in this manner. The other interesting point to note from Table 4.5 is the CIE coordinates, x=0.159, y=0.132, for the 0.06% relative $Cu_2S$ thickness device. This set of CIE coordinates is very near saturated blue, and until this result, it was thought that a blue color this rich in short-wavelength light could only be achieved with a SrS:Cu phosphor by Ag coactivation. Since no Ag is added to this sample, this result contradicts previous published research suggesting that Ag is the emitting center leading to deep blue emission from SrS:Cu,Ag via an energy transfer up-conversion process. [157, 158, 159] This suggests that deep-blue emission with a peak wavelength 450 nm or below can be achieved from isolated $Cu^+$ centers in a SrS phosphor host. This leads to the conclusion that Ag acts as a co-activator that aids in isolating the $Cu^+$ centers, perhaps by scavenging sulfur vacancies.

The final point that needs to be addressed regarding SrS:Cu deposited in this manner is the enigmatic role of the KCl flux in film growth. To gain insight in the role of KCl in film growth, a SrS film is grown on a substrate with a portion of its area shadowed from the KCl source, but with the entire area open to the SrS source. Post-deposition film thickness measurements reveals that the film in the area shadowed from the KCl had grown approximately 33% thicker than the KCl-fluxed area. In addition, the KCl-fluxed portion of the film is clear and uniform in appearance, whereas the non-fluxed portion is hazy. However, the most significant difference in these areas of this sample appears after rapid thermal annealing. The KCl-fluxed portion of the film shows bright bluish PL, and has a milky appearance characteristic of a recrystallized film. On the other hand, the non-fluxed portion of the film has little PL and does not appear to recrystallize significantly during the RTA cycle. In addition, it is found that alkali metal fluoride fluxing after phosphor deposition does not lead to a color shift to green, as it does for the previously investigated variants of SrS:Cu. This all points to the scenario that the KCl flux is arriving at the heated substrate and reacting with the SrS, probably in an exchange reaction such as

$$SrS + 2KCl \xrightarrow{heat} SrCl_2 + K_2S. \qquad (4.1)$$
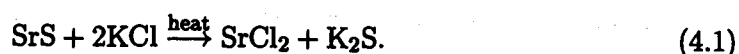
Upon reacting, the highly volatile $K_2S$ is probably reevaporated, whereas the less volatile $SrCl_2$ remains in the growing phosphor film. Therefore, the films grown in this section are apparently more correctly termed SrS:Cu,Cl than SrS:Cu.

### 4.2.6  Alkali metal coactivated SrS:Cu

It is known that the emission spectrum of SrS:Cu phosphors varies considerably with the concentration of $Cu^+$ in the host lattice. In particular, it has been recognized that a transition yielding a peak in the green region of the visible spectrum becomes active at $Cu^+$ concentrations above about 0.4 at% in SrS:Cu ACTFEL phosphors. This shift in emission spectrum was initially attributed to aggregated $Cu^+$ ions, where it was hypothesized that $Cu^+$ ions complex at higher concentrations, and

thereby emit at higher wavelengths. However, researchers have recently developed and tested a new coordination theory to explain the observed green shift in SrS:Cu with increasing $Cu^+$ concentration. [89] According to this theory, increasing $Cu^+$ concentration induces an increasing sulfur vacancy concentration as a result of self-compensation. When the $Cu^+$ concentration reaches a certain level, the $Cu^+$ ions are likely to be complexed with one of these sulfur vacancies, and hence, exist as green-emitting, 5-coordinated $Cu^+$. However, when donor coactivators are added, extrinsic compensation is achieved, relatively few sulfur vacancies are present, and the $Cu^+$ ions are mostly 6-coordinated, leading to blue light emission. This theory was verified in SrS:Cu powder phosphors through the addition of $Na_2S$ to create additional sulfur vacancies and red-shift the standard emission spectrum of SrS:Cu. After the spectrum of this powder phosphor was shifted to the green by the addition of $Na_2S$, Y donors were added to shift the emission spectrum back to the blue. This section employs the results of this groundbreaking work in powder phosphors to attempt to generate bright and efficient green SrS:Cu phosphors by alkali metal coactivation.

The fabrication of ACTFEL devices for a study of alkali metal coactivation first involves the deposition of a SrS:Cu phosphor by the "phosphor sandwich" technique described in Section 4.2.5, except that no KCl flux is employed. Then, the alkali metal fluoride flux is thermally evaporated atop the freshly deposited phosphor, as described in Section 4.2.2. After the phosphor is annealed, a 2000 Å $SiO_xN_y$ top insulator is PECVD-deposited atop the phosphor layer. Finally, 1000-1500 Å thick Al top electrodes are thermally evaporated to complete the ACTFEL structure.

The goal of this alkali metal coactivation study has a different focus than those presented in Sections 4.2.2 and 4.2.4 in that this section aims to find an optimum Cu concentration for the shifting of SrS:Cu to green. This is made possible by the heightened control available from phosphor deposition via the "phosphor sandwich" technique. Furthermore, the most effective green-shifting coactivators for coactivator flux doping have been identified in Sections 4.2.2 and 4.2.4 to be Na and K, so it is not

necessary for any more than a cursory investigation of Li, Rb, and Cs coactivation. The experiment that is performed in this section is the deposition of a sequence of SrS:Cu phosphor layers of different relative thicknesses of $Cu_2S$ to achieve different Cu concentrations. For each of these samples, a fixed 1.5 mol% layer of NaF is deposited over the entire sample and subsequently driven into the phosphor along with the $Cu_2S$ at an RTA temperature of 810°C in an Ar atmosphere. The performance of these devices is monitored by measuring the standard optoelectronic ACTFEL device characteristics of interest, luminance, efficiency, and CIE coordinates.

The implementation of this experiment involves deposition of SrS:Cu,Na ACTFEL devices by the "phosphor sandwich" technique with various relative $Cu_2S$ thicknesses. In addition, a fixed relative thickness of NaF (1.5%) is deposited atop the "phosphor sandwich" prior to the RTA cycle. The initiation of this experiment involves beginning with a very small relative $Cu_2S$ thickness such that the final Cu concentration in the SrS:Cu,Na thin-film is well below what is thought to be the optimum Cu concentration for SrS:Cu ACTFEL devices. Then, the relative $Cu_2S$ concentration is steadily increased for subsequent samples until the device luminance begins decreasing with concentration. Finally, additional samples are fabricated with relative $Cu_2S$ thicknesses near that yielding the peak luminance to attempt to find an optimum relative $Cu_2S$ thickness. The experiment is initiated with the deposition of a SrS:Cu,Na device with a relative $Cu_2S$ concentration 0.15% that of the SrS, as measured by the thickness monitor. Following this, the relative $Cu_2S$ thickness is increased 0.15% for each successive deposition until the measured luminance begins decreasing.

The results of this study of alkali metal coactivation of SrS:Cu are quite encouraging, perhaps even more so than those from the alkali metal coactivation of SrS:Cu,F and SrS:Cu,Cl. In fact, the luminance of the 0.3% relative $Cu_2S$ thickness device is the highest of any device fabricated for this thesis at 65.5 cd/m$^2$. A L-V/$\eta$-V plot of this device is shown in Fig. 4.25. Other $Cu_2S$ concentrations yield high-luminance

ACTFEL devices, but the optimal relative $Cu_2S$ thickness appears to be very close to 0.3% for Na-coactivated SrS:Cu. The results of this $Cu^+$ concentration study are shown in Table 4.6. Upon identification of this optimal relative $Cu_2S$ thickness, ACT-FEL device are fluxed doped with the fluorides of other alkali metal to determine if they incorporate as well as in SrS:Cu,F, or as poorly as in SrS:Cu,Cl. The results from this coactivator study are presented in Table 4.7. These results essentially reiterate what is determined from the previous studies of alkali metal coactivation presented in Sections 4.2.2 and 4.2.4, except that K performs poorly in this case. Perhaps, the optimum $Cu^+$ concentration for coactivation by K is different than the optimal concentration for Na coactivation.
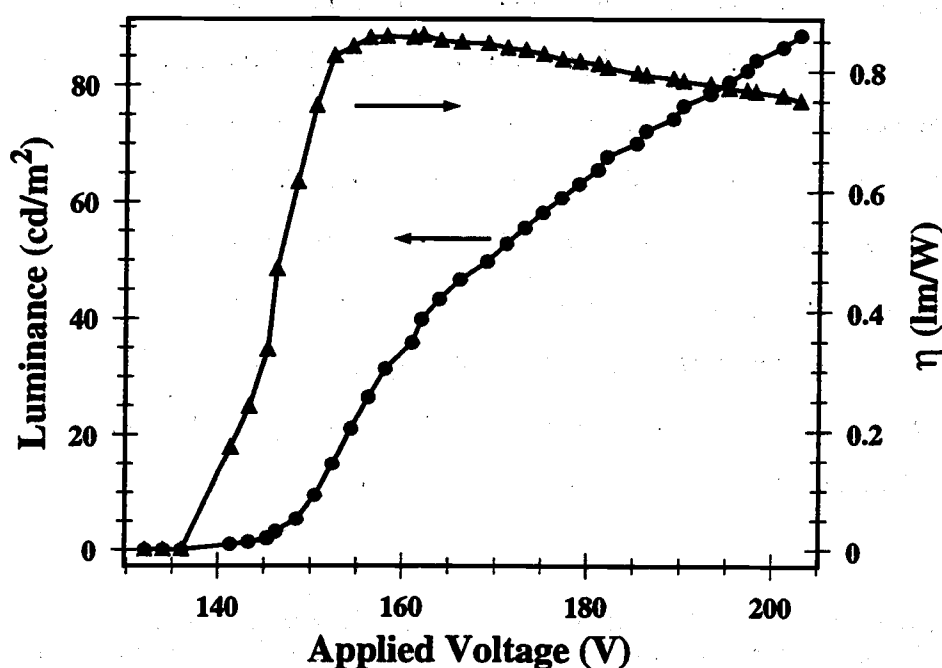


Figure 4.25: The L-V/$\eta$-V plot of a SrS:Cu,Na ACTFEL device deposited by the "phosphor sandwich" technique" with 0.31% relative $Cu_2S$ thickness (60 Hz bipolar trapezoidal drive).

Table 4.6: Luminance, efficiency, and CIE color coordinates of SrS:Cu,Na as a function of relative $Cu_2S$ thickness (60 Hz bipolar trapezoidal drive).

| thk (% $Cu_2S$) | $V_{th}(V)$ | $t_{phos}$ (Å) | $L_{40}$ (cd/m$^2$) | $\eta_{40}$ (lm/W) | CIE x | CIE y |
|---|---|---|---|---|---|---|
| 0.15 | 158 | 11000 | 24.5 | 0.215 | 0.285 | 0.603 |
| 0.23 | 151 | 11000 | 53.0 | 0.558 | 0.321 | 0.590 |
| 0.31 | 141 | 11000 | 66.5 | 0.812 | 0.333 | 0.580 |
| 0.39 | 157 | 11000 | 52.6 | 0.515 | 0.315 | 0.593 |
| 0.46 | 156 | 10500 | 41.4 | 0.407 | 0.317 | 0.595 |

### 4.2.7 Conclusions

In conclusion, it can certainly be said that bright, efficient, saturated green ACTFEL devices can be fabricated by coactivation of SrS:Cu with alkali metals. In fact, the major limitation of the alkali metal coactivated SrS:Cu processes described in this section appears to be the top insulator process. Development of a BTO top insulator of 3000 Å thickness should yield brightness improvements for all of the devices reported on in this section of either 48% or 94% depending on whether a 2000 Å or 3000Å $SiO_xN_y$ is used for the top insulator. This is because an insulator process with a high-dielectric constant insulator allows much better coupling of the applied voltage and the phosphor field, and hence much greater charge transfer [160].

Table 4.7: Luminance, efficiency, and CIE color coordinates of SrS:Cu (0.31% relative $Cu_2S$ thickness) fluxed by LiF, NaF, KF, and RbF (60 Hz bipolar trapezoidal drive).

| Flux | $V_{th}(V)$ | $t_{phos}$ (Å) | $L_{40}$ (cd/m$^2$) | $\eta_{40}$ (lm/W) | CIE x | CIE y |
|---|---|---|---|---|---|---|
| LiF | 146 | 11000 | 9.07 | 0.066 | 0.183 | 0.305 |
| NaF | 151 | 11000 | 66.5 | 0.812 | 0.333 | 0.580 |
| KF | 157 | 10800 | 14.7 | 0.144 | 0.288 | 0.601 |
| RbF | 147 | 10000 | 6.49 | 0.059 | 0.250 | 0.478 |

Applying these percentage improvements to the alkali metal doped SrS:Cu ACTFEL devices deposited for this section results in luminances in the neighborhood of world-record green. This leads to the conclusion that alkali metal coactivated SrS:Cu should overtake ZnS:Tb as the brightest known green-emitting ACTFEL phosphor in the very near future if improvements in this ACTFEL phosphor continue to be made. In addition, the investigation of blue-emitting SrS:Cu has revealed some insights into its operation and a likely misinterpretation of the emission mechanism of SrS:Cu,Ag in the literature.

## 4.3  BaS:Cu

The successful color-shifting of SrS:Cu from deep-blue to saturated green reported in Section 4.2, implies that it may be possible to color shift orange BaS:Cu to either saturated green, saturated red, or both. This section is concerned with the coactivation of BaS:Cu with various coactivators that are known to affect the color spectrum of SrS:Cu to test whether similar color shifts can be observed with the BaS:Cu phosphor system. This section begins with a discussion of results from BaS:Cu ACTFEL devices without any coactivators, because this is not a well-studied ACTFEL phosphor. The subsequent sections are devoted to the coactivation of BaS:Cu with Cl, Ag, and K in an attempt to induce a shift in the EL emission spectrum.

### 4.3.1  BaS:Cu

The investigation of BaS as a potential ACTFEL phosphor has been very limited compared to the other alkaline earth sulfide phosphors, SrS and CaS. This lack of interest is perhaps due to the fact that the alkaline earth-sulfide phosphors of the smaller cations tend to be much more efficient cathodoluminescent (CL) and PL phosphors. Researchers have presumably suspected that this reduced efficiency translates directly to EL phosphors, and hence, have mostly ignored BaS for this application. However, BaS has a much lower melting point than the other alkaline earth sulfide

phosphors, making it a very interesting material for EL phosphor applications because of the possibility of low temperature recrystallization. Therefore, this section is devoted to the investigation of orange-emitting BaS:Cu ACTFEL devices.

The investigation of BaS:Cu proceeds with the fabrication of several samples for a control to compare coactivated samples to. The fabrication of BaS:Cu is accomplished via both EB/thermal coevaporation and the "phosphor sandwich" technique described in Section 4.2.5. The phosphors are deposited to a thickness of approximately 8000 Å in all cases, with a substrate temperature of 250°C. Post-deposition annealing is performed via rapid thermal annealing in an Ar atmosphere at a temperature of 750°C for 2 minutes. Higher RTA temperatures for post-deposition annealing lead to poor quality films because of excessive grain growth. This excessive grain growth leads to jagged edges on the surface of the film which provide localized high-field regions that result in devices that burn out easily. This effect is presumably due to the lower melting temperature of BaS compared to the other alkaline earth sulfide phosphors. A standard 2000 Å $SiO_xN_y$ insulator layer is PECVD deposited atop all BaS:Cu samples.

The deposition of BaS:Cu ACTFEL phosphors leads to relatively bright and efficient ACTFEL devices with very little optimization. However, the emission color of BaS:Cu is orange, with CIE color coordinates similar to those of ZnS:Mn, thereby rendering investigation of pure BaS:Cu an academic exercise due to the relatively enormous luminance and efficiency of the ZnS:Mn ACTFEL phosphor. An EL spectrum of a BaS:Cu ACTFEL device is shown in Fig. 4.26. The spectrum shown in Fig. 4.26 reveals two closely spaced luminescent transitions centered around 600 nm that are of similar intensity. This seems to correspond to a rigid shift of the SrS:Cu emission spectrum that shows two emission peaks around 500 nm. Similar to SrS:Cu, the relative intensities of these peaks can be controlled by the activator doping level in the BaS:Cu phosphor. An ACTFEL device is fabricated with the "phosphor sandwich" technique with very thin $Cu_2S$ layers at the top and bottom of the phosphor
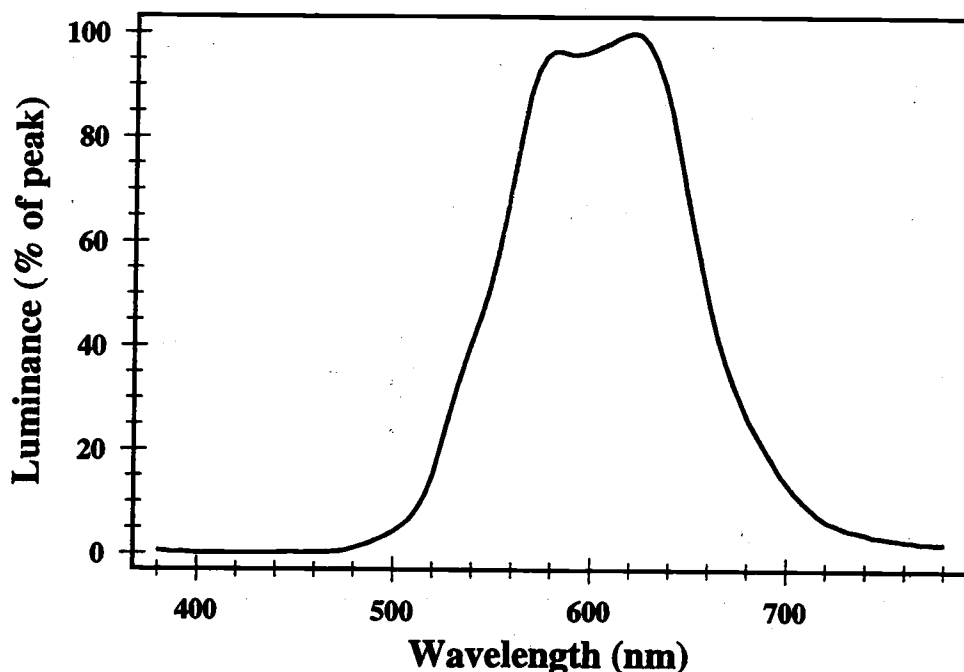
Figure 4.26: The electroluminescent spectrum of a BaS:Cu ACTFEL device.

in an attempt to select the transition centered at 584 nm as the dominant transition. The results from this device are shown in Fig. 4.27. However, this shift in the emission spectrum may be more of a result of the use of a KCl flux during the growth of the BaS layer, as discussed in Section 4.2.5.

Although BaS:Cu will never be as bright and efficient as ZnS:Mn, relatively bright and efficient samples can be fabricated with very little effort paid to optimization. In fact, a respectable 60 Hz $L_{40}$ and $\eta_{40}$ of 15 cd/m$^2$ and 0.22 lm/W is achieved after deposition of only several samples. The L-V/$\eta$-V plot of this BaS:Cu ACTFEL device is shown in Fig. 4.28. Further optimization in terms of activator doping levels and film thickness could probably yield generous improvements in terms of brightness and efficiency, although the twenty-fold improvement in $L_{40}$ necessary to compete with ZnS:Mn is unlikely.

Electrical measurements of BaS:Cu were performed in order to gather information regarding the operation of BaS as an ACTFEL phosphor and compare it to the
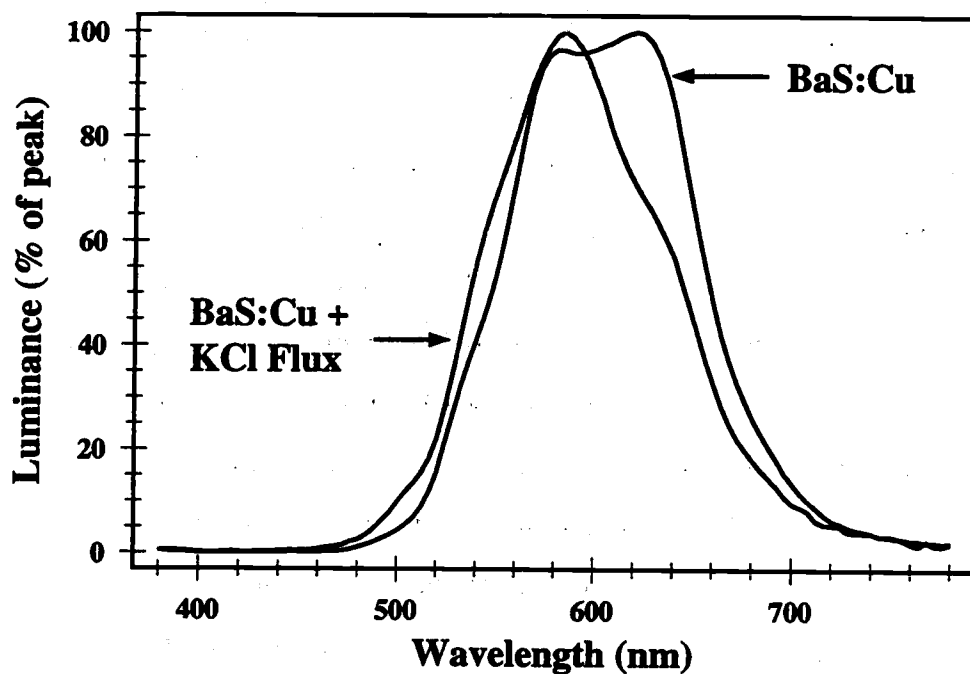
Figure 4.27: The electroluminescent spectrum of a BaS:Cu ACTFEL device deposited with a KCl flux.
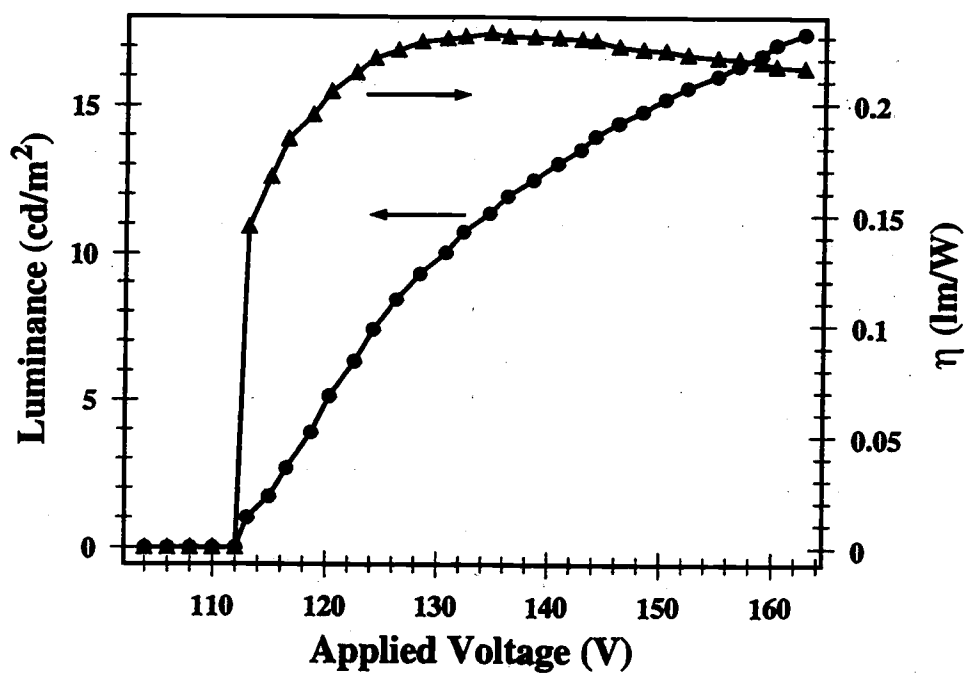


Figure 4.28: A L-V/$\eta$-V plot of a BaS:Cu ACTFEL device (60 Hz bipolar trapezoidal drive).

operation of other better studied phosphors. The electrical measurement of the most interest for comparing ACTFEL device operation across different phosphor materials is probably the Q-$F_p$ measurement because it yields a good deal of information regarding internal phosphor operation if the phosphor thickness is accurately known. Since these BaS:Cu devices are fabricated in-house, the phosphor thickness is known, allowing electrical characterization via the Q-$F_p$ technique with a reasonable degree of certainty. A family of Q-$F_p$ plots of a BaS:Cu ACTFEL with an 8000 Å thick phosphor layer are shown in Fig. 4.29. These plots reveal that BaS:Cu seems to perform in a very similar manner to SrS:Cu devices in terms of both phosphor field and charge transfer. In addition, this family of Q-$F_p$ plots reveal the existence of dynamic space charge effects as evidenced by the non-constant field profile during the $\overline{BC}$ and $\overline{GH}$ portions of the waveform.
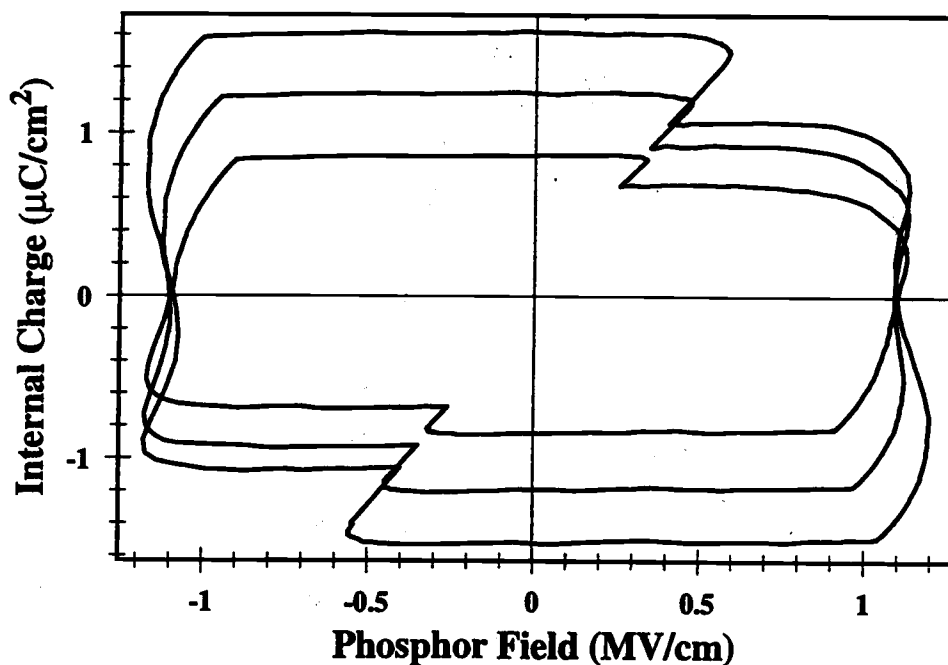


Figure 4.29: A family of Q-$F_p$ curves taken at voltages of $V_{th}$ + 20 V, $V_{th}$ + 40 V, and $V_{th}$ + 60 V, of a BaS:Cu device (1 kHz bipolar trapezoidal drive).

### 4.3.2   BaS:Cu,Cl

The use of CuCl$_2$ as the dopant source for SrS:Cu ACTFEL devices showed a distinct blue-shift of the emission spectrum with respect to that of SrS:Cu reported in the literature. Therefore, CuCl$_2$ is investigated as an activator source in an attempt to shift the emission color of BaS:Cu to green. Several ACTFEL devices are fabricated by EB/thermal coevaporation of BaS and CuCl$_2$, respectively. However, the incorporation of Cl into BaS:Cu phosphor films appears to lead to a shift of the emission spectrum towards, but not to the green, as seen in Fig. 4.30. In fact, the emission spectrum of BaS:Cu,Cl shown in Fig. 4.30 is quite similar to that of BaS:Cu deposited with a KCl flux shown in Fig. 4.27. This adds further weight to the assertion that KCl coevaporation during phosphor deposition preferentially incorporates Cl into the active areas of the phosphor film.
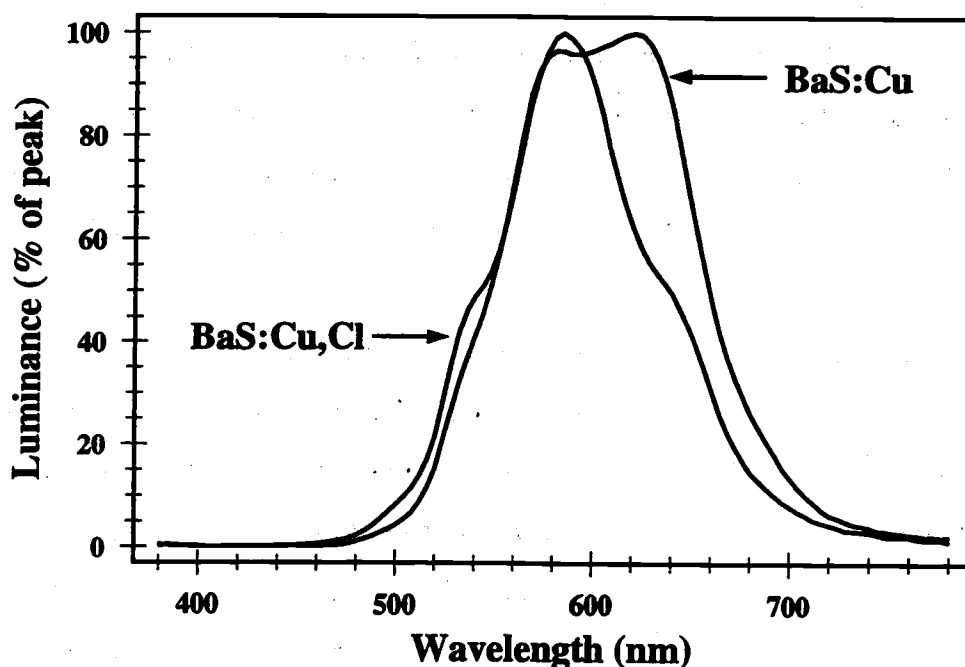


Figure 4.30: The electroluminescent spectrum of a BaS:Cu,Cl ACTFEL device.

### 4.3.3 BaS:Cu,Ag

Another technique that was recently discovered to significantly blue-shift the emission spectrum of SrS:Cu is Ag codoping. The effect of Ag codoping of SrS:Cu produces a dramatic blue-shift of the spectrum from CIE color coordinates of x=0.16, y=0.28 for SrS:Cu to x=0.15, y=0.13 for SrS:Cu,Ag. If a similar spectral shift could be obtained for BaS:Cu, there is a possibility that saturated green emission could be achieved from BaS:Cu,Ag. As a result, BaS:Cu,Ag is investigated as a potential green-emitting phosphor.

The investigation of BaS:Cu,Ag is initiated with the fabrication of several ACT-FEL devices doped with varying levels of Ag. First, EB/thermal coevaporation of BaS, $CuCl_2$, and AgCl is performed to deposit BaS:Cu,Ag phosphor layers. However, the simultaneous control of two thermal sources and an EB source is quite prone to error due to drift in evaporation rates over time and cross-talk between sources. Therefore, only two devices were fabricated by this technique because of its poor repeatability, the poor stability of devices deposited as such, and the limited amount of BaS source material available. Although control of the evaporation is challenging, one of the BaS:Cu,Ag,Cl devices contains a portion of the film that exhibits greenish PL under a Hg discharge lamp, leading to continuation of this effort in a more controlled manner.

The difficulties of simultaneous coevaporation of three sources is overcome by employment of the "phosphor sandwich" technique to repeatably deposit BaS:Cu,Ag. The deposition of BaS:Cu,Ag is achieved by capping an undoped BaS layer on the top and bottom by symmetrical $Cu_2S$ layers that total 1% of the thickness of the BaS layer as measured by the quartz crystal thickness monitor. Following this deposition, $AgF_2$ is deposited over one-half of the substrate area to varying thicknesses and then rapid thermal annealed at 750°C for 120 seconds in an Ar atmosphere in an effort to diffuse the Cu and Ag dopants into the BaS. Three samples are fabricated with $AgF_2$ thicknesses 0.5%, 1.5%, and 3.0% that of the BaS phosphor layer. The

ACTFEL devices with lower $AgF_2$ flux layer thicknesses both show a small degree of spectral shift for both PL and EL, but not significant enough to shift the emission color to green. However, the ACTFEL device with a 3.0% relative thickness of $AgF_2$ exhibits noticeably green PL on the half of the substrate flux-doped with Ag. The EL spectrum of this device reveals a dominant wavelength of 556 nm, as seen in Fig. 4.31, but the existence of a number of higher wavelength transitions results in a color that significantly deviates from saturated green. Furthermore, the luminance and efficiency of the Ag fluxed half of the substrate are reduced by more than ten times from that of the non-Ag fluxed half. As a result, it is not expected that BaS:Cu,Ag will result in saturated green emission of sufficient luminance to achieve a marketable product.
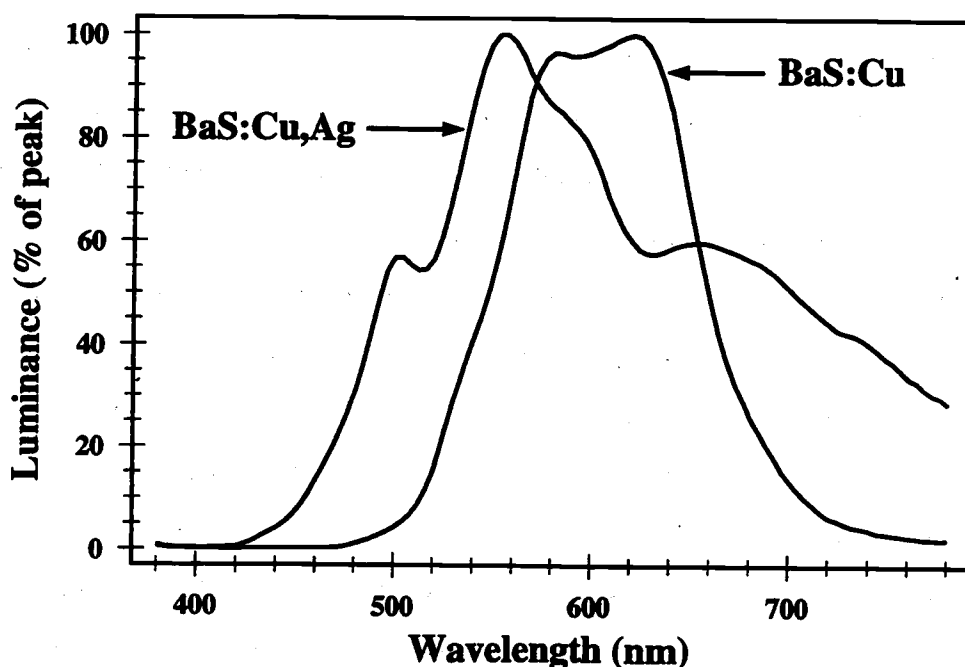


Figure 4.31: The electroluminescent spectrum of a BaS:Cu,Ag ACTFEL device.

### 4.3.4 BaS:Cu,K

In Lehmann's paper on Cu, Ag, and Au activated alkaline earth sulfide phosphors, he notes that K is the most effective coactivator he had discovered for red-shifting the emission spectrum of BaS:Cu PL and CL phosphors. [161] As a result, K coactivation is investigated as a means of red-shifting the emission spectrum of BaS:Cu as close to saturated red as possible. The investigation of BaS:Cu,K is carried out via "phosphor sandwich" deposition of BaS:Cu, with the addition of a thermally evaporated fluxing overlayer of KF over half of the substrate area. The activator and coactivator species are subsequently diffused into the undoped BaS during the RTA cycle.

The coactivation of BaS:Cu by K definitely leads to a marked red-shift of the spectrum of BaS:Cu as evidenced by both the PL and EL emission spectra of the BaS:Cu,K phosphor films. The EL emission spectrum of BaS:Cu,K is shown in Fig. 4.32 along with the baseline BaS:Cu spectrum. The spectra shown in Fig. 4.32 shows a definite red-shift of the spectrum, with the peak wavelength moving to approximately 640 nm. The resultant color spectrum of BaS:Cu,K has CIE coordinates of $x=0.570$, $y=0.424$, which lie in the orange region of the color spectrum due to the non-negligible side peaks occurring at 540 and 580 nm. However, these peaks may be able to be eliminated by optimizing the relative doping levels of Cu and K in the BaS phosphor. This should probably first be verified in powders due to the accurate control of activator and coactivator levels achievable in powder phosphor processing.

The luminance and efficiency results of the BaS:Cu,K ACTFEL phosphor are encouraging, although not to the degree that those of alkali metal activated SrS:Cu are. There is a noticeable drop in the brightness and efficiency of BaS:Cu,K from that of BaS:Cu, but this is in large part attributable to the shift of the emission spectrum to a region to which the eye is less sensitive. However, reasonably bright and efficient BaS:Cu,K ACTFEL devices can be fabricated with little optimization work, as evidenced by the B-V/$\eta$-V plots shown in Fig. 4.33. This device yields a
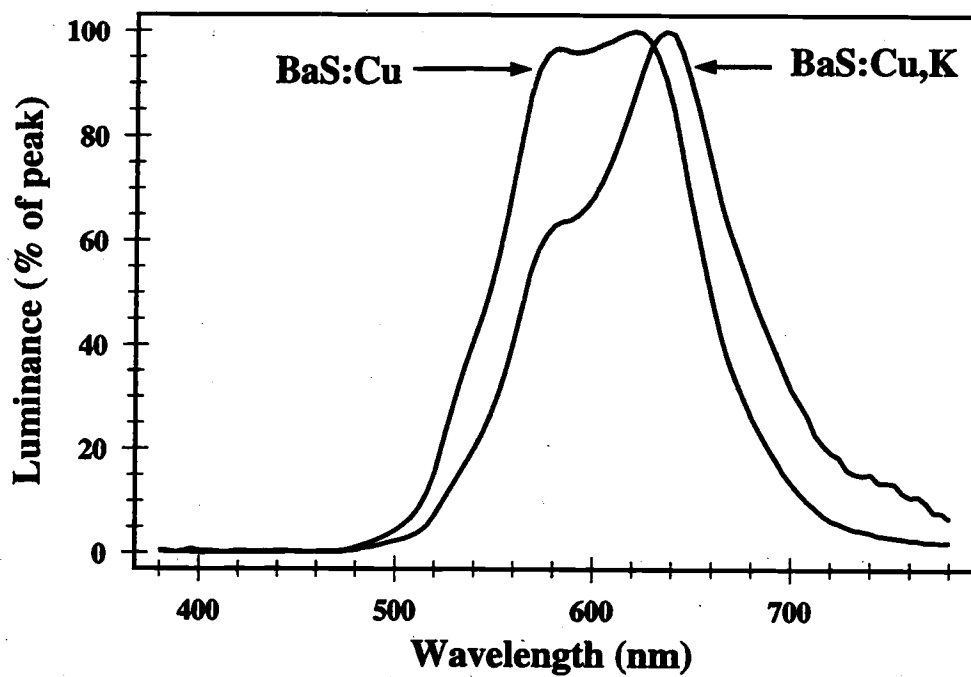
Figure 4.32: The electroluminescent spectrum of a BaS:Cu,K ACTFEL device.
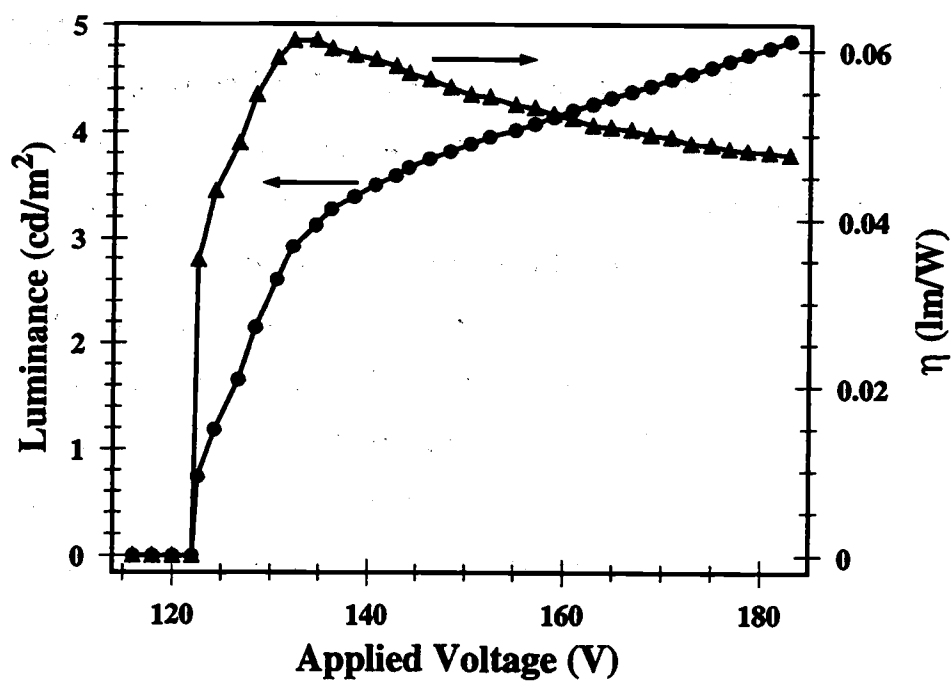


Figure 4.33: A L-V/$\eta$-V plot of a BaS:Cu,K ACTFEL device.

60 Hz $L_{40}$ and $\eta_{40}$ of 4.26 cd/m$^2$ and 0.052 lm/W, respectively, at CIE coordinates of x=0.570, y=0.424. This is certainly far from the Planar primary color phosphor targets shown in Table 2.2, but encouraging for the initial results from a new ACTFEL phosphor.

### 4.3.5  Conclusions

The most promising of the BaS:Cu phosphor derivatives appears to be the BaS:Cu,K phosphor due to its ability to generate a respectable amount of light in the red region of the spectrum. This phosphor deserves to be investigated more closely in an effort to optimize it for brightness and red light emission. Studies of the effects of Cu and K concentrations are certainly in order to determine the concentrations of Cu and K that lead to the best brightness and the highest degree of red light emission. If problems persist with shorter wavelength emission sidebands, an alloy with BaSe may shift the emission spectrum further to the red.

## 4.4  (Sr,Ba)S:Cu ACTFEL phosphors

The emission spectra of SrS:Cu and BaS:Cu is a natural system for color control by alloying because of the chemical similarity between Sr and Ba and the wide range of wavelengths spanned by their emission spectra. The purpose of this section is to provide insight into the feasibility of producing bright and efficient phosphors of a user-specified color via alloying of SrS:Cu and BaS:Cu. The investigation of this technique is carried out via the EBE of $Sr_{0.9}Ba_{0.1}S$ pellets synthesized, pressed and sintered by Ben Clark of the OSU Chemistry Department. The composition of the alloy is selected to be 90 mol% SrS to coincide with the optimum alloy composition in terms of PL brightness of (Sr,Ba)S:Cu,Na powder phosphors.

### 4.4.1 (Sr,Ba)S:Cu,Cl

The first step in the investigation of (Sr,Ba)S:Cu involves the deposition of thin-films of this alloy activated with $CuCl_2$ to determine the potential for this phosphor without alkali metal coactivation. All of the samples for this study are fabricated via EB/thermal coevaporation of $Sr_{0.9}Ba_{0.1}S$ and $CuCl_2$, respectively. The $Sr_{0.9}Ba_{0.1}S$ pellet is typically EB evaporated at a rate of approximately 40 Å/s while the $CuCl_2$ source is thermally evaporated at rates between 0.1 and 0.5 Å/s. The substrate temperature is kept at 250°C, and all samples are post-deposition rapid thermal annealed in an Ar atmosphere for 2 minutes at a temperature of 810°C. Following the RTA cycle, a top insulator of $SiO_xN_y$ is PECVD deposited to a thickness of 2000 Å, with the subsequent thermal evaporation of Al electrodes.

The deposition of (Sr,Ba)S:Cu,Cl in this manner yields ACTFEL devices with spectra intermediate between that of SrS:Cu,Cl and BaS:Cu,Cl, as anticipated. The fabrication of a number of ACTFEL devices yields a maximum 60 Hz luminance and efficiency of 11.5 cd/m$^2$ and 0.167 lm/W for a relative $CuCl_2$ evaporation rate 0.75% that of the $Sr_{0.9}Ba_{0.1}S$, as seen in Fig. 4.34. The CIE coordinates for this sample are x=0.327, y=0.517, which are representative of all of the deposited samples, although there is a certain degree of spectral shift with increasing Cu concentration. A spectrum of this (Sr,Ba)S:Cu,Cl sample is shown in Fig. 4.35.

### 4.4.2 (Sr,Ba)S:Cu,Na

The marginal performance of (Sr,Ba)S:Cu,Cl warrants an investigation of the effects of alkali metal coactivation on the characteristics of (Sr,Ba)S:Cu. The impressive performance gains witnessed in SrS:Cu coactivated by alkali metals indicates that a similar improvement may be achievable in an alloy of SrS:Cu and BaS:Cu. Therefore, the aim of this section is the investigation of (Sr,Ba)S:Cu coactivated with Na. The devices for this study are fabricated by the "phosphor sandwich" technique with $Cu_2S$ as the activator source. The Na coactivator is flux doped into the (Sr,Ba)S:Cu
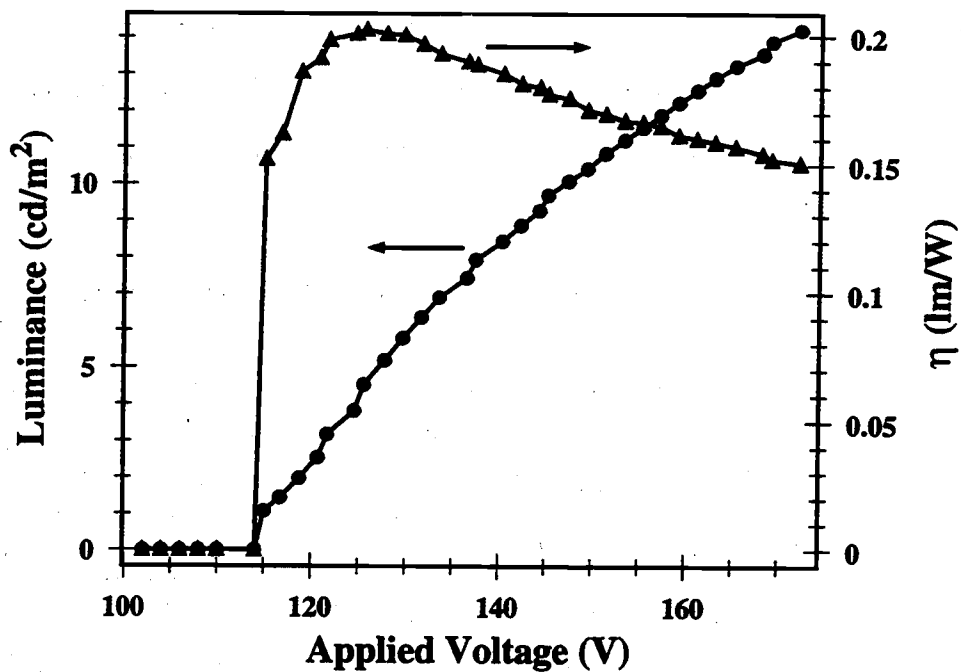
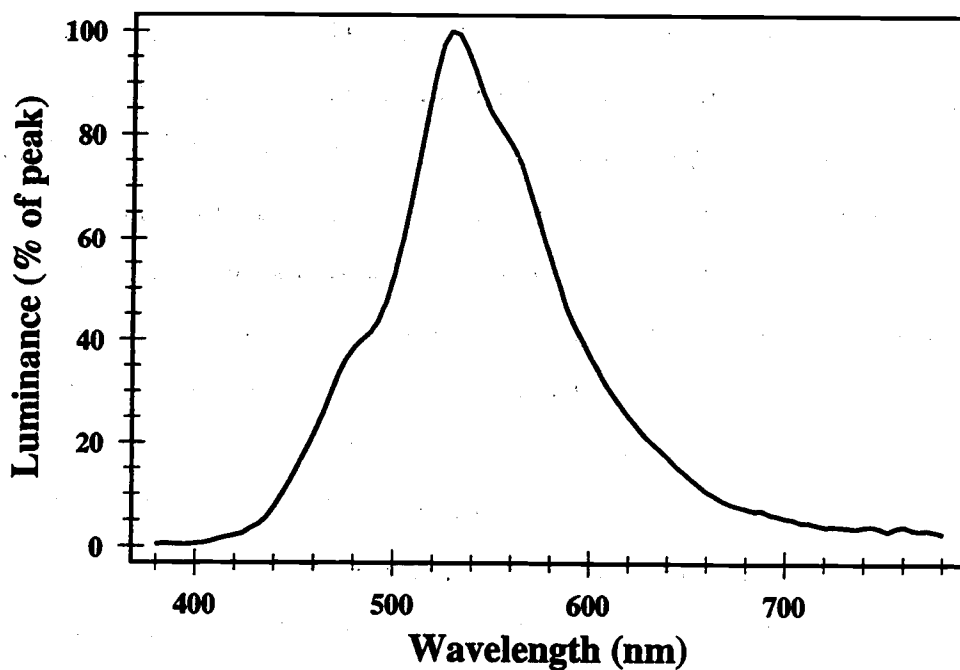Figure 4.34: A L-V/$\eta$-V of a (Sr,Ba)S:Cu,Cl ACTFEL device.



Figure 4.35: The electroluminescent spectrum of a (Sr,Ba)S:Cu,Cl ACTFEL device.

with NaF of thickness 1.5% that of the (Sr,Ba)S:Cu phosphor layer and subsequent rapid thermal annealed at 810°C for 120 seconds in an Ar atmosphere. Following flux doping of the coactivator, a $SiO_xN_y$ top insulator is PECVD-deposited to a thickness of 2000 Å, with subsequent thermal evaporation of Al electrodes.

Table 4.8: (Sr,Ba)S:Cu,Na ACTFEL device performance as a function of $Cu_2S$ relative thickness.

| thickness ($\% \ Cu_2S$) | $t_{phosphor}$ (Å) | $V_{th}$ (V) | $L_{40}$ ($cd/m^2$) | $\eta_{40}$ (lm/W) | CIE x | y |
|---|---|---|---|---|---|---|
| 0.30 | 9500 | 176 | 49.7 | 0.626 | 0.400 | 0.554 |
| 0.45 | 10500 | 180 | 53.1 | 0.592 | 0.395 | 0.560 |
| 0.60 | 11000 | 166 | 43.5 | 0.525 | 0.383 | 0.563 |

A Cu concentration study is performed by varying the relative thicknesses of the $Cu_2S$ layers at the phosphor-insulator interfaces in order to best utilize the limited amount of source material. Three devices are fabricated with total relative $Cu_2S$ thicknesses 0.30%, 0.45%, and 0.60% that of the (Sr,Ba)S phosphor layer as measured by a quartz crystal oscillator at a fixed setting. Similar to the results presented in Section 4.2 regarding alkali metal coactivation of SrS:Cu, the flux doping of NaF into (Sr,Ba)S:Cu results in impressive performance increases. The relevant characteristics of these devices are listed in Table 4.8. The data from Table 4.8 shows that the optimum relative thickness of $Cu_2S$ lies below 0.60%, but it is unclear whether the 0.3% or 0.45% $Cu_2S$ relative thickness device is better due to a ~10% difference in phosphor thickness between these two samples. Regardless, all of these samples yield very bright and efficient ACTFEL devices of a yellow-green color. The L-V/$\eta$-V plot and spectrum of the 0.45% $Cu_2S$ relative thickness ACTFEL device are shown in Figs. 4.36 and 4.37, respectively. The spectrum shown in Fig. 4.37 reveals a peak emission
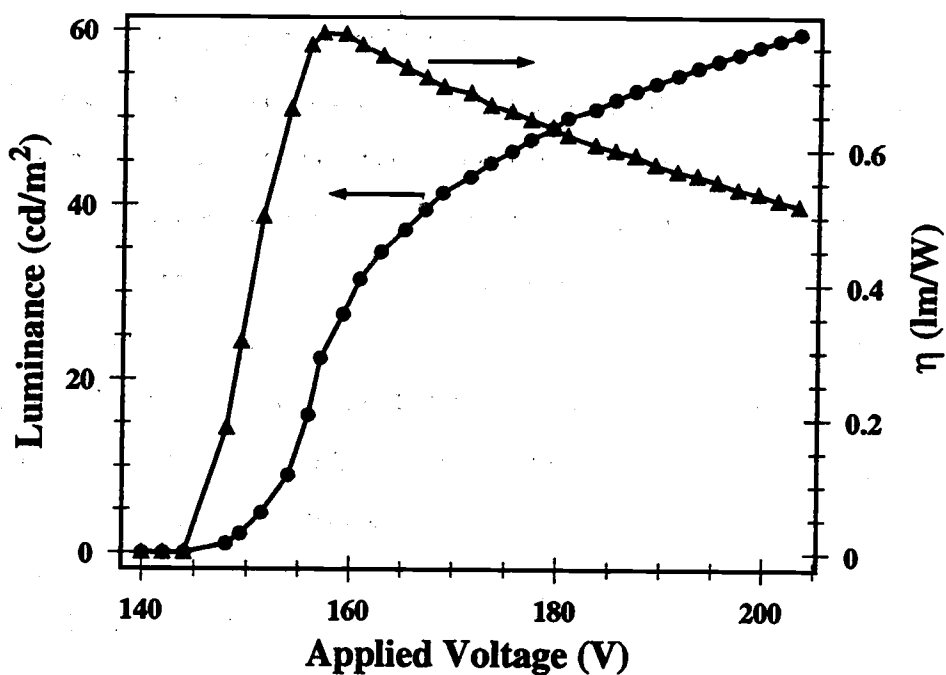
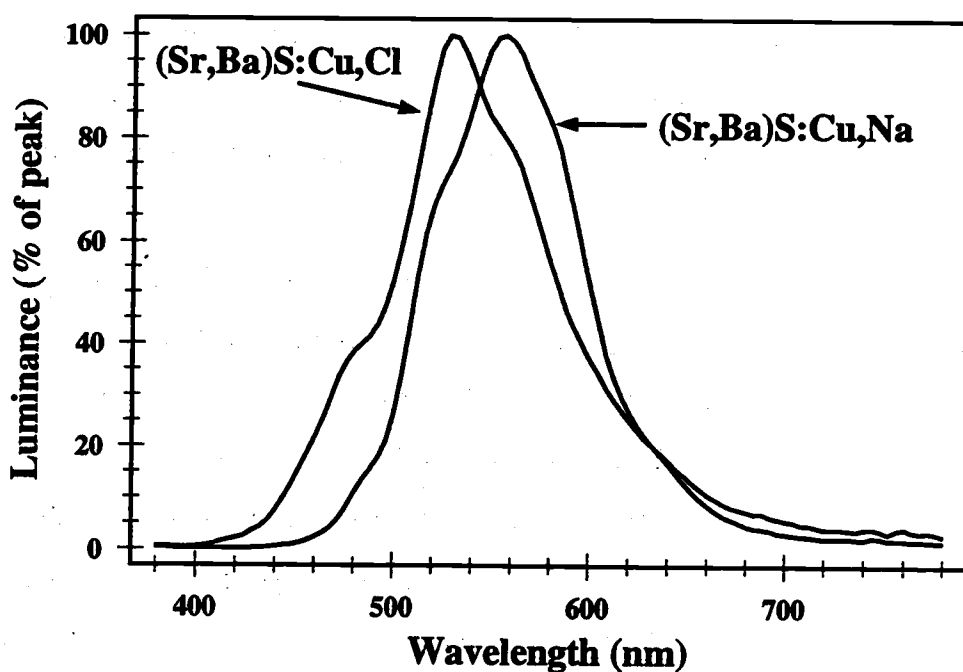Figure 4.36: A L-V/$\eta$-V of a (Sr,Ba)S:Cu,Na ACTFEL device.



Figure 4.37: The electroluminescent spectrum of a (Sr,Ba)S:Cu,Na ACTFEL device in comparison with a (Sr,Ba)S:Cu,Cl ACTFEL device.

wavelength of 556 nm, which is intermediate that of alkali metal coactivated SrS:Cu and BaS:Cu. When this peak wavelength is compared to data collected from powder phosphor PL spectra of (Sr,Ba)S:Cu of varying alloy compositions, it indicates that a Ba concentration of about 30% is present in the phosphor thin-film. [162] This is not surprising since the lower melting point of BaS leads to its preferential evaporation from the $Sr_{0.9}Ba_{0.1}S$ pellets. If this result can be linearly extrapolated back such that a Ba concentration of 10 mol% can be incorporated into the phosphor film, high-brightness devices of a more useful color may be possible. This is postulated because powder phosphor research has shown a significant increase in PL brightness and efficiency for $Sr_{0.9}Ba_{0.1}S$:Cu,Na over pure SrS:Cu,Na.

### 4.4.3 Conclusions

The results of this section indicate that a significant amount of color control can be achieved with alloys of SrS:Cu,Na and BaS:Cu,Na while sacrificing little, if any, brightness. This is an important result because it shows the possibility of application-specific chromaticity engineering. Additional research should be undertaken in this area to determine whether brightness and efficiency gains over SrS:Cu,Na can be realized with smaller concentrations of Ba added.

## 4.5 SrSe:Cu ACTFEL phosphors

The selenide family of materials is relatively unexplored in terms of ACTFEL phosphor materials, presumably due to their higher toxicity than sulfide compounds. Toxicity aside, the alkaline earth selenides possess several advantages over the corresponding sulfide phosphors; namely, smaller dielectric constant, smaller bandgap, and most importantly lower melting temperature. As a result, SrSe is an interesting phosphor host in that it is similar to SrS in many respects except that it should exhibit grain-growth at reduced temperatures owing to its reduced melting temperature. In addition, the lattice constant of SrSe lies between that of SrS and BaS, leading to the

conclusion that it is quite likely that SrSe:Cu will produce green light. To determine the viability of SrSe as an ACTFEL phosphor host, 10 g of 99.5% purity SrSe powder is obtained from Cerac, Inc., pressed into pellets, and sintered to achieve highly dense pellets.

The investigation of SrSe as an ACTFEL phosphor host is carried out by the EB/thermal coevaporation of SrSe, Se metal, and $CuF_2$. Samples are fabricated in precisely the same manner described for the deposition of SrS:Cu,F described in Section 4.2.1, except that the RTA temperature for SrSe is kept at 650°C and Se metal is coevaporated. The first several samples deposited are of poor quality due to the poor control over three simultaneously evaporating sources. However, after four or five depositions, enough experience is gained to be able to deposit several decent thin-film phosphors. Unfortunately, though, the quantity of material available does not allow for a concentration study or a study of coactivators. The best of the SrSe:Cu,F phosphors yields a 60 Hz luminance and efficiency of 4.14 cd/m$^2$ and 0.049 lm/W. A L-V/$\eta$-V of this device is shown in Fig. 4.38. The CIE coordinates of SrSe range from x=0.30 to x=0.34, y=0.53 to y=0.57, where the CIE coordinates of the ACTFEL device whose L-V/$\eta$-V is shown in Fig. 4.38 are x=0.338, y=0.533. The shape of the EL spectrum of SrSe:Cu is quite similar to SrS:Cu, but is shifted toward longer wavelength by about 40-50 nm, as seen in Fig. 4.39.

Since very little literature exists concerning SrSe ACTFEL phosphors, electrical characterization of SrSe:Cu is performed to gain some insight into its operation. The main technique of interest for determining the internal physics of operation of an ACTFEL phosphor is Q-F$_p$ characterization. As a result, a family of Q-F$_p$ plots of a SrSe:Cu ACTFEL device is shown in Fig. 4.40. Several noticeable features of this family of Q-F$_p$ plots are immediately evident; namely the relatively low average phosphor field at which charge transfer occurs, the small amount of charge transfer, and the large amount of relaxation charge that flows. The average phosphor field is quite low by ZnS standards, but is not appreciably different from that seen in SrS:Cu
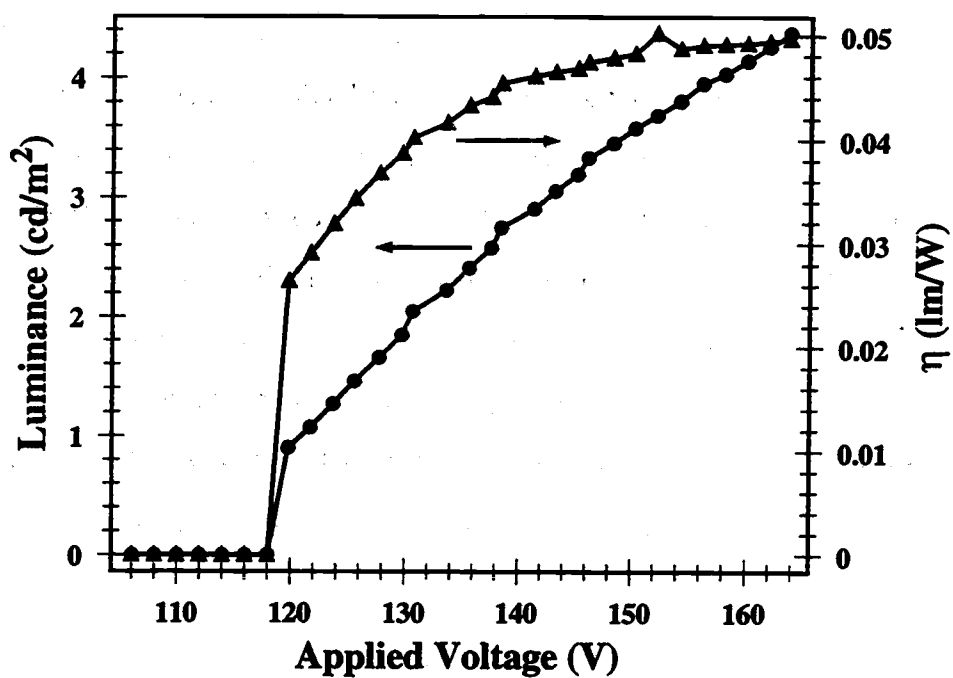
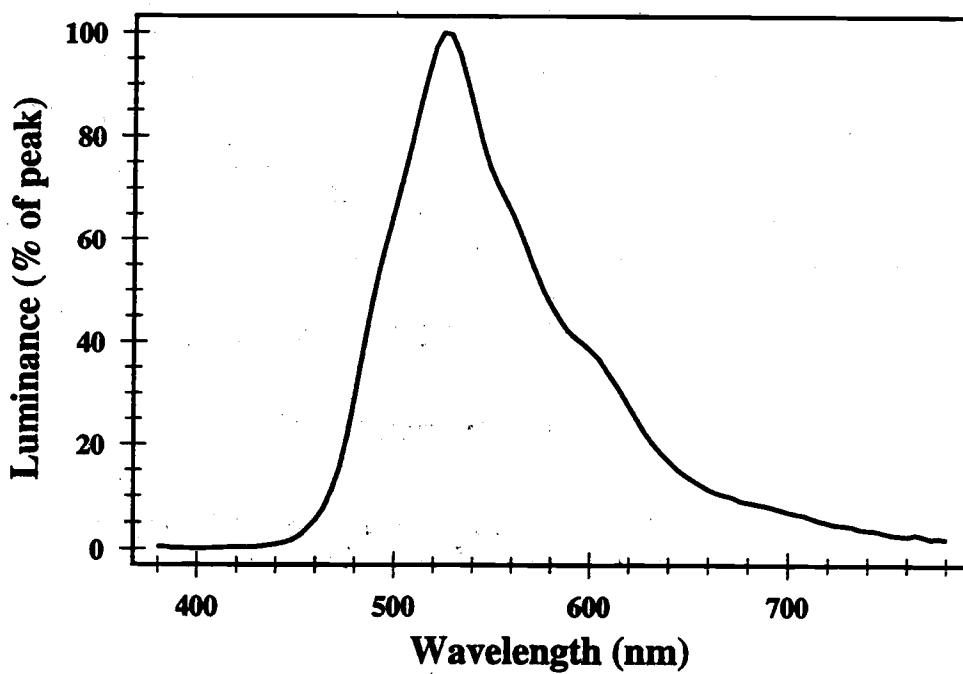Figure 4.38: A L-V/$\eta$-V of a SrSe:Cu ACTFEL device (60 Hz bipolar trapezoidal drive).



Figure 4.39: The electroluminescent spectrum of a SrSe:Cu ACTFEL device.

devices. The small amount of charge transfer and the gentle turn-on are in large part due to the device structure; thick, low dielectric constant $SiO_xN_y$ insulators (3000 Å) are employed, leading to poor coupling between the applied voltage and the phosphor field. The large amount of relaxation charge apparently is the result of some sort of phosphor conductivity because a finite slope of the sense capacitor voltage during this portion of the driving waveform is noticed even at applied voltages well below threshold. This conductivity is characteristic of poorly fabricated ACTFEL devices, probably as a result of the low purity of the starting material, or perhaps the presence of a large number of Se vacancies. Improvement in this area is expected with the continued investigation of this phosphor material.
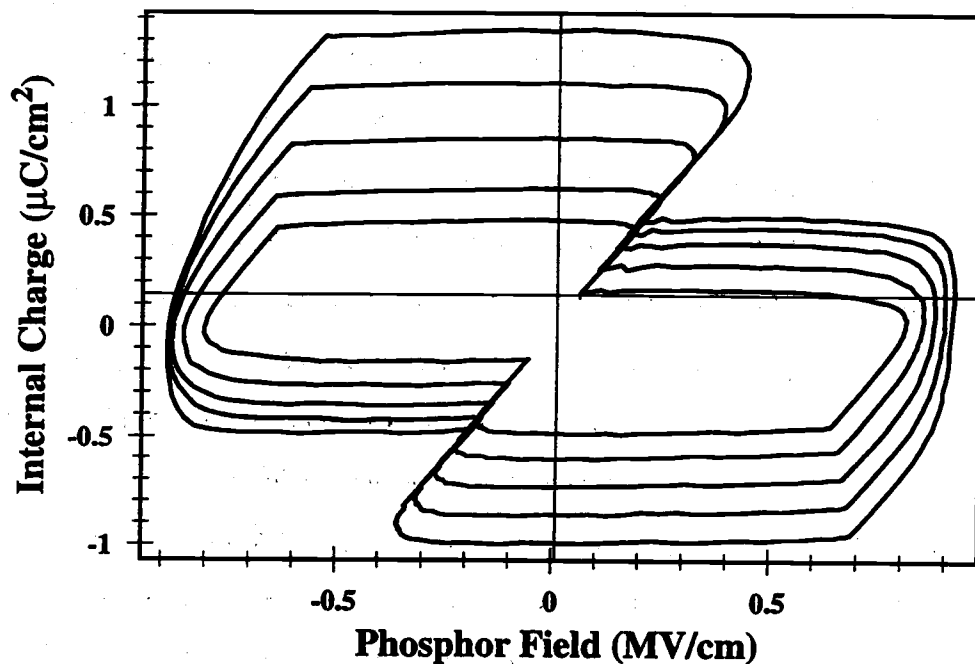


Figure 4.40: A family of $Q$-$F_p$ plots at $V_{th}$ + 20 V, $V_{th}$ + 30 V, $V_{th}$ + 40 V, $V_{th}$ + 50 V, and $V_{th}$ + 60 V of a SrSe:Cu ACTFEL device (1 kHz bipolar trapezoidal drive).

In conclusion, the results from deposition of SrSe:Cu-based ACTFEL devices are disappointing in terms of absolute performance numbers for comparison with other types of ACTFEL devices. However, when the low purity of the source material is considered, along with the dearth of information regarding deposition of this material, the results of this study could be considered to be promising. This phosphor should certainly be investigated in the future due to its potential for reducing the recrystallization temperature from the high values required for CaS and SrS.

## 4.6 $Zn_2GeO_4$:Mn ACTFEL phosphors

As interest in oxide phosphors grows, the oxide phosphor that can be said to have bridged the gap between the high-temperature ceramic substrate approach to ACTFEL fabrication and the "standard" structure approach using glass substrates is certainly $Zn_2GeO_4$:Mn. The primary advantage of $Zn_2GeO_4$:Mn over other oxide phosphors is the relatively low temperature required for recrystallization of this compound. In addition, the fact that this material is an oxide negates many of the typical worries about atmospheric contamination so prevalent with other families of phosphor materials. This property has driven research by several groups worldwide to seriously consider $Zn_2GeO_4$:Mn as a potential commercial ACTFEL phosphor [163, 140, 141]. The purpose of this section is to investigate $Zn_2GeO_4$:Mn as an ACTFEL phosphor in order to determine optimum RTA conditions, coactivators, and Mn concentration via RF magnetron sputtering. The experiment is carried out with three stoichiometric $Zn_2GeO_4$:Mn sputtering targets with Mn concentrations of 0.5 at%, 1.0 at%, and 2.0 at%. These targets are synthesized, pressed, and sintered by Judith Kissick of the OSU Chemistry Department.

### 4.6.1 $Zn_2GeO_4$:Mn (1.0 at%)

The first sputtering target investigated for the deposition of $Zn_2GeO_4$:Mn is the 1.0 at% target. Prior research with $Zn_2GeO_4$:Mn has shown the results to be

relatively independent of deposition conditions as long as the sputtering process gas is composed of at least 5% $O_2$. [163] However, the effect of RTA atmosphere on the performance of $Zn_2GeO_4$:Mn ACTFEL devices was not considered. In addition, no attempt has yet been undertaken to determine the possibility of coactivation of this ACTFEL phosphor. Furthermore, the results of Planar America's investigation into the feasibility of $Zn_2GeO_4$:Mn ACTFEL devices showed extremely accelerated aging; so severe that the devices aged to essentially zero luminance in the period of one hour. Therefore, it is the aim of this section to investigate each of these issues.

The first issue investigated with $Zn_2GeO_4$:Mn ACTFEL phosphors is the effect of RTA atmosphere upon the relevant device characteristics. This experiment is conducted by the RF sputter deposition of $Zn_2GeO_4$:Mn phosphor layers onto ITO/ATO coated glass substrates under the following process conditions: $T_{substrate} = 300°C$, Deposition Pressure = 20 mTorr, 40% He in Ar Flow Rate = 85 SCCM, $O_2$ Flow Rate = 15 SCCM, Target-Substrate Separation = $1\frac{1}{4}$ in. Following phosphor deposition, the sample is rapid thermal annealed at temperatures between 600°C and 800°C in an Ar, $O_2$, or 10% $H_2/N_2$ atmosphere. After annealing, a 2000 Å of $SiO_xN_y$ top insulator is PECVD deposited, and Al electrodes are subsequently thermally evaporated.

Initially, this experiment was intended to assess the influence of RTA temperature in 25°C increments between 600°C and 800°C. However, it was found that the $Zn_2GeO_4$:Mn phosphor films begin recrystallizing at a temperature very close to 625°C, and the degree of recrystallization at temperatures above 725°C is so large that the films readily peel from the substrate. The minimum temperature for complete recrystallization is identical to that found by prior researchers, although they did not seem to have trouble with the films peeling at higher anneal temperatures [163]. This is perhaps a result of their different target composition where excess $GeO_2$ was incorporated. In addition, it is found that annealing in a $H_2/N_2$ mixture results in dark, non-luminescent films, presumably due to the reduction of the $Zn_2GeO_4$ by the $H_2$. As a result, the investigation of the effects of RTA temperature is confined

to the temperature range of 650°C to 725° in atmospheres of Ar and $O_2$. The results of this study are presented in Table 4.9. As seen in Table 4.9, the luminances of $Zn_2GeO_4$:Mn ACTFEL devices annealed in $O_2$ are approximately 25% greater than those annealed in Ar for each RTA temperature. Therefore, $O_2$ appears to be a much better choice for the RTA atmosphere, and is employed for all subsequent processing of $Zn_2GeO_4$:Mn ACTFEL phosphors. The influence of RTA temperature on device performance is minimal for temperatures between 650°C and 700°, but increases noticeably for anneals performed at 725°C. As a result, the threshold temperature for recrystallization to occur appears to be between 625°C and 650°, while there is a second threshold for increased recrystallization between 700°C and 725°C.

Table 4.9: $Zn_2GeO_4$:Mn ACTFEL device performance as a function of RTA temperature and atmosphere (60 Hz bipolar trapezoidal drive).

| | | 650°C | 675°C | 700°C | 725°C |
|---|---|---|---|---|---|
| Ar | $L_{40}$ (cd/m$^2$) | 5.19 | 5.27 | 4.83 | 7.77 |
| | $\eta_{40}$ (lm/W) | 0.0627 | 0.0591 | 0.0601 | 0.0682 |
| | CIE x | 0.369 | 0.343 | 0.387 | 0.406 |
| | CIE y | 0.605 | 0.626 | 0.583 | 0.572 |
| $O_2$ | $L_{40}$ (cd/m$^2$) | 7.15 | 6.46 | 6.71 | 10.9 |
| | $\eta_{40}$ (lm/W) | 0.0601 | 0.0749 | 0.0637 | 0.0854 |
| | CIE x | 0.363 | 0.371 | 0.382 | 0.367 |
| | CIE y | 0.608 | 0.600 | 0.590 | 0.603 |

As with any new ACTFEL phosphor, it is important to characterize the resultant devices both electrically and optically to better understand the physics of device operation. The L-V/$\eta$-V plots of the devices fabricated for this RTA atmosphere study often show quite different shapes than those typically witnessed for sulfide

phosphors. As an example, the L-V/$\eta$-V plot of the brightest $Zn_2GeO_4$:Mn device from the preceding RTA atmosphere study is shown in Fig. 4.41. In addition, the
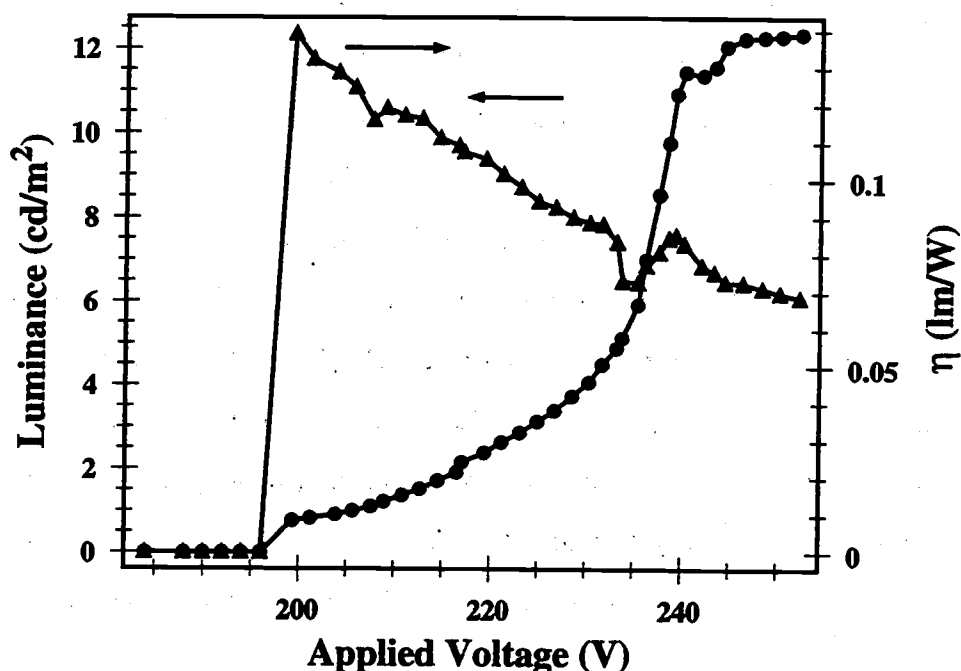


Figure 4.41: A L-V/$\eta$-V plot of a $Zn_2GeO_4$:Mn ACTFEL device (60 Hz bipolar trapezoidal drive).

EL spectrum of this sample is shown in Fig. 4.42. It is seen in Fig. 4.41 that the L-V characteristics of this device increases exponentially until about 40 V above threshold at which point the luminance essentially saturates. This exponential rise in luminance over a voltage range of 40 V is unusual in terms of sulfide phosphors which typically rise in an exponential manner for only several volts above the threshold voltage.

Although the electro-optical characteristics shown in Fig. 4.41 are unusual in the context of sulfide phosphors, the electrical characteristics of $Zn_2GeO_4$:Mn prove to be even more unusual. The average phosphor fields measured in these phosphor materials are typically very high compared to common sulfide-based ACTFEL de-

vices. In addition, most of the conduction charge in these $Zn_2GeO_4$:Mn is relaxation charge, in stark contrast to sulfide phosphor which show the bulk of the charge transfer during the rising edge of the applied voltage pulse. A family of Q-$F_p$ plots of a typical $Zn_2GeO_4$:Mn ACTFEL device is shown in Fig. 4.43. The Q-$F_p$ plots of Fig. 4.43 reveal an average steady-state phosphor field of approximately 5 MV/cm, which is enormous by any standard. In addition, the turn-on of these devices is quite sluggish in comparison with most sulfide-based ACTFEL devices, and there appears to be some charge collapse taking place. However, the phosphor field profile of this device is borderline field-clamped. Another type of characteristic that is sometimes witnessed when operating $Zn_2GeO_4$:Mn devices is a large current spike during the relaxation charge portion of the driving waveform. The $Zn_2GeO_4$:Mn devices that exhibit this type of effect generally produce extremely bizarre electrical characteristics in the context of sulfide phosphors. In addition, this current spike is often associated with visible filaments that move with time over the device area. A family of Q-$F_p$
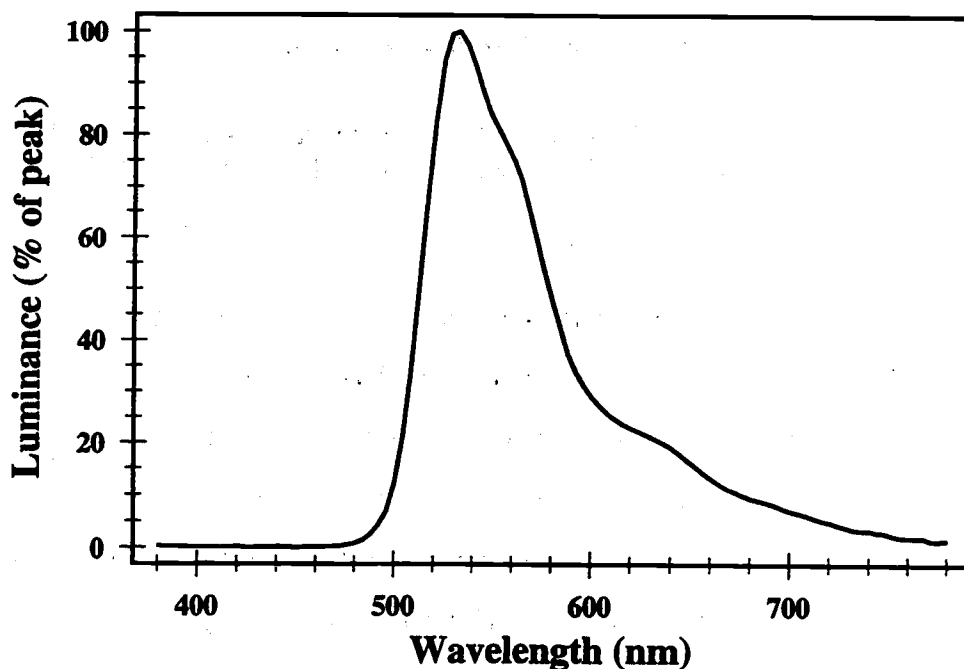


Figure 4.42: The electroluminescent spectrum of a $Zn_2GeO_4$:Mn ACTFEL device.

plots of such a device is show in Fig. 4.44. This set of $Q$-$F_p$ plots is unusual in that it is highly asymmetrical, shows large steady-state phosphor fields, exhibits charge collapse, and has an anomalous steady-state phosphor field profile for negative phosphor fields only that appears only when driven to 50 V above threshold or greater.
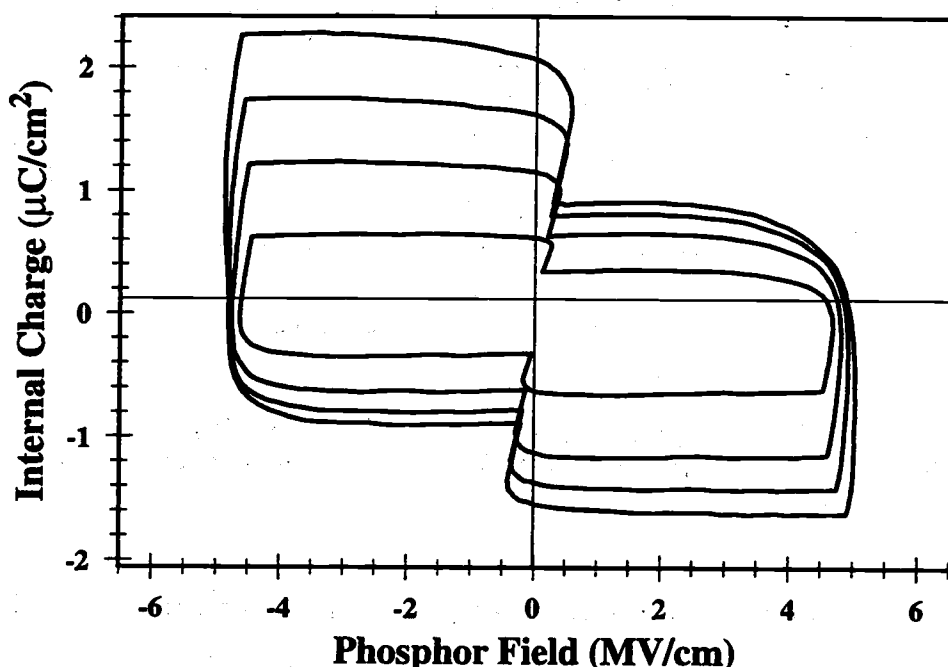


Figure 4.43: A family of $Q$-$F_p$ plots at $V_{th}$ + 20 V, $V_{th}$ + 30 V, $V_{th}$ + 40 V, and $V_{th}$ + 50 V of a $Zn_2GeO_4$:Mn ACTFEL device (1 kHz bipolar trapezoidal drive).

With the identification of the optimum RTA atmosphere currently available, the next step in investigation of $Zn_2GeO_4$:Mn as an ACTFEL phosphor is the identification of suitable coactivators. The processing conditions are identical to those employed for the RTA experiment, except that the RTA cycle that all samples from this experiment are subjected to is a 650°C anneal in $O_2$ for 2 minutes. The coactivators are thermally evaporated onto the freshly sputtered $Zn_2GeO_4$:Mn films and driven into the phosphor in the RTA cycle. This is an advantageous technique be-
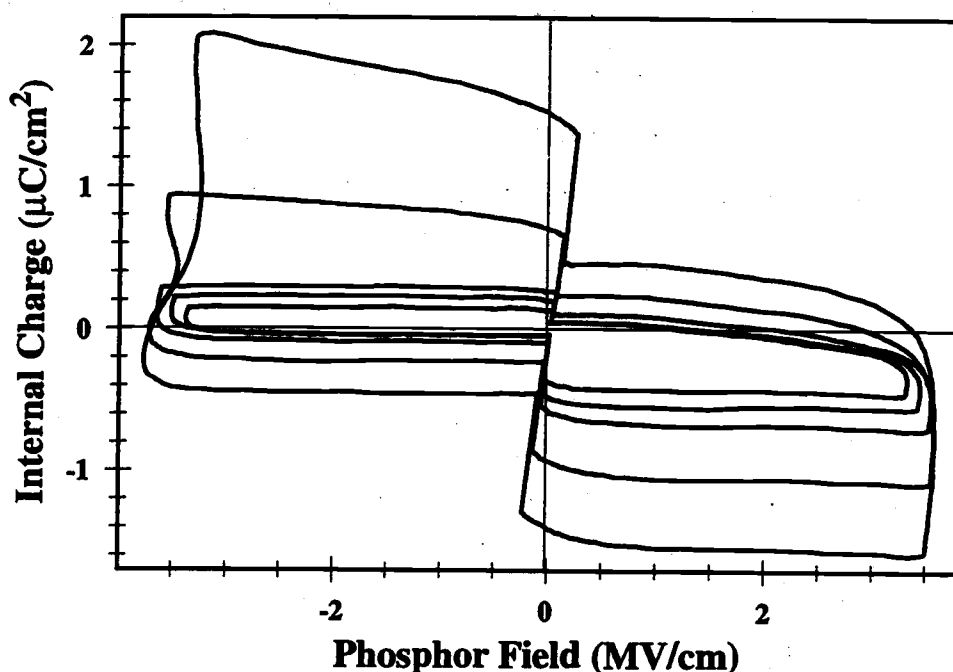
Figure 4.44: A family of Q-$F_p$ plots at $V_{th}$ + 20 V, $V_{th}$ + 30 V, $V_{th}$ + 40 V, $V_{th}$ + 50 V, and $V_{th}$ + 60 V of a $Zn_2GeO_4$:Mn ACTFEL device (1 kHz bipolar trapezoidal drive).

cause many different coactivators can be incorporated without the need to fabricate new sputter targets for each coactivator. The top insulator for all samples in this study is a 2000 Å PECVD-deposited $SiO_xN_y$ layer. The top electrodes are 1000-1500 Å thick thermally evaporated Al.

The study of coactivators is meant to cover a broad range of coactivators without performing an exhaustive search of inorganic chemicals. The coactivators are selected according to one or more of the following criteria: diffusive species, known flux agents for ZnO or $GeO_2$, and effective coactivators in other phosphor systems. Although this selection technique may not be satisfying in terms of knowledge of exactly which species to incorporate, there is a certain amount of guesswork necessary for this study because very little research has been performed on the coactivation of oxide ACTFEL phosphors. From these selection criteria, fifteen compounds are selected for study as coactivators of $Zn_2GeO_4$:Mn. The selected compounds are LiF,

NaF, KF, RbF, CsF, LiCl, NaCl, KCl, RbCl, CsCl, $Bi_2O_3$, $Ga_2O_3$, $CuF_2$, $AgF_2$, and $ZnF_2$. Due to the large volume of information contained in the results from coactivation of $Zn_2GeO_4$:Mn with these compounds, the results are broken up into two tables, the fluoride coactivators in Table 4.10 and the chloride and oxide coactivators in Table 4.11.
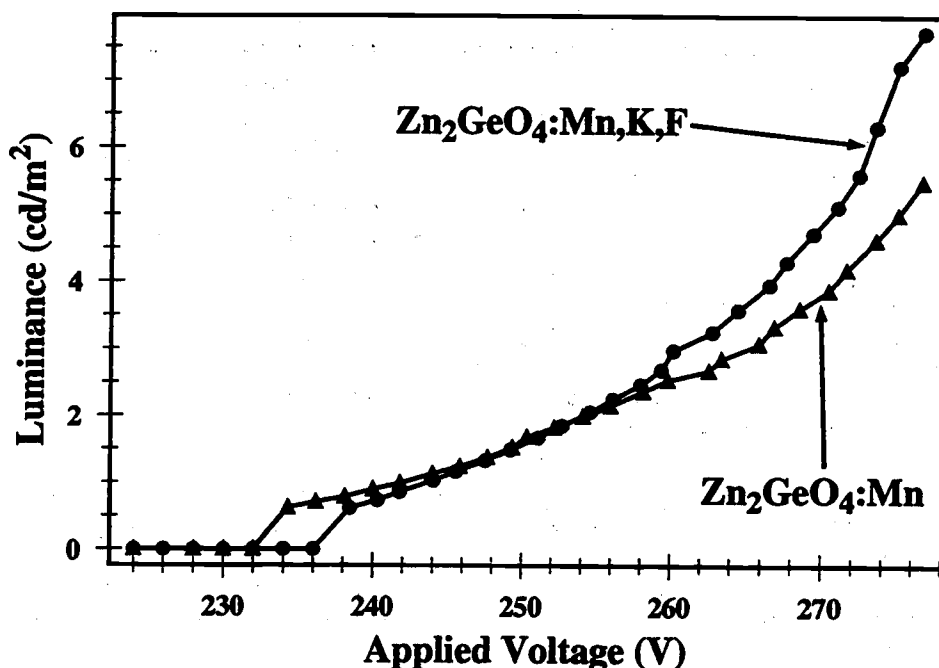


Figure 4.45: L-V plots of a $Zn_2GeO_4$:Mn and a $Zn_2GeO_4$:Mn,K,F ACTFEL device on the same substrate.

An analysis of Tables 4.10 and 4.11 reveals several coactivators that appear promising for $Zn_2GeO_4$:Mn. Most of the listed coactivators have either a negative or small positive effect on the measured luminance of the $Zn_2GeO_4$:Mn ACTFEL devices, with the notable exceptions being KF, RbF, and RbCl. The best of these in terms of percentage increase in luminance is KF, whose incorporation results in a 66.9% increase, as seen in Fig. 4.45. Curiously, while less than half of the coactivators

Table 4.10: Results of fluoride coactivator incorporation into $Zn_2GeO_4$:Mn ACTFEL phosphors via flux doping (60 Hz bipolar trapezoidal drive).

| Coactivator | | With coactivation | Without coactivation | % change |
|---|---|---|---|---|
| LiF | $L_{40}$ (cd/m$^2$) | 3.09 | 6.90 | -55.2 |
| | $\eta_{40}$ (lm/W) | 0.0891 | 0.0590 | +51.0 |
| | CIE | 0.343, 0.628 | 0.358, 0.613 | |
| NaF | $L_{40}$ (cd/m$^2$) | 5.09 | 13.2 | -61.4 |
| | $\eta_{40}$ (lm/W) | 0.0986 | 0.0773 | +27.6 |
| | CIE | 0.320, 0.646 | 0.375, 0.600 | |
| KF | $L_{40}$ (cd/m$^2$) | 7.71 | 4.62 | +66.9 |
| | $\eta_{40}$ (lm/W) | 0.0610 | 0.0505 | +20.8 |
| | CIE | 0.350, 0.621 | 0.358, 0.614 | |
| RbF | $L_{40}$ (cd/m$^2$) | 14.7 | 11.1 | +32.4 |
| | $\eta_{40}$ (lm/W) | 0.081 | 0.0656 | +23.5 |
| | CIE | 0.345, 0.627 | 0.374, 0.597 | |
| CsF | $L_{40}$ (cd/m$^2$) | 12.1 | 9.84 | +23.0 |
| | $\eta_{40}$ (lm/W) | 0.0489 | 0.0655 | -25.3 |
| | CIE | 0.369, 0.600 | 0.375, 0.597 | |
| ZnF$_2$ | $L_{40}$ (cd/m$^2$) | 5.99 | 9.35 | -35.9 |
| | $\eta_{40}$ (lm/W) | 0.0531 | 0.0515 | +3.11 |
| | CIE | 0.353, 0.618 | 0.357, 0.612 | |
| CuF$_2$ | $L_{40}$ (cd/m$^2$) | <0.5 | 11.0 | ? |
| | $\eta_{40}$ (lm/W) | <0.001 | 0.0596 | ? |
| | CIE | 0.407, 0.563 | 0.366, 0.608 | |
| AgF$_2$ | $L_{40}$ (cd/m$^2$) | 3.97 | 8.89 | -55.3 |
| | $\eta_{40}$ (lm/W) | 0.0876 | 0.0664 | +31.9 |
| | CIE | 0.331, 0.638 | 0.361, 0.611 | |

Table 4.11: Results of chloride and oxide coactivator incorporation into $Zn_2GeO_4$:Mn ACTFEL phosphors via flux doping (60 Hz bipolar trapezoidal drive).

| Coactivator | | With coactivation | Without coactivation | % change |
|---|---|---|---|---|
| LiCl | $L_{40}$ $(cd/m^2)$ | 12.1 | 11.3 | +7.08 |
| | $\eta_{40}$ $(lm/W)$ | 0.0737 | 0.0657 | +12.2 |
| | CIE | 0.358, 0.616 | 0.356, 0.617 | |
| NaCl | $L_{40}$ $(cd/m^2)$ | 8.71 | 7.74 | +12.5 |
| | $\eta_{40}$ $(lm/W)$ | 0.0635 | 0.0523 | +21.4 |
| | CIE | 0.323, 0.647 | 0.363, 0.609 | |
| KCl | $L_{40}$ $(cd/m^2)$ | 14.5 | 14.5 | 0.0 |
| | $\eta_{40}$ $(lm/W)$ | 0.0622 | 0.0684 | -9.06 |
| | CIE | 0.357, 0.614 | 0.372, 0.601 | |
| RbCl | $L_{40}$ $(cd/m^2)$ | 14.7 | 9.56 | +53.8 |
| | $\eta_{40}$ $(lm/W)$ | 0.0693 | 0.0674 | +2.82 |
| | CIE | 0.357, 0.612 | 0.372, 0.600 | |
| CsCl | $L_{40}$ $(cd/m^2)$ | 12.7 | 10.6 | +19.8 |
| | $\eta_{40}$ $(lm/W)$ | 0.0553 | 0.0570 | -2.98 |
| | CIE | 0.383, 0.593 | 0.378, 0.596 | |
| $Bi_2O_3$ | $L_{40}$ $(cd/m^2)$ | 7.40 | 11.7 | -36.8 |
| | $\eta_{40}$ $(lm/W)$ | 0.114 | 0.0740 | +54.1 |
| | CIE | 0.325, 0.641 | 0.366, 0.609 | |
| $Ga_2O_3$ | $L_{40}$ $(cd/m^2)$ | 1.66 | 3.67 | -54.8 |
| | $\eta_{40}$ $(lm/W)$ | 0.00577 | 0.0671 | -91.4 |
| | CIE | 0.367, 0.602 | 0.361, 0.611 | |

tested had a positive influence on the measured luminance, two-thirds served to improve the luminous efficiency. In several cases, such as the LiF and NaF coactivated samples, the luminance drops considerably with coactivation while the luminous efficiency is noticeably improved. Since drops in luminance typically result in drops in luminous efficiency because of the direct proportionality between these values, a distinct modification of the charge transfer characteristics of these devices is expected. To illustrate the noticeable power savings with LiF coactivation, the Q-V plots of the LiF and non-LiF coactivated halves of this sample are shown in Fig. 4.46. From the data given in Tables 4.10 and 4.11, the fluoride compounds are especially prone to increases in luminous efficiency, as six of the eight coactivation compounds tested exhibit luminous efficiency increases, and these increases are sizable for five of these six coactivators. Particularly impressive is the 54% increase in luminous efficiency
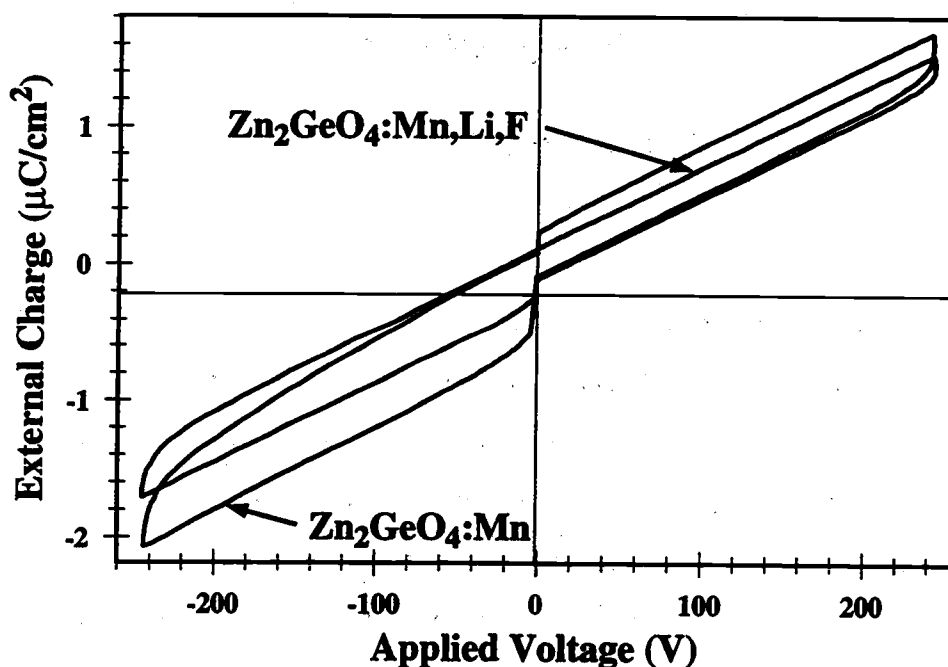


Figure 4.46: Q-V plots of a $Zn_2GeO_4$:Mn and a $Zn_2GeO_4$:Mn,Li,F ACTFEL device on the same substrate (1 kHz bipolar trapezoidal drive).

generated by the addition of $Bi_2O_3$ to $Zn_2GeO_4$:Mn. The $\eta$-V plots of the $Bi_2O_3$- and non-$Bi_2O_3$-fluxed halves of this sample are shown in Fig. 4.47.
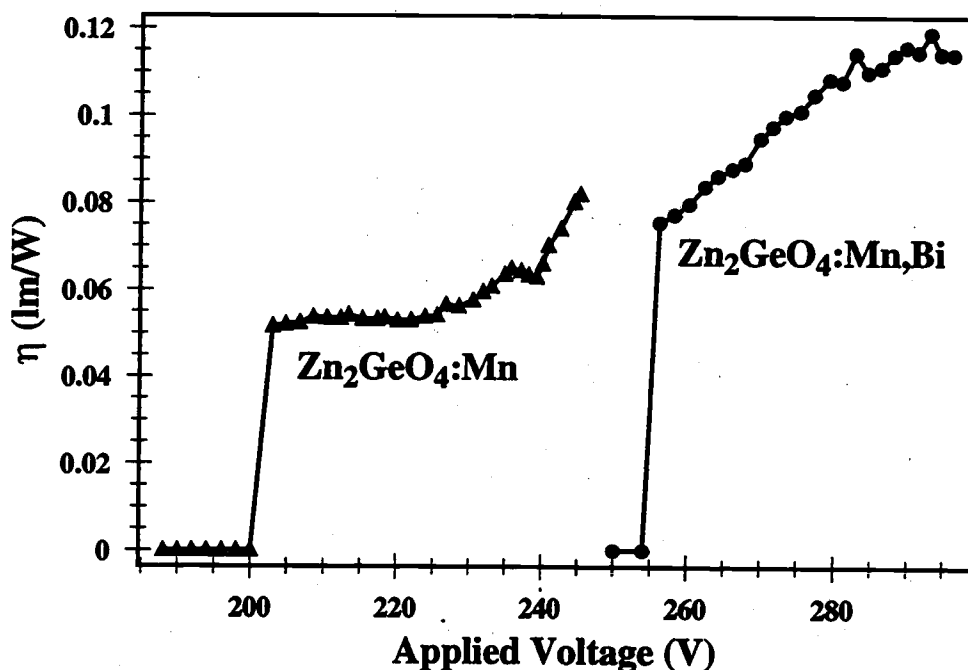


Figure 4.47: $\eta$-V plots of a $Zn_2GeO_4$:Mn and a $Zn_2GeO_4$:Mn,Bi ACTFEL device on the same substrate (60 Hz bipolar trapezoidal drive).

In contrast to much of the work presented earlier in this chapter on sulfide phosphors, coactivation of $Zn_2GeO_4$:Mn appears to have a relatively weak effect upon the EL emission spectra in most cases. In fact, many coactivation compounds show changes in CIE coordinates that are well within the bounds of experimental error. Several coactivation compounds lead to visually noticeable shifts in the emission spectrum, however. The compounds that are most effective at shifting the color are the Na halides, $AgF_2$, and $Bi_2O_3$. Coactivation with all of these compounds reduces the yellow component of the color spectrum, resulting in a color spectrum closer to saturated green. The only coactivation compound of these four that leads

to a brightness increase, however, is NaCl, although coactivation with all of these compounds results in a markedly increased efficiency. The spectral shifts induced by coactivation with these compounds are shown in Figs. 4.48, 4.49, 4.50, and 4.51.
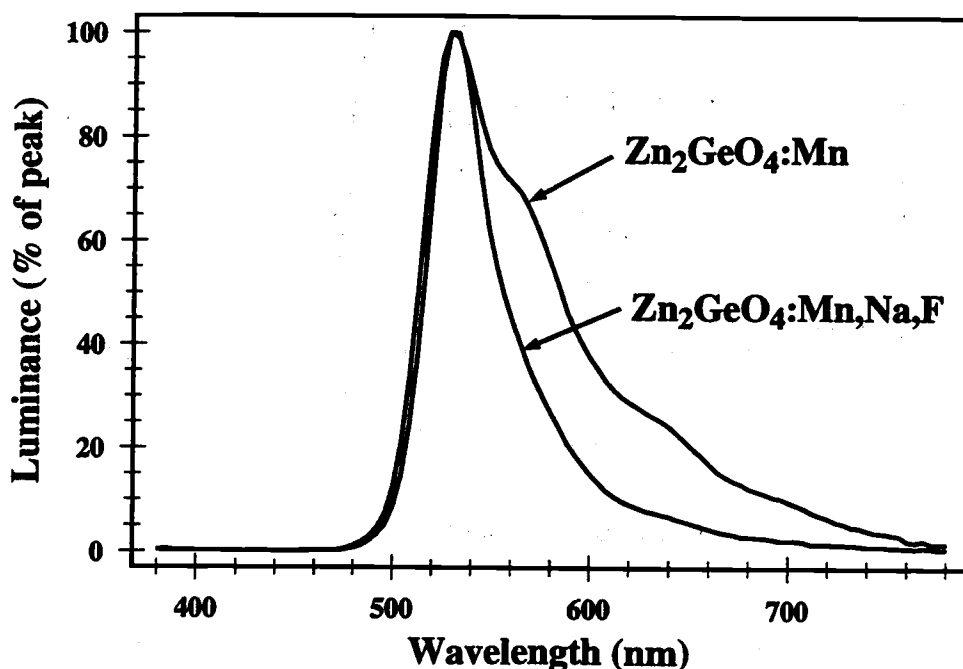


Figure 4.48: Spectral shift of $Zn_2GeO_4$:Mn as a result of NaF coactivation.

The main concern voiced in the Planar report on the feasibility of ACTFEL display fabrication from $Zn_2GeO_4$:Mn phosphors is extremely poor device stability. [163] The results of this report show that the brightness of the $Zn_2GeO_4$:Mn devices fabricated became essentially zero in under an hour of aging at a frequency of 850 Hz. Therefore, this is an area that is especially important to investigate for this project. The testing of aging characteristics is undertaken by lighting up a $Zn_2GeO_4$:Mn ACT-FEL device at 1 kHz and a voltage 40 V above the 60 Hz threshold. Brightness measurements are conducted at increasing intervals (15 min., 30 min., 1 hr., 2 hr., 4 hr., 8 hr., and 12 hr.) up to a stopping time of 12 hours. The results of this aging study are
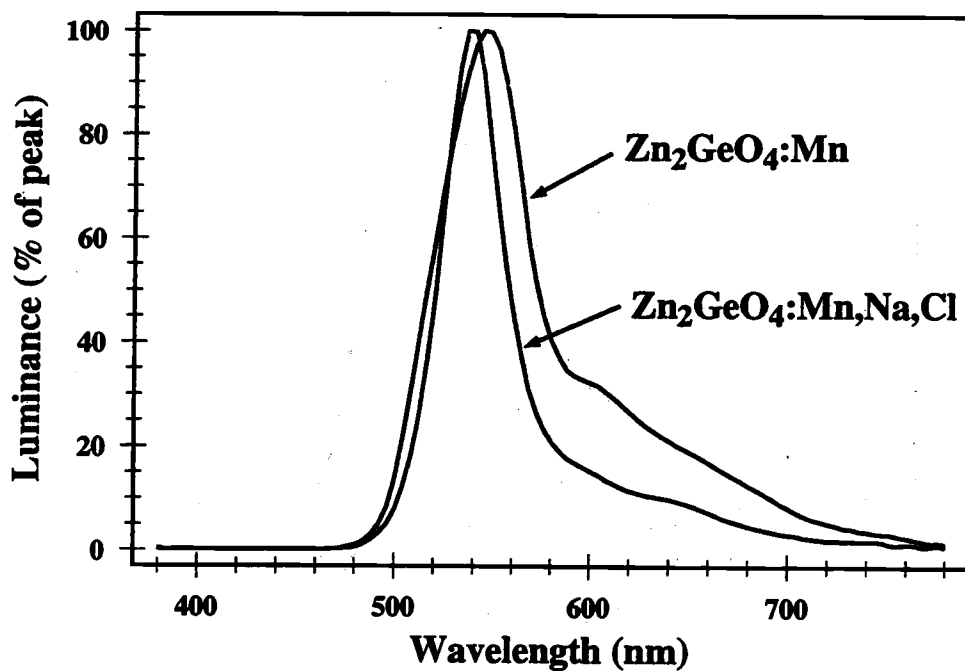
Figure 4.49: Spectral shift of $Zn_2GeO_4$:Mn as a result of NaCl coactivation.



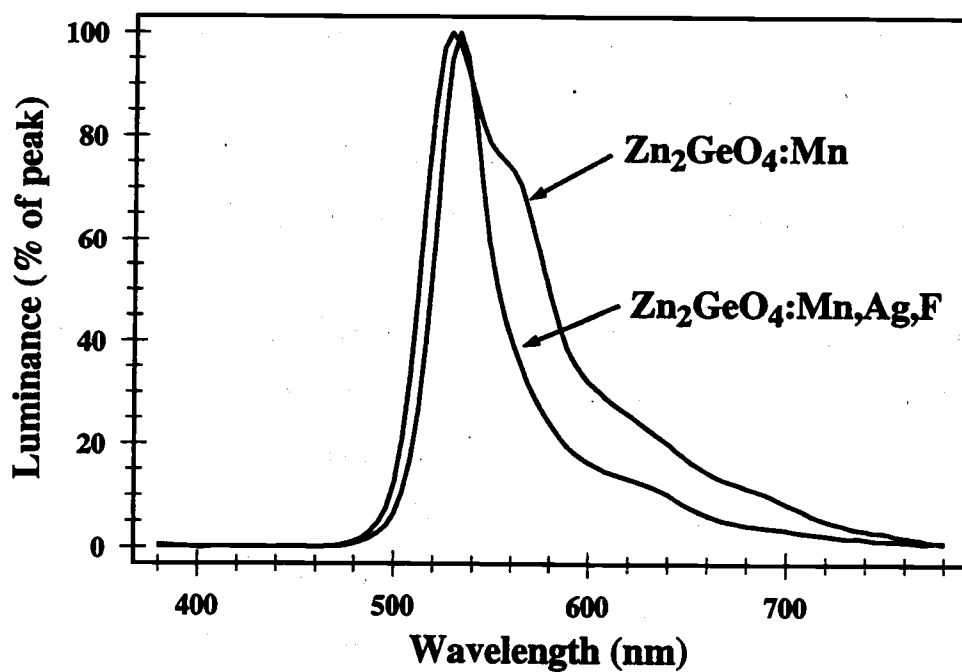Figure 4.50: Spectral shift of $Zn_2GeO_4$:Mn as a result of $AgF_2$ coactivation.
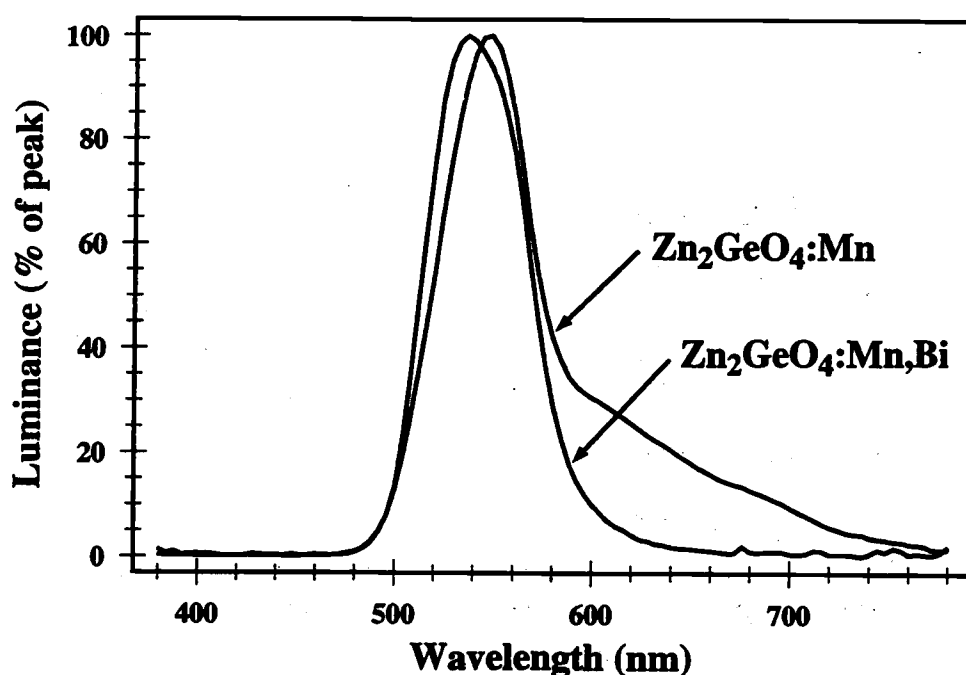
Figure 4.51: Spectral shift of $Zn_2GeO_4$:Mn as a result of $Bi_2O_3$ coactivation.

presented in the form of a plot of luminance as a function of aging time in Fig. 4.52 for both a non-coactivated and a RbCl coactivated sample. As shown in Fig. 4.52, the non-coactivated sample shows relatively stable brightness characteristics, perhaps better than most sulfide phosphors. However, the coactivated sample shows a much greater amount of aging taking place than the non-coactivated sample, although the initial luminance is higher.

The enormous difference in aging characteristics between these samples and the samples fabricated at Planar may be due in part to either the excess $GeO_2$ incorporation, the larger $Mn^{2+}$ concentration, or the addition of an unmentioned coactivator. In an attempt to induce this accelerated aging, a study is performed in which a non-coactivated $Zn_2GeO_4$:Mn ACTFEL device is aged for a period of 48 hours with a 1 kHz bipolar trapezoidal drive at 40 V above the threshold voltage, and a $Zn_2GeO_4$:Mn ACTFEL device heavily coactivated with LiF is also aged in the same manner. The non-coactivated sample showed a 28% drop in luminance from
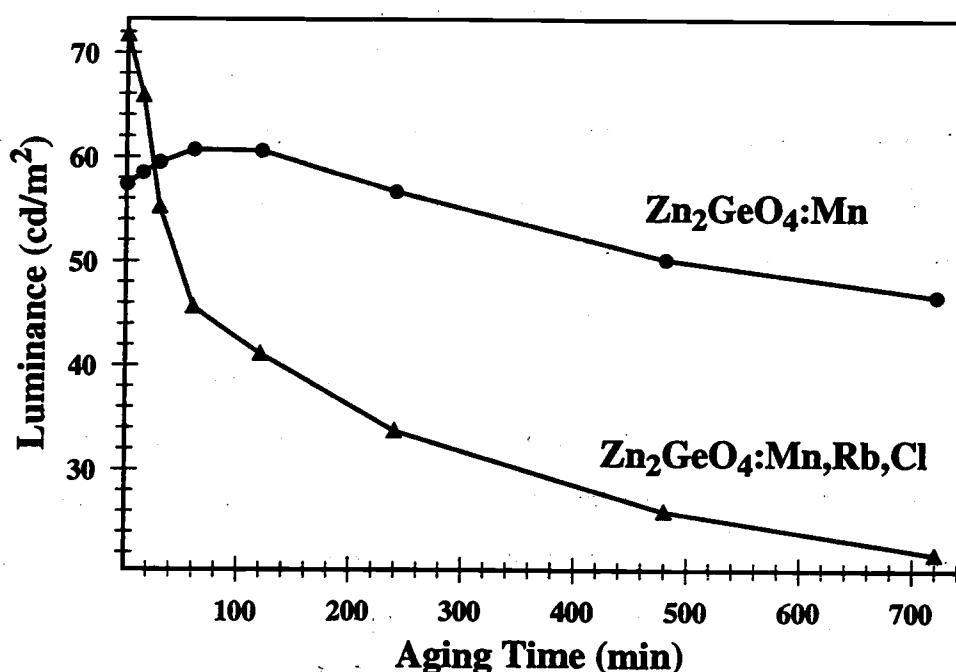
Figure 4.52: The luminance of both a $Zn_2GeO_4$:Mn and a $Zn_2GeO_4$:Mn,Rb,Cl ACT-FEL device as a function of aging time (aged with a 1 kHz bipolar trapezoidal drive at 40 V above the 60 Hz $V_{th}$.

54.1 to 39.1 cd/m$^2$ over this 48 hour period, whereas the LiF-coactivated sample aged to zero luminance in approximately 30 minutes. As a result of this study, it seems that the underlying cause of the accelerated aging characteristics of the $Zn_2GeO_4$:Mn ACTFEL devices presented in the Planar report is probably coactivation with an alkali halide flux agent.

### 4.6.2    $Zn_2GeO_4$:Mn (0.5 at%)

The successful fabrication of moderately bright green ACTFEL devices from a $Zn_2GeO_4$ target activated with 1.0 at% Mn motivates the study of the effect of Mn concentration on the measured device characteristics. The investigation of alternate activator doping levels is initiated with the sputter deposition of samples from a target activated by 0.5 at% Mn. The deposition parameters are all identical to those employed for the deposition of the 1 at% Mn $Zn_2GeO_4$ ACTFEL phosphors. The

RTA temperature and atmosphere employed for these devices is the standard 650°C anneal in $O_2$ for 2 minutes used for the coactivation study.

The results of this study show significantly reduced luminance and efficiency for 0.5 at% Mn $Zn_2GeO_4$ ACTFEL devices compared to 1.0 at% Mn devices. In addition, the yellow component of the spectrum of these samples is enhanced considerably, as seen by comparison of the spectrum of a 0.5 at% Mn $Zn_2GeO_4$:Mn ACTFEL device shown in Fig. 4.53 with those presented in the Section 4.6.1. In addition, the addition of an alkali halide coactivator does not significantly reduce the magnitude of the yellow and red peaks in the spectrum, making the CIE coordinates substantially differ from those of saturated green. A L-V/$\eta$-V plot of the highest luminance 0.5 at% Mn $Zn_2GeO_4$:Mn device fabricated for this project is shown in Fig. 4.54. In addition, the coactivation of these samples with RbF provides only a modest increase in luminance, that is insufficient to compete with the luminances obtained with the 1 at% Mn target. As a result, it appears that the optimal Mn concentration in $Zn_2GeO_4$:Mn lies at Mn concentrations greater than 1 at%, rather than smaller concentrations.

## 4.6.3  $Zn_2GeO_4$:Mn (2.0 at%)

The deterioration of ACTFEL device performance with a reduction in the Mn concentration in the $Zn_2GeO_4$:Mn phosphor leads to the conclusion that it is wise to consider larger Mn concentrations. As a result, a $Zn_2GeO_4$:Mn sputter target coactivated with 2 at% Mn is obtained. From this target, phosphor layers are rf sputtered under the same conditions as those employed for sputtering of the 0.5 at% and 1.0 at% Mn $Zn_2GeO_4$:Mn targets in the preceding sections.

In all respects, samples sputtered from the $Zn_2GeO_4$:Mn target activated with 2 at% Mn show the best characteristics of any of the ACTFEL devices sputtered in this investigation of $Zn_2GeO_4$:Mn. The luminance and efficiency of these device is high in comparison with ACTFEL devices activated with 0.5 at% or 1.0 at% Mn, as seen from the L-V/$\eta$-V plot shown in Fig. 4.55. In addition, the color purity of
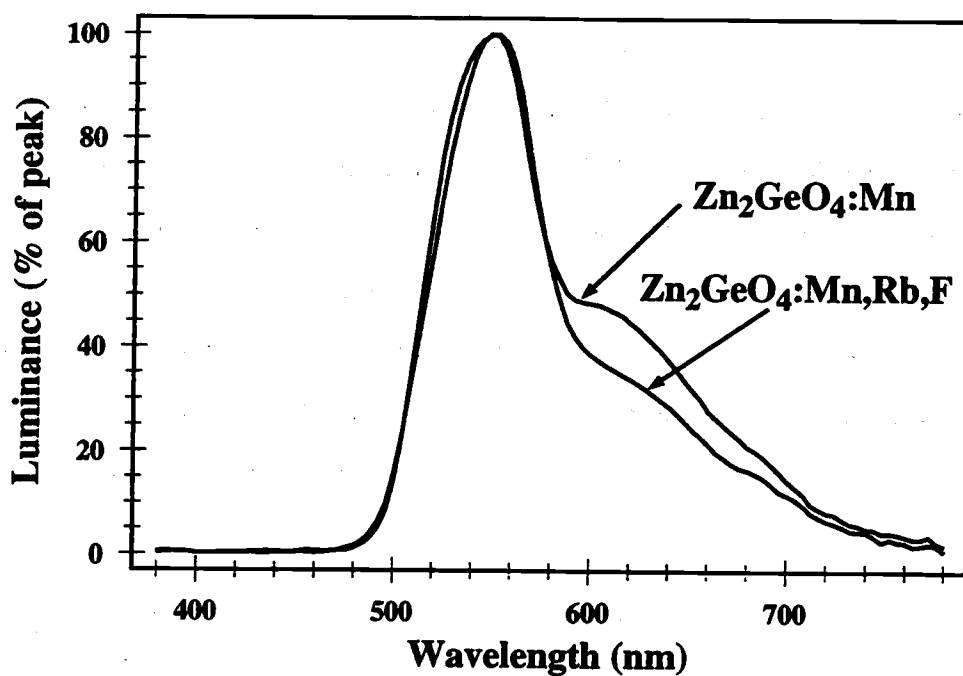
Figure 4.53: Electroluminescence spectra of a $Zn_2GeO_4$:Mn and a $Zn_2GeO_4$:Mn,Rb,F ACTFEL device activated with 0.5 at% Mn.
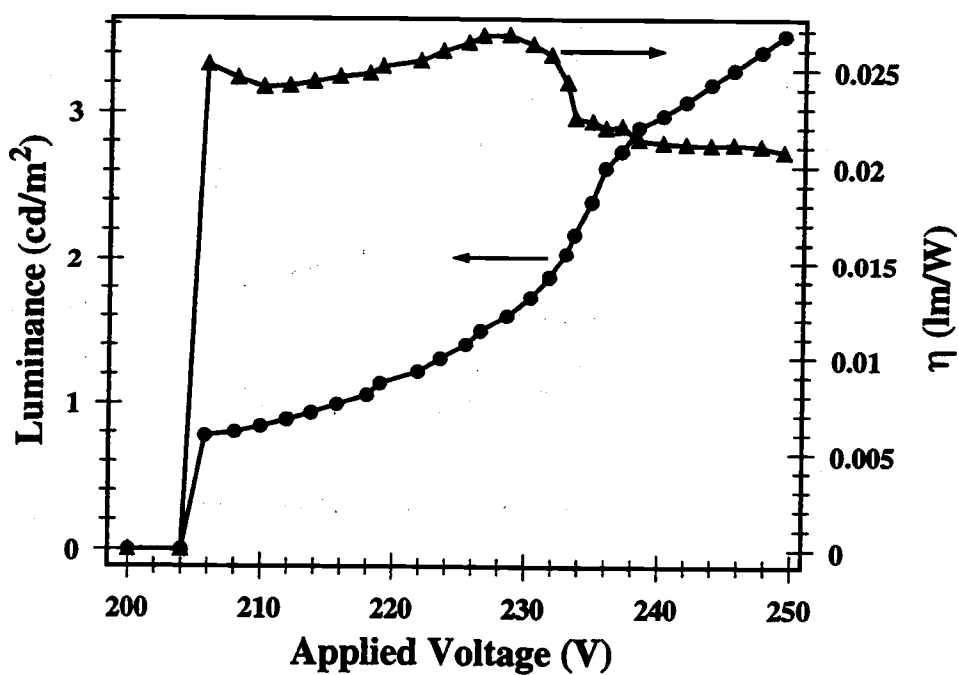


Figure 4.54: A L-V/$\eta$-V plot of a $Zn_2GeO_4$:Mn ACTFEL device activated with 0.5 at% Mn (60 Hz bipolar trapezoidal drive).

ACTFEL devices sputtered from this 2 at% Mn target exhibit CIE coordinates very close to saturated green due to the reduction of the longer wavelength peaks that appear for the 0.5 at% and 1.0 at% Mn devices. Also, alkali halide coactivation does not show a noticeable shift in the spectrum of these ACTFEL devices, as shown in the spectrum of Fig. 4.56. However, aging characteristics are not investigated because these devices tend to be less stable than those fabricated from the 1.0 at% Mn target. This situation may be improved with continued sputtering of this target, however, because ACTFEL phosphor characteristics tend to improve with the total amount of time that a sputter target is sputtered. [154]
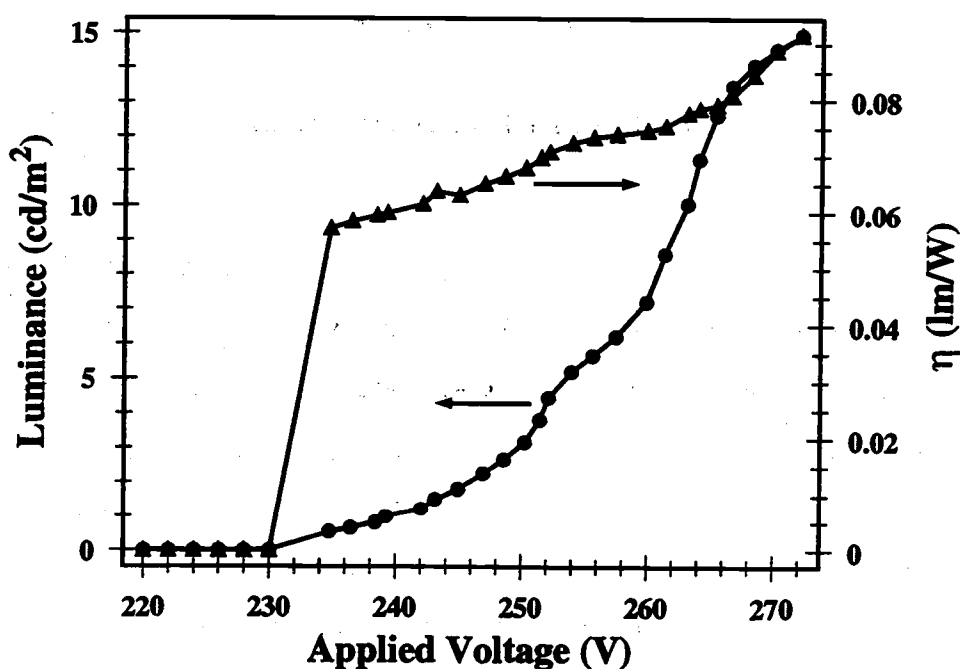


Figure 4.55: A L-V/$\eta$-V plot of a $Zn_2GeO_4$:Mn ACTFEL device activated with 2.0 at% Mn (60 Hz bipolar trapezoidal drive).
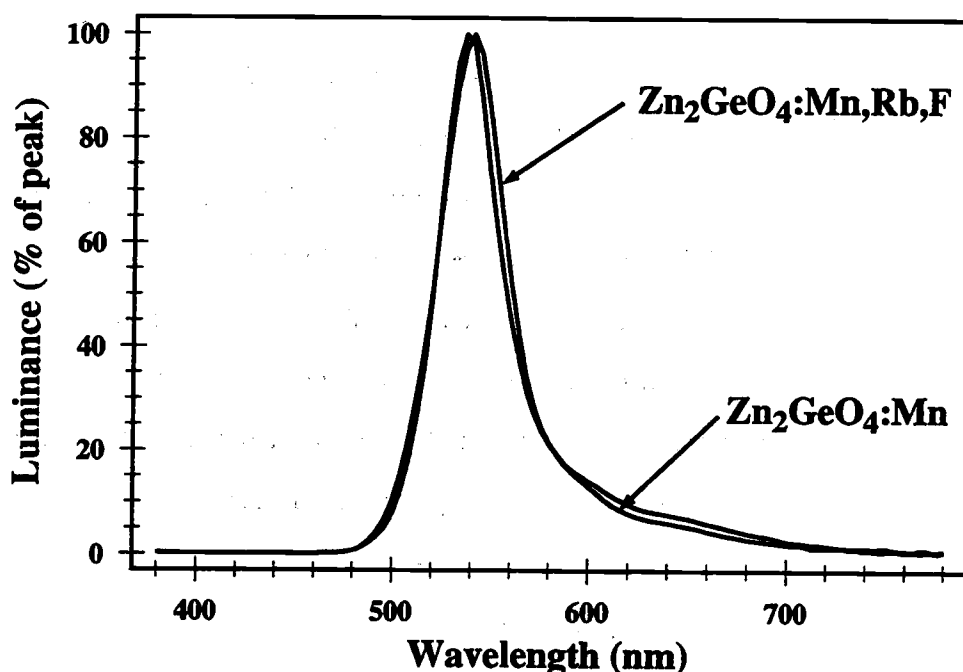
Figure 4.56: The electroluminescence spectrum of a $Zn_2GeO_4$:Mn and a $Zn_2GeO_4$:-Mn,Rb,F ACTFEL device activated by 2.0 at% Mn.

### 4.6.4   Conclusions

The results of this section show that $Zn_2GeO_4$:Mn is a promising phosphor for the production of ACTFEL displays. The accelerated aging witnessed in the Planar America study of $Zn_2GeO_4$:Mn is apparently a result of their target composition, not an innate property of $Zn_2GeO_4$:Mn itself, as evidenced by the aging charateristics presented in Section 4.6.1. The results of this section also show that increasing the Mn concentration in the sputter target leads to improvements in the brightness, efficiency, and chromaticity of the resultant ACTFEL devices. More research should be conducted to determine the optimal Mn concentration, and aging and coactivation studies should be performed on samples produced from this optimized target.

## 4.7 Conclusions

Several ideas for the fabrication of green-emitting ACTFEL phosphors are investigated in this chapter. The most encouraging reults are obtained from the coactivation of SrS:Cu phosphors with alkali metals. The results of this study promise to provide an ACTFEL phosphor that is competitive with ZnS:Tb in terms of brightness, efficiency, and color purity. Other phosphors investigated also give promising results, but the timeframe for applicability of most of these phosphors is further away than alkali metal coactivated SrS:Cu. Continuing research should be conducted with many of the more promising of these phosphor materials such as BaS:Cu,K, (Sr,Ba)S:Cu,Na, SrSe:Cu, and $Zn_2GeO_4$:Mn.

# 5. ACTFEL CHARACTERIZATION

One of the primary advantages of having the ability to readily change the activator and coactivator species and concentrations is the possibility for much more powerful characterization studies than otherwise possible. The capability of readily changing the activator and coactivator species and concentration is an inherent property of the currently available EBE system, as demonstrated in Chapter 4. This capability greatly enhances the ability to perform meaningful characterization studies because of the possibility of isolating optical and electrical effects due to the presence or concentration of an activator or coactivator. In essence, the synergy between ACTFEL device fabrication and characterization is quite strong, and the ability to do both in a high-quality manner provides a powerful tool for solving quite complex physical problems. As a result, the aim of this chapter is to exploit the ability to fabricate ACTFEL devices in an effort to gain insight into the operation of ACTFEL phosphors. The primary focuses of this chapter are the SrS and ZnS phosphor systems due to their current technological importance in the field of thin-film electroluminescence.

## 5.1  Rare earth activation of ZnS and SrS ACTFEL devices

Many of the rare earth luminescent activators are relatively insensitive to the crystal field effects of a host lattice due to their well-shielded 4f→4f luminescent transitions, as discussed in Section 3.2. As a result of their insensitivity to crystal field effects, these activators should show very similar electroluminescent spectra independent of the host lattice. With crystal field effects decoupled from the choice of phosphor host, the main variables determining the emission spectrum of a phosphor activated with this type of impurity are thus the branching ratios of emission transitions and the electron energy distribution. Therefore, if ACTFEL devices are fabricated with several of these rare earth activators, it may be possible to obtain

information related to the electron energy distribution inside an operating ACTFEL phosphor.

The two most common and practical ACTFEL phosphor hosts currently known are ZnS and SrS, and are hence selected as the phosphor hosts to investigate via rare earth activation. In addition, the SrS phosphor host is the primary focus of the fabrication efforts presented in this thesis, making better knowledge of its operation beneficial. As a result, ZnS and SrS phosphors activated with $Tb^{3+}$, $Ho^{3+}$, $Dy^{3+}$, $Er^{3+}$, and $Tm^{3+}$ are deposited via EB/thermal coevaporation of undoped SrS or ZnS and a fluoride of one of the rare earth activators mentioned. The EBE of the undoped SrS or ZnS pellets is performed at a rate of approximately 40 Å/s to a total thickness between 8000 and 10,000 Å. The SrS pellets are cold-pressed and sintered SrS powder that is synthesized by Ben Clark of the OSU Chemistry Department, whereas the ZnS pellets are 99.99% pure, pressure-sintered cubes acquired from Cerac, Inc. The rare earth fluorides are thermally coevaporated at a rate of approximately 0.5% that of the phosphor host material as measured by the thickness monitor. The substrate temperature as measured by the thermocouple mounted in the EBE chamber is 250°C for all SrS depositions, and 75°C for all ZnS depositions. The RTA cycle for all SrS phosphors is 810°C for 120 seconds in an Ar atmosphere, whereas for the ZnS phosphors it is 600°C for 120 seconds in an Ar atmosphere. Following phosphor deposition and annealing, 3000 Å thick $Al_2O_3$ top insulators are EB evaporated by evaporating 99.99% pure $Al_2O_3$ pieces obtained from Cerac, Inc., in a 20% $O_2$ in Ar gas mixture. The deposition pressure after backfilling with the $O_2$/Ar mixture is approximately $10^{-4}$ Torr as measured by a W filament ionization gauge. The substrate temperature for this deposition is held at 250°C throughout the deposition in an effort to deposit dense, stoichiometric $Al_2O_3$ thin-films. Finally, after deposition of the top insulator, 1000-1500 Å thick Al top electrodes are thermally evaporated.

The ACTFEL devices fabricated for this study are then subjected to an arsenal of tests in an effort to gather information regarding their operation. First, spectra

of the samples are measured by a Photo Research PR-650 spectracolorimeter. Then, standard electrical characterization techniques (C-V, Q-V, and Q-$F_p$) are performed in an effort to gather information regarding the the presence of space charge in the phosphor layer in question and determine the phosphor fields at which these devices operate. Next, transient luminance measurements are performed with a Hamamatsu Photosensor Module H5783 photomultiplier tube (PMT) to determine whether trailing edge light emission is observed, and to what extent. Trailing edge light emission is important, because its presence is an indicator that large concentrations of space charge are present in the phosphor layer. Finally, $Q_{max}$-$V_{max}$ measurements are performed in an effort to determine the height of the "step" in these plots that has been linked to space charge generation in the phosphor layer. [31]

The motivation for this experiment has its origins in the effort to fabricate green-emitting SrS:Tb ACTFEL devices presented in Section 4.1. In Section 4.1, it is noted that the CIE color coordinates of SrS:Tb are consistently blue-shifted in relation to those of ZnS:Tb. Upon comparison of the spectra of these two types of ACTFEL device, a startling feature was noticed; transitions originating from the $^5D_3$ excited state of $Tb^{3+}$ are witnessed in SrS:Tb, whereas they are not in ZnS:Tb, as seen by comparing Figs. 5.1 and 5.2. To determine whether this effect is the result of an anomalous sample, several ZnS:Tb ACTFEL devices are fabricated and an RF sputtered ZnS:TbOF sample is obtained from Planar America in an effort to determine the consistency of spectra between ZnS:Tb devices. Spectral measurements of the ZnS:Tb and SrS:Tb ACTFEL devices revealed that the luminescent transitions originating from the $^5D_3$ excited state of $Tb^{3+}$ are witnessed exclusively in the SrS:Tb ACTFEL devices. The mechanism behind this discrepancy in spectra has three possible causes; a hotter electron distribution in SrS:Tb than ZnS:Tb, different branching ratios in ZnS:Tb than SrS:Tb that preclude emission from the $^5D_3$ excited state, or absorption of short wavelength blue light in ZnS. However, ZnS:Ag is the principal blue-emitting phosphor for CRT applications with a peak emission wavelength of
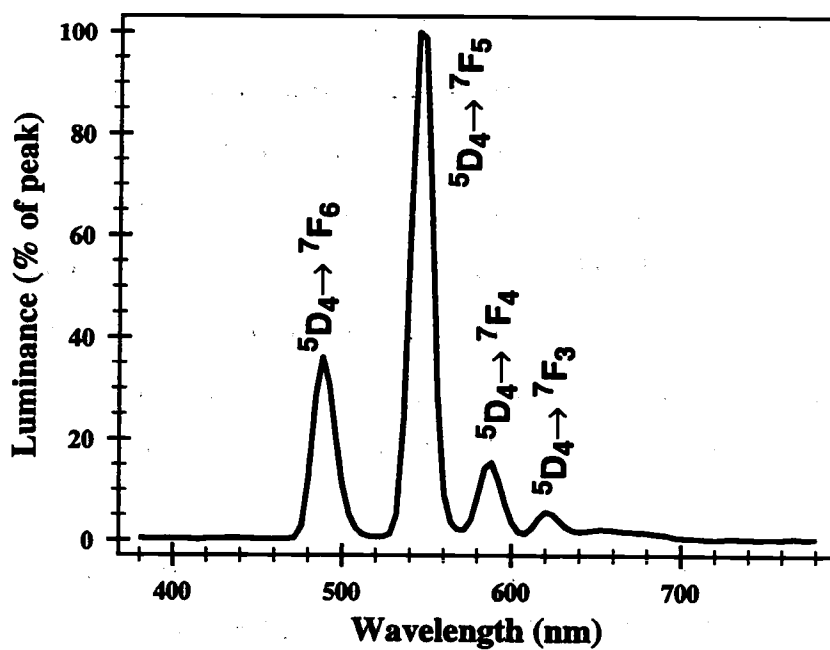
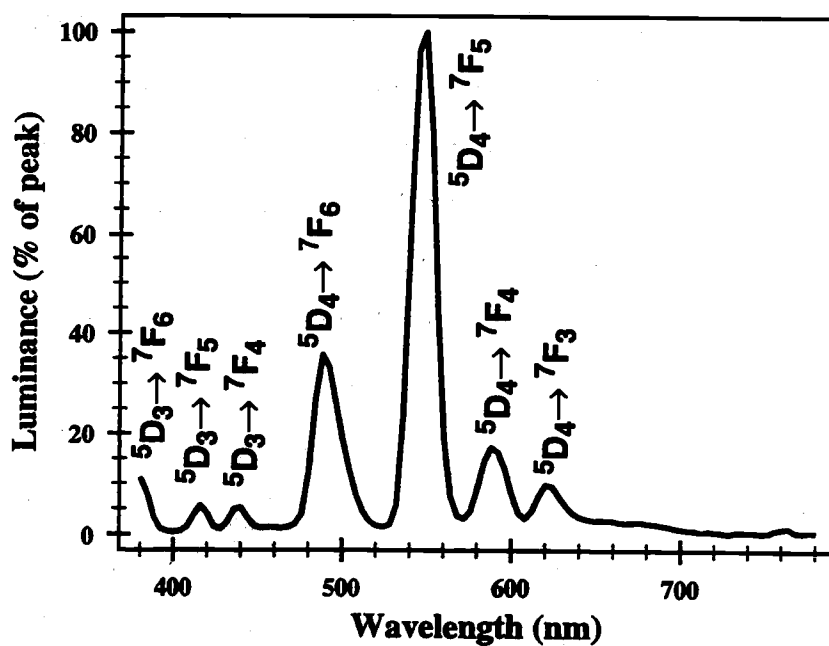Figure 5.1: The electroluminescent spectrum of a ZnS:Tb,F ACTFEL device.



Figure 5.2: The electroluminescent spectrum of a SrS:Tb,F ACTFEL device.

450 nm and $ZnS:Cl + In_2O_3$ is the principal blue-emitting FED phosphor with an emission peak at 464 nm, making it highly unlikely that the ZnS phosphor host is absorbing blue light. In addition, while testing absorption in a ZnS:Mn phosphor at different wavelengths, Cleary noted that little absorption is witnessed in the ZnS at wavelengths greater than 340 nm. [164] In view of this, the mechanism behind the observed spectral shift of the $Tb^{3+}$ activator from a ZnS to a SrS phosphor host must be either the electron distribution or the branching ratio. Since the electron energy distribution in an operating ACTFEL phosphor is a relatively unknown quantity, it is necessary to pursue whether the branching ratio of emission is the cause of this effect.

The testing of the branching ratio hypothesis is conducted through the fabrication of ZnS and SrS ACTFEL devices activated by $Dy^{3+}$, $Ho^{3+}$, $Er^{3+}$, and $Tm^{3+}$ and comparing the resultant spectra. The activators $Tb^{3+}$, $Dy^{3+}$, $Ho^{3+}$, $Er^{3+}$, and $Tm^{3+}$ are chosen for this study due to their well-shielded 4f intrashell transition and their richness of emission lines in the blue and UV regions of the spectrum. If this discrepancy in emission spectra between ZnS and SrS phosphor hosts activated by these rare earth centers is indeed a branching ratio issue, it would be expected that the short wavelength transition should not be preferentially observed in SrS for all of these activators. Therefore, elimination of different branching ratios as the underlying cause for the observed difference in EL spectra between 4f intrashell transition rare earth activators in ZnS and SrS leaves the electron energy distributions as the likely cause of this effect.

The investigation of the remaining four rare earth activators, $Dy^{3+}$, $Tm^{3+}$, $Ho^{3+}$, and $Er^{3+}$, is thus undertaken in an effort to explore whether branching ratio effects could account for the observed differences in spectra between ZnS:Tb and SrS:Tb. The first of these activators considered in $Tm^{3+}$ because it is a well-known blue-emitting rare earth activator. The electroluminescent spectrum of ZnS:Tm shown in Fig. 5.3 reveals the existence of two primary peaks, the well-known $^1G_4 \rightarrow{}^3H_6$

blue transition peaking around 480 nm and the competing IR transition, $^1G_4 \rightarrow {}^3H_5$

transition. This spectrum is dominated by the $^1G_4 \rightarrow {}^3H_5$ transition whose relatively
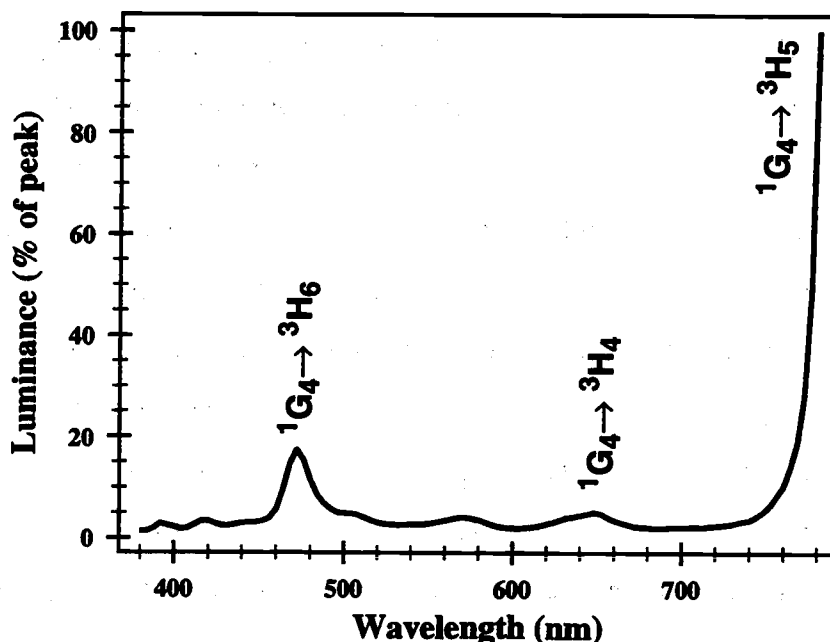


Figure 5.3: The electroluminescent spectrum of a ZnS:Tm,F ACTFEL device.

large intensity is probably a branching ratio issue because both the $^1G_4 \rightarrow {}^3H_6$ and

the $^1G_4 \rightarrow {}^3H_5$ transition share the same excited state, but differ in ground states.

The complex electroluminescent spectrum of SrS:Tm, in contrast, shows a relatively

large number of transitions, many originating from excited states much higher in en-

ergy than the $^1G_4$ state that feeds the luminescent transitions in ZnS:Tm, as seen by

inspection of Fig. 5.4. Furthermore, the luminance of the SrS:Tm ACTFEL device

is approximately 100 times greater than that of the ZnS:Tm device, indicating that

the observed luminance may be a function of the ability of a phosphor host material

to support hot enough electrons to excite these higher energy excited states. In addi-

tion, very little light emission at wavelengths below 460 nm is observed in ZnS:Tm,

whereas a fairly significant amount of light emission from this range of wavelengths is observed in SrS:Tm, as seen by comparison of Figs. 5.3 and 5.4.

With the result that $ZnS:Tm^{3+}$ emits relatively little light at wavelengths below 460 nm, whereas significant emission in the wavelength range in $SrS:Tm^{3+}$ is observed, $Dy^{3+}$ is next investigated as an activator in ZnS and SrS phosphor hosts. The ZnS:Dy phosphor exhibits yellow electroluminescence of almost identical CIE coordinates to ZnS:Mn; $x = 0.47$, $y = 0.47$. The spectrum of ZnS:Dy, however, is quite different from that of ZnS:Mn, as seen in Fig. 5.5. Four distinct luminescent transitions are observed in the ZnS:Dy spectrum of Fig. 5.5, all originating from the same excited state, $^4F_{9/2}$, with subsequent relaxation to different ground states. However, the spectrum of SrS:Dy shows several additional luminescent transitions originating from the higher level excited states, $^4I_{15/2}$ and $^4G_{15/2}$, as seen in Fig. 5.6. These additional luminescent transitions reside in the blue and green regions of the visible spectrum, and hence, when mixed with the luminescent transitions originating from
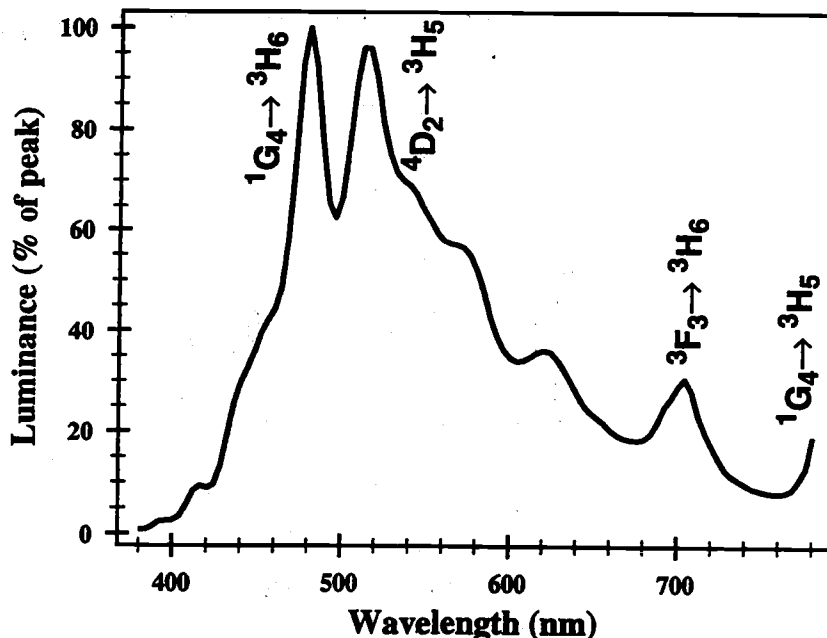


Figure 5.4: The electroluminescent spectrum of a SrS:Tm,F ACTFEL device.

$^4F_{9/2}$, result in white electroluminescence with CIE coordinates x = 0.34, y = 0.38. In addition, the blue peak of $Dy^{3+}$ at 480 nm contributes a much higher percentage of the total luminance of SrS:Dy than ZnS:Dy. Finally, the appearance of a peak at 520 nm originating from $^4I_{15/2}$ that is completely absent in ZnS rules out the possibility that ZnS is absorbing the higher energy light. This is because if the electrons were heated enough to excite the $^4I_{15/2}$ state in ZnS, and ZnS was absorbing photons of wavelength less than or equal to 460 nm, the 520 nm $^4I_{15/2} \rightarrow {}^6H_{13/2}$ transition would appear in the ZnS electroluminescence spectrum, whereas the 460 nm $^4I_{15/2} \rightarrow {}^6H_{15/2}$ transition would be either reduced or absent. However, neither peak is apparent in the spectrum of ZnS:Dy, as seen in Fig. 5.5, whereas both are observed in SrS:Dy, as seen in Fig. 5.6. The appearance of peaks originating from higher energy states and the augmentation of the blue peak witnessed by comparison of the spectra of SrS:Dy and ZnS:Dy adds fuel to the argument that the electron distribution is hotter in SrS than ZnS phosphor hosts.



Figure 5.5: The electroluminescent spectrum of a ZnS:Dy,F ACTFEL device.
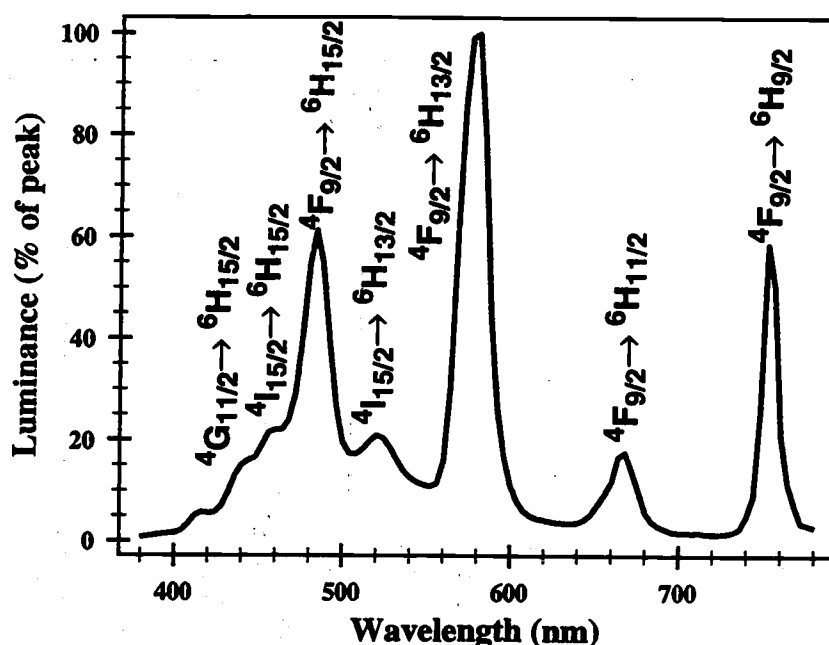
Figure 5.6: The electroluminescent spectrum of a SrS:Dy,F ACTFEL device.

With the elimination of absorption in ZnS as the cause of the lack of short wavelength light in rare earth activated ZnS ACTFEL phosphors, additional information must be gathered from other rare earth activators exhibiting short wavelength luminescent transitions. Another of this type of activator is $Ho^{3+}$, which possesses a plethora of luminescent transitions in the visible region of the spectrum. As a result, $Ho^{3+}$ is the next activator considered in an attempt to uncover the physical mechanism behind the differences in the spectra of 4f intrashell transition rare earth activator doped ZnS and SrS. The emission color of ZnS:Ho is a saturated green color as a result of the spectral dominance of the green, 550 nm $^5S_2 \rightarrow {}^5I_8$ luminescent transition of $Ho^{3+}$, as seen in Fig. 5.7. In addition, several smaller side peaks appear in the spectrum of ZnS:Ho from emissions originating from the higher lying $^5F_3$ excited state. However, the spectrum of SrS:Ho shown in Fig. 5.8 shows the existence of a number of luminescent transitions of $Ho^{3+}$ that are completely absent
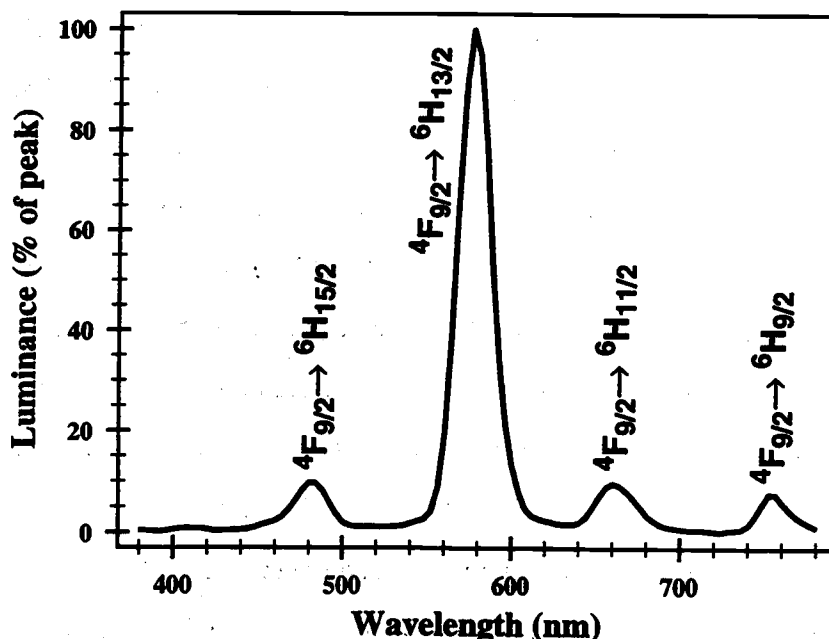
Figure 5.7: The electroluminescent spectrum of a ZnS:Ho,F ACTFEL device.
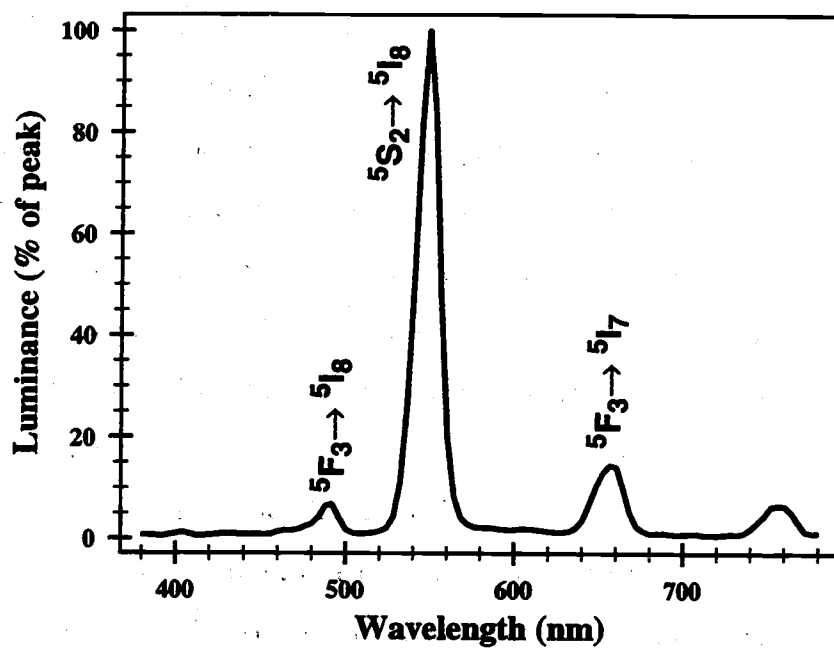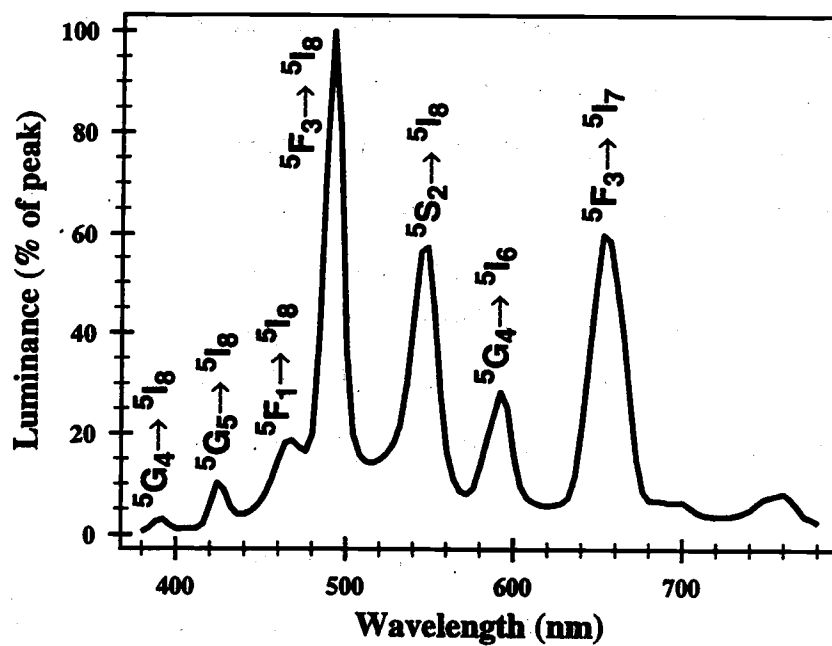


Figure 5.8: The electroluminescent spectrum of a SrS:Ho,F ACTFEL device.

in the spectrum of ZnS:Ho. These additional luminescent transitions originate from the higher-lying $^5G_4$, $^5G_5$, and $^5F_1$ excited states of $Ho^{3+}$, once again demonstrating the propensity of the SrS phosphor host to exhibit transitions originating from higher energy states than are observed in the ZnS phosphor host. In addition, the luminescent transitions originating from the $^5F_3$ excited state of $Ho^{3+}$ dominate the spectrum of SrS:Ho, whereas the luminescent transition originating from the lower-lying $^5S_2$ excited dominates in ZnS. Finally, the appearance of the luminescent peak at 600 nm due to the $^5G_4 \rightarrow ^5I_6$ transition in SrS:Ho but not ZnS:Ho adds further weight to the argument against the absorption of short wavelength visible photons in ZnS, as discussed in the analysis of ZnS:Dy and SrS:Dy above.

To complete the analysis of 4f intrashell transition rare earth activators in ZnS and SrS phosphors hosts, both ZnS and SrS are activated by $Er^{3+}$, another rare earth activator rich in short wavelength emission lines. Emission from ZnS:Er ACTFEL devices is dominated by three luminescent transitions, $^2H_{11/2} \rightarrow ^4I_{15/2}$, $^4S_{3/2} \rightarrow ^4I_{15/2}$, and $^4F_{9/2} \rightarrow ^4I_{15/2}$ in the red and green regions of the visible spectrum, as seen in Fig. 5.9. Once again, however, essentially no emission is witnessed in the blue region of the visible spectrum, despite the availability of blue-emitting transitions from higher-lying excited states. Furthermore, several of these short wavelength transitions appear in the spectrum of SrS:Er, as seen in Fig. 5.10. In fact, the near UV dominant wavelength of SrS:Er, 384 nm, does not even register in the spectrum of ZnS:Er. This is certainly a compelling piece of evidence to the effect that the electron distribution is responsible for the observed spectral differences between ZnS and SrS phosphor hosts activated by relatively phosphor host-insensitive 4f intrashell transition rare earth activators.

To further associate the spectral differences of rare earth activated ZnS and SrS ACTFEL devices to the hot electron distribution, temperature dependent spectra of ZnS:Dy and SrS:Dy are measured. The direct temperature dependence of phonon scattering leads to the conclusion that short wavelength luminescent transitions may
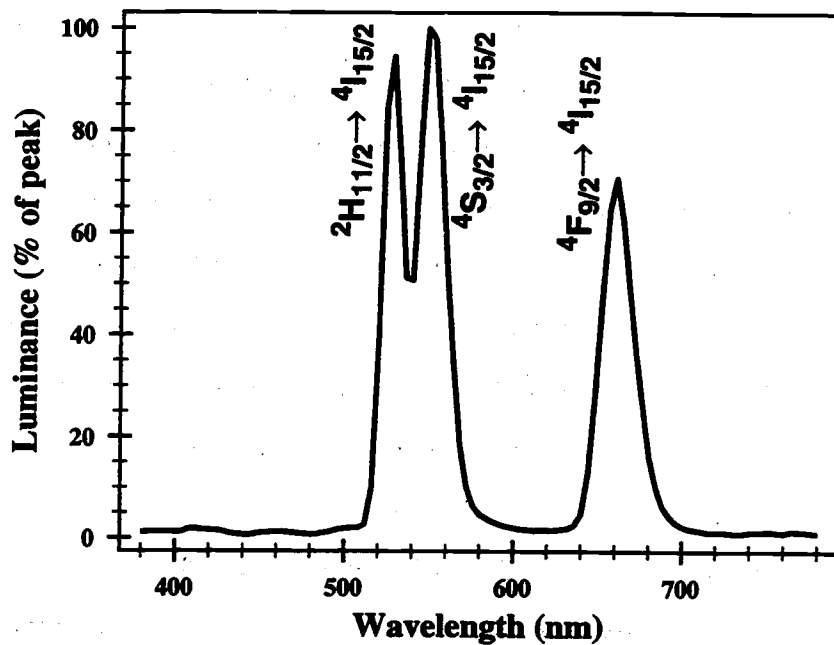
Figure 5.9: The electroluminescent spectrum of a ZnS:Er,F ACTFEL device.
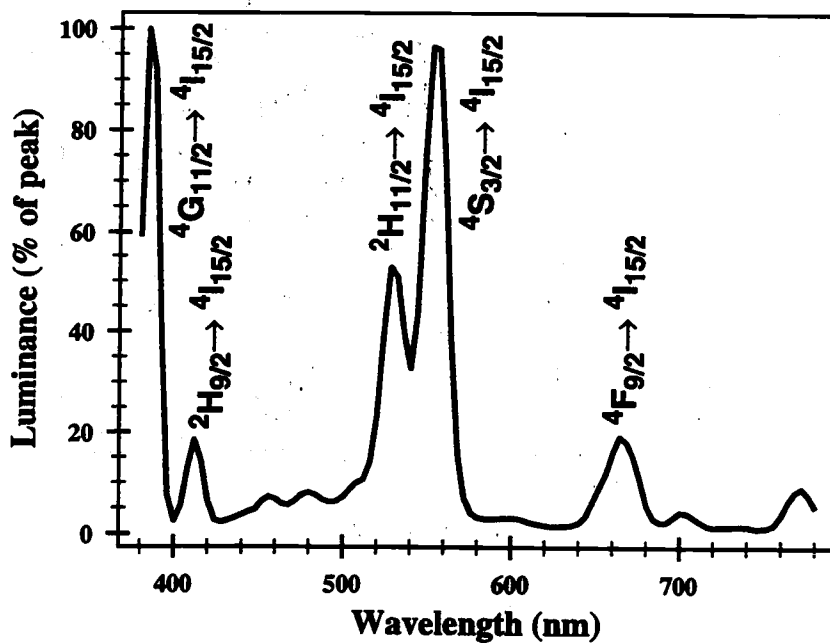


Figure 5.10: The electroluminescent spectrum of a SrS:Er,F ACTFEL device.

appear in the ZnS spectra as the temperature is reduced. In fact, short wavelength luminescent transitions that are in the noise at room temperature do indeed appear in the spectra of ZnS:Dy as the temperature is decreased, as shown in Fig. 5.11. This appearance of luminescent transitions from higher energy excited states at lower temperatures is very strong evidence for the association of the spectral differences between rare earth activated SrS and ZnS with the hot electron distribution. If this luminescent transition is not observed at room temperature due to crystal field or symmetry issues that preclude its existence, the situation would not be expected to change with temperature. For completeness, a family of electroluminescent spectra of SrS:Dy at various temperatures is shown in Fig. 5.12. This family of spectra shows significant augmentation of the short wavelength portion of the spectrum, further implicating the hot electron distribution as the origin of this effect.
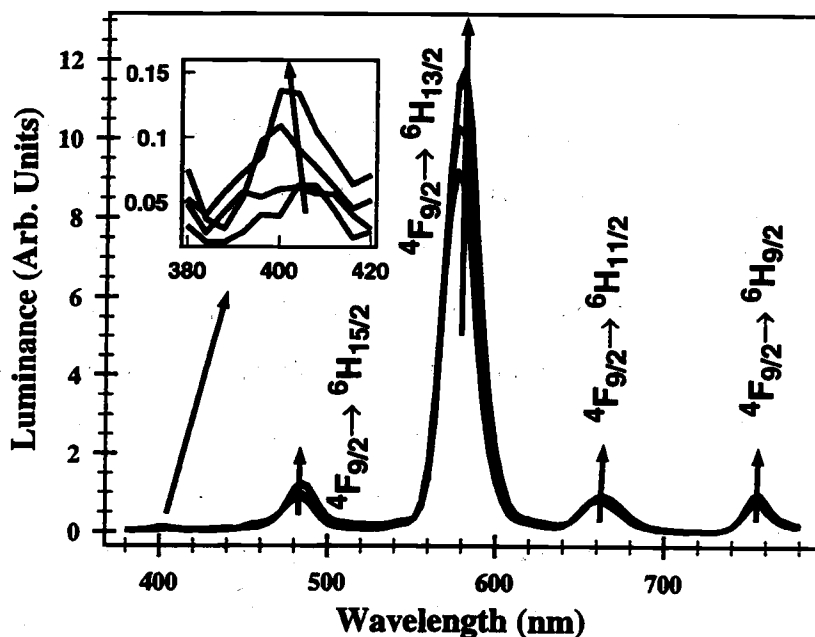


Figure 5.11: A family of electroluminescence spectra of a ZnS:Dy,F ACTFEL device at 30, 150, 300, and 360 K (arrows indicate increasing temperature).
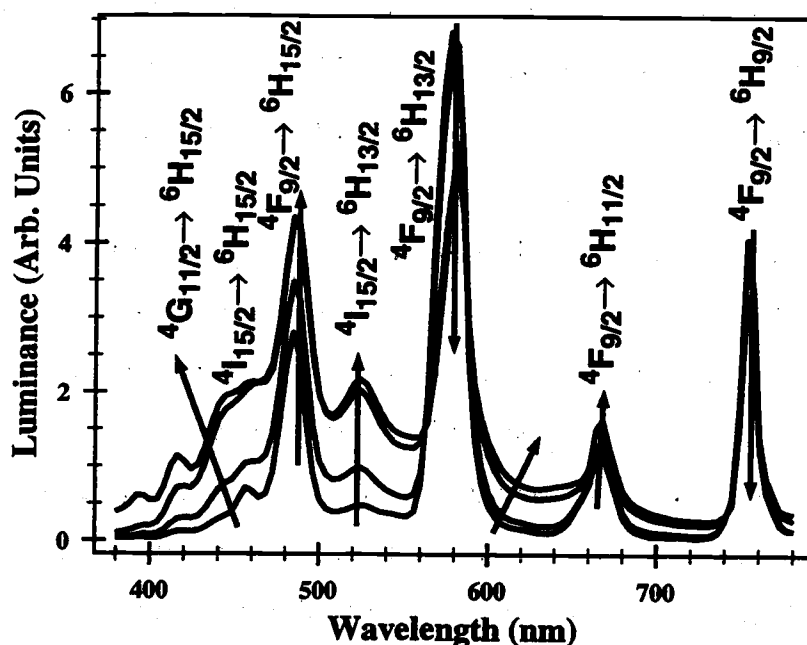
Figure 5.12: A family of electroluminescence spectra of a SrS:Dy,F ACTFEL device at 30, 150, 300, and 360 K (arrows indicate increasing temperature).

The appearance, and even dominance of short-wavelength visible and near UV peaks for all of the 4f intrashell transition rare earth activators known to emit in this region of the spectrum in SrS but not ZnS ACTFEL phosphor hosts provides a good deal of evidence that the hot electron distribution peaks at quite different energies for these phosphor hosts. In fact, the emission peaks of all such activated ZnS ACTFEL phosphors except the poor ZnS:Tm phosphor exhibit peak emission wavelengths in the 2.07-2.30 eV (540-600 nm) range of the visible spectrum, indicating that there is a good possibility that the electron energy distribution of an operating ZnS ACTFEL phosphor is peaked in this energy range. Furthermore, examination of the spectra of all of the rare earth activated ZnS ACTFEL phosphors presented in this section reveals an abrupt cut-off of all luminescent transitions with wavelength below 460 nm (2.70 eV). Since this behavior is apparently activator independent, it is probable that the electron energy distribution in an operating ZnS ACTFEL phosphor is es-

sentially zero for energies greater than 2.70 eV. This result is discouraging regarding the prospects for full-color ZnS-based ACTFEL displays due to the apparent lack of hot electrons in the blue energy regime of the visible spectrum in an operating ZnS ACTFEL phosphor.

The SrS ACTFEL phosphor, on the other hand, is rich in luminescent transitions originating from excited states lying well above 3.0 eV in energy. Since this is likely a direct result of the hot electron distribution of SrS, it seems that the electrons exciting these luminescent transitions are significantly hotter in SrS than ZnS. This result reiterates the current progress in blue-emitting ACTFEL phosphors that shies away from the ZnS phosphor host in favor of alkaline earth sulfide and thiogallate phosphors. Unlike the close proximity of the dominant wavelength for all of the ZnS ACTFEL phosphors in this study, the dominant wavelengths of the SrS phosphors are quite scattered. In fact, with the dominant wavelengths of the SrS phosphors stretching from 384 nm (3.23 eV) for SrS:Er to 580 nm (2.14 eV) for SrS:Dy, an easy identification of the peak energy of the electron distribution is not possible. However, from this data, it is likely that the hot electron distribution in SrS ACTFEL phosphors is quite broad and could quite possibly extend well into the near UV portion of the spectrum. Therefore, in view of these results, SrS appears to be a much better choice for a full-color ACTFEL phosphor host than ZnS because of its apparent hotter electron electron distribution. In addition, this study shows the possibility that SrS could be employed as the phosphor host for a UV emitting ACTFEL phosphor.

Although it is possible to ascertain that the electron distribution in a SrS ACTFEL device is hotter than in ZnS ACTFEL devices under similar operating conditions, other more fundamental physical data is clouded by the presence of space charge in these phosphor layers. The average steady-state phosphor field of the five rare earth activated SrS ACTFEL devices at 40 V above $V_{th}$ ranged between 1.2 and 1.45 MV/cm, whereas the same quantity for the ZnS phosphors ranged from 1.8 to 2.1 MV/cm, as seen in Table 5.1. However, because of the propensity for the SrS

devices to exhibit dynamic space charge effects, the smaller fields witnessed for the SrS phosphor may be a direct result of a greater concentration of space charge. The standard yardsticks for determining the presence of space charge in ACTFEL devices, C-V overshoot, $\frac{\partial Q_{max}}{\partial V_{max}}$ overshoot, and trailing edge (TE) luminescence are evaluated in Table 5.1 to provide an indication of the space charge related effects occurring in these phosphors. Furthermore, the presence of the shadowy "static" space charge in these devices may further muddle the picture of transport efficiency provided by this study. As a result, it appears that the electron energy distribution as a function of field cannot be ascertained from these spectra without making unqualified assumptions about the electric field distribution inside these phosphor layers.

Table 5.1: A summary of the characteristics of rare earth doped ZnS and SrS ACTFEL phosphors.

| Phosphor | C-V Overshoot | $\frac{\partial Q_{max}}{\partial V_{max}}$ Overshoot | TE Luminescence | $F_{ss}$ (MV/cm) | CIE x, y |
|---|---|---|---|---|---|
| ZnS:Tb | none | none | none | 1.9 | 0.31, 0.59 |
| SrS:Tb | 10% | 60% | 10% | 1.45 | 0.32, 0.55 |
| ZnS:Tm | none | 10% | none | 2.1 | 0.27, 0.27 |
| SrS:Tm | 150% | 100% | none | 1.3 | 0.29, 0.40 |
| ZnS:Dy | none | none | none | 1.95 | 0.47, 0.47 |
| SrS:Dy | none | none | 5% | 1.45 | 0.34, 0.38 |
| SrS:Dy (aged) | none | none | 1% | 1.4 | 0.43, 0.44 |
| ZnS:Ho | none | none | none | 1.9 | 0.31, 0.63 |
| SrS:Ho | 30% | 60% | none | 1.3 | 0.31, 0.43 |
| ZnS:Er | none | 40% | none | 1.8 | 0.31, 0.35 |
| SrS:Er | 15% | 100% | none | 1.2 | 0.28, 0.58 |

Due to the wealth of short wavelength transitions present in SrS:Dy and the drastic color shift that occurs with operating time, this SrS phosphor was selected as a candidate for a study of spectral aging behavior. The spectrum of a SrS:Dy ACTFEL device that has been aged for 12 hours at 40 V above threshold under a 1 kHz bipolar trapezoidal drive is shown in Fig. 5.13. Comparison of this spectrum to the unaged spectrum shown in Fig. 5.6 reveals that the short wavelength luminescent transitions are either substantially decreased in magnitude or eliminated altogether. If the spectra of these rare earth activated samples provide an indication of the electron energy distribution, as the evidence presented seems to indicate, perhaps one of the implications of ACTFEL device aging for SrS phosphors is am elimination of the high energy tail of the hot electron distribution. If this result holds for more common SrS ACTFEL phosphors, this could lead to problems with the white chromaticity of a display changing with total operation time due to preferential aging of the blue component of the phosphor.

## 5.2  Bulk phosphor charge in SrS:Cu

The presence of space charge in the phosphor bulk appears to be a universal feature of the common sulfide ACTFEL phosphors. The most well-known ACTFEL phosphor, ZnS:Mn, has typically been assumed to possess a minimum amount of bulk phosphor space charge because it exhibits electrical characteristics consistent with an interfacial model of charge injection. However, the work of Hitt et al. demonstrated the existence of a non-interacting "static" space charge in the phosphor bulk of evaporated ZnS:Mn samples. [29] This static space charge was identified by the noticeable decrease in clamping field of the ZnS:Mn phosphor with increasing phosphor thickness. Since this effect is inconsistent with a completely interfacial model of operation, and no evidence for space charge generation, or "dynamic" space charge, appears in the electrical characteristics, the presence of static space charge was deduced. In addition, most SrS-based ACTFEL devices exhibit anomalous electrical characteristics
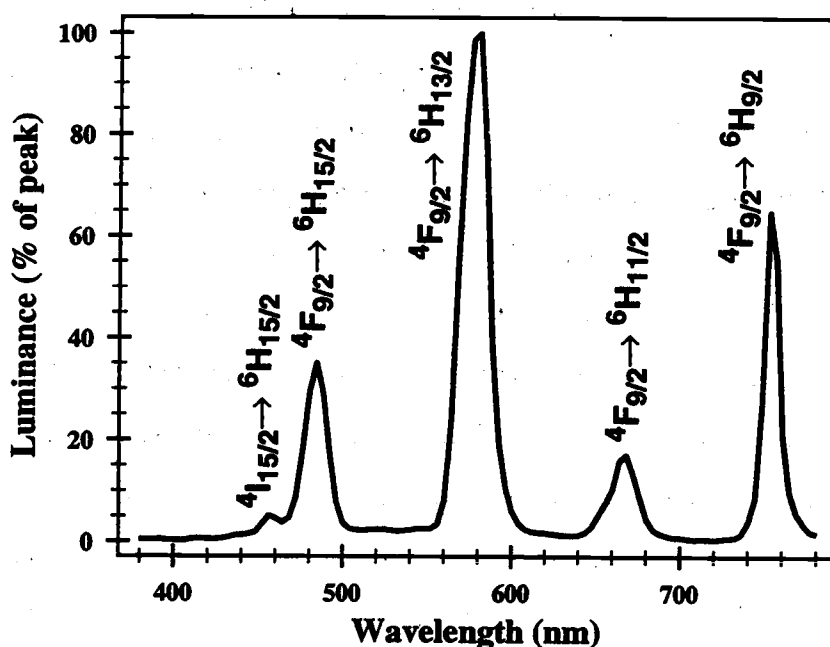
Figure 5.13: The electroluminescence spectrum of a SrS:Dy,F ACTFEL device aged for 12 hours at 40 V above $V_{th}$ under a 1 kHz bipolar trapezoidal drive.

in terms of an interfacial model of operation, such as capacitance overshoot in C-V plots and field overshoot in Q-$F_p$ plots. These effects are all a result of dynamic space charge creation in the SrS ACTFEL phosphors. However, this section attempts to identify static space charge in SrS:Cu ACTFEL phosphors by an analysis of the differences in operating phosphor fields of a series of SrS:Cu ACTFEL devices with different phosphor thicknesses.

To initiate this study, four SrS:Cu ACTFEL devices of varying thicknesses are fabricated. The SrS:Cu ACTFEL phosphors are EB evaporated from Cu-doped SrS pellets on ATO/ITO coated glass substrates to thicknesses of 2000 Å, 4700 Å, 7500 Å, and 9700 Å. These phosphors are subsequently rapid thermal annealed at 810°C for 120 seconds in an Ar atmosphere for recrystallization. Then, a 2000 Å $SiO_xN_y$ top insulator is PECVD-deposited atop the phosphor layer. Finally, 1000-1500 Å Al top electrodes are thermally evaporated.

Following completion of the fabrication of these four devices, electrical characterization via Q-$F_p$ analysis is conducted. The driving waveform for this study is the standard 1 kHz bipolar trapezoidal waveform, and the amplifier series resistance is selected to be the minimum value (100 $\Omega$) in an effort to avoid overstating the effect of dynamic space charge on the electrical characteristics. A family of Q-$F_p$ plots taken at 40 V above $V_{th}$ for each of these devices is shown in Fig. 5.14. The $C_t$ and $C_i$ values used for the Q-$F_p$ transformation are measured from the Q-V plot. It should be noted that the $C_i$ values measured vary by about $\pm 10\%$ for these samples of similar insulator structure, indicating that gross fitting errors are probably not significantly influencing the shapes of these curves. The steady-state phosphor field, $F_{ss}$, drops considerably as a function of phosphor thickness for SrS:Cu, as seen in Fig. 5.14. In fact, the change in $F_{ss}$ from the thinnest to the thickest SrS:Cu ACTFEL device is approximately 1.5 MV/cm, compared to about 0.5 MV/cm difference in phosphor fields for ZnS:Mn devices of a similar thickness range. [39] Furthermore, the turn-on characteristics of these devices become increasingly abrupt as the phosphor thickness increases. These effects add up to the conclusion that SrS:Cu ACTFEL devices are very dependent upon the sourcing of charge from the phosphor bulk for efficient operation. In addition, it can safely be concluded that the density of static space charge in SrS:Cu is significantly larger than that in ZnS:Mn. This is perhaps the reason why these wide bandgap alkaline earth sulfide phosphors are very good ACTFEL phosphors.

Another interesting feature of the Q-$F_p$ family of Fig. 5.14 is the relative magnitude of the phosphor field perturbation caused by dynamic space charge. Comparison of the magnitudes of the average phosphor field perturbation induced by static space charge and that induced by dynamic space charge, it is seen that the effect of static space charge is about an order of magnitude greater than that of dynamic space charge. Although there may be some positional dependencies involved, the magnitude of the average phosphor field perturbation caused by space charge should be
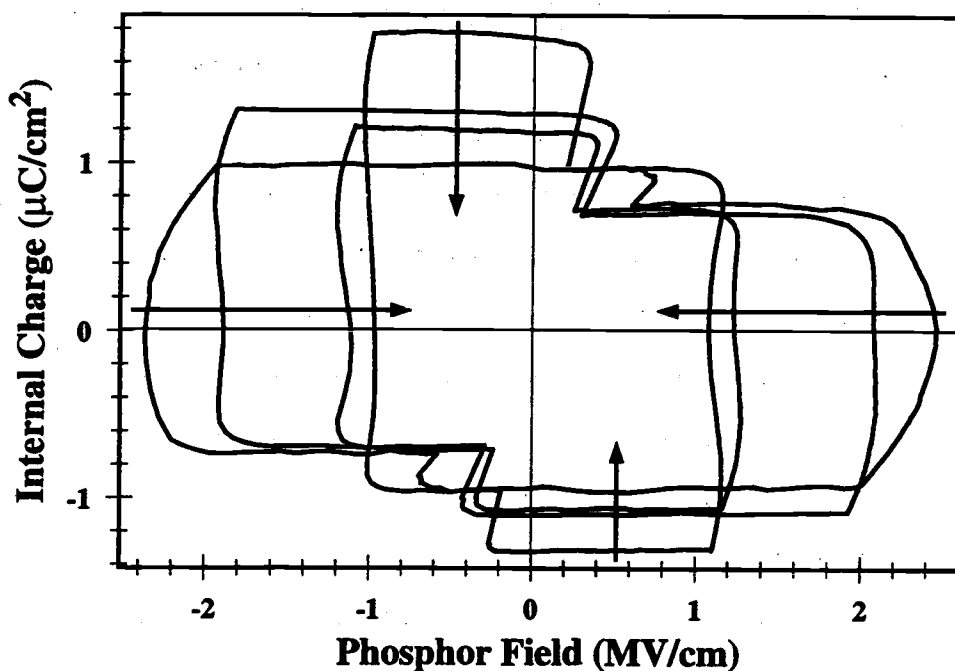
Figure 5.14: A family of Q-$F_p$ plots of SrS:Cu samples of thickness 2000 Å, 4700 Å, 7500 Å, and 9700 Å (arrows indicate increasing thickness, all devices driven at 1 kHz, 40 V above $V_{th}$).

roughly proportional to the charge density causing the perturbation. In addition, the magnitude of the field perturbation due to dynamic space charge may be even smaller than indicated because of significant voltage drops across the series resistance. This indicates that the ionized trap density due to static space charge in SrS:Cu is perhaps an order of magnitude larger than that due to dynamic space charge in these ACT-FEL devices. This is a surprising result, and may provide a clue as to the physical nature of the two types of space charge.

## 5.3  Characterization of Na halide fluxes

One of the questions that should arise in the reading of Chapter 4 is why are the color shifting alkali halide fluxes that are diffused into ACTFEL phosphors always fluorides. The aim of this section is to answer this question by fabricating and

characterizing SrS:Cu ACTFEL devices flux doped with NaF, NaCl, and NaBr. The fabrication of these three ACTFEL devices is performed via the "phosphor sandwich" technique described in Section 4.2.5. All three devices are deposited with 0.31 thickness% $Cu_2S$ to coincide with the optimum sample fabricated in Section 4.2.6, and no flux agents are coevaporated with the undoped SrS pellets. Following phosphor deposition, either NaF, NaCl, or NaBr is thermally evaporated atop one-half of the freshly deposited phosphor and subsequently rapid thermal annealed at 775°C in Ar for 120 seconds to diffuse the Cu and Na halide into the phosphor bulk. The final thicknesses of these phosphor layers are 9000 Å, 10000 Å, and 8500 Å for the NaF, NaCl, and NaBr fluxed samples, respectively. Following phosphor deposition, a 2000 Å $SiO_xN_y$ top insulator is PECVD-deposited atop each of these samples. Finally, 1000-1500 Å thick Al top electrodes are thermally evaporated.

The characterization of the resultant samples is conducted both electrically and optically in an effort to determine the effects of these fluxes on the operation of SrS:Cu. The optical characterization of these samples is centered upon examining the spectral difference between the Na halide fluxed half of each sample and the non-Na halide fluxed side. In addition, the spectral behavior of each of the Na halide fluxed portions of each sample are compared and contrasted to examine the difference in the incorporation of these three Na halide fluxes. The electrical characterization is focused upon $Q-F_p$ analysis because this analysis provides the most insight into internal device operation of the electrical characterization techniques. The electrical behavior of each half of each sample is then compared with both the other half of the sample and the other two samples.

The first sample investigated is the NaF-fluxed SrS:Cu sample. This sample is fluxed with NaF via the thermal evaporation of 135 Å (1.5% thickness) of NaF atop one-half of the 9000 Å phosphor film prior to the RTA cycle. After the RTA cycle, this sample shows bright green PL on the side of the sample fluxed with NaF, and essentially no PL on the other side. In addition, visual inspection of the sample

indicates that significant polycrystalline grain growth has taken place in the NaF-fluxed side of the sample, whereas very little has taken place in the non-NaF fluxed half. The polycrystalline grain growth is detected by a "milky" appearance to the NaF-fluxed half of the sample. The EL behavior of this sample follows the PL behavior very closely; bright green electroluminescence ($\sim$40 cd/m$^2$ at 60 Hz, CIE: x = 0.301, y = 0.599) is witnessed on devices on the NaF-fluxed side of the sample, whereas very dim, brownish electroluminescence (<0.5 cd/m$^2$ at 60 Hz, CIE: x = 0.368, y = 0.451) is obtained from the non-NaF fluxed half. This brownish electroluminescence is characteristic of SrS:Cu ACTFEL devices with a very low active Cu concentration. A spectral comparison of the two halves of the sample is shown in Fig. 5.15. The
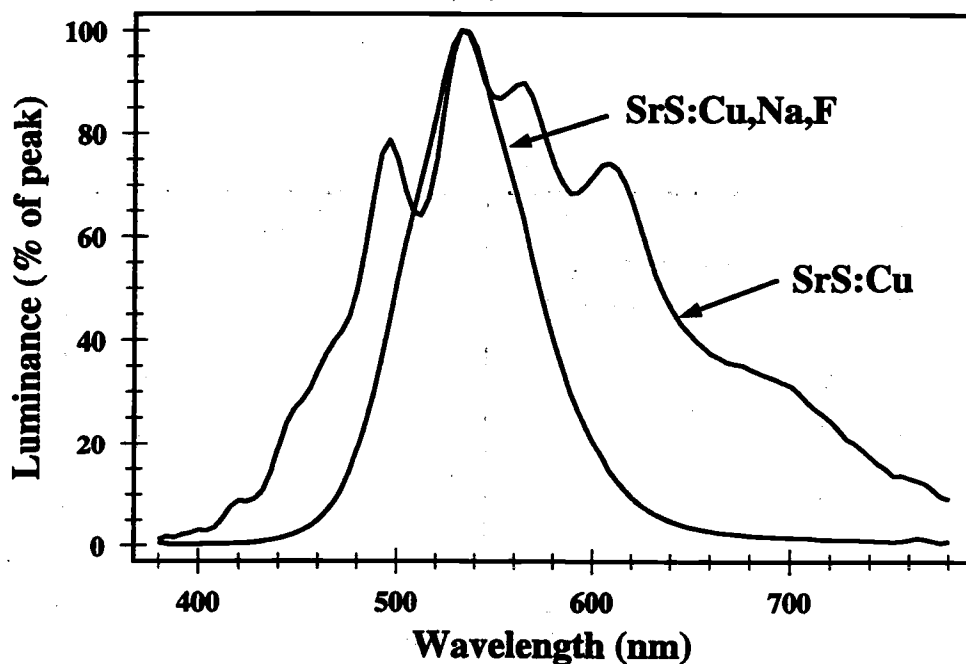


Figure 5.15: Spectra of a SrS:Cu sample both unfluxed and fluxed with NaF.

spectrum of the NaF-fluxed half of the sample is seen to be very pure, whereas the spectrum of the non-NaF fluxed half is extremely complex. The pure spectrum of

the NaF-fluxed half of the sample centered at 530 nm is a result of the emission from
5-coordinated $Cu^+$ centers in SrS according to the coordination theory of SrS:Cu
luminescence. The fluxing of SrS:Cu with NaF is very effective at creating sulfur
vacancies that result in 5-coordinated $Cu^+$, because $SrF_2$ is not soluble in SrS, and
hence, F donors segregate to the grain boundaries leaving behind Na acceptors and
sulfur vacancies. A $Q$-$F_p$ analysis of each half of this sample is conducted, and the
results are shown in Fig. 5.16. The $Q$-$F_p$ analysis of Fig. 5.16 shows minor differences
in the electrical behavior of these sides of the sample, most noticeably a decrease in
the leakage charge and elimination of offset for the NaF-fluxed side of the sample. It
should be noted that the change in the $Q$-$F_p$ plot is not as drastic as that shown in
Fig. 4.9, presumably because the Cu concentration of the sample made for this study
is smaller, and the Cu source for the sample shown in Fig. 4.9 is $CuF_2$ instead of
$Cu_2S$.
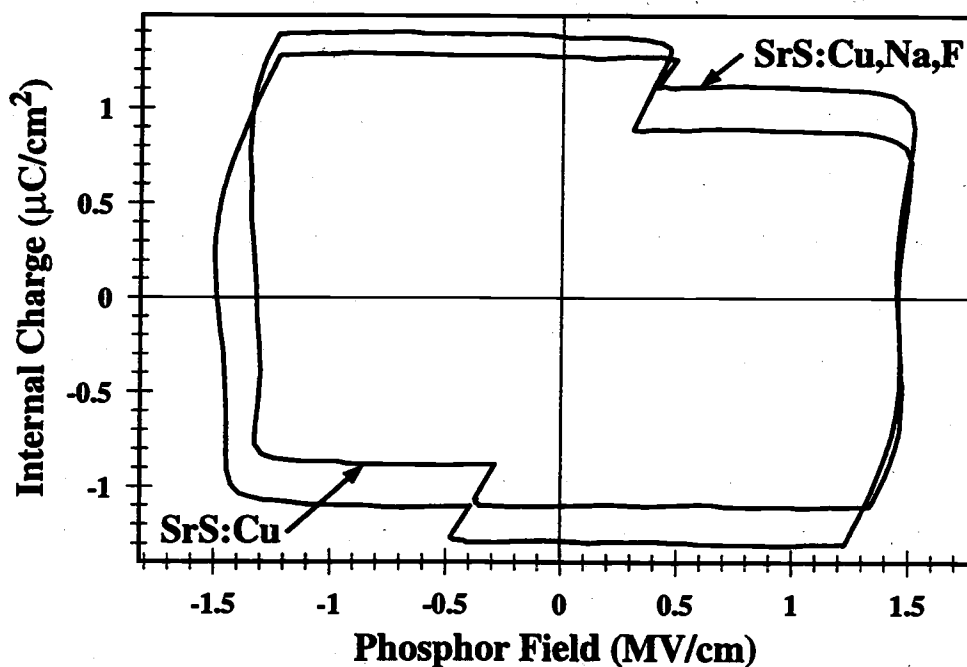


Figure 5.16: $Q$-$F_p$ plots of a SrS:Cu sample both unfluxed and NaF-fluxed (1 kHz,
40 V above $V_{th}$).

Following the investigation of NaF-fluxing of "phosphor sandwich" deposited SrS:Cu, NaCl-fluxing is investigated. The fluxing of this sample is performed by thermally evaporating the molar equivalent of the amount of NaF deposited atop one-half of the NaF-fluxed sample prior to the RTA cycle. However, no change in the PL response of this sample is witnessed as a result of the NaCl fluxing. Therefore, additional NaCl is deposited atop the fluxed half of the sample until a PL response is detected. Eventually, after deposition of 1000 Å of NaCl (total thickness) atop the NaCl-fluxed side of this sample, moderate whitish blue PL is observed, whereas none is witnessed on the non-NaCl fluxed half. In addition, visual inspection reveals a degree of polycrystalline grain growth on the NaCl-fluxed half of the sample after this thickness of NaCl is deposited, whereas none is witnessed for NaCl thicknesses up to 500Å. Similar to the NaF-fluxed sample, the EL behavior of this sample parallels the PL behavior very closely in that the NaCl-fluxed sample shows marginal whitish blue electroluminescence ($\sim$2.5 cd/m$^2$ at 60 Hz, CIE: x = 0.223, y = 0.274). In addition, the non-NaCl fluxed half of this sample emits very dim brownish electroluminescence ($<$ 0.5 cd/m$^2$ at 60 Hz, CIE: x = 0.378, y = 0.451) similar to the unfluxed half of the NaF-fluxed sample. A spectral comparison of the two halves of the sample is shown in Fig. 5.17. The unfluxed half of this sample shows essentially the same spectrum as that for the unfluxed half of NaF-fluxed sample, and thus, is not considered further. However, the NaCl-fluxed half of the sample shows a broadband emission centered at 496 nm with a tail into the IR region of the spectrum. In view of the coordination theory of Cu emission in SrS:Cu, the broad emission spectrum of this sample probably arises due to a convolution of the emission spectra of 5-coordinated, green-emitting Cu$^+$ centers and 6-coordinated, blue-emitting Cu$^+$ centers. The coexistence of 5-coordinated and 6-coordinated Cu$^+$ luminescent centers is probably due to the fact that SrCl$_2$ is soluble in SrS, and hence, Cl from the NaCl flux is incorporated into the active region of the phosphor and complexes with the Cu$^+$ centers, resulting in blue emission. A number of sulfur vacancies are created in addition, thereby leading to

some of the Cu$^+$ luminescent centers complexing with these vacancies and becoming 5-coordinated, green-emitting Cu$^+$. The IR tail of the spectrum is probably due to this film retaining some of the amorphous character of the unfluxed side of the sample because NaCl is not as effective for achieving polycrystallinity in SrS:Cu as NaF. This is seen by the similar shapes of the long wavelength sides of the unfluxed spectrum and the NaCl-fluxed spectrum.
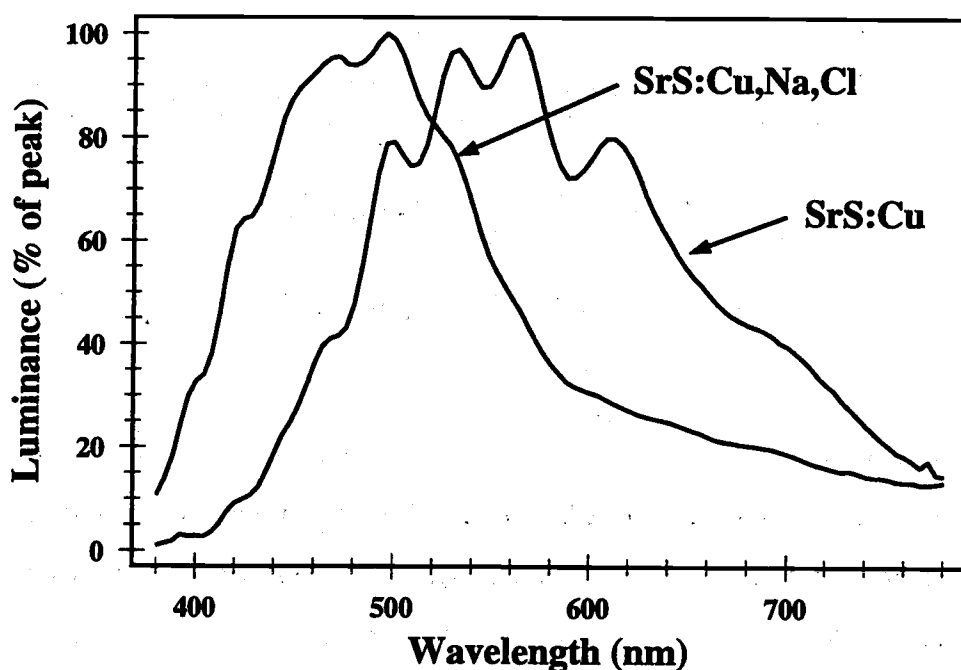


Figure 5.17: Spectra of a SrS:Cu sample both unfluxed and fluxed with NaCl.

In addition to optical characterization, electrical characterization via the Q-F$_p$ technique is performed on this NaCl-fluxed sample. The Q-F$_p$ plots of the NaCl-fluxed and unfluxed side of this sample are shown in Fig. 5.18. Inspection of Fig. 5.18 reveals striking differences in the Q-F$_p$ characteristics of the NaCl-fluxed and the unfluxed halves of the sample. The unfluxed half of the sample shows a small degree of "dynamic" space charge related effects, including a small amount of offset, some
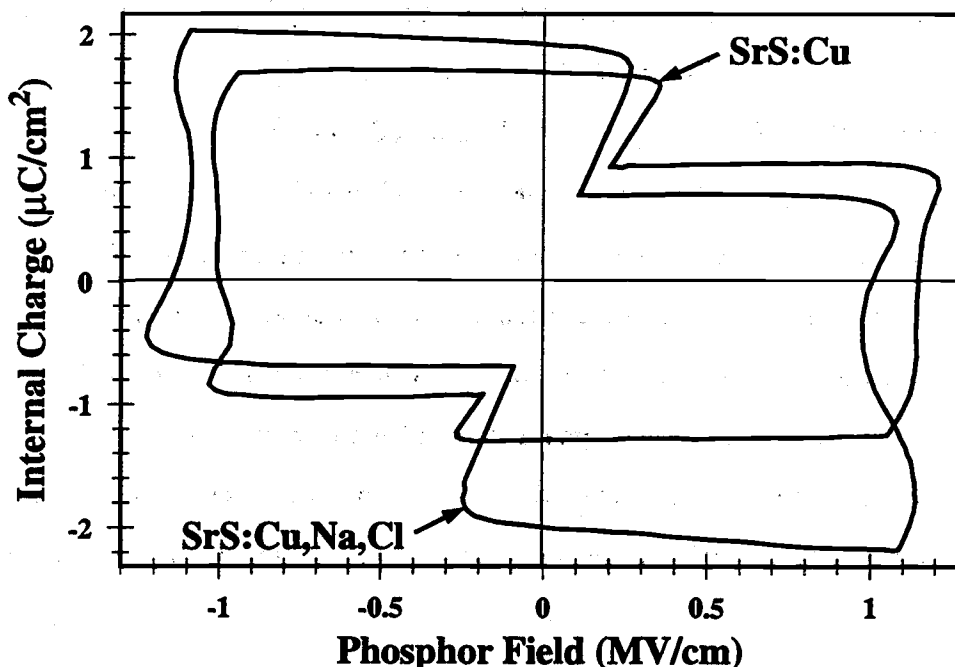
Figure 5.18: Q-F$_p$ plots of a SrS:Cu sample both unfluxed and NaCl-fluxed (1 kHz, 40 V above V$_{th}$).

phosphor field overshoot, and slightly asymmetrical transferred charge and leakage charge characteristics. In contrast, the NaCl-fluxed half of the sample shows moderate to extreme dynamic space charge effects including transferred charge during the falling edge of the driving waveform, and severe variation in the steady-state phosphor fields, F$_{ss}^+$ and F$_{ss}^-$. The proliferation of dynamic space charge effects in the NaCl-fluxed sample shown in Fig. 5.18 combined with the slight to moderate reduction in dynamic space charge effects witnessed for NaF-fluxed SrS:Cu shown in Figs. 4.9 and 5.16 gives an indication of the origins of dynamic space charge in SrS:Cu. The NaF-fluxed SrS:Cu samples are known to contain a relatively large concentration of sulfur vacancies in view of their pure green spectra shown in Figs. 4.5 and 5.15. On the other hand, the NaCl-fluxed SrS:Cu sample is known to contain Cl as a result of the fluxing of NaCl and the solubility of SrCl$_2$ in SrS. Further evidence for the incorporation of Cl into alkaline earth sulfide phosphors is presented in Chapter 4. Therefore, the

main difference between the NaF-fluxed and NaCl-fluxed SrS:Cu sample is that the presence of $Cu^+$ and $Na^+$ is compensated by the creation of sulfur vacancies in NaF-fluxed SrS:Cu, whereas the presence of $Cu^+$ and $Na^+$ is compensated by both sulfur vacancies and Cl donors in NaCl-fluxed SrS:Cu. This results in the fairly surprising conclusions that sulfur vacancies are not the physical basis of dynamic space charge in SrS:Cu ACTFEL devices, but shallow donor impurities such as Cl and their related complexes are. The role of sulfur vacancies in the operation of SrS:Cu ACTFEL phosphors then must be associated with the less interacting "static" space charge in SrS:Cu because the device characteristics of SrS:Cu ACTFEL devices known to contain large sulfur vacancy concentrations do not show evidence of increased dynamic space charge effects.

The final sample investigated for this experiment is a NaBr-fluxed SrS:Cu sample. This sample is fluxed by the thermal evaporation of a thickness of NaBr that is the molar equivalent of that deposited atop the the NaF- and NaCl-fluxed sample atop one-half of a freshly deposited SrS:Cu thin-film and subsequent annealing cycle to diffuse the NaBr into the SrS:Cu bulk. However, no differences in PL between the two sides of the sample are witnessed, even with up to 2000 Å of NaBr deposited atop one-half of the SrS:Cu phosphor film. In addition, no obvious signs of polycrystalline grain growth are witnessed for either side of this sample. The EL spectra of the two sides of this sample are strikingly similar, as seen in the comparison shown in Fig. 5.19, with both sides exhibiting dim, brownish electroluminescence characteristic of low Cu concentrations of unfluxed SrS:Cu. In addition, the $Q$-$F_p$ results from the electrical characterization of both the NaBr-fluxed and unfluxed side of this sample show remarkably similar characteristics, as seen in Fig. 5.20. As a result, it is demonstrated that NaBr is not an effective color-shifting or coactivation flux for SrS:Cu, and does not appear to incorporate into the phosphor film.

The results of this study show NaF to be a superior flux agent to NaCl and NaBr in terms of both polycrystalline grain growth and color shifting. The is probably due
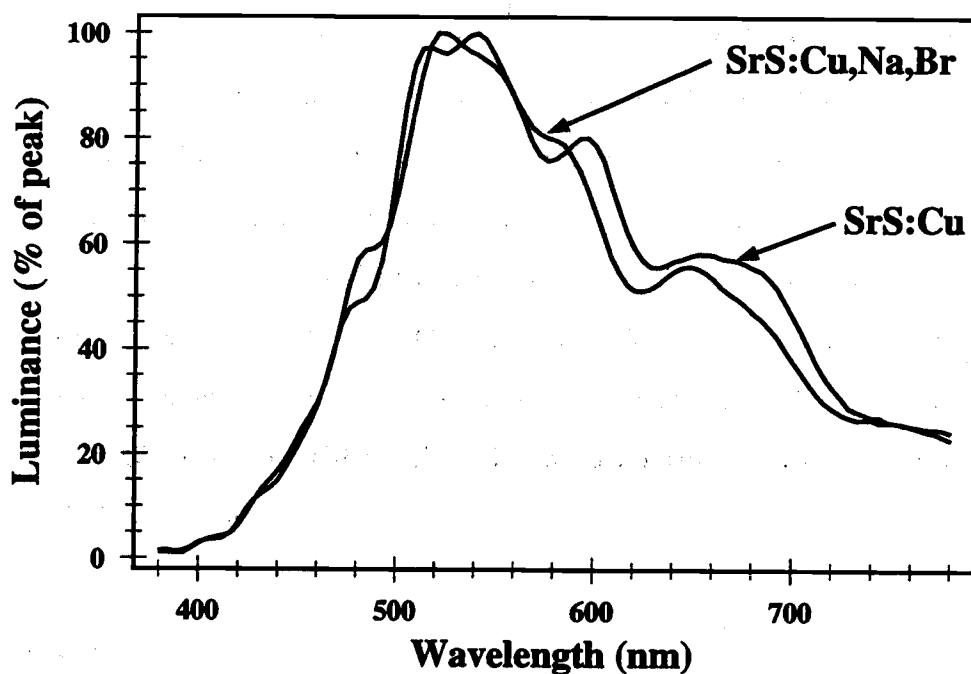
Figure 5.19: Spectra of a SrS:Cu sample both unfluxed and fluxed with NaBr.
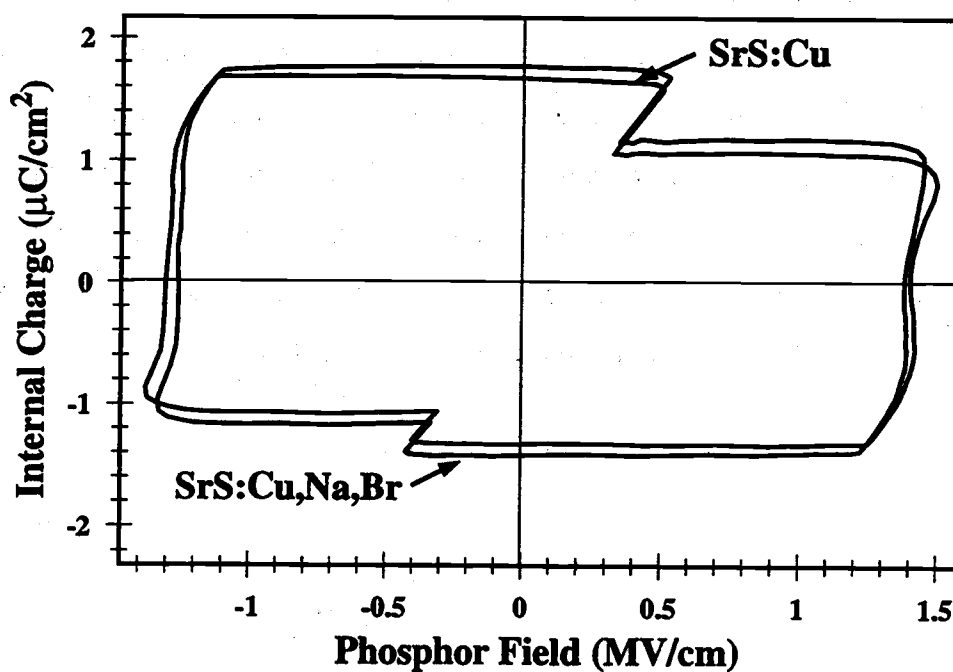


Figure 5.20: Q-F$_p$ plots of a SrS:Cu sample both unfluxed and NaBr-fluxed (1 kHz, 40 V above V$_{th}$).

to the extremely aggressive nature of F, and its ability to "drag" alkali metal atoms along with it as it reacts with Sr with eventual segregation to the grain boundaries. In addition, the small size of F probably aids its ability to diffuse into the SrS:Cu thin-film and react during an annealing cycle. Furthermore, the insolubility of $SrF_2$ in SrS should lead to a $SrF_2$ phase that segregates to the grain boundaries, resulting in little incorporation of F into the active areas of the SrS:Cu phosphor thin-film, and hence, making alkali metal fluorides the clear choice for color-shifting fluxes of SrS:Cu. In view of these results, the alkali metal halides should be less and less effective fluxes for alkaline earth sulfide ACTFEL phosphors with increasing atomic number of the halogen atom.

## 5.4   Conclusions

This chapter investigates the characterization of the two most common ACT-FEL phosphor hosts, ZnS and, in particular, SrS, from several angles in an effort to determine some of the more elusive physical characteristics of their operation. A rough sketch of the electron energy distributions of the two phosphor hosts is obtained through comparison of the spectra of 4f intrashell transition rare earth activators in the two phosphor hosts. In addition, some insight into the nature and relative magnitudes of the two types of space charge, static and dynamic space charge is gained. Finally, a comparison of flux agents of different halogen atoms yields some valuable insight into the microscopic details of the incorporation of coactivators via fluxing.

# 6. CONCLUSIONS AND RECOMMENDATIONS FOR FUTURE WORK

## 6.1  Conclusions

This thesis has focused on generating primary color ACTFEL phosphors by EBE and RF sputter deposition. A high-luminance, high-efficiency, saturated green ACTFEL phosphor, SrS:Cu,AM (AM = Na or K), has been identified as a phosphor that will likely surpass the prototypical green ACTFEL phosphor, ZnS:Tb, in the near future. In addition, several other phosphor hosts that show promise for the ACTFEL applications of the future are identified. The primary focus for identification of these promising phosphor hosts is on materials that exhibit polycrystalline grain growth at temperatures below 650°C. Also, several novel processing techniques for ACTFEL phosphor deposition are introduced, including the "phosphor sandwich" technique, which may prove extremely useful for research and perhaps manufacturing of ACTFEL phosphors.

In addition to research regarding ACTFEL fabrication, the fabrication of ACT-FEL devices to drive characterization research is undertaken. The ability to fabricate ACTFEL devices of varying compositions on demand has added an extremely powerful tool to enhance the characterization effort at OSU. This has been demonstrated by the identification of differences in the electron energy distribution between SrS and ZnS by activation with rare earth luminescent impurities that possess well-shielded luminescent transitions. In addition, the ability to fabricate custom ACTFEL devices in-house has allowed the identification of potential solutions to the "thermal quenching" problem associated with SrS:Cu ACTFEL phosphors, and has provided insight into several other classic issues regarding ACTFEL device operation. In summary, this thesis outlines a plan of attack to identify and deposit promising new ACTFEL

phosphors and to explore the physics of operation of the currently known ACTFEL phosphors from an experimental point-of-view.

## 6.2  Recommendations for future work

The observant researcher identifies many unanswered questions during the course of an extensive research project. This project is certainly no different; as most of the results obtained in this thesis lead to the identification of future research projects. The goal of this section is to provide a coherent outline from which to further the results presented in this thesis. In addition, a section outlining improvements in the currently available equipment is provided in an effort to spur future researchers into allotting time to improvement of the facilities.

### 6.2.1  Recommendations for future ACTFEL fabrication

1. Deposition of BTO top insulators on alkali metal coactivated SrS:Cu: The results of this thesis demonstrate the potential for deposition of high-luminance, high-efficiency, saturated green ACTFEL devices based on SrS:Cu. The main limitation of the current ACTFEL process here at OSU in terms of device performance is the $SiO_xN_y$ top insulator. $SiO_xN_y$ is a limitation for these devices because its relatively low dielectric constant of 6-7 results in relatively low insulator capacitances which lead to reduced coupling between the applied voltage and the phosphor field. The relatively large dielectric constant of BTO yields a top insulator capacitance that is 3-4 times larger for the same top insulator thickness. The result of an increase of the top insulator capacitance by 3 times yields a 67% increase in $C_i$. Since conduction current is directly proportional to $C_i$ for ACTFEL devices not exhibiting significant space charge generation effects, this should result in a 67% increase in conduction current. Furthermore, since luminance is proportional to conduction current, the result is a 67% increase in luminance. An increase of this magnitude in the luminance of

the phosphors investigated for this thesis should yield saturated green ACT-FEL devices with luminances above 110 cd/m$^2$. As a result, some SrS:Cu,Na and SrS:Cu,K,F phosphor layers should be deposited and sent to Planar to deposit BTO top insulators in an effort to achieve world-record luminance green ACTFEL devices.

2. Utilization of the "phosphor sandwich" ACTFEL phosphor deposition technique to investigate SrS:Cu,F and SrS:Cu,Cl: The development of the "phosphor sandwich" technique occurred rather late in the timeframe of the research conducted for this thesis. In fact, this process was developed following the completion of research on SrS:Cu,F and SrS:Cu,Cl. The increased control of dopant concentrations available with the "phosphor sandwich" technique will allow much more consistent deposition of SrS:Cu,F and SrS:Cu,Cl than achievable with the multisource evaporation technique. As a result, the "phosphor sandwich" technique should be applied to SrS:Cu,F and SrS:Cu,Cl in an effort to deposit better blue and green SrS:Cu phosphors.

3. Low-temperature processing of SrS:Cu,Cl: It is noticed that SrS:Cu ACTFEL devices deposited with the "phosphor sandwich" technique and a KCl flux during SrS evaporation recrystallize to a much greater degree than devices deposited in the same manner, but without the KCl flux. This leads to the conclusion that the incorporation of Cl from the KCl may lead to a phosphor that possesses a lower recrystallization temperature than pure SrS. This avenue should be investigated as a means of depositing a blue phosphor with an RTA temperature at or below 650°C in an effort to develop a manufacturable process for blue-emitting SrS:Cu.

4. Optimization of the (Sr,Ba)S:Cu,Na alloy system: The alloying of SrS:Cu,Na and BaS:Cu,Na is demonstrated in this thesis to be an effective means of controlling the color spectrum of ACTFEL devices based on such a phosphor. Results

from powder phosphors show that a small (<10 mol%) concentration of BaS leads to a markedly increased efficiency over pure SrS. This result may translate into an increase in the performance of ACTFEL devices based on such an alloy as well, and should be investigated as a means of improving the performance of SrS:Cu,Na. Incorporation of small amounts of Ba should not shift the color of SrS:Cu,Na so much as to significantly shift the color away from saturated green. The results of the evaporation of $Sr_{0.9}Ba_{0.1}S$ pellets for this thesis show that about 30 mol% BaS is incorporated into the phosphor film due to the preferential evaporation of BaS in view of its lower evaporation temperature. As a result, pellets of the approximate composition $Sr_{0.97}Ba_{0.03}S$ should be fabricated to generate films of the appropriate alloy composition.

5. The optimization of BaS:Cu,K: In view of the results with BaS:Cu,K, an effort should be undertaken to optimize the Cu and K concentrations for maximum luminance and efficiency in the red region of the spectrum. This effort can be undertaken in the short-term with the fabrication of a set of undoped BaS pellets. This optimization should be performed in a manner akin to that employed for the optimization of SrS:Cu,Na presented in Section 4.2.6. If it is deemed impossible to achieve a saturated red color with this phosphor system, an alloy such as $BaS_xSe_{1-x}$:Cu,K should be considered as a means of color-shifting further into the red region of the spectrum.

6. Further investigation into the SrSe:Cu ACTFEL phosphor: Considering the low purity and small amount of the SrSe source material for the investigation of SrSe:Cu, the results thus obtained are quite encouraging. In view of this, an effort should be undertaken to more seriously evaluate the potential of SrSe:Cu for ACTFEL applications. This effort should include the acquisition or synthesis of higher purity source material, along with a thorough investigation of coactivators and flux agents for this material. If high-luminance SrSe-based ACTFEL

devices can be deposited, this phosphor could challenge SrS as a full-color ACT-FEL phosphor host in view of its decreased recrystallization temperature.

7. Alkali halide coactivation of alkaline earth sulfides and selenides other than SrS: The similarities between the alkaline earth sulfides and selenides are quite numerous. As a result, the drastic performance increases achieved by coactivation of SrS:Cu with alkali halides may also be attainable with any of the other alkaline earth sulfide or selenide phosphors. Compared to SrS, the remaining alkaline earth sulfides are relatively unknown, and some excellent ACTFEL phosphors may be amongst these. In addition, the alkaline earth selenides are quite uncommon materials, and alkali halide coactivation of some of these compounds may produce some tantalizing results.

8. Investigation of the feasibility of telluride phosphors: Taking the next logical step in attempting to reduce the recrystallization temperature of ACTFEL phosphors, the alkaline earth tellurides may provide an answer. With the periodic table trend of reduced melting point as one progresses down a column of the periodic table, the recrystallization temperature of the alkaline earth tellurides may be quite depressed from that of the alkaline earth sulfides. However, these materials appear to be absolutely unexplored for phosphor applications, and an attempt should be made to determine if there is a good reason for this. In addition to the advantages in terms of reduced recrystallization temperature, the instability of $H_2Te$ may mean that the alkaline earth tellurides will possess a low moisture sensitivity. The only telluride compounds of interest for ACTFEL applications appear to be CaTe and SrTe, mainly due to bandgap concerns.

9. Optimization of the Mn concentration of $Zn_2GeO_4$:Mn: The results of the study of $Zn_2GeO_4$:Mn show that this phosphor is especially sensitive to the Mn concentration in terms of luminance and efficiency. However, because this compound is typically deposited via RF sputtering, it is time and material consum-

ing to perform concentration studies. As a result, the Mn concentration in this phosphor should be optimized through different means. A possible solution is the acquisition of an undoped $Zn_2GeO_4$ target with Mn incorporation by the deposition of thin layers of Mn, MnO, $MnF_2$, or $MnCl_2$ to be RTA diffused into the undoped $Zn_2GeO_4$:Mn phosphor. Then, once an optimum concentration has been determined, an optimized film could be sent for analysis to determine the Mn concentration in the phosphor film, and hence, a game plan for the fabrication of Mn optimized $Zn_2GeO_4$:Mn sputtering targets could be realized.

10. Investigation of $Zn_2Si_xGe_{1-x}O_4$:Mn: Several research groups have reported very high-luminance, high-efficiency ACTFEL devices based on the alloy $Zn_2Si_x$-$Ge_{1-x}O_4$:Mn. If these results are reliable, this phosphor should be investigated in an effort to improve on previous results and to understand its operation. If oxide ACTFEL phosphors typically operate in a similar manner to $Zn_2GeO_4$:Mn, there is still much to be learned about their operation. A concerted fabrication/characterization effort on this ACTFEL phosphor has the potential to pay large dividends.

## 6.2.2 Recommendations for future ACTFEL characterization

The ability to fabricate ACTFEL devices for characterization projects allows for the implementation of much more focused characterization projects. Specifically, the effects of incorporation of many common impurities and coactivators can be studied through the controlled addition of impurities and subsequent characterization. As a result of this capability, there are fabrication/characterization projects that should be investigated in the immediate future.

1. A rare earth activation study of CaS and BaS: The rare earth activation study presented in Section 5.1 should be repeated for both CaS and BaS in order to assess the potential of these phosphor materials for full-color phosphor applications. This may also be an appropriate experiment for the alkaline earth

selenides to assess whether these materials are worth pursuing as full-color ACT-FEL phosphor hosts.

2. "Thermal quenching" of SrS:Cu: The ability to fabricate ACTFEL devices of any composition allows the investigation of the effects of a variety of coactivators on the thermal quenching behavior of SrS:Cu. In this manner, the origins of thermal quenching should be able to be pinpointed.

3. Static space charge in ACTFEL phosphors: Static space charge in alkali metal coactivated SrS:Cu phosphors should be investigated by the means presented in Section 5.2 to assess its importance in terms of the operation of these devices. In addition, this may provide information linking sulfur vacancies to static space charge.

### 6.2.3 Equipment

The goal of having a world-class ACTFEL phosphor characterization and fabrication research facility here at OSU is certainly within sight. To achieve this goal, however, attention must be paid to the addition of some new equipment and the enhancement of the current equipment. The availability of quality equipment can certainly be a limiting factor when competing for research money with some of the best-funded research universities in the nation. As a result, several new pieces of equipment should be added to enhance the ACTFEL device fabrication process here at OSU.

1. A BTO sputtering system: The biggest obstacle holding back the effort here at OSU to deposit the brightest ACTFEL devices in the world is the top insulator process. As discussed in Section 6.2.1, an improvement in the insulator process to the level available to Planar or some of the other top ACTFEL phosphor labs worldwide is critical to fabricating extremely high-luminance ACTFEL devices. Probably the best insulator for ACTFEL applications yet identified is BTO

due to its high dielectric constant and concomitant large breakdown field. A sputtering system to allow the deposition of such an insulator could pay huge dividends in the fabrication effort and the ability to investigation new phosphor materials. A system for this application, however, should have a very large cathode (>6") in order to uniformly and rapidly deposit a top insulator over an ACTFEL sample. In addition, this system should have a moving substrate to enhance uniformity and film density.

2. Optical thickness measurement: Another obstacle hindering the ACTFEL fabrication project is the availability of a reliable optical film thickness measurement system. Currently, it is necessary to measure film thicknesses with a profilometer, which requires exposure of unannealed phosphor films to the atmosphere for longer than would be necessary if a phosphor thickness could be measured following insulator deposition. Since moisture sensitive materials are most sensitive to moisture incorporation before annealing because this is the stage of the process where the phosphor film is most likely to be underdense and contain pores for moisture to bind to, minimization of atmospheric contact for unannealed phosphor materials is critical to their performance. Fortunately, most of the equipment necessary to perform this measurement has been obtained, but time must be spent implementing a reliable method for using this equipment to measure thicknesses of stacked films.

In addition to the new equipment that should be added, there are many pressing needs for upgrading the existing equipment to achieve higher film quality. The existing systems will be investigated on a system-by-system basis to accomplish the task of identifying critical system upgrades.

- Ellipsometer: The ellipsometer should be sent in to the manufacturer for a complete rebuild and the installation of a new computer interface. The lack of

a working ellipsometer greatly hinders PECVD work due to its place as a rapid feedback loop for the characterization of PECVD depositions.

- E-beam evaporator: The e-beam evaporator could use several enhancements that would be beneficial to its performance. The first and most expensive is the acquisition of a newer model electron gun and power supply. The 1960's generation electronics in the electron-beam power supply produce excessive drift in the electron gun emission current that often leads to difficulty in controlling evaporation rate. In addition, newer electron guns and power supplies are equipped with the capability to raster the electron beam over the source material, and hence, avoid changes in the evaporation distribution and characteristics with changing source material geometry. Furthermore, a newer electron beam system in combination with a deposition rate controller may provide an extremely controllable means of evaporating ACTFEL phosphor materials. In addition, a cryopump should be considered for this system because of its high capacity for the pumping of water vapor, which is the most troublesome species for ACTFEL phosphor deposition. Also, the addition of a sorption pump to this system may help reduce residual water vapor levels inside the chamber.

- RF sputtering system: The most pressing need for the RF sputtering system is the acquisition of a turbomolecular pump to replace the current diffusion pump. Turbomolecular pumps are the most versatile pumps for ACTFEL phosphor deposition because they are the most reliable pumps for the pumping of sulfur-based vapors. In addition, turbomolecular pumps are very clean because their mechanics are completely sealed from the vacuum chamber.

- PECVD system: The biggest need for the PECVD system is a new matching network. The existing matching network is not reliable in terms of automatching the PECVD plasma. The addition of a reliable automatching network would allow more consistent PECVD deposition because the drift in plasma charac-

teristics during a deposition could be negated. In addition, the implementation of a computer controller for this system would allow the deposition of inhomogeneous dielectrics for optical coating and ACTFEL insulator applications.

- RTA: The RTA system should be fitted with a scrubber and gas tank containment cabinet to allow the annealing of samples in atmospheres of gases such as $H_2S$, methyl mercaptan, $NH_3$, and $N_2O$. The loss of anionic species during the annealing cycle can be counteracted through the annealing of sample in such gases, necessitating their use for increased device performance.

# BIBLIOGRAPHY

1. K. Werner, "U.S. display industry on the edge," *IEEE Spectrum*, vol. 32, pp. 62–69, May 1995.

2. B. R. Chalamala, Y. Wei, and B. Gnade, "FED up with fat tubes," *IEEE Spectrum*, vol. 35, pp. 42–51, Apr. 1998.

3. I. Khormaei, *High resolution electroluminescent displays using active matrix approach*. PhD thesis, Oregon State University, 1995.

4. Y. A. Ono, *Electroluminescent displays*. Singapore: World scientific, 1995.

5. T. Minami, T. Miyata, K. Kitamura, H. Nanto, and S. Takata, "Low-voltage driven MOCVD-grown ZnS:Mn thin-film electroluminescent devices using insulating BaTiO$_3$ ceramic sheets," *Jpn. J. Appl. Phys.*, vol. 27, pp. L876–L879, May 1988.

6. T. Minami, T. Miyata, S. Takata, and I. Fukuda, "High-luminance green Zn$_2$SiO$_4$:Mn thin-film electroluminescent devices using an insulating BaTiO$_3$ ceramic sheet," *Jpn. J. Appl. Phys.*, vol. 33, pp. L117–L119, 1991.

7. T. Inoguchi, M. Takeda, Y. Kakihora, and M. Yoshida, "Stable high luminance thin-film electroluminescenct panels," *SID Digest*, vol. 5, p. 84, 1974.

8. D. H. Smith, "Modeling a.c. thin-film electroluminescent devices," *J. Lumin.*, vol. 23, pp. 209–235, 1981.

9. E. Bringuier, "Charge transfer in ZnS-type electroluminescence," *J. Appl. Phys.*, vol. 66, pp. 1314–1325, Aug. 1989.

10. K. A. Neyts and P. De Visschere, "Analytical model for thin-film electroluminescent devices," *J. Appl. Phys.*, vol. 68, pp. 4163–4171, Oct. 1990.

11. J. F. Wager and P. D. Keir, *Electrical characterization of thin-film electroluminescent devices*, vol. 27, pp. 223–248. Annual Review of Materials Science, 1997.

12. K. Bhattacharyya, S. M. Goodnick, and J. F. Wager, "Monte-carlo simulation of high-field electron transport in alternating-current thin-film electroluminescent devices," *J. Appl. Phys.*, vol. 73, no. 7, pp. 3390–3395, 1993.

13. E. Bringuier, "Tentative anatomy of ZnS-type electroluminescence," *J. Appl. Phys.*, vol. 75, no. 9, pp. 4291–4312, 1994.

14. E. Bringuier, "High-field conduction in semi-insulating ZnS films," *Philos. Mag. B*, 1996.

15. E. Bringuier, "Charge transfer in ZnS-type electroluminescence revisited," *Appl. Phys. Lett.*, vol. 60, no. 10, pp. 1256–1258, 1992.

16. P. D. Keir, W. M. Ang, and J. F. Wager, "Modeling space charge in alternating-current thin-film electroluminescent devices using a single-sheet charge model," *J. Appl. Phys.*, vol. 78, pp. 4668–4680, Oct. 1995.

17. K.-W. C. Yang and S. J. T. Owen, "Mechanisms of the negative-resistance characteristics in ac thin-film electroluminescent devices," *IEEE Trans. Electron Devices*, vol. ED-30, pp. 452–459, May 1983.

18. N. E. Rigby, T. D. Thompson, and J. W. Allen, "Hot-electron effects in zinc sulphide," *J. Phys. C: Solid State Phys.*, vol. 21, pp. 3295–3303, 1988.

19. T. D. Thompson and J. W. Allen, "Electroluminescence from minority carrier injection produced by deep-level impact ionization," *J. Crystal Growth*, vol. 101, pp. 981–984, 1990.

20. S.-P. Shih, P. D. Keir, and J. F. Wager, "Space charge generation in ZnS:Mn alternating-current thin-film electroluminescent devices," *J. Appl. Phys.*, vol. 78, pp. 5775–5781, Nov. 1995.

21. W. E. Howard, O. Sahni, and P. M. Alt, "A simple model for the hysteretic behavior of ZnS:Mn thin-film electroluminescent devices," *J. Appl. Phys.*, vol. 53, pp. 639–647, Jan. 1982.

22. J. M. Jarem and V. P. Singh, "A computationally simple model for hysteretic thin-film electroluminescent devices," *IEEE Trans. Electron Devices*, vol. ED-35, pp. 1834–1841, Nov. 1988.

23. K. A. Neyts, "Simple model for the hysteretic behavior of thin-film electroluminescent devices," *IEEE Trans. Electron Devices*, vol. 38, pp. 2604–2611, Dec. 1991.

24. A. Goldenblum, A. Oprea, and V. Bogatu, "Time behavior of currents in ZnS:Mn metal-insulator-semiconductor-insulator-metal structures," *J. Appl. Phys.*, vol. 75, pp. 5177–5185, May 1994.

25. K. A. Neyts, D. Corlatan, P. D. Visschere, and J. V. den Bossche, "Observation and simulation of space-charge effects and hysteresis in ZnS:Mn ac thin-film electroluminescent devices," *J. Appl. Phys.*, vol. 75, pp. 5339–5346, May 1994.

26. N. A. Vlasenko, A. I. Beletskii, Z. L. Denisova, and Y. F. Kononets, "Transient characteristics and photodepolarization spectra of SrS:Ce," in *Extended abstracts of the third international conference on the science and technology of display phosphors*, (Huntington Beach), pp. 77–80, Nov. 1997.

27. S. Kobayashi, J. F. Wager, and A. Abu-Dayah, "Distribution of trapped electrons at interface states in ACTFEL devices," in *Proceedings of the 6th international conference on electroluminescence* (V. P. Singh and J. C. McClure, eds.), pp. 234–239, Cinco Puntos, May 1992.

28. K. Ohmi, K. Ishitani, S. Tanaka, and H. Kobayashi, "Role of space charge in SrS:Ce thin-film electroluminescent devices studied by the photoirradiation effect," *Appl. Phys. Lett.*, vol. 67, pp. 944–946, Aug. 1995.

29. J. C. Hitt, P. D. Keir, J. F. Wager, and S.-S. Sun, "Static space charge in evaporated ZnS:Mn alternating-current thin-film electroluminescent devices," *J. Appl. Phys.*, vol. 83, pp. 1141–1145, Jan. 1998.

30. M. Beale, "Uniform and filamentary transport in d.c. thin-film ZnS:Mn electromluminescent devices," *Philos. Mag. B*, vol. 68, pp. 573–594, Nov. 1993.

31. W. M. Ang, S. Pennathur, L. Pham, J. F. Wager, and S. M. Goodnick, "Evidence for band-to-band impact ionization in evaporated ZnS:Mn alternating-current thin-film electroluminescent devices," *J. Appl. Phys.*, vol. 77, pp. 2719–2724, Mar. 1995.

32. D. Corlatan, K. Neyts, P. D. Visschere, J. V. den Bossche, and B. Maximus, "Properties of charge carriers in ZnS and their effect on the excitation of Mn," *J. SID*, vol. 5, no. 2, pp. 131–136, 1997.

33. B. A. Cleary, P. D. Keir, J. C. Hitt, T. K. Plant, and J. F. Wager, "Photoinduced charge and luminescence measurements of evaporated ZnS:Mn ACTFEL devices," in *Extended abstracts of the third international conference on the science and technology of display phosphors*, (Huntington Beach), pp. 65–68, Nov. 1997.

34. J. B. Peery, P. D. Keir, W. M. Ang, and J. F. Wager, "Simulation of evaporated ZnS:Mn ACTFEL devices," in *Extended abstracts of the third international conference on the science and technology of display phosphors*, (Huntington Beach), pp. 69–72, Nov. 1997.

35. D. A. Buchanan, M. V. Fischetti, and D. J. DiMaria, "Coulombic and neutral trapping centers in silicon dioxide," *Phys. Rev. B: Condens. Matter*, vol. 43, pp. 1471–1486, Jan. 1991.

36. A. A. Douglas, "Alternating-current thin-film electroluminescent device physics and modeling," M.S. thesis, Oregon State University, 1993.

37. A. Aguilera, V. P. Singh, and D. C. Morton, "Electron energy distribution at the insulator-semiconductor interface in AC thin-film electroluminescent display devices," *IEEE Trans. Electron Devices*, vol. 41, pp. 1357–63, Aug. 1994.

38. S. Bhaskaran, V. P. Singh, and D. C. Morton, "Electron ejection processes at insulator-semiconductor interfaces in ACTFEL display devices," *IEEE Trans. Electron Devices*, vol. 42, pp. 1756–1762, Oct. 1995.

39. J. C. Hitt, "Static space charge in evaporated ZnS:Mn alternating-current electroluminescent devices," M.S. thesis, Oregon State University, 1998.

40. J. B. Peery, "State space modeling of alternating-current thin-film electroluminescent devices," M.S. thesis, Oregon State University, 1998.

41. S.-S. Sun, E. Dickey, J. Kane, and P. N. Yocom, "A bright and efficient new blue TFEL phosphor," in *Conference record '97 IDRC*, pp. 301–304, Sept. 1997.

42. U. Troppenz, B. Huttl, U. Storz, P. Kratzert, K. O. Velthaus, S.-S. Sun, and R. T. Tuenge, "Photoluminescence and electroluminescence studies on Cu and Ag doped SrS ACTFEL devices," in *Extended abstracts of the fourth international conference on the science and technology of display phosphors / the ninth international workshop on inorganic and organic electroluminescence*, pp. 187–190, Sept. 1998.

43. P. D. Keir, H. Le, R. L. Thuemler, J. Hitt, and J. F. Wager, "Relaxation charge anomalies in the charge-voltage characteristics of alternating-current thin-film electroluminescent devices," *Appl. Phys. Lett.*, pp. 2421–2422, Oct. 1996.

44. P. Atkins, *Physical chemistry*. New York: W. H. Freeman and Company, fifth ed., 1994.

45. R. Glang, "Vacuum evaporation," in *Handbook of thin film technology* (L. I. Maissel and R. Glang, eds.), ch. 1, New York: McGraw-Hill, 1970.

46. S. Wolf and R. N. Tauber, *Silicon processing for the VLSI era*, vol. 1: Process technology. Sunset Beach, CA: Lattice Press, 1986.

47. K. Onisawa, M. Fuyama, K. Taguchi, K. Tamura, and Y. A. Ono, "Luminance improvement of blue-green emitting SrS:Ce EL cell by controlling vacuum conditions with sulfur addition," *J. Electrochem. Soc.*, vol. 135, pp. 2631–2634, Oct. 1988.

48. S. Okamoto and E. Nakazawa, "Transient emission mechanisms in thin-film electroluminescent devices with rare-earth-ion-activated SrS phosphor layers," *Jpn. J. Appl. Phys.*, vol. 34, pp. 521–526, Feb. 1995.

49. H. Kina, Y. Tamura, Y. Yamada, and Y. Maruta, "The characteristics of SrS:Ce thin film electroluminescent devices," *Jpn. J. Appl. Phys.*, vol. 36, pp. 150–154, Jan. 1997.

50. T. Minami, T. Nishiyama, S. Tojo, and S. Takata, "An electroluminescent device using sintered manganese-doped zinc sulfide phosphor ceramics," in *Proceedings of the 4th international conference on electroluminescence* (S. Shionoya and H. Kobayashi, eds.), (Berlin), Springer-Verlag, 1989.

51. R. Bensalem, N. J. Barrett, and B. J. Sealy, "AlN capped annealing of Se and Sn implanted semi-insulating GaAs," *Electron. Lett.*, vol. 19, no. 3, pp. 112–113, 1983.

52. B. Chapman, *Glow discharge processes*. New York: John Wiley & Sons, 1980.

53. S. M. Rossnagel, "High-vacuum-based processes: Sputtering," in *Handbook of vacuum science and technology* (D. M. Hoffman, B. Singh, and J. H. Thomas, III, eds.), ch. 5.1, San Diego: Academic Press, 1998.

54. T. Suntola and J. Hyvärinen, *Atomic layer epitaxy*, vol. 15, pp. 177–195. Annual Review of Materials Science, 1985.

55. W. E. Howard, "Memory in thin-film electroluminescent devices," *J. Lumin.*, vol. 23, pp. 155–173, 1981.

56. D. Corlatan, K. Neyts, and P. D. Visschere, "The influence of space charge and electric field on the excitation efficiency in thin film electroluminescent devices," *J. Appl. Phys.*, vol. 78, pp. 7259–7264, Dec. 1995.

57. F. W. Billmeyer and M. Saltzman, *Principles of color technology*. New York: John Wiley & Sons, second ed., 1981.

58. A. C. Hardy, *Handbook of colorimetry*. Cambridge, MA: The Technology Press, 1936.

59. R. D. Overheim and D. L. Wagner, *Light and color*. New York: John Wiley & Sons, 1982.

60. Y. A. Ono, H. Kawakami, M. Fuyama, and K. Onisawa, "Transferred charge in the active layer and EL device characteristics of TFEL cells," *Jpn. J. Appl. Phys.*, vol. 26, pp. 1482–1492, Sept. 1987.

61. R. C. McArthur, J. D. Davidson, J. F. Wager, I. Khormaei, and C. N. King, "Capacitance-voltage characteristics of alternating-current thin-film electroluminescent devices," *Appl. Phys. Lett.*, vol. 56, pp. 1889–1891, May 1990.

62. P. D. Keir, "Modeling phosphor space charge in alternating-current thin-film electroluminescent devices," M.S. thesis, Oregon State University, 1996.

63. A. Abu-Dayah, S. Kobayashi, and J. F. Wager, "Internal charge-phoshor field characteristics of alternating-current thin-film electroluminescent devices," *Appl. Phys. Lett.*, vol. 62, pp. 744–746, Feb. 1993.

64. S.-P. Shih, "Electrical characterization and aging studies of ALEZnS:Mn ACT-FEL devices with varying phosphor thickness," M.S. thesis, Oregon State University, 1996.

65. R. L. Thuemler, "Characterization of alternating-current thin-film SrS:Ce electroluminescent devices," M.S. thesis, Oregon State University, 1997.

66. A. Abu-Dayah, "Internal charge-phosphor field analysis, electrical characterization, and aging studies of ac thin-film electroluminescent devices," M.S. thesis, Oregon State University, 1993.

67. L. V. Pham, "Electrical characterization, maximum charge-maximum voltage ($Q_{max}$-$V_{max}$) analysis, aging and temperature studies of thiogallate thin-film electroluminescent devices," M.S. thesis, Oregon State University, 1996.

68. R. Myers and J. F. Wager, "Transferred charge analysis of evaporated ZnS:Mn alternating-current thin-film electroluminescent devices," *J. Appl. Phys.*, vol. 81, pp. 506–510, Jan. 1997.

69. G. Vincent, A. Chantre, and D. Bois, "Electric field effect on the thermal emission of traps in semiconductor junctions," *J. Appl. Phys.*, vol. 50, pp. 5484–5487, Aug. 1979.

70. A. Fuh, R. P. Gallinger, P. Schuster, J. Adolph, and O. Caporaletti, "The effects of post-deposition annealing on Zns:Mn film crystalline structure and electroluminescent characteristics," *Thin Solid Films*, vol. 10, pp. 202–5, Jan. 1992.

71. Z. K. Kun, D. Leskell, P. R. Malmberg, J. Murphy, and L. J. Sienkiewicz, "The influence of chlorine on the crystal structure and electroluminescent behavior of ZnS:Mn film crystalline structure and electroluminescent characteristics," *J. Electron. Mater.*, vol. 10, pp. 287–300, Jan. 1981.

72. S. Takata, T. Minami, and T. Miyata, "Crystallinity of emitting layer and electroluminescence characteristics in multicolour ZnS thin film electroluminescent device with a thick dielectric ceramic insulating layer," *Thin Solid Films*, vol. 193-4, pp. 481–488, Dec. 1990.

73. Y. Nakanishi, Y. Fukuda, Y. Matanaka, and G. Shimaoka, "The dependence of the polycrystalline structure and electroluminescent properties of ZnS:Mn deposited on $Y_2O_3$ films on thickness," *Appl. Surf. Sci.*, vol. 48-9, pp. 297–300, May 1991.

74. S. Okamoto, T. Kuki, and T. Suzuki, "SrS:Ce thin-film electroluminescent devices fabricated by post-annealing technique and their electrical properties," *Jpn. J. Appl. Phys.*, vol. 32, no. 4A, pp. 1672–1680, 1993.

75. G. Blasse and B. C. Grabmaier, *Luminescent materials.* Berlin: Springer-Verlag, 1994.

76. Y.-M. Chiang, D. P. Birnie, III, and W. D. Kingery, *Physical ceramics: Principles for ceramic science and engineering.* New York: John Wiley & Sons, 1997.

77. R. M. German, *Sintering theory and practice.* New York: John Wiley & Sons, 1996.

78. C. M. Wolfe, N. Holonyak, Jr., and G. E. Stillman, *Physical properties of semiconductors.* Englewood Cliffs, NJ: Prentice Hall, 1989.

79. J. F. Wager, "Electroluminescent phosphors: Intrinsic point defects," in *Inorganic and organic electroluminescence* (R. H. Mauch and H.-E. Gumlich, eds.), (Berlin), Wissenschaft und Technik Verlag, 1996.

80. Y. Tamura and H. Kozawaguchi, "Sulphur defects and deep levels in SrS:Ce thin films," in *Proceedings of the 4th international conference on electroluminescence* (S. Shionoya and H. Kobayashi, eds.), (Berlin), Springer-Verlag, 1989.

81. J. C. Phillips, *Bonds and bands in semiconductors.* New York: Academic Press, 1973.

82. W. Lehmann, "Activators and co-activators in calcium sulfide phosphors," *J. Lumin.*, vol. 5, pp. 87–107, 1972.

83. S. M. Sze, *Physics of semiconductor devices.* New York: John Wiley & Sons, second ed., 1981.

84. R. H. Bube, *Electrons in solids.* New York: Academic Press, 1981.

85. H. Lüth, *Surfaces and interfaces of solids.* Berlin: Springer-Verlag, third ed., 1995.

86. W. A. Harrison, *Electronic structure and the properties of solids.* New York: Dover, 1989.

87. J. C. Bailar, Jr., T. Möller, J. Kleinberg, C. O. Guss, M. E. Castellion, and C. Metz, *Chemistry.* New York: Academic Press, 1978.

88. Cerac, Inc., *Vacuum deposition chemicals & evaporation materials*, third ed., 1988.

89. D. Li, *Phosphor development: synthesis, characterization, and chromatic control.* PhD thesis, Oregon State University, 1999.

90. C. E. Schäffer and C. K. Jørgensen, "The nephelauxetic series of ligands corresponding to increasing tendency of partly covalent bonding," *J. Inorg. Nucl. Chem.*, vol. 8, pp. 143–148, 1958.

91. C. E. Schäffer and C. K. Jørgensen, "Some examples of different spectroscopic and magnetic properties connected with the chromium III - oxygen bond," *J. Inorg. Nucl. Chem.*, vol. 8, pp. 149–154, 1958.

92. T. A. Oberacker and H. W. Schock, "Investigations of the influence of halides on the properties of CeX$_3$-doped (X=Cl,F) strontium sulfide thin film electroluminescent devices," *J. Crystal Growth*, vol. 159, no. 1-4, pp. 935–8, 1996.

93. S. Tanaka, S. Ohshio, J. Nishiura, H. Kawakami, H. Yoshiyama, and H. Kobayashi, "Bright white-light electroluminescence in potassium- and praseodymium-doped strontium sulfide thin films," *Appl. Phys. Lett.*, vol. 52, no. 25, pp. 2102–2104, 1988.

94. S.-S. Sun, T. Nguyen, M. S. Bowen, J. Kane, P. N. Yocom, A. Naman, K. Jones, P. H. Holloway, D. R. Evans, and W. M. Dennis, "High-luminance SrS:Ce,Ga,F thin-film electroluminescent devices," *J. SID*, vol. 6, no. 1, pp. 61–65, 1998.

95. C. N. King, "Electroluminescence: an industry perspective," *J. SID*, vol. 4, no. 3, pp. 153–156, 1996.

96. M. Kawata and H. Uchiike, "Evaluation of SrS:CeN phosphor thin films," *IEICE Trans. Electron.*, vol. E80-C, pp. 1109–1113, Aug. 1997.

97. W. Lehmann, "Cathodoluminescence of CaS:Ce$^{3+}$ and CaS:Eu$^{2+}$ phosphors," *J. Electrochem. Soc.*, vol. 118, Mar. 1971.

98. S. Shionoya, "Principle phosphor materials and their optical properties: IIb-IVb compounds," in *Phosphor handbook* (S. Shionoya, ed.), pp. 231–257, Boca Raton: CRC Press, 1999.

99. S. Shionoya, ed., *Phosphor Handbook*. Boca Raton: CRC Press, 1999.

100. C. R. Abernathy, "Grwoth of group III nitrides from molecular beams," in *GaN and related materials* (S. J. Pearton, ed.), vol. 2, ch. 2, pp. 11–51, Amsterdam: Gordon and Breach Science, 1997.

101. B. P. Keller, S. Keller, D. Kopolnek, W.-N. Jiand, Y.-F. Wu, H. Masui, X. Wu, B. Heying, and J. S. Speck, "Metalorganic chemical vapor deposition growth of high optical quality and high mobility GaN," *J. Electron. Mater.*, vol. 24, no. 11, pp. 1707–1709, 1995.

102. S. Strite and H. Markoc, "Gallium nitride, aluminum nitride, and indium nitride: A review," *J. Vac. Sci. Technol. B*, vol. 10, no. 4, pp. 1237–1266, 1992.

103. L. B. Pankratz, "Thermodynamic properties of carbides, nitrides, and other selected substances," Bulletin 696, U. S. Bureau of Mines, 1995.

104. O. J. Gregory and E. E. Crisman, "Applications of oxides and nitrides of germanium for semiconductor devices," in *Integrated circuits: Chemical and physical processing* (P. Stroeve, ed.), no. 290 in American Chemical Society Symposium Series, ch. 11, pp. 178–220, Washington, D.C.: American Chemical Society, 1985.

105. D. R. Lide, ed., *CRC handbook of physics and chemistry*. Boca Raton: CRC Press, 71 ed., 1990.

106. D. Sangeeta, *Inorganic materials chemistry desk reference*. Boca Raton: CRC Press, 1997.

107. E. C. Franklin, *The nitrogen system of compounds*. New York: Reinhold Publishing Corp., 1935.

108. T. D. O'Brien, M. C. Sneed, and R. C. Brasted, "Scandium, yttrium, and the lanthanide series," in *Zinc, cadmium, and mercury; Scandium, yttrium, and the lanthanide series* (M. C. Sneed and R. C. Brasted, eds.), vol. 4 of *Comprehensive Inorganic Chemistry*, Princeton: D. Van Nostrand Co., 1955.

109. K. Clusius, "Rubidium and cesium nitrides," *Z. Anorg. Allgem. Chem.*, vol. 194, pp. 47–50, 1930.

110. K. W. Bagnell, "Selenium, tellurium, and polonium," in *Comprehensive inorganic chemistry* (J. C. Bailar, H. J. Emeléus, S. D. Nyholm, and A. F. Trotman-Dickenson, eds.), vol. 2, ch. 24, Oxford: Pergamon Press, 1973.

111. R. Schwarz and A. Jeanmarie, "The ammonolysis of antimony trichloride," *Ber.*, vol. 65, pp. 1662–1664, 1932.

112. N. V. Sidgwick, *The chemical elements and their compounds*. Oxford: Clarendon Press, 1950.

113. R. E. Honig and H. D. Hook, "Vapor pressure data for some common gases," *RCA Rev.*, vol. 21, p. 360, Sept. 1960.

114. H. L. Caswell, "Analysis of the residual gases in several types of high-vacuum evaporators," *IBM J. Res. Develop.*, vol. 4, p. 130, Apr. 1960.

115. R. Glang, R. A. Holmwood, and J. A. Kurtz, "High-vacuum technology," in *Handbook of thin film technology* (L. I. Maissel and R. Glang, eds.), ch. 2, New York: McGraw-Hill, 1970.

116. D. L. Smith, *Thin-Film Deposition Principle & Practice*. New York: McGraw-Hill, 1995.

117. B. Monemar, J. P. Bergman, and I. A. Buyanova, "Optical characterisation of GaN and related materials," in *GaN and related materials* (S. J. Pearton, ed.), ch. 4, pp. 85–139, Amsterdam: Gordon and Breach Scientific, 1997.

118. G. A. Slack and T. F. M. Chelly, "Growth of high purity AlN crystals," *J. Crystal Growth*, vol. 34, no. 2, pp. 263–279, 1976.

119. A. Abid, R. Bensalem, and B. J. Sealy, "The thermal stability of AlN," *J. Mater. Sci.*, vol. 21, no. 4, pp. 1301–1304, 1986.

120. W. H. Strehlow and E. L. Cook, "Compilation of energy band gaps in elemental and binary compound semiconductors," *J. Phys. Chem. Ref. Data*, vol. 2, no. 1, pp. 163–193, 1973.

121. H. Braedecke and W. Bludau, "Optical absorption of lithium nitride," *J. Appl. Phys.*, vol. 50, pp. 4743–4746, July 1979.

122. G. P. Dubrovskii and B. V. Chernovets, "Forbidden band width of $Mg_3N_2$ [spectra observations]," *Inorg. Mater.*, vol. 16, pp. 970–972, Aug. 1980.

123. K. Kuriyama, Y. Takahashi, and F. Sunohara, "Optical bandgap of $Zn_3N_2$ films," *Phys. Rev. B: Condens. Matter*, vol. 48, no. 4, pp. 2781–2782, 1993.

124. M. L. Cohen, "Structural, electronic, and optical properties of carbon nitride," *Mat. Sci. & Eng.*, vol. A209, pp. 1–4, 1996.

125. F. Hulliger, "Rare earth pnictides," in *Handbook on the physics and chemistry of rare earths* (J. K[arl] A. Gschneider and L. Eyring, eds.), vol. 4, ch. 33, Amsterdam: North-Holland Publishing Co., 1979.

126. Y. Pauleau, J. J. Hautzpergue, and J. C. Remy, "Le nitrure de germanium (iv)," *Mat. Chem.*, vol. 5, pp. 371–96, 1980.

127. U. Hahn and W. Weber, "Electronic structure and chemical bonding mechanism of $Cu_3N$, $Cu_3NPd$ and related Cu(I) compounds," *Phys. Rev. B: Condens. Matter*, vol. 53, no. 19, pp. 12684–12693, 1996.

128. F. Kido, N. Matsuda, H. Yoshikawa, and M. Tamatami, "Thin film electroluminescence device with ZN concentration gradient." United States Patent, July 1991.

129. G. J. Moody and J. D. R. Thomas, "Alkali metal nitrides," *J. Chem. Ed.*, vol. 43, pp. 205–206, Apr. 1966.

130. M. S. Bhamara and D. J. Fray, "The electrochemical properties of $Li_3AlN_2$ and $Li_2SiN_2$," *J. Mater. Sci.*, vol. 30, no. 21, pp. 5381–5388, 1995.

131. G. K. Gaido, G. P. Dubrovskii, and A. M. Zykov, "Photoluminescence of $MgSiN_2$ activated by europium," *Inorg. Mater.*, vol. 10, no. 3, pp. 487–495, 1974.

132. T. Endo, Y. Sato, and M. Shimada, "High-pressure synthesis of new compounds $ZnSiN_2$ and $ZnGeN_2$ with distorted wurtzite structure," *J. Mater. Sci. Lett.*, vol. 11, pp. 424–426, Apr. 1992.

133. U. Berger and W. Schnick, "Syntheses, crystal structure, and vibrational spectroscopic properties of $MsCN_2$, $SrCN_2$, and $BaCN_2$," *J. Alloys. & Comp.*, vol. 206, pp. 179–184, 1994.

134. W. A. Groen, M. J. Kraan, and G. De With, "New ternary nitride ceramics: $CaSiN_2$," *J. Mater. Sci.*, vol. 29, pp. 3161–3166, 1994.

135. T. T. Nguyen, "Phosphor development for alternating-current thin-film electroluminescent applications," M.S. thesis, Oregon State University, 1994.

136. M. R. Mueller, "Development and characterization of AlInN as an alternating-current thin-film electroluminescent display phosphor," M.S. thesis, Oregon State University, 1995.

137. L. E. Toth, *Transition metal carbides & nitrides*. New York: Academic Press, 1971.

138. K. Klemm, L. F. Johnson, W. E. Kosik, D. R. McKenzie, I. Perez, and M. Pontelandolfo, "Hafnium nitride dielectric phase films fabricated by ion-beam sputtering," in *Covalent ceramics II: non-oxides* (A. R. Barron, G. S. Fischman, M. A. Fury, and A. F. Hepp, eds.), vol. 327, pp. 97–102, Pittsburgh: Materials Research Society, 1994.

139. P. D. Johnson, "Oxygen-dominated lattices," in *Luminescence of Inorganic Solids* (P. Goldberg, ed.), ch. 5, pp. 287–336, New York: Academic Press, 1966.

140. A. H. Kitai, "Thin film electroluminescent oxide phosphors," in *Extended abstracts of the fourth international conference on the science and technology of display phosphors / the ninth international workshop on inorganic and organic electroluminescence*, pp. 199–202, Sept. 1998.

141. T. Minami, "Oxide phosphor thin-film electroluminescent devices using thick insulating ceramic sheets," in *Extended abstracts of the fourth international conference on the science and technology of display phosphors / the ninth international workshop on inorganic and organic electroluminescence*, pp. 195–198, Sept. 1997.

142. K. Morimoto, "Phosphors for vacuum fluorescent displays and field emission displays," in *Phosphor handbook* (S. Shionoya, ed.), pp. 561–580, Boca Raton: CRC Press, 1999.

143. H. H. Henning and S. G. Luxon, "Hazardous substances," in *Hazards in the chemical laboratory* (S. G. Luxon, ed.), pp. 180–675, Cambridge: Royal Society of Chemistry, fifth ed., 1992.

144. M.-A. Armour, *Hazardous laboratory chemicals disposal guide*. Boca Raton: Lewis Publishers, second ed., 1996.

145. P. N. Yocom. Private Communication, Dec. 1995.

146. S. Shionoya, "Luminescence of lattices of the ZnS type," in *Luminescence of Inorganic Solids* (P. Goldberg, ed.), ch. 4, pp. 205–286, New York: Academic Press, 1966.

147. I. Szczurek and H. Lozykowski, "Electroluminescence of zinc selenide thin-films doped with the rare-earth fluorides," *J. Lumin.*, vol. 14, no. 5-6, pp. 389–402, 1976.

148. J. Shah and A. E. DiGiovanni, "The ac electroluminescence in thin-film manganese-doped zinc selenide (ZnSe)," *Appl. Phys. Lett.*, vol. 33, no. 12, pp. 995–996, 1978.

149. D. C. Morton and F. E. Williams, "A new thin-film electroluminescent material-$ZnF_2$:Mn," *Appl. Phys. Lett.*, vol. 35, pp. 671–672, Nov. 1979.

150. T. Suyama, K. Okamoto, and Y. Hamakawa, "New type of thin-film electroluminescent device having a multilayer structure," *Appl. Phys. Lett.*, vol. 41, pp. 462–464, Sept. 1982.

151. N. Miura, T. Sasaki, H. Matsumoto, and R. Nakano, "Electroluminescence of $ZnF_2$ thin-films dopes with rare-earth ions," *Jpn. J. Appl. Phys.*, vol. 31, no. 1, 1992.

152. K. Ohmi, S. Tanaka, H. Kobayashi, and T. Nire, "Electroluminescent devices with $(Y_2O_2S:Tb/ZnS)_n$ multilayered phosphor thin films prepared by multi-source deposition," *Jpn. J. Appl. Phys.*, vol. 31, pp. L1366–L1369, Sept. 1992.

153. D. Poelman, R. Vercaemst, R. L. Van Meirhaeghe, W. H. LaFlere, and F. Cardon, "The influence of se-coevaporation on the emission spectra of CaS:Eu and SrS:Ce thin film electroluminescent devices," *J. Lumin.*, vol. 65, no. 1, pp. 7–10, 1995.

154. S.-S. Sun. Private Communication, Feb. 1998.

155. Target Materials, Inc., Columbus, OH, *Care and feeding of your sputtering target*, Mar. 1994.

156. J. Lewis, K. E. Waldrip, M. R. Davidson, D. Moorehead, P. H. Holloway, and S.-S. Sun, "Improved brightness and efficiency in EL thin-film phosphors by fluxing," in *Extended abstracts of the fourth international conference on the science and technology of display phosphors / the ninth international workshop on inorganic and organic electroluminescence*, pp. 227–230, Sept. 1998.

157. S.-S. Sun, "Blue emitting SrS:Ag,Cu TFEL devices," in *Extended abstracts of the fourth international conference on the science and technology of display phosphors / the ninth international workshop on inorganic and organic electroluminescence*, pp. 183–186, Sept. 1998.

158. W. Park, T. C. Jones, E. Mohammed, C. J. Summers, and S.-S. Sun, "Luminescence properties of SrS:Cu,Ag thin-film electroluminescent phosphors," in *Extended abstracts of the fourth international conference on the science and technology of display phosphors / the ninth international workshop on inorganic and organic electroluminescence*, pp. 215–218, Sept. 1998.

159. W. Park, T. C. Jones, and C. J. Summers, "Optical properties of SrS:Cu,Ag two-component phosphors for electroluminescent devices," *Appl. Phys. Lett.*, Mar. 1999.

160. P. M. Alt, "Thin-film electroluminescent displays: device characteristics and performance," *Proc. SID*, vol. 25/2, pp. 123–146, 1984.

161. W. Lehmann, "Alkaline earth sulfide phosphors activated by copper, silver, and gold," *J. Electrochem. Soc.*, vol. 117, Nov. 1970.

162. B. Clark. Private Communication, June 1999.

163. J. Lewis, "Summary report for sputter deposition study of $Zn_2GeO_4$:Mn." Planar proprietary, Aug. 1997.

164. B. Cleary. Private Communication, 1997.

165. S. des Nitrures, "Synthesis of $Be_3N_2$." British Patent no. 5,795, Mar. 1912.

166. F. Frichter and E. Brunner, "Beryllium nitride," *Z. Anorg. Allgem. Chem.*, vol. 93, pp. 84–94, 1915.

167. C. M. Lieber and Z. J. Zhang, "Synthesis of covalent carbon-nitride solids:alternatives to diamond?," *Adv. Mater.*, vol. 6, no. 6, 1994.

168. K. Wade and A. J. Banister, "Aluminum, gallium, indium, and thallium," in *Comprehensive inorganic chemistry* (J. C. Bailar, H. J. Eméleus, S. D. Nyholm, and A. F. Trotman-Dickenson, eds.), vol. 1, ch. 12, Oxford: Pergamon Press, 1973.

169. A. Hahn and A. Juze, "Something about ge," *Z. Anorg. Allgem. Chem.*, vol. 244, pp. 111–?, 1940.

170. A. Lodzina, T. N. Miller, and A. Vitola, "Reaction of phosphorous (III) chloride with ammonia," *Kim. Ser.*, no. 2, pp. 135–141, 1979.

171. A. Mikogami, M. Hasegawa, and M. Yamashita, "Blah blah blah!!!." Japan Kokai 75 54,600, July 1973.

172. H. M. Cyr, M. C. Sneed, and R. C. Brasted, "Zinc, cadmium, and mercury," in *Zinc, cadmium, and mercury; Scandium, yttrium, and the lanthanide series* (M. C. Sneed and R. C. Brasted, eds.), vol. 4 of *Comprehensive Inorganic Chemistry*, Princeton: D. Van Nostrand Co., 1955.
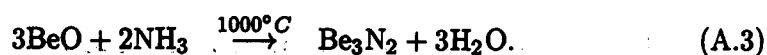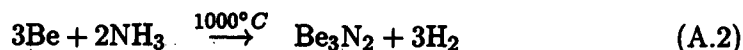
# APPENDICES

# A. SYNTHESIS OF NITRIDE COMPOUNDS

Many of the nitride materials that are necessary for investigation of phosphor properties are either prohibitively expensive, or difficult to obtain. For these reasons, it may be necessary to synthesize some of these materials from more common and/or less expensive materials. This appendix is provided as a guide to synthesis of many of these compounds in the simplest and safest method possible. To most effectively follow these guidelines, the starting materials for nitride synthesis are generally pure elements or their oxides, because these are generally the most available and affordable forms of the elements. Furthermore, the byproducts of these elemental sources are not typically hazardous. The entries in this appendix are organized alphabetically by the most electronegative cation and provide the desired chemical reaction, synthesis temperature, synthesis atmosphere, and references to the sources of this information.

- $Be_3N_2$: Three techniques for synthesis of $Be_3N_2$ appear in the literature that lead to the emanation of only non-toxic and non-corrosive gases. These techniques all employ either Be or BeO as the starting material because these are the most affordable and readily available sources of Be. The first technique involves the mixture of stoichiometric amounts of C and BeO with subsequent firing in a $N_2$ atmosphere at 1400°C to drive the reaction [165]

$$6BeO + 3C + 2N_2 \overset{1400°C}{\longrightarrow} 2Be_3N_2 + 3CO_2. \qquad (A.1)$$

The second method produces $Be_3N_2$ by heating either Be or BeO powder to 1000°C in an $NH_3$ atmosphere to drive one of the following reactions: [166]

$$3Be + 2NH_3 \overset{1000°C}{\longrightarrow} Be_3N_2 + 3H_2 \qquad (A.2)$$

$$3BeO + 2NH_3 \overset{1000°C}{\longrightarrow} Be_3N_2 + 3H_2O. \qquad (A.3)$$

- $C_3N_4$: The synthesis of $C_3N_4$ source material is not possible with conventional high-temperature driven reactions. [167] Synthesis of this compound reported

in the literature has always been conducted via rf and/or microwave plasma deposition of thin-films.

- GaN: The synthesis of GaN should begin with either Ga metal or $Ga_2O_3$ as the starting material because these are the most affordable and readily available sources of Ga. Researchers have successfully synthesized GaN by heating Ga metal to 1100°C in an $NH_3$ atmosphere to drive the following reaction: [128]

$$2Ga + 2NH_3 \xrightarrow{1100°C} 2GaN + 3H_2. \tag{A.4}$$
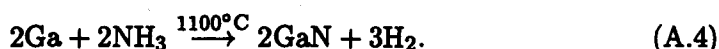
This reaction can be accelerated by the addition of ammonium carbonate which provides gases that stir up the liquid metal and facilitate access to the nitriding agent. [168]

- $Ge_3N_4$: The synthesis of $Ge_3N_4$ should begin with either Ge metal or $GeO_2$ because these are the most affordable and readily available forms sources of Ge. The synthesis of $Ge_3N_4$ has been achieved by the ammonolysis of both of these compounds at 700°C. [104, 169] The reactions of interest are

$$3Ge + 4NH_3 \xrightarrow{700°C} Ge_3N_4 + 6H_2 \tag{A.5}$$

$$3GeO_2 + 4NH_3 \xrightarrow{700°C} Ge_3N_4 + 6H_2O. \tag{A.6}$$
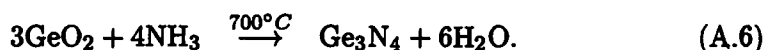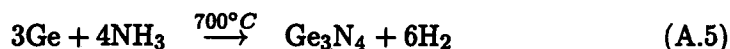
- InN: The synthesis of InN has been performed through the ammonolysis of $In_2O_3$ at 620-630°C. [168] The reaction

$$In_2O_3 + 2NH_3 \xrightarrow{620-630°C} 2InN + 3H_2O \tag{A.7}$$
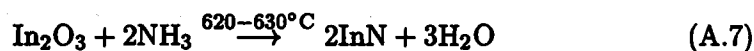
should proceed to completion in about 4 hours when held at these temperatures.

- $P_3N_5$: The preparation of $P_3N_5$ is in general more complex than the preparation of most of the more common nitrides. One method for the synthesis of this compound is via the ammonolysis of $PCl_3$, [170]

$$3PCl_3 + 5NH_3 \xrightarrow{850°C} P_3N_5 + 9HCl + 3H_2. \tag{A.8}$$
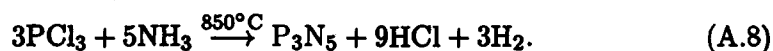
Another method for the nitridation of phosphorous is to convert the sulphide, $P_2S_5$,

$$3P_2S_5 + 10NH_3 \longrightarrow 2P_3N_5 + 15H_2S. \tag{A.9}$$
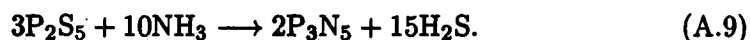
The first step in accomplishing this is to treat $P_2S_5$ powder in flowing $NH_3$ in a quartz tube for 2 hours. Next, the $P_2S_5$ is heated to 250°C in 30 minutes while still under flowing $NH_3$ and allowed to rest at that temperature for 4 hours. Then, with the $NH_3$ still flowing, the temperature is raised to 600°C in 1.5 hours and held for 2 additional hours. Finally, the powder is allowed to cool to room temperature and pulverized until the average particle size is <1mm. The powder resulting from this pulverization is then heated in flowing $NH_3$ to 900°C and held for several hours to complete the nitridation of phosphorous. [171]

- $Sn_3N_4$: The synthesis of $Sn_3N_4$ by the ammonolysis of $SnCl_4$ and subsequent decomposition of the products has been reported. First, the ammonolysis of $SnCl_4$ is performed to yield

$$SnCl_4 + NH_3 \xrightarrow{270°C} SnNCl + 3HCl. \tag{A.10}$$
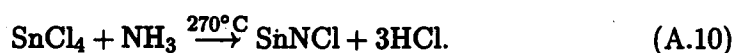
- $Zn_3N_2$: The synthesis of $Zn_3N_2$ by the ammonolysis of Zn powder has been reported. [172] This reaction is performed by reacting Zn powder with flowing $NH_3$ at 600°C,

$$3Zn + 2NH_3 \xrightarrow{600°C} Zn_3N_2 + 3H_2. \tag{A.11}$$
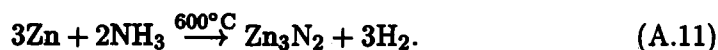
# B. SYNTHESIS OF SULFIDE COMPOUNDS

The importance of sulfide phosphor materials in the ACTFEL display industry cannot be understated. However, some of the best sulfide ACTFEL phosphor hosts are either unavailable in pure enough form, or are prohibitively expensive. As a result, it may often be necessary to synthesize several of these compounds in-house to achieve affordability and proper purity levels. This Appendix presents synthesis techniques that have been successful for the most important of these compounds.

Alkaline Earth Sulfides (CaS,SrS,BaS): The alkaline earth sulfides, especially SrS, are generally quite expensive to purchase from chemical companies. In addition, CaS and BaS may not be available in phosphor grade purities. As a result, in-house synthesis is often necessary to perform research with these ACTFEL phosphors. The synthesis of these compounds is typically initiated from the alkaline earth carbonates because these are the most inexpensive and stable sources of the alkaline earth elements. The sulfurization of the alkaline earth carbonates begins by the thermal conversion of the carbonates to oxide. Then, sulfurization is initiated with the addition of $H_2S$ to the synthesis furnace at temperatures greater than 1000°C. The chemical reaction for this is as follows:

$$AeCO_3 \xrightarrow{heat} AeO + CO_2 AeO + H_2S \xrightarrow{>1000°C} AeS + H_2O, \qquad (B.1)$$
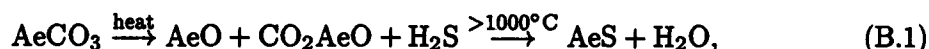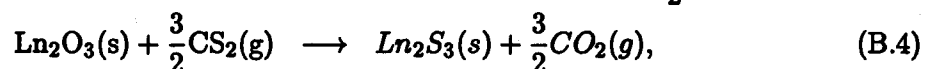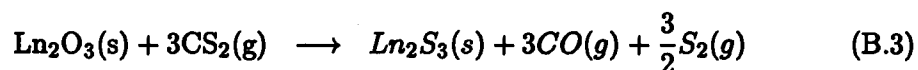
where Ae is Ca, Sr, or Ba.

$Ln_2S_3$: The sesquisulfides of the lanthanide series elements are typically prepared from the reaction of the corresponding sesquioxides with $H_2S$ or $CS_2$. When the sesquioxides are heated to temperatures in excess of 1100°C in an $H_2S$ atmosphere, the reaction,

$$Ln_2O_3 + 3H_2S \longrightarrow Ln_2S_3 + 3H_2O, \qquad (B.2)$$

occurs where Ln represents any of the lanthanide series elements except for Pm and Eu. This reaction must be performed at temperatures in excess of 1100°C in order

to obtain oxygen-free samples. The time required to complete this reaction is on the order of 24 hours.

The alternative method for synthesizing the sesquisulphides of the lanthanide series elements from their corresponding sesquioxides is by reaction with $CS_2$. The reaction of $CS_2$ with the lanthanide series sesquioxides leads to both of the following reactions,

$$Ln_2O_3(s) + 3CS_2(g) \longrightarrow Ln_2S_3(s) + 3CO(g) + \frac{3}{2}S_2(g) \tag{B.3}$$

$$Ln_2O_3(s) + \frac{3}{2}CS_2(g) \longrightarrow Ln_2S_3(s) + \frac{3}{2}CO_2(g), \tag{B.4}$$

of which the first is energetically favored. This method has several advantages over the previous method in terms of temperature required and time of reaction. Generally, the temperature range required for these reactions to proceed to completion is in the range between 800°C and 1100°C.